

Lewis/Grant
292 pages

IN-21889

(NASA-CR-176947) THERMODYNAMIC EVALUATION
OF TRANSONIC COMPRESSOR ROTORS USING THE
FINITE VOLUME APPROACH Status Report

N86-30731

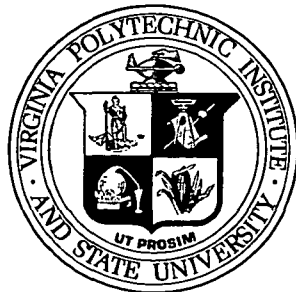
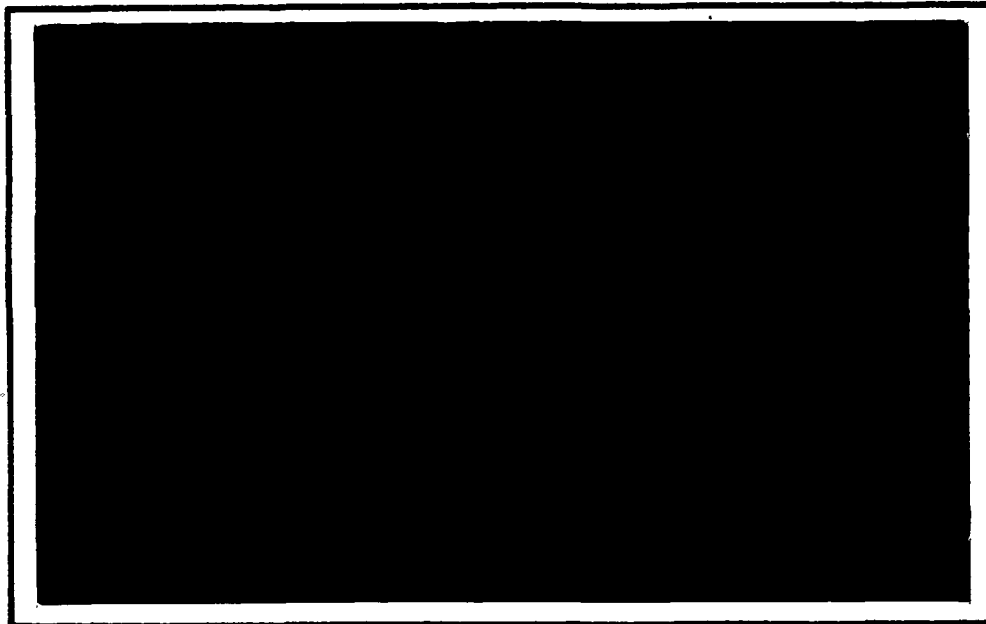
(Virginia Polytechnic Inst. and State Univ.)

Unclas

292-p

CSC 21E G3/07 43454

**COLLEGE
OF
ENGINEERING**



**VIRGINIA
POLYTECHNIC
INSTITUTE
AND
STATE
UNIVERSITY**

**BLACKSBURG,
VIRGINIA**

Status Report - August 1986
on
NASA Grant No. NAG 3-593
Thermodynamic Evaluation of Transonic Compressor Rotors
Using the Finite Volume Approach

Extension of the Finite Volume Method
to Laminar and Turbulent Flow

by
Stephen Nicholson
Instructor

John Moore
Professor of Mechanical Engineering
Principal Investigator

Grantee Institution -
NASA Lewis Research Center
21000 Brookpark Road
Cleveland, Ohio 44135

Turbomachinery Research Group
Report No. JM/86-6

Mechanical Engineering Department
Virginia Polytechnic Institute and State University
Blacksburg, Virginia 24061

**Extension of the Finite Volume Method
to Laminar and Turbulent Flow**

by

Stephen Nicholson
John Moore, Chairman
Mechanical Engineering

(ABSTRACT)

A method has been developed which calculates two-dimensional, transonic, viscous flow in ducts. The finite volume, time marching formulation is used to obtain steady flow solutions of the Reynolds-averaged form of the Navier Stokes equations. The entire calculation is performed in the physical domain. The method is currently limited to the calculation of attached flows.

The features of the current method can be summarized as follows. Control volumes are chosen so that smoothing of flow properties, typically required for stability, is not needed. Different time steps are used in the different governing equations to improve the convergence speed of the viscous calculations. A new pressure interpolation scheme is introduced which improves the shock capturing ability of the method. A multi-volume method for pressure changes in the boundary layer allows calculations which use very long and thin control volumes ($\text{length/height} \cong 1000$). A special discretization technique is also used to stabilize these calculations which use long and thin control volumes. A special formulation of the energy equation is used to provide improved transient behavior of solutions which use the full energy equation.

The method is then compared with a wide variety of test cases. The freestream Mach numbers range from 0.075 to 2.8 in the calculations. Transonic viscous flow in a converging diverging nozzle is calculated with the method; the Mach number upstream of the shock is approximately 1.25. The agreement between the calculated and measured shock strength and total pressure losses is good. Essentially incompressible turbulent boundary layer flow in an adverse pressure gradient is calculated and the computed distribution of mean velocity and shear stress are in good agreement with

the measurements. At the other end of the Mach number range, a flat plate turbulent boundary layer with a freestream Mach number of 2.8 is calculated using the full energy equation; the computed total temperature distribution and recovery factor agree well with the measurements when a variable Prandtl number is used through the boundary layer.

Acknowledgements

First I would like to thank my wife Martha for her patience and understanding through these four years. Also due great thanks are John and Joan Moore. Without both of their help, this work would not have been possible. John has been available every step of the way to ensure that we did not sway from our goal. He also kept us honest with his very astute observations. Joan has provided me with immeasurable help in understanding and discovering the ideas that were developed in this disseratation. Together they are a team which is hard to beat. I would also to thank the members of my committee; Dr. Bernard Grossman, Dr. Hal Moses, Dr. Walter O'Brien, and Dr. George Swift, for their participation in this endeavor. Thanks are also due to NASA Lewis Research Center, specifically Mr. Jerry Wood and Dr. Lou Povinelli, for supporting this work through NASA Grant NAG 3-593. Finally I would like to thank Dr. J.B. Jones for providing me with an opportunity to be an instructor at V.P.I. & S.U. which has made my work here financially possible.

Table of Contents

1.0 INTRODUCTION AND LITERATURE REVIEW	1
DENTON'S METHOD	10
PRESENT CONTRIBUTION	12
2.0 ANALYSIS SECTION	15
2.1 GOVERNING EQUATIONS	15
2.2 CONTROL VOLUMES	20
2.3 DISTRIBUTION OF PROPERTIES	26
2.4 PRESSURE INTERPOLATION PROCEDURE	34
2.5 TIME STEPS	59
DIFFERENTIAL FORM	63
DESCRETIZED FORM	67
2.6 BOUNDARY CONDITIONS AND INITIAL GUESS	84
BOUNDARY CONDITIONS	84
INITIAL GUESS	85
2.7 CALCULATION OF VISCOUS FORCES	85
2.8 MULTI-VOLUME METHOD FOR PRESSURE CHANGES	102

2.9 TRANVERSE UPWIND DIFFERENCING	103
2.10 ENERGY EQUATION	116
3.0 RESULTS	126
3.1 FLAT PLATE BOUNDARY LAYER	126
3.2 INVISCID CALCULATIONS OF SAJBEN'S DIFFUSER	129
3.3 THE INFLUENCE OF TRANSVERSE SMOOTHING ON A STEP PROFILE IN A STRAIGHT DUCT	133
3.4 1-D COMPUTATIONAL TESTS OF SHOCK CAPTURING USING PRESSURE INTERPOLATION FORMULAE TO CALCULATE EFFECTIVE DENSITY	147
3.5 LAMINAR BOUNDARY LAYER IN TWO CONVERGING DUCTS	170
3.6 SAMUEL AND JOUBERT INCOMPRESSIBLE TURBULENT BOUNDARY LAYER	199
3.7 SAJBEN'S DIFFUSER CALCULATIONS	206
3.8 ENERGY EQUATION TEST CASES	232
4.0 SUMMARY AND CONCLUSIONS	255
Appendix A. TRUNCATION ERROR OF PRESSURE INTERPOLATION EQUATION	263
Appendix B. VELOCITY GRADIENT IN A NON-ORTHOGONAL GRID	265
REFERENCES	270

LIST OF ILLUSTRATIONS

Fig. 1.1	Cell Centered Nodes	6
Fig. 1.2	Convergence History for Dawes' Calculations	9
Fig. 1.3	Typical Control Volume Used by Denton	11
Fig. 2.2.1	New Control Volumes	21
Fig. 2.2.2	Typical Control Volumes Used by Denton	23
Fig. 2.2.3	New Control Volumes in Three Dimensions	24
Fig. 2.2.4	New Control Volumes in Non-Uniform Grid	25
Fig. 2.3.1	Typical Control Volume	27
Fig. 2.3.2	1-D Example With Momentum Imbalance	28
Fig. 2.3.3	1-D Example With Continuity Imbalance (Pressure Update Method) ..	30
Fig. 2.3.4	1-D Example With Continuity Imbalance (Density Update Method) ..	32
Fig. 2.4.1	Calculation of Effective Pressure	36
Fig. 2.4.2	Geometry Used For 1-D Steady Flow Analysis	39
Fig. 2.4.3	Comparison of Calculated and Theoretical 1-D Static Pressure Distributions	50
Fig. 2.4.4	Acceptable Values of a_0 as a Function of Mach Number	55
Fig. 2.4.5	Acceptable Values of a_1 as a Function of Mach Number	57

Fig. 2.4.6	Stability Limits For a_0 when $a_2 = 0$ and $a_0 + a_1 = 1$, and for a_1 when $a_0 = 0$ and $a_1 + a_2 = 1$	58
Fig. 2.4.7	M&M Mach Number Dependent Values for the Coefficients in Eq. 2.4.57	60
Fig. 2.5.1	Identification of the Control Volume Faces	64
Fig. 2.5.2	Typical Flux Arrangement for a Control Volume	68
Fig. 2.5.3	1-D Geometry Used for Time Step Determination	73
Fig. 2.5.4	Time Steps Using CFL Condition and Current Stability Method	78
Fig. 2.5.5	Time Steps Comparison	79
Fig. 2.5.6	Simplified Geometry for Determination of Y-Momentum Equation Contribution to Time Step	80
Fig. 2.6.1	Periodicity Condition	86
Fig. 2.7.1	Typical Control Volume	88
Fig. 2.7.2	Two Typical Control Volumes	91
Fig. 2.7.3	Two Typical Control Volumes With Directional Vectors Identified For South Face	93
Fig. 2.7.4	Upper Wall Control Volume	94
Fig. 2.7.5	Lower Wall Control Volume	95
Fig. 2.7.6	Control Volume Arrangement for West Face Force evaluation	97
Fig. 2.7.7	Distances Normal to the Wall	98
Fig. 2.7.8	Normal Distance to the South Face of the Control Volume	100
Fig. 2.8.1	Multi-Volume Method For Pressure Changes in the Boundary Layer Using Successively Smaller Control Volumes	104
Fig. 2.9.1	Convective Momentum Fluxes For a Control Volume	107
Fig. 2.9.2	Schematic of Case #1	112
Fig. 3.1.1	Geometry and Grid For Flat Plate Laminar Boundary Layer Calculations	127

Fig. 3.1.2	Flat Plate Laminar Boundary Layer Velocity Profile	128
Fig. 3.2.1	Geometry and Grid for Inviscid Calculations of Sajben's Diffuser	130
Fig. 3.2.2	Comparison of Static Pressure With Effective Pressure for Sajben's Diffuser	131
Fig. 3.2.3	Comparison of Total Pressures Calculated Using Thermodynamic and Effective Pressure For Sajben's Diffuser	132
Fig. 3.2.4	Comparison of Static Pressures Calculated Using The Effective Pressure and Effective Density Methods for Sajben's Diffuser	134
Fig. 3.2.5	Comparison of Total Pressures Calculated Using The Effective Pressure and Effective Density Methods	135
Fig. 3.3.1	Non-Linear Smoothing	139
Fig. 3.3.2	Geometry and Grid Used For Step Profile	140
Fig. 3.3.3	Inlet Total Pressure Profile	141
Fig. 3.3.4	Mach Number Profiles At Different Axial Locations With Linear Smoothing	142
Fig. 3.3.5	Total Pressure Along Grid Lines With Linear Smoothing	143
Fig. 3.3.6	Exit Mach Number Profile Comparison Non-Linear And Linear Smoothing	144
Fig. 3.3.7	Mach Number Profiles At Inlet and Exit No Smoothing New Control Volumes	145
Fig. 3.3.8	Total Pressure Along Grid Lines No Smoothing - New Control Volumes	146
Fig. 3.4.1	Denton's Convergent-Divergent Nozzle With a Linear Variation of Mach Number With Distance	148
Fig. 3.4.2	Theoretical 1-D Solutions For Denton's Nozzle for Three Exit Static Pressures	
Fig. 3.4.2a	$PW = P / P_{t,inlet}$	149

Fig. 3.4.2b	Mach Number	150
Fig. 3.4.2c	$PTOT = P_t / P_{t,inlet}$	151
Fig. 3.4.3	M&M Mach Number Dependent Values For The Coefficients in Eq. 3.4.2	155
Fig. 3.4.4	Calculated 1-D Solutions For Denton's Nozzle Using Three Point Interpolation	
Fig. 3.4.4a	$PW = P / P_{t,inlet}$	157
Fig. 3.4.4b	Mach Number	158
Fig. 3.4.4c	$PTOT = P_t / P_{t,inlet}$	159
Fig. 3.4.5	Calculated 1-D Solutions For Denton's Nozzle Using Two Point Interpolation	
Fig. 3.4.5a	$PW = P / P_{t,inlet}$	160
Fig. 3.4.5b	Mach Number	161
Fig. 3.4.5c	$PTOT = P_t / P_{t,inlet}$	162
Fig. 3.4.6	Calculated 1-D Solutions For Denton's Nozzle Using M&M Formula	
Fig. 3.4.6a	$PW = P / P_{t,inlet}$	163
Fig. 3.4.6b	Mach Number	164
Fig. 3.4.6c	$PTOT = P_t / P_{t,inlet}$	165
Fig. 3.4.7	Comparison of Calculated Results With the Theoretical 1-D Solution For $P_{exit} / P_{t,inlet} = 0.80$	
Fig. 3.4.7a	$PW = P / P_{t,inlet}$	166
Fig. 3.4.7b	Mach Number	167
Fig. 3.4.7c	$PTOT = P_t / P_{t,inlet}$	168
Fig. 3.5.1	Smooth Geometry Using Non-Uniform Grid	172
Fig. 3.5.2	Smooth Geometry Using Uniform Grid	173
Fig. 3.5.3	Non-Smooth Geometry Using Uniform Grid	174
Fig. 3.5.4	Second Derivative of Radius For Converging Duct	175

Fig. 3.5.5	Skin Friction Coefficient Finite Volume Method vs Thwaites Method	178
Fig. 3.5.6	Skin Friction Coefficient Finite Volume Method Non-Uniform Vs Uniform Gridding	179
Fig. 3.5.7	Skin Friction Coefficient Smooth Geometry Vs Non-Smooth Geometry	180
Fig. 3.5.8	Transverse Pressure Coefficient Non-Smooth Geometry Uniform Grid	181
Fig. 3.5.9	Transverse Pressure Coefficient Smooth Geometry Non-Uniform Grid	183
Fig. 3.5.10	Transverse Pressure Coefficient Smooth Geometry Uniform Grid	184
Fig. 3.5.11	Transverse Pressure Coefficient Non-Uniform Grid Inlet V-Velocity Specified	185
Fig. 3.5.12	Pressure Coefficient Non-Smooth Geometry Uniform Grid	187
Fig. 3.5.13	Pressure Coefficient Smooth Geometry Non-Uniform Grid	188
Fig. 3.5.14	Pressure Coefficient Smooth Geometry Uniform Grid	189
Fig. 3.5.15	Pressure Coefficient Non-Uniform Grid Inlet V-Velocity Specified	190
Fig. 3.5.16	Momentum Residual For Laminar Boundary Layer Calculations	192
Fig. 3.5.17	Mass Flow Error For Laminar Boundary Layer Calculations	193
Fig. 3.5.18	Momentum Residual For Laminar Boundary Layer Calculation Local Vs Global Time Steps	195
Fig. 3.5.19	Mass Flow Error For Laminar Boundary Layer Calculations Local Vs Global Time Steps	196
Fig. 3.5.20	Momentum Residual For Laminar Boundary Layer Calculations Coarse Vs Fine Grid	197
Fig. 3.5.21	Mass Flow Error For Laminar Boundary Layer Calculations Coarse Vs Fine Grid	198
Fig. 3.6.1	Geometry and Grid For Samuel and Joubert	200
Fig. 3.6.2	Skin Friction Coefficient For Samuel and Joubert	202
Fig. 3.6.3	Shear Stress Distributions at $x = 1.04$ m, $x = 1.44$ m, and $x = 1.79$ m	203
Fig. 3.6.4	Shear Stress Distributions at $x = 2.38$ m, $x = 2.89$ m, and $x = 3.39$ m	204
Fig. 3.6.5	Mean Velocity Profiles For Samuel and Joubert Calculations	205

Fig. 3.7.1	Geometry and Grid For Sajben's Diffuser Calculations	207
Fig. 3.7.2	Static Pressure Contours for Sajben's Diffuser	210
Fig. 3.7.3	Mach Number Contours For Sajben's Diffuser	211
Fig. 3.7.4	Curved Wall Static Pressure For Sajben's Diffuser	212
Fig. 3.7.5	Comparison of Computed and Measured Shock Position	213
Fig. 3.7.6	Mach Number Along Grid Line at $y/h = 0.0950$	214
Fig. 3.7.7	Velocity Profile at $x/h = 2.31$	215
Fig. 3.7.8	Velocity Profile at $x/h = 4.03$	216
Fig. 3.7.9	Velocity Profile at $x/h = 6.34$	217
Fig. 3.7.10	Velocity Profile at $x/h = 8.20$	218
Fig. 3.7.11	Static Pressure Contours for Sajben's Diffuser Using Three Point Interpolation	220
Fig. 3.7.12	Mach Number Contours for Sajben's Diffuser Using Three Point Interpolation Scheme	221
Fig. 3.7.13	Mass-Averaged Total Pressure Losses For Boundary Layers and Shock	222
Fig. 3.7.14	Total Pressure Loss For Sajben's Diffuser Shock Vs Total Loss	224
Fig. 3.7.15	Momentum Residual For Sajben's Diffuser	226
Fig. 3.7.16	Momentum Residual For Denton's Nozzle	227
Fig. 3.7.17	Sample Results From Liou, Coakley, and Bergman	228
Fig. 3.7.18	Sample Results From Liu, Shamroth, and McDonald	230
Fig. 3.7.19	Sample Results From Talcott and Kumar	231
Fig. 3.8.1	Static Temperature Distribution Through The Boundary Layer For Samuel and Joubert at $M = 0.55$, $x = 200$ mm	234
Fig. 3.8.2	Total Temperature Distribution Through The Boundary Layer For Samuel and Joubert at $M = 0.55$, $x = 200$ mm	236
Fig. 3.8.3	Geometry and Grid For Boundary Layer Calculations at $M = 0.95$. . .	237

Fig. 3.8.4	Total Temperature Distribution For Flat Plate Boundary Layer at $M = 0.95$	239
Fig. 3.8.5	Energy Residual For Flat Plate Boundary Layer at $M = 0.95$	241
Fig. 3.8.6	Static Pressure Contours for Sajben's Diffuser With the Energy Equation	242
Fig. 3.8.7	Mach Number Contours for Sajben's Diffuser With Energy Equation	243
Fig. 3.8.8	Sajben's Diffuser Velocity Profiles at $x/h = 7.9$	244
Fig. 3.8.9	Total Temperature Distribution For Sajben's Diffuser	245
Fig. 3.8.10	Experimental Total Temperature Distribution of Van Driest	247
Fig. 3.8.11	Geometry and Grid for Boundary Layer Calculations at $M = 2.8$	248
Fig. 3.8.12	Total Temperature Distribution For Flat Plate Boundary Layer at $M = 2.8$	250
Fig. 3.8.13	Ratio of the Turbulent Transfer Coefficient Over The Length of a Radius in Turbulent Pipe Flow	252
Fig. 3.8.14	Total Temperature Distribution For Flat Plate Boundary Layer at $M = 2.8$ Computation Vs Experiment	253
Fig. 3.8.15	Total Temperature Distribution For Flat Plate Boundary Layer at $M = 0.95$ With Variable Prandtl Number	254
Fig. A2.1	Identification of Directional Vectors	266

LIST OF TABLES

Table 2.7.1	Prandtl Mixing Length Model	90
Table 2.9.1	Upwinded Interpolation Parameters	117
Table 3.3.1	Linear Smoothing of Flow Properties	137
Table 3.3.2	Procedure for Non-Linear Smoothing	138
Table 3.4.1	Results of Calculations for Denton's 1-D Nozzle	169
Table 3.5.1	Transverse Distribution of Grid Points for Laminar Calculations	177
Table 3.6.1	Node Distribution and Inlet Velocity Profile for Samuel and Joubert	201
Table 3.7.1	Transverse Distribution of Grid Points for Sajben's Diffuser	208
Table 3.7.2	Example Calculation of Total Pressure Loss for a Boundary Layer	223
Table 3.8.1	Transverse Distribution of Grid Points For M = 0.95 Test Case	238
Table 3.8.2	Transverse Distribution of Grid Points For M = 2.8 Test Case	249

NOMENCLATURE

a_0, a_1, a_2 constants used in pressure interpolation scheme

A Area vector

A_x x-component of area vector

A_y y-component of area vector

c speed of sound

CFL Courant, Friedrichs, and Lewy

CF correction factor for pressure

CL characteristic length

C_f skin friction coefficient

C_p constant pressure specific heat or pressure coefficient

C_{pt}	transverse pressure coefficient
C_v	constant volume specific heat
\underline{D}	directional vectors
e	internal energy
e_t	total internal energy
E_t	total energy per unit volume
\vec{F}	force vector
$FRATIO$	mass flux ratio
FT	time factor used by Denton
g_{int}	geometric interpolation parameter
g_N	north face interpolation parameter
g_s	south face interpolation parameter
h	enthalpy
h_t	total enthalpy
I, J, and K	grid indices
k	thermal conductivity

l	length
L	mixing length
\dot{m}	mass flow rate
\dot{m}_T	transverse mass flow rate
M	Mach number
P	static pressure
P_{eff}	effective pressure
P_s	pressure acting on the side of the control volume
P_0	total pressure
Pr_l	laminar Prandtl number
Pr_t	turbulent Prandtl number
q	heat flux vector
r	recovery factor
R	ideal gas constant
t	time
δt	time step

δt_c	continuity time step
δt_m	momentum time step
T	static temperature
T_{aw}	adiabatic wall temperature
T_0	total temperature
$T_{0\infty}$	freestream total temperature
<i>TIMEF</i>	time factor for current method
\underline{u}	velocity vector
u	x component of velocity vector
v	y component of velocity vector
v_{eff}	effective velocity used in time step calculation
V	magnitude of velocity vector
Vol	volume of control volume
w	z component of velocity vector
$x, y, \text{ and } z$	cartesian axis components
α	constant to adjust effective pressure in region of high gradients

δ	small change
δ_{ij}	Kronecker delta
γ	ratio of specific heats
λ	second coefficient of viscosity
μ	absolute viscosity
μ_{eff}	effective viscosity
μ_l	laminar viscosity
μ_t	turbulent viscosity
ρ	density
τ	shear stress

1.0 INTRODUCTION AND LITERATURE REVIEW

Computational Fluid Dynamics (CFD) has become a powerful tool in the past 20 years in predicting the fluid mechanics and heat transfer characteristics of certain flow fields. The advent of the modern, high speed computer has been the major driving force for the evolution and success of computational fluid mechanics. Because of the rapid decrease in computer costs as well as the equally rapid increase in computer speed, the solution of many complex fluid mechanics problems is possible on the digital computer. Computational fluid dynamics is used extensively in the aerospace and turbomachinery industries to predict flow over wings, around fuselages, through engine inlets, as well as the flow through components within the gas turbine engine.

Computational fluid dynamics solves a fluid mechanics problem by first discretizing the flow domain using a grid network of some kind. The governing partial differential equations are approximated and an approximate form of the governing equations is used to solve for the discrete values of flow properties at node points of the grid network. There are a number of ways of approximating the governing equations (continuity, momentum, and energy) and the most common are the finite difference method, the finite element method, and the finite volume method. The net result of all these methods is that the non-linear partial differential equations (governing equations) are re-

placed by many simultaneous algebraic equations. These algebraic equations can then be solved for the unknowns, which are the flow properties at the node points within the grid. This discrete solution is an approximation of the continuous solution provided by nature.

Experimental and analytical methods are also used in the analysis of fluid mechanics problems. Before the advent of the modern computer and modern computational algorithms, experimental methods were used extensively and were the main tool by which fluid systems were studied. The advantage of the experimental approach was and still is that it is capable of being the most realistic model of the true flow situation. However, the experimental approach does have a few disadvantages, namely (1) equipment is required to run the experiment (2) problems may arise in scaling the model to the actual flow, (3) measurement difficulties may be encountered, and (4) the cost of the experiment may be excessive.

Analytical methods have the restrictions that they are typically limited to simple geometries and to linear problems. They are usually restricted to linear problems because the mathematics involved becomes too unwieldy or the solution technique is not known. The exact solutions from analytical methods can be used to measure the accuracy of various numerical methods. However, because of the above restrictions on the geometry and linearity, analytical methods are of little practical use in solving today's complex engineering problems.

When compared to the previously described experimental and analytical methods, numerical methods have the following advantages and disadvantages. Numerical methods have no restriction on the linearity of the governing equations. Because of this, complicated physical situations can be modeled. However, because of the discrete nature of the formulation, the solution accuracy is limited because of truncation error. This truncation error is caused by the coarseness of a grid and the type of discretization used in a particular algorithm. If the flow field is discretized using a finer and finer grid, the truncation error will typically be reduced. However, as the grid becomes finer, the cost of the computations may become excessive and the computer's storage capacity may be exceeded. Even though modern computational algorithms can be very powerful tools in the anal-

ysis of fluid mechanics problems, there are practical limitations to the problems which can be solved.

The numerical techniques used to solve for the flow properties within a flow field can be classified into three main groups: they are (1) finite difference methods (2) finite element methods and (3) finite volume methods. The dominant method presently used in fluid mechanics is the finite difference method. In the finite difference method, the continuous flow domain is "discretized" so that the dependent variables (flow properties) are considered to exist only at discrete points or considered to vary between grid points in a simple algebraic fashion (for example linearly). The governing equations in differential form are approximated by replacing the derivatives in these equations with their approximate algebraic representations. The resulting algebraic equations are then solved for the unknown flow properties using an appropriate algorithm.

The finite element method has been used extensively in the area of solid mechanics but it has not enjoyed as much success and popularity in the fields of aerospace and turbomachinery fluid mechanics. In the finite element method, the flow domain is discretized into finite elements which are usually triangular in shape. The unknown properties are represented within each element by an interpolating polynomial which is continuous and derivatives of the properties are also continuous to a specified order within the element. As is typical of all finite element methods, information is obtained on an element by element basis and then this information is assembled into a global representation of the problem. To solve the governing equations, finite element solution techniques have used both the Galerkin method formulation and the variational formulation.

A popular way of solving fluid mechanics problems in turbomachinery is the finite volume method. As with the finite difference and finite element methods, there are a number of different approaches which can be classified as finite volume methods. The identifying features of the finite-volume method are that the flow domain is discretized into finite control volumes and the governing equations in integral form are used to solve for the unknown properties at grid points within this control volume network. When the equations of motion are written in integral form, the fluxes of

all quantities are identically conserved once the steady state is reached. If the finite difference formulation is used, all quantities are not necessarily conserved. Another advantage of the finite volume method is its simplicity. Since the solution is obtained in a physical grid, no coordinate transformations are necessary and therefore the method is more easily understood.

The finite volume method has been used extensively to solve the Euler equations for transonic flow including flow at high Mach numbers. Potential flow methods have been used in the past for calculations of inviscid transonic flow at Mach numbers close to one. However, potential flow methods assume that the flow is isentropic and therefore their solutions cannot satisfy the Rankine-Hugoniot shock relations. Therefore, when the Mach numbers in the flow field become greater than 1.2 to 1.3, the entropy increase across a shock wave becomes important enough that neglecting its effect would degrade the solution accuracy. For flows in which the Mach number exceeds 1.2 to 1.3, the Euler equations or Navier Stokes should be used so that the calculations correctly predict the shock strength and shock position within the flow field. However rather than solving just one second-order partial differential equation as is done for the two dimensional potential methods, the Euler equation formulation must solve the continuity equation, x and y momentum equations, and the energy equation simultaneously. The finite volume formulation is preferred over the finite difference method for solving the Euler equations because of its property of conserving mass and momentum.

When deciding upon a solution procedure which will calculate the properties at the node points in a transonic flow field, it should be noted that the steady form of the Euler equations is elliptic in nature when the flow is subsonic and hyperbolic in nature when the flow is supersonic. A different algorithm is required in the subsonic and supersonic regions of the flow field. The unsteady form of the Euler equations is always hyperbolic in nature; therefore the unsteady Euler equations may be solved with the same algorithm for both subsonic and supersonic regions of the flow. Shock waves in the flow field evolve as part of the solution. The solution to the steady problem is found by marching the unsteady solution in time until it reaches a steady state. This is the time marching method.

In the area of external aerodynamics, the principal development of the time marching, finite volume method has been by A. Jameson (1). In Jameson's method, as with all finite volume methods, the differential form of the governing equations is converted to the integral form using some form of Gauss' theorem. The unsteady form of the governing equations is used in obtaining a steady state solution by taking the asymptote of the unsteady solution. Jameson has solved the Euler equations for transonic flow over airfoils. The unsteady solution is advanced in time using an explicit 4-step Runge-Kutta method. He discretizes the flow domain into finite quadrilateral cells (see Fig. 1.1) and places node points at the center of these cells. The properties at cell faces are determined by taking the mean of the properties at adjacent cell centers. This discretization results in a simple central difference scheme which must be augmented by the addition of dissipative terms which have a magnitude determined by the local flow gradients. These dissipative terms are designed to suppress the tendency for odd and even point oscillations, and to limit the generation of wiggles and overshoots near shock waves. Currently Jameson has limited the use of his finite volume method to inviscid flow.

In internal aerodynamics, McDonald (2) was the first investigator to use the time marching, finite-volume method. McDonald's method was limited to two-dimensions because of his choice of control volumes. Denton (3) extended McDonald's finite-volume method to three dimensions; the shape of the control volume was simplified and the solution procedure for the governing equations was modified to improve its accuracy.

Versions of Denton's method have been used in inviscid viscous interaction programs for turbomachinery calculations. Singh (4,5) used Denton's method to calculate the inviscid region of the flow. The boundary layer was calculated using an extended Pohlhausen approach for the laminar flow. The turbulent region of the boundary layer was calculated using a method similar to that of Green (6) (lag-entrainment). Calvert (7,8, and 9) also used Denton's inviscid method for turbomachinery calculations. The laminar boundary layer was calculated using a momentum integral approach utilizing Thwaites' parameter. The turbulent boundary layer was calculated using

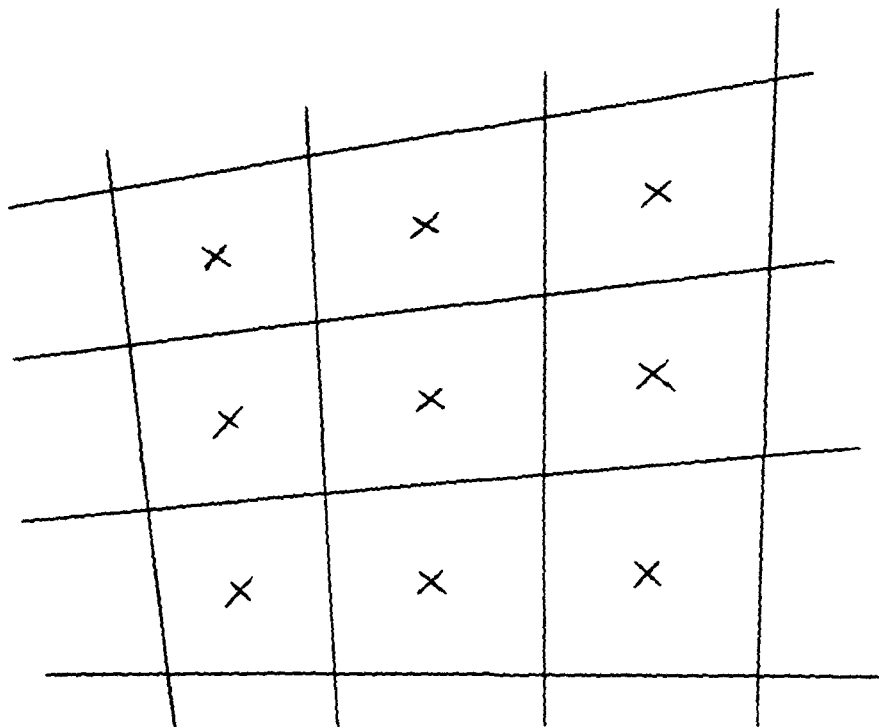


Fig. 1.1 Cell-Centered Nodes

the method of Green et al. (10) which was further modified by East et al. (11) to handle regions of separation. The separation region was handled using an inverse boundary layer type calculation.

Currently the principal workers using the finite volume method for internal flow field calculations are Denton(12,13,14), Van Hove(15), Holmes and Tong(16), Dawes(17) and Subramanian(18); all use the time marching approach. The majority of these finite volume methods have solved the Euler equations for inviscid transonic flow in turbomachinery blade passages [12,13,14,15,16 and 18]. Denton (13) has simulated the effect of the boundary layer using an inviscid-viscous interaction method. Fluid is injected through the surface of the blades to simulate the blockage effect of the boundary layer. An integral method is used to calculate the boundary layer. Dawes (17) has formulated a method which solves the Navier Stokes equations in a transonic compressor cascade. Each of these internal flow methods will now be discussed in more detail.

The method of Holmes and Tong (16) is based upon the scheme used by Jameson. Modifications to the boundary conditions and the grid have been made to calculate flow in turbomachinery blade rows. The code is capable of calculating three dimensional inviscid flow in turbomachinery blade rows. The same fourth-order Runge Kutta scheme is used to advance the solution in time and the node points are again cell centered. Holmes and Tong comment that because cell centered node points are used, the accuracy of the scheme drops "precipitously" when a non-uniform grid is used. A non-uniform grid results in control volumes of varying shapes and sizes. For inviscid calculations, a flow field can be discretized such that the grid is fairly uniform. For viscous calculations, however, highly stretched grids are required and the accuracy of the scheme could become suspect. The method of Subramanian(18) also uses Jameson's finite-volume algorithm for inviscid turbomachinery flow calculations.

Van Hove(15) has presented a finite-volume method for solving the Euler equations in a cylindrical coordinate system; this method is capable of calculating three dimensional flow in axial turbomachinery blade rows. Van Hove describes his method as a fully explicit, time marching, corrected viscosity, finite volume method. Artificial dissipation is needed to stabilize the transient

solution, but if the artificial dissipation were retained at the steady state the solution accuracy would be degraded. The corrected viscosity scheme is the means by which the artificial dissipation is removed as the steady state solution is approached. Typically some viscosity is retained to allow the capturing of shock waves without overshoots or undershoots.

Of the finite volume methods used for turbomachinery calculations, the method of Dawes (17) is the only one to solve the Navier-Stokes equations. The grid points in the computation are cell centered like those seen in Fig. 1.1. The properties at cell faces are determined by assuming that the properties vary linearly between cell centers. This linear interpolation is contrasted with the method used by Jameson where properties at cell faces are the average of the cell centered properties. The interpolation is needed for these viscous calculations because of the highly stretched grids used. A form of upwind differencing is used in the transient solution to enhance stability and is called a defect operator. This defect operator is added to the spatial flux operator to make the transient solution more robust and hence improve the stability of the method. The spatial flux operator is the actual flux imbalance for a given time level. To improve the accuracy of the solution, this defect operator is reduced as the solution approaches a steady state. However, the convergence rate of the method is degraded when the centered differencing is retained near the steady state (see Fig. 1.2). The residual seen in Fig. 1.2 decreases rapidly when the defect operator is used; however, when the defect operator becomes small the residual appears to approach a steady state. This behavior is typical of the cell centered nodal structure when the artificial dissipation is removed. In addition, separate residual steady state artificial smoothing is needed. This residual smoothing is needed to capture shock waves and to prevent odd-even point oscillations. The method is implicit; however, the local time step cannot be unlimited and is typically set equal to 10 times the explicit CFL condition.

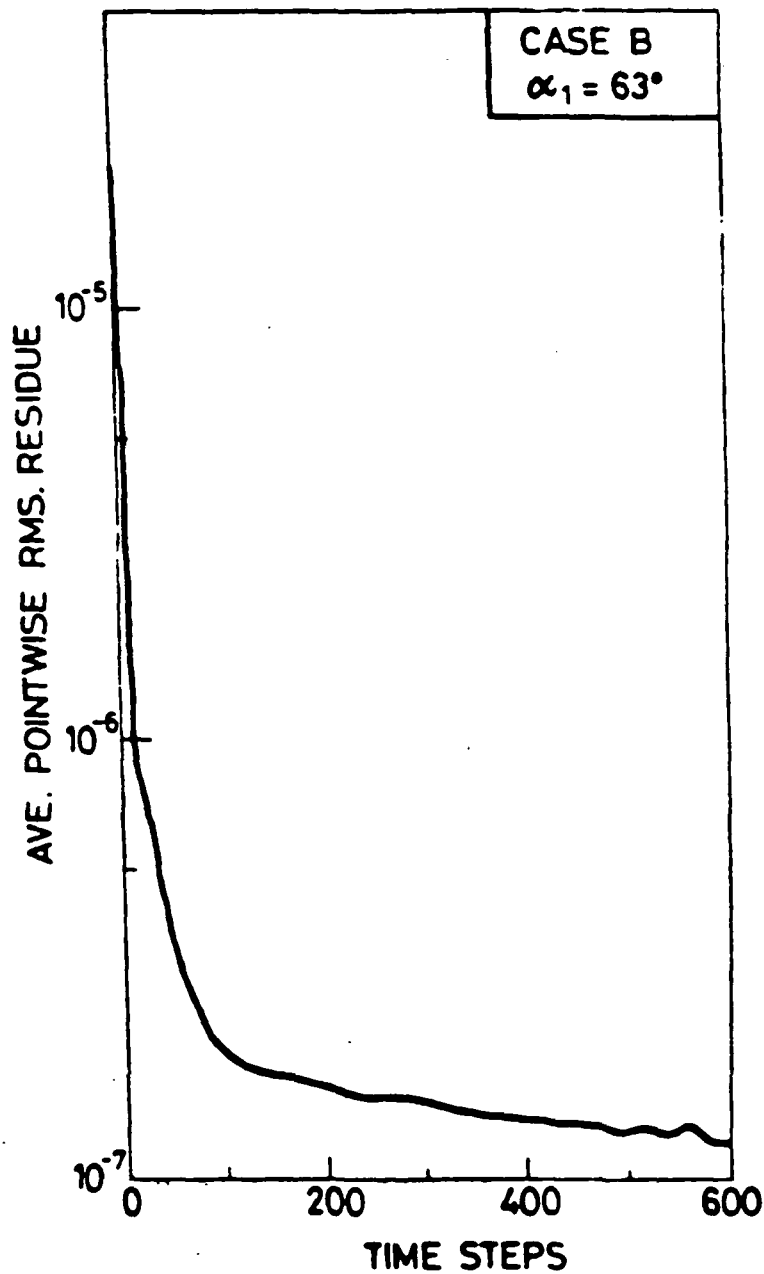


Fig. 1.2 Convergence History for Dawes' Calculations

DENTON'S METHOD

The method of Denton(12,13, and 14) has been widely used in the turbomachinery area. The new method to be discussed later in the body of this dissertation most closely resembles Denton's method. For this reason, his method will be discussed in more detail than the other finite volume methods.

The control volumes are quadrilaterals cells with the node points located at the corners of the control volumes(see Fig. 1.3). This contrasts with the cell centered node arrangement used by most of the other workers. Properties for control volume faces are determined by taking the averages of the properties at the node points corresponding to the ends of a control volume face. It should be noted that Denton's method is not restricted to two dimensions but the following description of his method is based upon the assumption that we are dealing with a two dimensional coordinate system.

In the previously described finite volume methods, the properties at node points are updated simultaneously over one time step either explicitly or implicitly. Denton updates the properties sequentially in the order of density, total energy per unit volume, pressure, (ρu) , and (ρv) using the continuity equation, energy equation, equation of state, x-momentum equation, and y-momentum equation respectively. Properties are used from the previous time level to evaluate all terms in the governing equations except the updated pressure which is used in the momentum equations as soon as it is available.

If the true pressure at a node point were used in the momentum equations , the solution procedure would be unstable. For this reason, Denton uses an effective pressure in the momentum equations. This effective pressure is interpolated from surrounding grid points and the interpolation function does not include the actual grid point in its formulation. As the solution proceeds towards a steady state, the effective pressure is adjusted towards the actual pressure. This adjustment is needed to

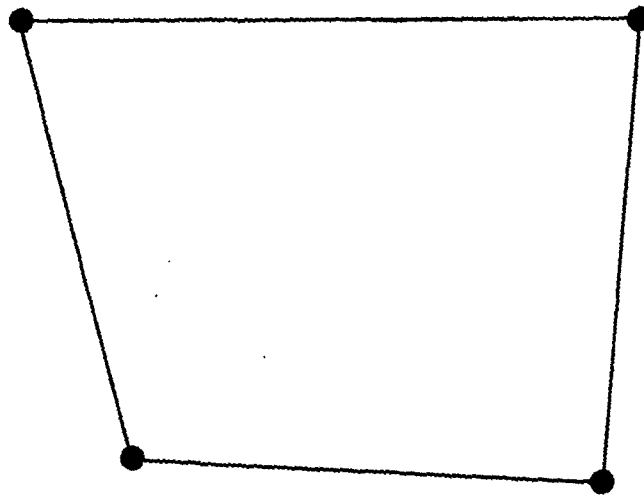


Fig. 1.3 Typical Control Volume Used by Denton

improve the accuracy of the final solution. However even at steady state, the effective pressure may not equal the actual pressure. This correction towards the actual pressure at steady state is another form of the defect operator used by Dawes.

Denton's method is explicit in nature and he uses the CFL condition to determine allowable time steps. The CFL condition has been the criterion used in explicit methods to determine a maximum stable time step. Smoothing of flow properties is needed in Denton's method to stabilize the solution. Typically this smoothing is only needed in the blade to blade direction.

Since Denton's method does resemble the method currently under development, further details of Denton's method will be introduced in the body of the report. Denton's scheme will then be compared and contrasted with the current scheme.

PRESENT CONTRIBUTION

The scope of the present work is to extend a finite-volume method like that of Denton's to be able to calculate laminar or turbulent flow in ducts. The method will have the capability to calculate subsonic as well as transonic flow. In the process of developing the necessary ideas to extend Denton's inviscid method to viscous flow, the current work has also resulted in improved explanations for the inviscid methodology used by Denton. Some of the "black art" used in Denton's method has been explained and explored.

Some of the specific developments to be presented in the body of the report will be summarized here. Control volumes have been introduced which remove the necessity to smooth flow properties in the transverse direction. This development has significance in the reduction of numerical mixing and in the accurate modelling of viscous flows. A new pressure interpolation scheme has been developed which results in solutions for transonic flow which have vastly improved shock wave defi-

dition. In contrast to all previous time marching methods where the same time step is used in all governing equations, different time steps are used in the continuity and momentum equations. These time steps result in improved convergence rates for viscous flow calculations.

A method of discretization, called transverse upwind differencing, allows calculations to be made with highly stretched control volumes which are used in the viscous boundary layers near walls (aspect ratio [length/height] greater than 1000). A multi-volume approach for pressure changes in the boundary layer contributes to the stability of calculations with highly stretched control volumes and variable time steps. A new updating procedure is used which updates the pressure directly from the continuity equation. All previous finite-volume methods have updated the density through the continuity equation.

A number of test cases are used to evaluate the accuracy of the new method. Test cases are also used to illustrate the effects of certain features of the method. For the moment, the test cases will just be listed. The details and purpose of each test case will be discussed later. Test cases 1 through 7 use the assumption of constant total temperature as the energy equation. Test cases 8 through 11 use the full energy equation. The test cases are

1. Laminar boundary layer flow with a zero-pressure gradient.
2. Inviscid transonic flow in Sajben's diffuser (23).
3. Inviscid flow in a straight duct with inlet step profile in total pressure.
4. One-dimensional nozzle calculations to demonstrate the new pressure interpolation scheme.
5. Laminar flow in a converging duct with the boundary layer on one wall only.
6. Turbulent boundary layer flow in an adverse pressure gradient approaching separation.

7. Attached boundary layer in transonic flow in Sajben's diffuser.
8. Turbulent boundary layer in an adverse pressure gradient with an inlet freestream Mach number of 0.55.
9. Flat plate turbulent boundary layer with a freestream Mach number of 0.95.
10. Sajben's diffuser calculations including the energy equation.
11. Flat plate turbulent boundary layer with a freestream Mach number of 2.8.

Some of these cases will allow comparison with experimental or theoretical results (cases 1,2,4,6,7,10 and 11), some can be compared with other computational results (cases 2,4,5,6,7, and 10) and some can only be judged qualitatively (cases 3,8 and 9).

2.0 ANALYSIS SECTION

2.1 GOVERNING EQUATIONS

The unsteady form of the continuity equation, the x-momentum equation, and the y-momentum equation, in integral form, are used to obtain a steady-state solution for flow through 2-dimensional ducts by taking the limit of the unsteady solution as it approaches a steady value. The ideal gas equation of state and the assumption of constant total temperature complete the governing equations needed to solve for the unknown variables, ρ , u , v , P , and T .

The unsteady continuity equation in differential form is

$$\frac{\partial \rho}{\partial t} + \nabla \cdot \rho \underline{u} = 0 \quad . \quad (2.1.1)$$

To transform the governing equations from differential form to integral form Gauss' theorem is used. Gauss' theorem says that

$$\iiint \nabla \cdot \underline{\Phi} \, dVol = \iint \underline{\Phi} \cdot d\underline{A} \quad (2.1.2)$$

where Φ is an arbitrary vector and Δ is an outward normal area vector. When Gauss' theorem is applied to the continuity equation (Eq. 2.1.1), we get

$$\iiint \left(\frac{\partial \rho}{\partial t} + \nabla \cdot \rho \mathbf{u} \right) dVol = \frac{\partial}{\partial t} \iiint \rho dVol + \iint \rho \mathbf{u} \cdot d\Delta = 0 . \quad (2.1.3)$$

For a finite control volume where we can assign one value of density to the control volume, and for a finite time step δt , we get

$$\frac{\delta \rho}{\delta t} \delta Vol = - \iint \rho \mathbf{u} \cdot d\Delta . \quad (2.1.4)$$

So for one time step in our calculation, we get a change in density $\delta \rho$,

$$\rho^{n+1} - \rho^n = \delta \rho = \left[- \iint \rho \mathbf{u} \cdot d\Delta \right]^n \frac{\delta t}{\delta Vol} \quad (2.1.5)$$

where the integral is evaluated explicitly at the current time step, n . The term in the brackets is the continuity error at time, n , therefore Eq. 2.1.5 can be rewritten as

$$\delta \rho = (\text{continuity error}) \frac{\delta t}{\delta Vol} . \quad (2.1.6)$$

Previous finite volume methods , like Denton's (13), update the density after each time step using Eq. 2.1.6. When the density is updated in this way, the method will be referred to as a density update method. The current method , however, updates the pressure directly from the continuity equation for reasons which will be discussed later. When the pressure is updated directly from the continuity error, we will refer to the method as a pressure update method. In arriving at an expression which relates the pressure change directly to the continuity error, we will assume that changes in temperature are small in comparison to other changes for one time step. With the above assumption about temperature changes, we can relate changes in pressure to changes in density through the ideal gas equation of state, in other words,

$$\delta P = RT \delta \rho . \quad (2.1.7)$$

If at this point the alternative assumption was made that the changes in pressure were isentropic, then

$$\delta P = \gamma RT \delta \rho \quad . \quad (2.1.8)$$

If Eq. 2.1.6 and Eq. 2.1.7 are combined we get,

$$\delta P = (\text{continuity error}) RT \frac{\delta t}{\delta Vol} \quad . \quad (2.1.9)$$

In other finite volume methods, like Denton's, the conservative form of the momentum equations is used to update the velocities for a control volume. The unsteady conservative form of the momentum equations is

$$\frac{\partial \rho \underline{u}}{\partial t} + \nabla \cdot \rho \underline{u} \underline{u} = - \nabla \cdot P \delta_{ij} + \nabla \cdot \mu \nabla \underline{u} + \nabla \cdot \mu \overline{\nabla \underline{u}^T} \quad (2.1.10)$$

where δ_{ij} is the Kronecker delta. When Gauss' theorem is applied to Eq. 2.1.10, we get.

$$(\rho \underline{u})^{n+1} - (\rho \underline{u})^n = \delta(\rho \underline{u}) =$$

$$[- \iint \rho \underline{u} \underline{u} \cdot d\mathbf{A} - \iint P \delta_{ij} \cdot d\mathbf{A} + \iint (\mu \nabla \underline{u} + \mu \overline{\nabla \underline{u}^T}) \cdot d\mathbf{A}] \frac{\delta t}{\delta Vol} \quad . \quad (2.1.11)$$

Another way of writing Eq. 2.1.11 is

$$\delta(\rho \underline{u}) = (\text{momentum error}) \frac{\delta t}{\delta Vol} \quad . \quad (2.1.12)$$

The velocity at the new time step , $n + 1$, is found by

$$\underline{u}^{n+1} = \frac{(\rho \underline{u})^{n+1}}{\rho^{n+1}} \quad .$$

For the method introduced in the current work, a non-conservative form of the unsteady momentum equations is used. The non-conservative form is used because it allows the current method to

use different time steps for the continuity and momentum equations. The idea of different time steps will be discussed in further detail in section 2.5 (TIME STEPS). The differences between the non-conservative form and the conservative form of the unsteady momentum equations are associated with the unsteady and convective terms. Specifically, we let

$$\frac{\partial(\rho \underline{u})}{\partial t} + \nabla \cdot \rho \underline{u} \underline{u} = \rho \frac{\partial \underline{u}}{\partial t} + \rho \underline{u} \cdot \nabla \underline{u} . \quad (2.1.13)$$

The right hand side of Eq. 2.1.13 can be rewritten as

$$\rho \frac{\partial \underline{u}}{\partial t} + \rho \underline{u} \cdot \nabla \underline{u} = \rho \frac{\partial \underline{u}}{\partial t} + \nabla \cdot \rho \underline{u} \underline{u} - \underline{u} (\nabla \cdot \rho \underline{u}) . \quad (2.1.14)$$

In the current method, the right hand side of Eq. 2.1.14 is used in the momentum equation.

Three observations can be made about the right hand side of Eq. 2.1.14. First, the velocity is updated directly from the momentum equation, rather than being updated indirectly through $(\rho \underline{u})$. Secondly, the second term in Eq. 2.1.14 is the conservative form of the convective terms used in Eq. 2.1.10. Finally, the third term can be recognized as the continuity error contribution to the momentum error. This term becomes zero at a steady state because the continuity equation at a steady state becomes

$$\nabla \cdot \rho \underline{u} = 0 . \quad (2.1.15)$$

When the new unsteady and convective terms are combined with the pressure and viscous terms and Gauss' theorem is applied, the momentum equations in integral form are

$$(\underline{u})^{n+1} - (\underline{u})^n = \delta(\underline{u}) =$$

$$\left[- \iint \rho \underline{u} \underline{u} \cdot d\underline{A} + \bar{u} \iint \rho \underline{u} \cdot d\underline{A} - \iint P \delta_{ij} \cdot d\underline{A} + \iint (\mu \nabla \underline{u} + \mu \overline{\nabla \underline{u}^T}) \cdot d\underline{A} \right] \frac{\delta t}{\rho \delta Vol} . \quad (2.1.16)$$

Another way of writing Eq. 2.1.16 is

$$\delta u = (\text{momentum error}) \frac{\delta t}{\rho \delta Vol} . \quad (2.1.17)$$

The ideal gas equation of state

$$P = \rho R T \quad (2.1.18)$$

is used in other finite volume methods to update the pressure. In the current method the ideal gas equation of state is used to update the density since the pressure has already been updated through the continuity equation. Typically, the energy equation is simplified to the assumption of constant total temperature

$$T_0 = T + \frac{(u^2 + v^2)}{2C_p} = constant . \quad (2.1.19)$$

A more detailed explanation of the energy equation is included in a separate section (ENERGY EQUATION Section 2.10).

To maintain stability, the properties must also be updated in the proper sequence. In Denton's method, the sequence was

1. Update the density from the continuity equation.
2. Update the pressure from the equation of state.
3. Update the (ρu) and (ρv) from the momentum equations using the new pressure and old velocities and old density.
4. Update the temperature from constant total temperature.

In the current method, the sequence is

1. Update the pressure from the continuity equation.
2. Update the velocities from the momentum equation. using the new pressure and old velocities and old density.
3. Update the density from the equation of state.
4. Update the temperature from constant total temperature.

2.2 CONTROL VOLUMES

A new control volume has been introduced for this method. To eliminate the need for smoothing of flow properties, there must be as many control volumes across the duct as there are nodes where these variables are calculated. We need as many equations as unknowns. The control volumes also need to be located so that errors in continuity and momentum can correctly influence the changes in pressure or density and velocity without smoothing. The current control volume accomplishes this and is shown in Fig. 2.2.1. There are no nodes located along the wall. The nodes are located in the middle of the upstream and downstream faces of the control volumes. When calculating the flux through a streamwise face of an element, the values of the flow properties at the node on that face are used. This is equivalent to using step profiles on streamwise faces. When calculating the flux through a cross-stream face, first the properties are calculated at the corners of the element using linear interpolation, then the flux is calculated using the average of the flow properties at the ends of that face.

Linear profiles on the streamwise face were also investigated. The results were essentially the same for linear and step profiles. Since step profiles are simpler they are used.

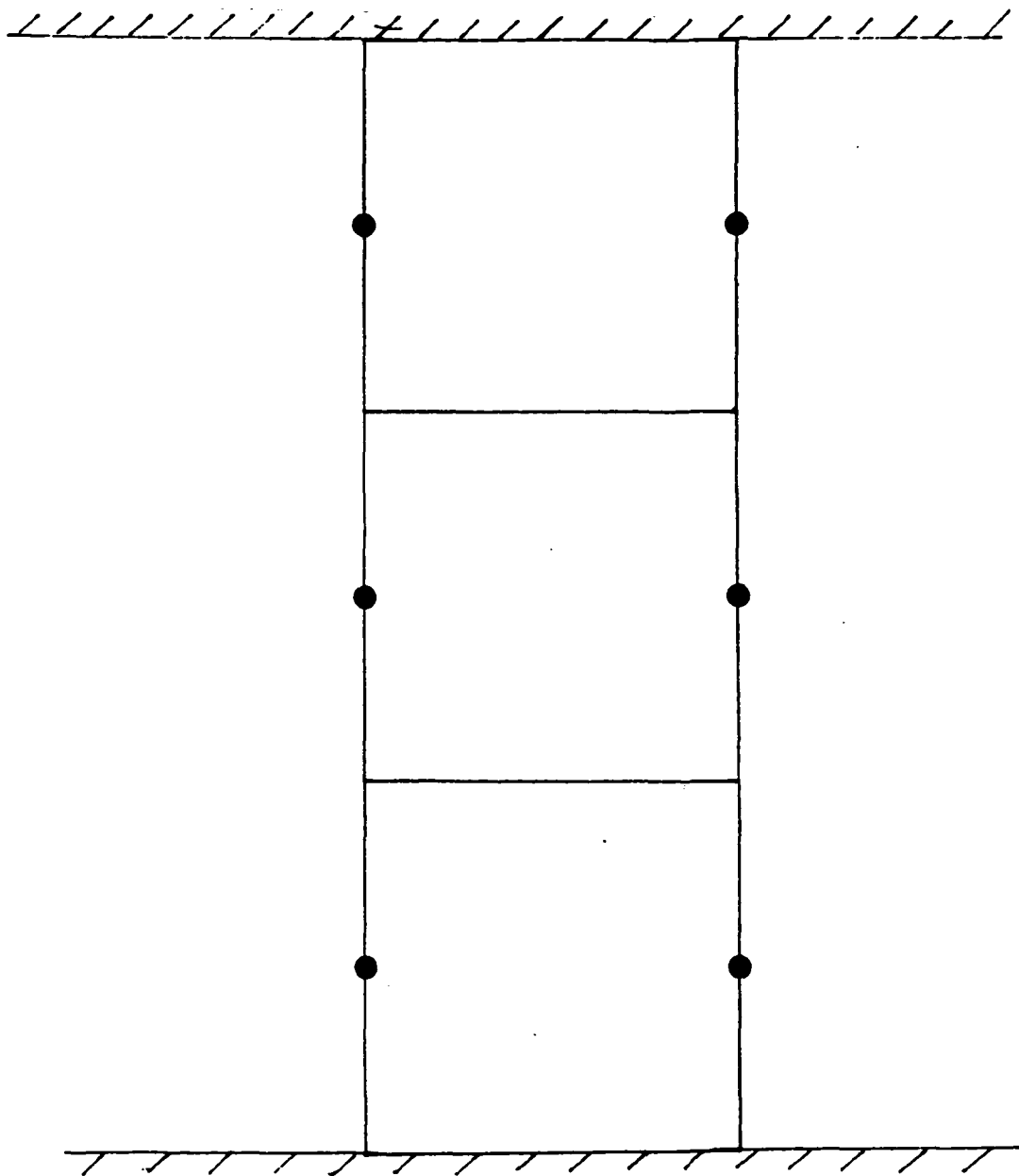


Fig. 2.2.1 New Control Volumes

The control volumes used by Denton (13) look like those shown in Fig. 2.2.2. Fluxes of mass and momentum through each face are found by using averages of the flow properties stored at the ends of each face. However, since the number of nodes (unknowns) is greater than the number of control volumes (equations), smoothing of flow properties is needed in the crossflow direction to remove the dependence of the final solution on the initial guess.

If the current method were to be extended to three dimensions the following additions would need to be made. An example of a typical three dimensional control volume is shown in Fig. 2.2.3. The location of control volume boundaries are specified in the input data and the control volume surfaces are constructed from this information. Once the control volume boundaries are known then the grid points are placed in the middle of the upstream and downstream faces of the control volume. The fluxes through the transverse faces of the control volume needed for the continuity and momentum balances are determined from interpolated properties using the nodes adjacent to the face. Fig. 2.2.4 shows two adjacent control volumes of different sizes. The procedure for calculating the properties to be used in calculating the fluxes on the common boundary (face I) can be shown in the following way. For face I, any property, X , is determined from the average of the property at points A and B, where the values of the properties X_A and X_B are determined by linearly interpolating between the values of the property at nodes 1 and 2, and between the values of the property at nodes 3 and 4, respectively.

Assuming that face II corresponds to a solid boundary, the values of a property at points C and D are determined by linear extrapolation using the values of the property at nodes 1 and 2, and 3 and 4; respectively. For the present calculations, only the pressure needs to be calculated at the solid boundaries since the fluxes of mass are set equal to zero through these solid boundaries.

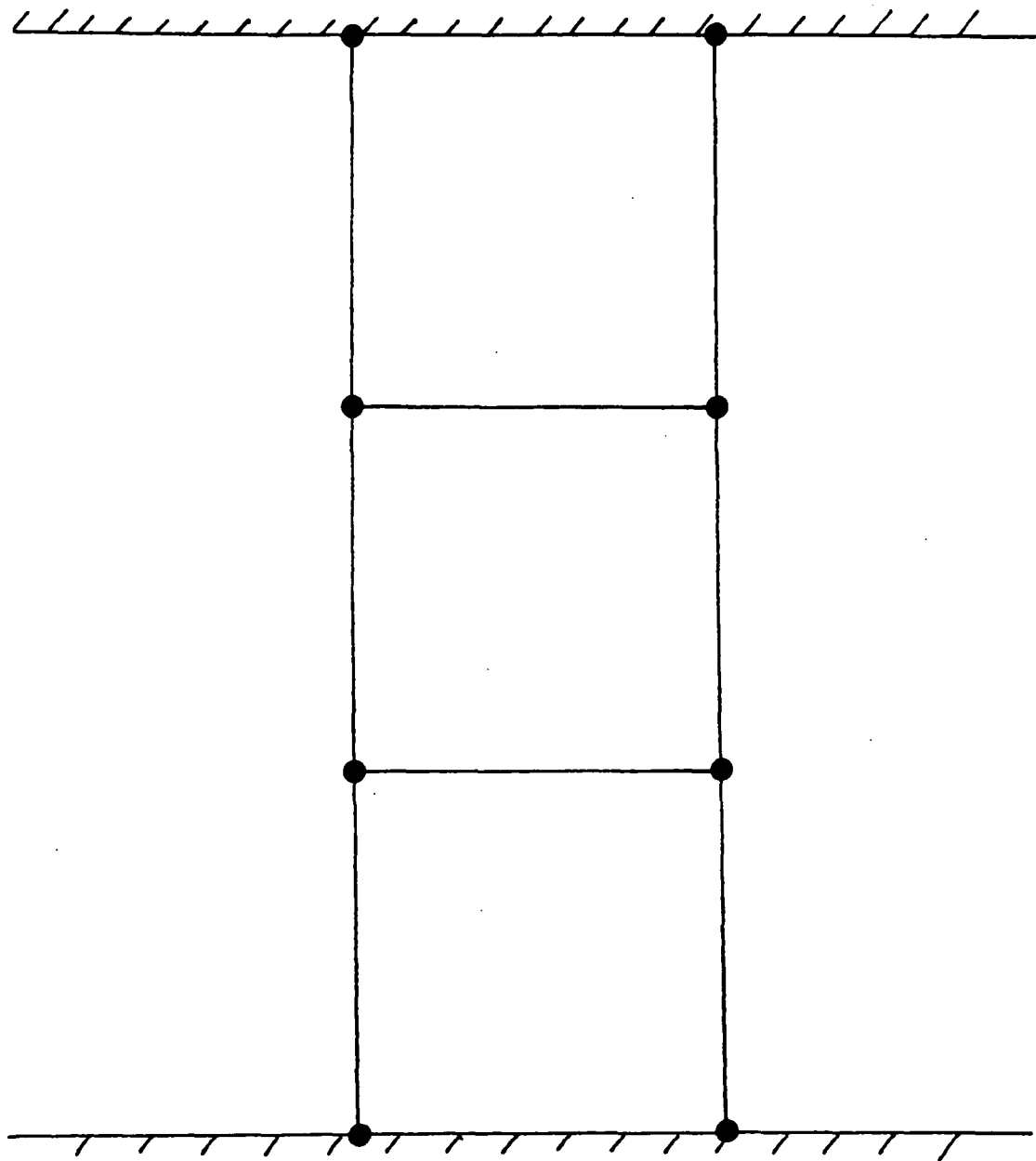


Fig. 2.2.2 Typical Control Volumes Used by Denton (12)

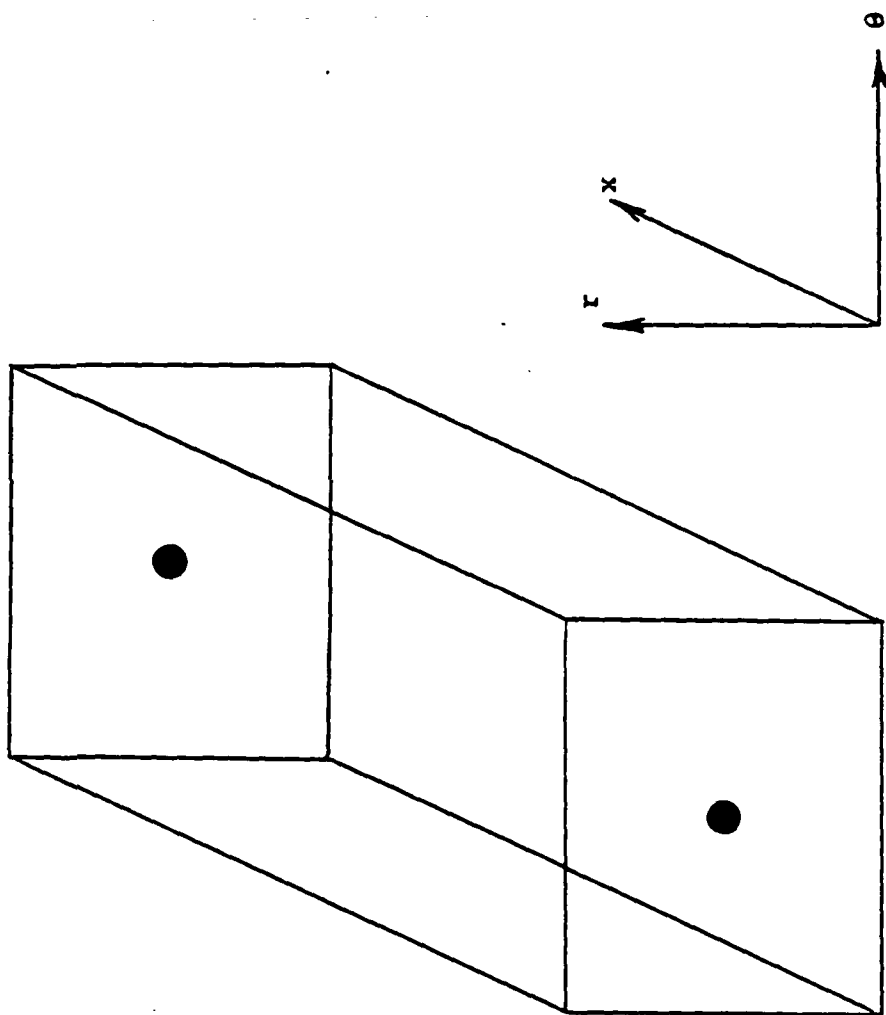


Fig. 2.2.3 New Control Volumes in Three Dimensions

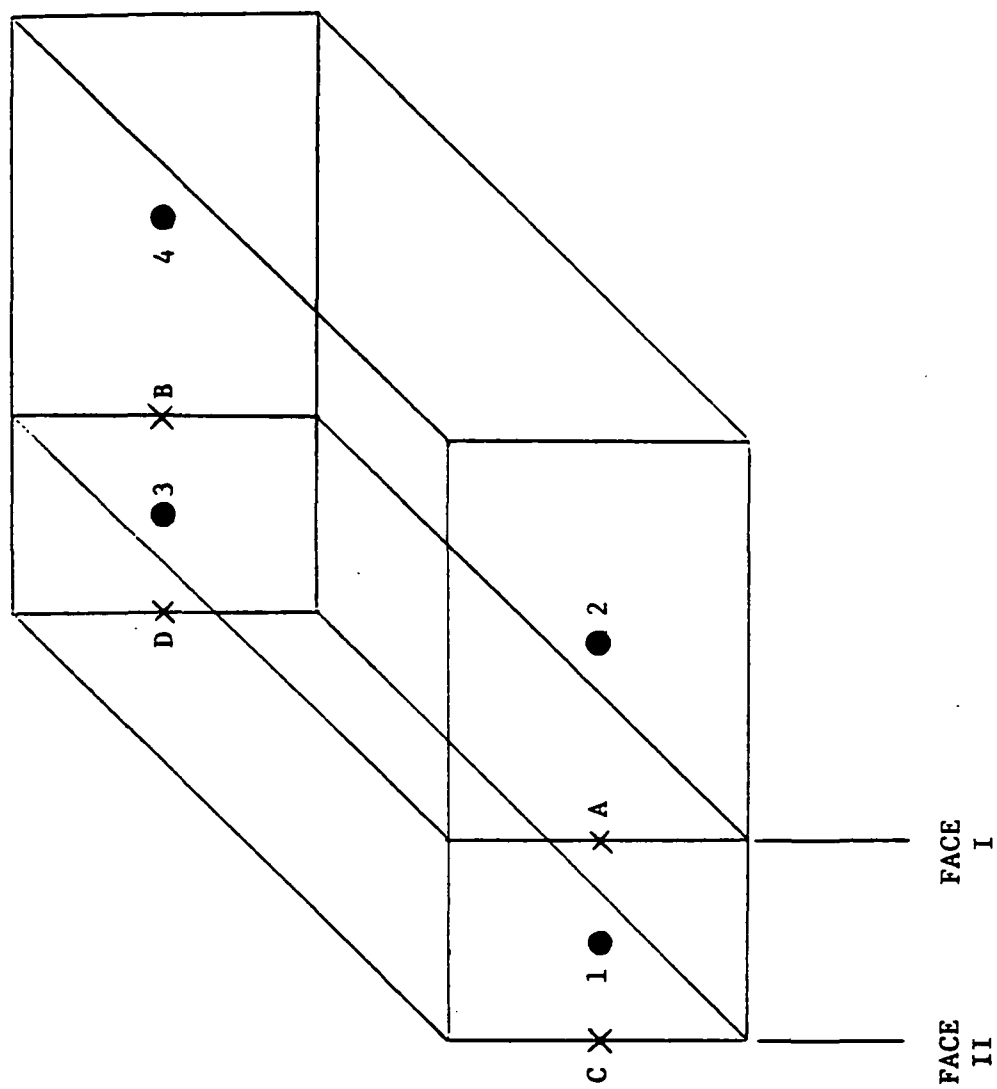


Fig. 2.2.4 New Control Volumes in Non-Uniform Grid

2.3 DISTRIBUTION OF PROPERTIES

The properties at node points are changed in the flow field after each time step because the continuity and momentum equations are not satisfied for a given control volume. The amount that properties are changed at nodes depends upon the extent to which continuity and momentum are not satisfied, the volume of the control volume, and the time step. A decision must also be made about which node, either upstream or downstream (I or $I+1$ in Fig. 2.3.1), these changes should be allocated to. The criterion to be used in determining where changes in properties should be sent is that these distributions result in reduced errors in continuity and momentum. Let us start with the momentum equations.

In the current method, the momentum equation specifies a change in velocity for the control volume based upon the momentum error (Eq. 2.1.17),

$$\delta u = (\text{momentum error}) \frac{\delta t}{\rho \delta Vol} . \quad (2.3.1)$$

This change in velocity is assigned to the downstream node of the control volume. This change will result in a stable calculation procedure and can be explained using a simple example.

Referring to Fig. 2.3.2, if we assume that the only contribution to the momentum imbalance is caused by the convective terms through the streamwise faces, the momentum error for that control volume is

$$\text{momentum error} = (\rho_I u_I A_I) u_I - (\rho_{I+1} u_{I+1} A_{I+1}) u_{I+1} . \quad (2.3.2)$$

Suppose that the net momentum error for the control volume is positive(in other words, $(\rho_I u_I A_I) u_I > (\rho_{I+1} u_{I+1} A_{I+1}) u_{I+1}$). Using Eq. 2.3.1, this error will result in an increase in velocity for the control volume and this increase will be assigned to the downstream node($I+1$). This increase in velocity at $I+1$ will act through Eq. 2.3.2 to reduce the momentum error for the control volume.

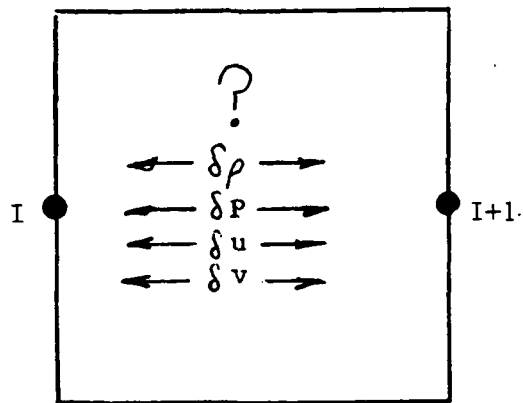
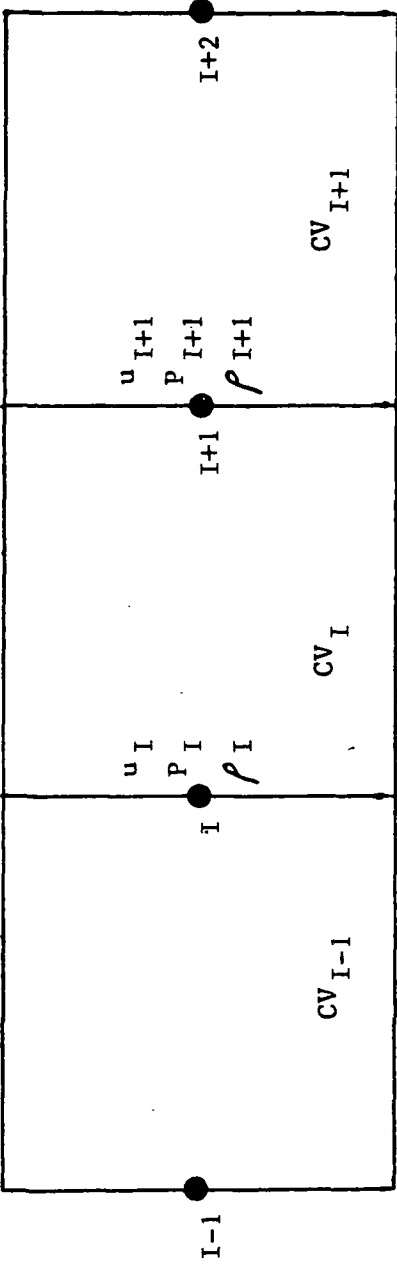


Fig. 2.3.1 Typical Control Volume



- momentum error = +
- δ^u_{I+1} = +
- momentum error reduced
- stable procedure

Fig. 2.3.2 1-D Example With Momentum Imbalance

Therefore sending the velocity change to the downstream node is stable. If the change in velocity (increase) was sent to the upstream node, the momentum error would increase and this distribution would therefore lead to an unstable procedure.

When the conservative form of the momentum equation is used by Denton (Eq. 2.1.10), the x-momentum error results in a change in (ρu) for a control volume. For the same reasons as outlined above, the change in (ρu) is also sent to the downstream node.

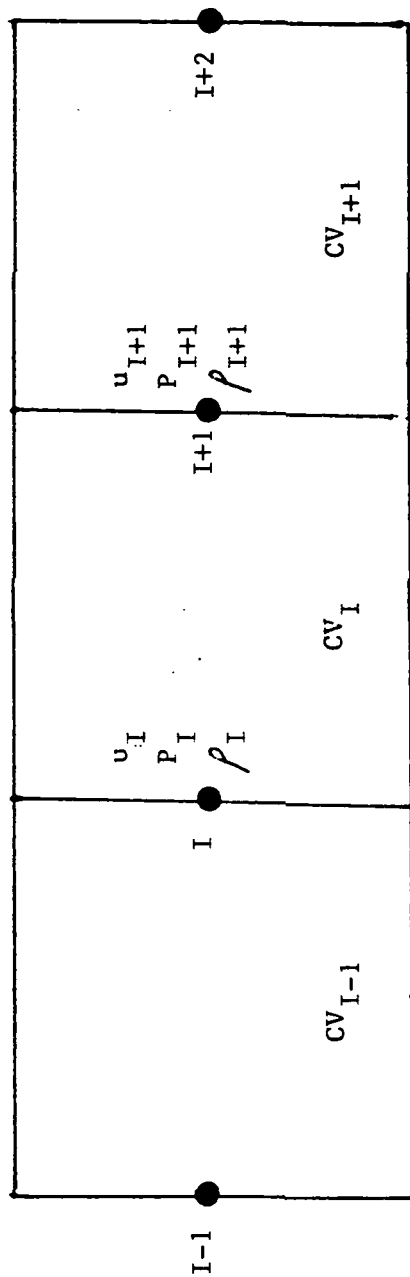
In the current method, the pressure is updated directly from the continuity equation (pressure update method) rather than the density being updated (density update method) . The pressure change is assigned to the upstream node (I) (see Fig. 2.3.1) to satisfy stability considerations. The change in pressure for a control volume is related to the continuity error by

$$\delta P = (\text{continuity error}) RT \frac{\delta t}{\delta Vol} . \quad (2.3.3)$$

Referring to Fig. 2.3.3, if the error in continuity is due only to errors in streamwise velocity and density then the continuity error for that control volume is

$$\text{continuity error} = \rho_I u_I A_I - \rho_{I+1} u_{I+1} A_{I+1} . \quad (2.3.4)$$

If, for example, the continuity error is positive for the control volume, the pressure will increase for the control volume (see Eq. 2.3.3) and that increase will be assigned to the upstream node. Let us assume for clarity that the momentum equation is initially balanced. This pressure increase will change the surface force on the face of the control volume coincident with node I and this force will unbalance the momentum equation and introduce a momentum error for the control volume of interest and also for the upstream control volume. This increase in pressure at node I will result in a positive momentum error for the control volume of interest and a negative momentum error for the upstream control volume. The velocity at node I + 1 will increase (δu_{I+1} (+)) and the velocity at node I will decrease (δu_I (-)) because of these momentum errors. These changes in



- continuity error = +
- δp = +
- $p_I \uparrow$
- momentum error for CV_I positive, $u_{I+1} \uparrow$
- momentum error for CV_{I-1} negative, $u_I \downarrow$
- continuity error reduced
- stable procedure

Fig. 2.3.3 1-D Example With Continuity Imbalance (Pressure Update Method)

velocity reduce the error in continuity (see Eq. 2.3.4), therefore sending pressure changes upstream is a stable procedure.

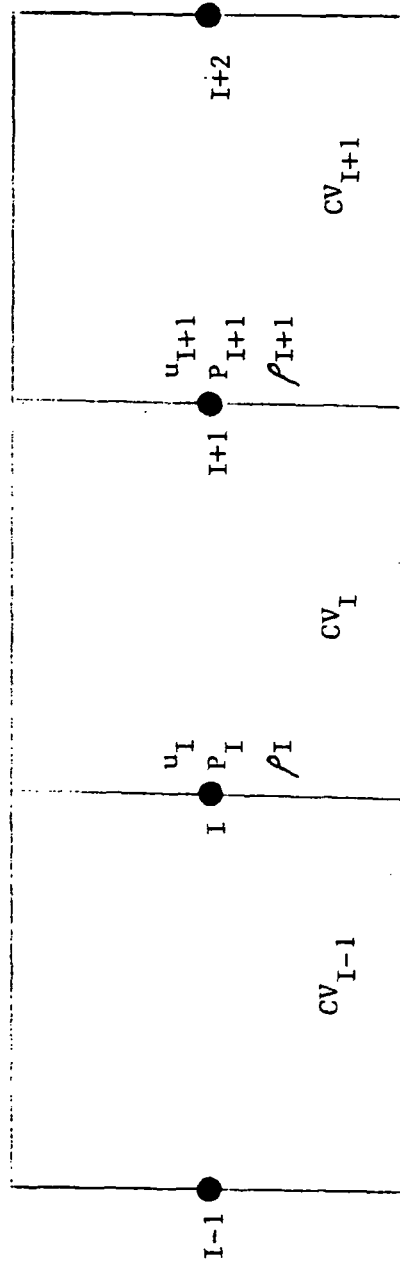
In contrast, if the pressure change was sent downstream, the momentum equation would cause the downstream velocity to decrease. This distribution causes the continuity error to increase and this decision would result in an unstable calculation method.

In the current method, the density used in the continuity and momentum equations may be different than that determined from the ideal gas equation of state. The reason for using an effective density rather than the true density is that the density change at a node will be of the same sign as the pressure change since $\delta P \propto \delta \rho RT$. These density changes may act to violate the stability criterion that the distribution in properties results in improved conservation of mass and momentum. Therefore an effective density which satisfies our stability criterion must be chosen. This topic will be discussed in more detail in section 2.4 (PRESSURE INTERPOLATION METHOD).

In the finite volume method of Denton , if the continuity error for a control volume is not zero, the continuity equation specifies a change in density for the control volume (density update method)

$$\delta \rho = (\text{continuity error}) \frac{\delta t}{\delta Vol} \quad (2.3.6)$$

and the change is typically sent to the downstream node ($I + 1$) shown in Fig. 2.3.1. This distribution of density results in a stable calculation procedure because of the following reasoning (refer to Fig. 2.3.4). If, for example, the continuity error is positive, in other words, too much mass flows into the control volume, then the continuity equation will specify an increase in density ; Eq. (2.3.6),). If the density at the downstream node is increased ($\delta \rho_{I+1}$ (+)) then this increase in density will act through Eq. 2.3.4 to decrease the continuity error. So sending density changes to the downstream node will result in a stable method. In contrast, if the density change was sent up-



- continuity error = +
- δp = +
- ρ_{I+1}
- continuity error decreases
- stable calculation procedure

Fig. 2.3.4 1-D Example With Continuity Imbalance (Density Update Method)

stream (δp_i (+)) then the continuity error would increase. This decision would result in an unstable calculation method.

When Denton uses the density update method and sends changes in density to the downstream node, the pressure used in the momentum equations is an effective pressure which may be different from the pressure determined from the ideal gas equation of state using the density and temperature at that node. This is because the density change at the downstream node will cause a pressure change at that node in the same sense as the density change. This pressure change, acting through the momentum equation, will cause the velocity to change at the downstream node and this velocity change will contribute towards violating the stability criterion. For example, the positive continuity error discussed above would result in an increase in pressure at node $I + 1$. This pressure change would cause the momentum equation to have a negative momentum error. The downstream velocity would decrease because of this error and a decrease in velocity at node $I + 1$ (see Eq. 2.3.4) would increase the continuity error. It is because of this interaction between density changes and pressure changes that the density update method must use an effective pressure in the momentum equation which will satisfy our stability criterion. This topic will be covered in more detail in section 2.4 (PRESSURE INTERPOLATION METHOD) .

In review, the current method uses the following sequence in updating properties over one time step.

1. the pressure is updated through the continuity equation and the pressure change is sent to the upstream node.
2. the u and v velocities are updated through the momentum equations using the new pressure and the velocity changes are sent to the downstream node.
3. the effective density is updated through the ideal gas equation of state using an interpolated pressure.

4. the static temperature is updated from the assumption of constant total temperature.

In the finite volume method of Denton, the following sequence is used to update properties over one time step.

1. the density is updated through the continuity equation and the density change is sent to the downstream nodes.
2. the pressure is updated using the ideal gas equation of state and the updated density.
3. an effective pressure is calculated from an interpolation formula using the new pressures.
4. (ρu) and (ρv) are updated through the momentum equations using the new effective pressure and changes in (ρu) and (ρv) are sent to the downstream nodes.
5. the static temperature is updated from the assumption of constant total temperature.

Both the sequence in which properties are changed and the nodes to which these changes are sent are very important in maintaining stability for these finite volume methods.

2.4 PRESSURE INTERPOLATION PROCEDURE

As part of the updating procedure used by Denton (13), an effective pressure is used in the momentum equations rather than the true thermodynamic pressure determined from the equation of state. This effective pressure is needed because if the true pressure is used in the momentum equations the solution may not converge. A simple explanation for this instability is that pressure changes caused by the continuity error will act through the momentum equation to cause the error

in continuity to increase rather than decrease. As discussed in the section 2.3 (DISTRIBUTION OF PROPERTIES) this will lead to an unstable calculation method.

In the current method, the density used in the continuity and momentum equations is an effective density which may be different than the density obtained using the ideal gas equation of state. The use of an effective density is required because of stability considerations. If the actual density is used in the continuity and momentum equations, the solution procedure may be unstable as mentioned in section 2.3 (DISTRIBUTION OF PROPERTIES).

Stability of Denton's Method: In order to achieve stability for Denton's scheme the pressure used in the momentum equations is not the true pressure but an effective pressure, P_{eff} which is only an approximation to the true pressure. The use of the effective pressure is described by Denton (13) in the following manner. Stability is obtained by setting

$$P_{eff,I} = P_{I+1} + CF_I \quad (2.4.1)$$

where CF_I is a correction factor which is an approximation to the difference in pressure between node points I and I+1 (see Fig. 2.4.1). The scheme is unstable if CF_I is found directly from the difference in the true pressures, even if the changes in CF_I are highly damped in time. However, several stable methods of estimating CF_I are possible and two of them are used by Denton. With reference to Fig. 2.4.1, a simple estimate of the correction is

$$CF_I = \alpha \frac{(P_{I-1} - P_{I+1})}{2} \quad (2.4.2)$$

where $\alpha = 1$ would give a centered difference 1st order accurate estimate of the correction. It should be noted that the accuracy of the solution is determined by the accuracy of the difference in effective pressures between adjacent grid points and hence the above estimate will give a second order accurate solution.

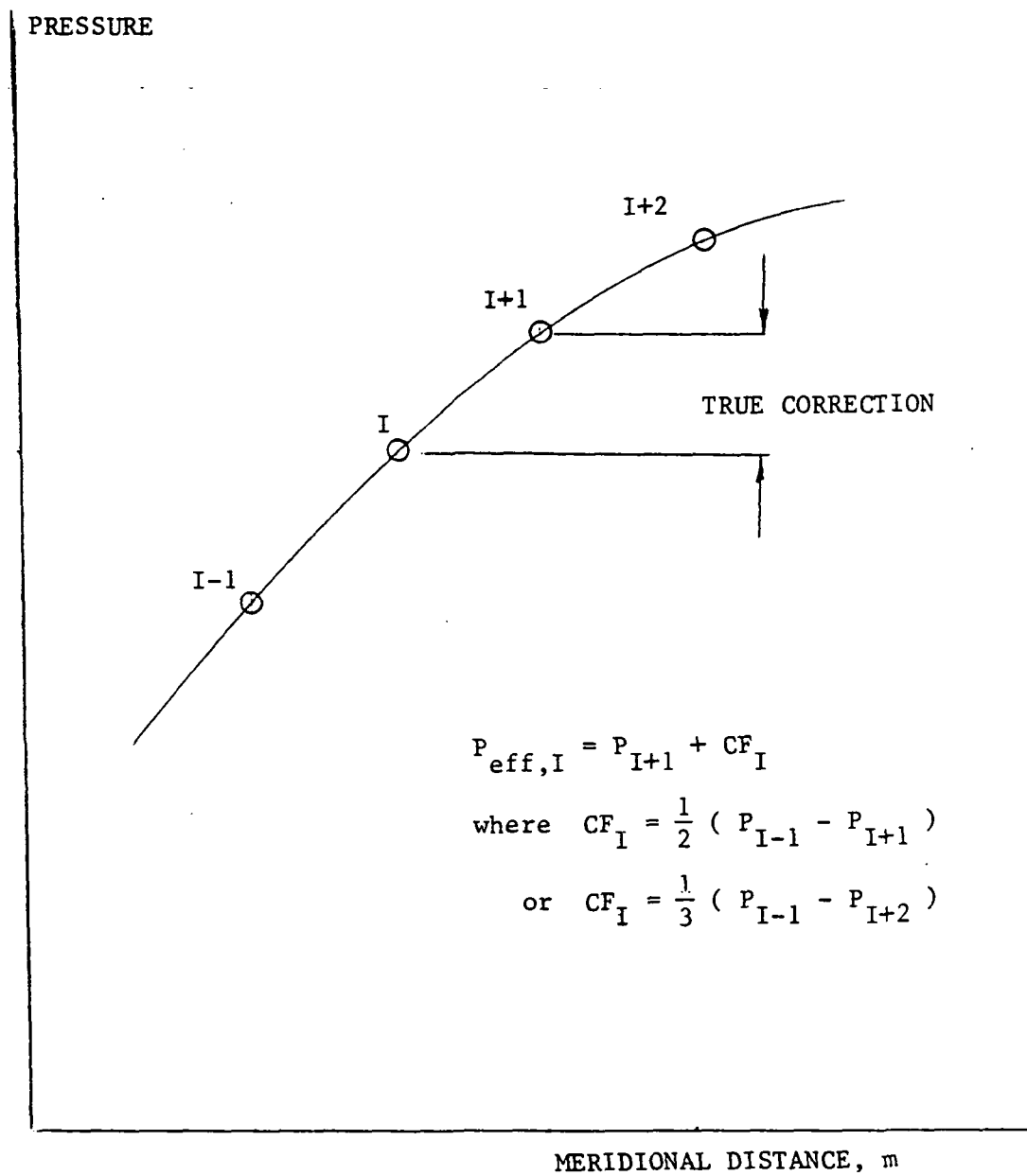


Fig. 2.4.1 Calculation of Effective Pressure

An alternative scheme is to base the correction on a parabolic interpolation between points $I+1$, $I+2$, and $I-1$. This leads to

$$CF_I = \alpha \frac{(P_{I-1} - P_{I+2})}{3} \quad (2.4.3)$$

which is second order accurate when $\alpha = 1$. In order to provide sufficient numerical damping to capture shock waves cleanly it is found desirable to make the value of α slightly less than 1, say 0.8 - 0.9. An optional alternative is to make the value of α depend on the density gradient in such a way that α is automatically decreased in the region of a shock wave. The expression for α , based upon the density gradient is,

$$\alpha = (1 - \frac{\rho_{I+1} - \rho_{I-1}}{\rho_I}) \quad (2.4.4)$$

This method provides additional stability in regions of large gradients in properties like those seen through a shock. The density gradient correction is applied only when there is an increase in density.

Stability of the Pressure Update Method: Currently the pressure update method is used and an effective density based upon an interpolated pressure can be used to stabilize the calculation procedure. Using a three point interpolation scheme, like Eq. 2.4.3 above, one possible expression for calculating an effective density is

$$\rho_{I+1} = [\rho_I + \frac{(P_{I+1} - P_{I-2})}{3}] \times \frac{1}{RT_{I+1}} \quad (2.4.5)$$

This effective density will result in a stable calculation procedure for all Mach numbers but will smear a shock wave out over several grid points.

As mentioned previously, when the effective pressure or effective density used in the governing equations is relaxed to ideal gas, the solution procedure may become unstable. In the remainder

of section 2.4, this instability mechanism will be investigated, the above three point interpolation schemes will be shown to be stable, and a new Mach number dependent interpolation scheme will be introduced which gives much better shock capturing properties than the previously used two or three point interpolation schemes. A 1-D inviscid flow example will be used as a vehicle to develop these ideas. These ideas were developed by J.G. Moore in reference 19.

1-D Flow Example: For the geometry shown in Fig. 2.4.2, we are seeking a 1-D steady flow solution which satisfies the continuity equation

$$\nabla \cdot \rho \underline{u} = 0 \quad (2.4.6)$$

and the momentum equation

$$\nabla \cdot \rho \underline{u} \underline{u} = - \nabla P \quad (2.4.7)$$

and which also satisfies the ideal gas equation of state and maintains constant total temperature throughout the flow field.

Continuity: In discretized or integral form, the continuity equation for a converged 1-D solution becomes,

$$\rho_{I+1}^f u_{I+1}^f A_{I+1} - \rho_I^f u_I^f A_I = 0 \quad (2.4.8)$$

where the superscript f stands for the final converged values.

For an intermediate solution the velocity will be u and the density will be ρ . The differences between the current properties and the correct properties are δu and $\delta \rho$. The continuity equation, Eq. 2.4.8, can be rewritten as

$$(\rho_{I+1} + \delta \rho_{I+1})(u_{I+1} + \delta u_{I+1})A_{I+1} - (\rho_I + \delta \rho_I)(u_I + \delta u_I)A_I = 0. \quad (2.4.9)$$

Expanding and rearranging, Eq. 2.4.9 becomes

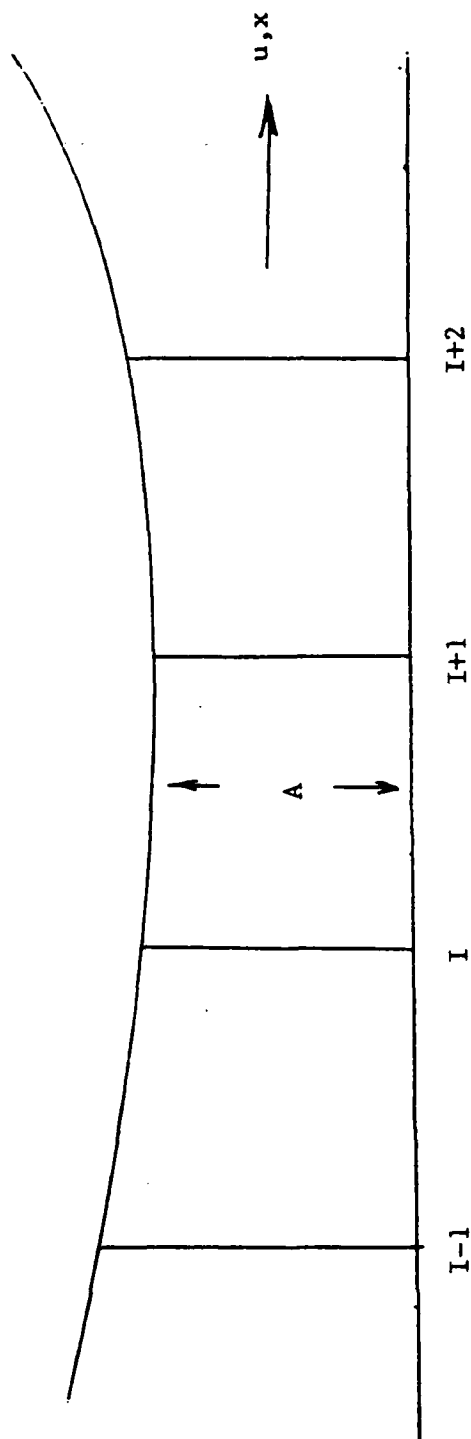


Fig. 2.4.4.2 Geometry Used For 1-D Steady Flow Analysis

$$\begin{aligned} \rho_{I+1}A_{I+1}\delta u_{I+1} - \rho_I A_I \delta u_I + u_{I+1}A_{I+1}\delta \rho_{I+1} - u_I A_I \delta \rho_I = \\ (\rho_I u_I A_I - \rho_{I+1} u_{I+1} A_{I+1}) + (\delta \rho_I \delta u_I A_I - \delta \rho_{I+1} \delta u_{I+1} A_{I+1}). \end{aligned} \quad (2.4.10)$$

The first two terms on the right hand side of Eq. 2.4.10 represent the continuity error and the last two terms are of the order δ^2 and will be negligible when the computation is nearly converged (i.e. $\delta \rho \ll \rho$ and $\delta u \ll u$).

Therefore Eq. 2.4.10 can be rewritten as

$$\rho_{I+1}A_{I+1}\delta u_{I+1} - \rho_I A_I \delta u_I + u_{I+1}A_{I+1}\delta \rho_{I+1} - u_I A_I \delta \rho_I = \dot{m}_{error} + small. \quad (2.4.11)$$

In a time marching method, the left hand side of Eq. 2.4.11 can also be used to evaluate the change in mass flow rate for one time step where the changes in properties in Eq. 2.4.11 are for one time step.

In the density update time marching calculation procedure (Denton), the density is updated from the continuity error. From the integral form of the unsteady continuity equation, the density on the downstream side of the control volume is changed according to

$$\delta \rho_{I+1} = \dot{m}_{error,I} \frac{\delta t}{Vol_I}. \quad (2.4.12)$$

The density change, $\delta \rho_{I+1}$, affects the change in mass flow rate directly, but it also acts through the ideal gas equation of state to change the pressure. This pressure change then acts through the momentum equation to change the velocity (δu_{I+1}).

In the pressure update time marching calculation procedure (Nicholson/Moore), the pressure is updated directly from the continuity error. The pressure is changed at the upstream node according to

$$\delta P_I = \dot{m}_{error,I} \delta t_c R T / Vol_I \quad (2.4.13)$$

This pressure change acts through the momentum equation to change the velocities, u_{I+1} and u_I , and it also acts through the ideal gas equation of state to change the density. We will now look at the discretized form of the momentum equation for our 1-D example.

Momentum: The steady state momentum equation discretized over the control volume between points I and I + 1 is

$$(\rho u A)_{I+1} u_{I+1} - (\rho u A)_I u_I = - [P_{I+1} A_{I+1} - P_I A_I - P_s (A_{I+1} - A_I)] \quad (2.4.14)$$

where P_s is the pressure acting on the sides of the control volume. Traditionally, the pressure has been

$$P_s = \frac{(P_{I+1} + P_I)}{2} \quad (2.4.15)$$

Eq. 2.4.14 can therefore be rewritten as

$$(\rho u A)_{I+1} u_{I+1} - (\rho u A)_I u_I = - (P_{I+1} - P_I)(A_{I+1} + A_I)/2. \quad (2.4.16)$$

We may rewrite Eq. 2.4.16 as,

$$\dot{m}_{I+1} u_{I+1} - \dot{m}_I u_I = - (P_{I+1} - P_I) Vol_I / \delta x_I \quad (2.4.17)$$

where $\dot{m} = \rho u A$ is the local mass flow rate, $Vol_I = \delta x_I (A_{I+1} + A_I)/2$ is the volume of the control volume and $\delta x_I = x_{I+1} - x_I$ is the grid spacing for the control volume, I. Eq. 2.4.17 may be rewritten as

$$(u_{I+1} - u_I)(\dot{m}_{I+1} + \dot{m}_I)/2 + (\dot{m}_{I+1} - \dot{m}_I)(u_{I+1} + u_I)/2 = - (P_{I+1} - P_I) Vol_I / \delta x_I \quad (2.4.18)$$

or

$$\dot{m}(u_{I+1} - u_I) + \bar{u}\dot{m}_{error,I} = - (P_{I+1} - P_I)Vol_I/\delta x_I . \quad (2.4.19)$$

In the current method, the continuity error term , $\bar{u}\dot{m}_{error,I}$, is omitted because of the non-conservative form of the momentum equation that is used (Eq. 2.1.16) . Therefore, the change in velocity on the downstream side of the control volume is changed in direct proportion to the momentum error. From the unsteady form of the momentum equation, the change in velocity at the downstream node is

$$\delta u_{I+1} = [- (P_{I+1} + \delta P_{I+1} - P_I - \delta P_I)Vol_I/\delta x_I - \dot{m}(u_{I+1} - u_I)]\delta t/(\rho_{I+1}Vol_I) \quad (2.4.20)$$

where the pressure change, δP , has been calculated from the continuity error.

In the method used by Denton, the conservative form of the momentum equation is used to calculate the change in (ρu) ;and that change is

$$\delta(\rho u)_{I+1} = u_{I+1}\delta\rho_{I+1} + \rho_{I+1}\delta u_{I+1} =$$

$$[- (P_{I+1} + \delta P_{I+1} - P_I - \delta P_I)Vol_I/\delta x_I - \dot{m}(u_{I+1} - u_I) - \bar{u}\dot{m}_{error,I}]\delta t/Vol_I . \quad (2.4.21)$$

By taking the mean velocity for the control volume , \bar{u} , approximately equal to the velocity on the downstream side , u_{I+1} , we may subtract u times Eq. 2.4.12 from Eq. 2.4.21 to get the change in velocity, δu_{I+1} , for one time step. The resulting equation is

$$\delta u_{I+1} = [- (P_{I+1} + \delta P_{I+1} - P_I - \delta P_I)Vol_I/\delta x_I - \dot{m}(u_{I+1} - u_I)]\delta t/(\rho_{I+1}Vol_I) \quad (2.4.22)$$

having assumed that the same time step is used in both density and velocity updates. This is the same result that is obtained using the Nicholson/Moore method (Eq. 2.4.20).

Let us assume that at the beginning of a time step that the momentum equation is balanced except for the pressure change introduced through the continuity error, in other words,

$$\dot{m}(u_{I+1} - u_I) = - (P_{I+1} - P_I) Vol_I / \delta x_I. \quad (2.4.23)$$

The momentum balances for both methods, Eq. 2.4.20 and Eq. 2.4.22, give us

$$\delta u_{I+1} = (\delta P_I - \delta P_{I+1}) \frac{\delta t}{(\rho_{I+1} \delta x_I)}. \quad (2.4.24)$$

In general, in the density update (Denton) method, the time step is calculated from the CFL condition, which for 1-dimensional flow is

$$\delta t \leq \frac{\delta x}{(u + c)} \quad (2.4.25)$$

where c is the speed of sound. In the pressure update method the time step for momentum is obtained from the coefficient of u_{I+1} in the steady flow momentum equation and is

$$\delta t = \frac{\delta x}{u}. \quad (2.4.26)$$

A more detailed description of the time steps is presented in section 2.5 (TIME STEPS) . We may combine these two equations by saying

$$\delta t = \frac{\delta x}{(u + ec)} \quad (2.4.27)$$

where e = 1 for the density update method and e = 0 for the pressure update method. Eq. 2.4.24, which is valid for both methods becomes,

$$\rho_{I+1} \delta u_{I+1} = \frac{(\delta P_I - \delta P_{I+1})}{(u + ec)}. \quad (2.4.28)$$

The changes in density and velocity can now be substituted into Eq. 2.4.11 to evaluate the change in mass flow rate for one time step.

Change in Continuity for One Time Step: The left hand side of Eq. 2.4.11 may be used to evaluate the change in mass flow rate for one time step. Substituting Eq. 2.4.28 into Eq. 2.4.11 to eliminate $\rho \delta u$ yields

$$A_{I+1} \frac{(\delta P_I - \delta P_{I+1})}{(u + ec)_{I+1}} - A_I \frac{(\delta P_{I-1} - \delta P_I)}{(u + ec)_I} + u_{I+1} A_{I+1} \delta \rho_{I+1} - u_I A_I \delta \rho_I = \dot{m}_{change,I} \quad (2.4.29)$$

If we now rearrange Eq. 2.4.29 to order the coefficients of the δP 's and $\delta \rho$'s, we get

$$\left. \begin{array}{l} \frac{-A_I}{(u + ec)_I} \delta P_{I-1} \\ \left[\frac{A_{I+1}}{(u + ec)_{I+1}} + \frac{A_I}{(u + ec)_I} \right] \delta P_I - u_I A_I \delta \rho_I \\ \frac{A_I}{(u + ec)_{I+1}} \delta P_{I+1} + u_{I+1} A_{I+1} \delta \rho_{I+1} \end{array} \right\} = \dot{m}_{change,I} \quad (2.4.30)$$

For stability we require that the change in mass flow rate be of the same sign as the error in mass flow rate. Note that this stability requirement is a necessary condition for stability but it may not be a sufficient condition to ensure stability.

Stability of the Density Update Method Using Ideal Gas: The density update method updates the density directly from the continuity error and then the pressure is updated through the ideal gas equation of state. For an intermediate solution where there is a continuity error only between nodes I and I + 1, Eq. 2.4.12 yields

$$\delta \rho_{I+1} = \dot{m}_{error,I} \frac{\delta t}{Vol_I} \quad (2.4.31a)$$

$$\delta \rho_I = 0 \quad (2.4.31b)$$

$$\delta \rho_{I-1} = 0 \quad (2.4.31c)$$

and from ideal gas, assuming temperature changes over the time step are negligible,

$$\delta P_{I+1} = \delta \rho_{I+1} RT = \dot{m}_{error,I} RT \frac{\delta t}{Vol_I} \quad (2.4.32a)$$

$$\delta P_I = \delta \rho_I RT = 0 \quad (2.4.32b)$$

$$\delta P_{I-1} = \delta \rho_{I-1} RT = 0. \quad (2.4.32c)$$

Substituting these results into Eq. 2.4.30, we get

$$\left[\frac{-A_{I+1} RT}{(u+c)_{I+1}} + u_{I+1} A_{I+1} \right] \dot{m}_{error,I} \frac{\delta t}{Vol_I} = \dot{m}_{change,I} \quad (2.4.33)$$

Since for stability we require that \dot{m}_{error} and \dot{m}_{change} have the same sign, we must have

$$\left[\frac{-RT}{(u+c)_{I+1}} + u_{I+1} \right] A_{I+1} > 0. \quad (2.4.34)$$

If we substitute c^2/γ for RT into Eq. 2.4.34, we get

$$\frac{-c^2}{\gamma(u+c)_{I+1}} + u_{I+1} > 0 \quad (2.4.35)$$

or

$$\gamma u_{I+1} (u+c)_{I+1} > c^2. \quad (2.4.36)$$

For a γ of 1.4, Eq. 2.4.36 will be satisfied if

$$u > 0.48c \quad (2.4.37a)$$

or

$$M > 0.48. \quad (2.4.37b)$$

Thus for low Mach number flows, this density update method is unstable.

Stability of the Pressure Update Method Using Ideal Gas: The pressure update method updates the pressure directly from the continuity error and then the density is updated through the ideal gas equation of state. Again, for an intermediate solution where there is a continuity error only between nodes I and I + 1, Eq. 2.4.13 yields

$$\delta P_I = \dot{m}_{error,I} \delta t_c RT / Vol_I \quad (2.4.38a)$$

$$\delta P_{I+1} = 0 \quad (2.4.38b)$$

$$\delta P_{I-1} = 0 \quad (2.4.38c)$$

and from the ideal gas equation of state assuming that temperature changes over one time step are negligible, we get

$$\delta \rho_I = \frac{\delta P_I}{RT} = \dot{m}_{error,I} \frac{\delta t_c}{Vol_I} \quad (2.4.39a)$$

$$\delta \rho_{I+1} = \frac{\delta P_{I+1}}{RT} = 0 \quad (2.4.39b)$$

Substituting these results into Eq. 2.4.30, we get

$$\left(\frac{A_{I+1}}{u_{I+1}} + \frac{A_I}{u_I} - \frac{u_I A_I}{RT} \right) \dot{m}_{error,I} \frac{\delta t_c RT}{Vol_I} = \dot{m}_{change,I} \quad (2.4.40)$$

For \dot{m}_{error} and \dot{m}_{change} to have the same sign, we will require that

$$\frac{A_{I+1}}{u_{I+1}} + \frac{A_I}{u_I} - \frac{u_I A_I}{RT} > 0. \quad (2.4.41)$$

If we assume that the values of properties at node I are approximately the same as the values at node I + 1 and if we substitute c^2/γ for RT, Eq. 2.4.41 becomes

$$\frac{2}{u} - \frac{\gamma u}{c^2} > 0 \quad (2.4.42)$$

or

$$u < \sqrt{\frac{2c^2}{\gamma}} . \quad (2.4.43)$$

For $\gamma = 1.4$, for stability to be maintained

$$u < 1.2c \quad (2.4.44a)$$

$$M < 1.2 . \quad (2.4.44b)$$

Thus for high Mach number flows, this pressure update method is unstable.

A Downwind Effective Pressure or an Upwind Effective Density Method: If an inconsistency in the pressure-density relation (the ideal gas equation of state) is introduced such that the pressure used in the momentum equation is offset by 1 grid point from the density used in the continuity equation, the equation of state may be written as

$$P_I = \rho_{I+1}RT \quad (2.4.45)$$

In a density update method, the pressure used in the momentum equation, an effective pressure , is evaluated using properties downwind of the actual node. Similarly, in a pressure update method, the density used in both continuity and momentum equations is evaluated using a pressure upwind of the actual node. For both the density and pressure update methods, the changes in density and pressure are

DENSITY

$$\delta p_{I-1} = 0 \quad (2.4.46a)$$

$$\delta p_I = \dot{m}_{error,I-1} \frac{\delta t}{Vol_I} \quad (2.4.46b)$$

$$\delta\rho_{I+1} = \dot{m}_{error,I} \frac{\delta t}{Vol_{I+1}} \quad (2.4.46c)$$

PRESSURE

$$\delta P_{I-1} = \dot{m}_{error,I-1} RT \frac{\delta t}{Vol_{I-1}} \quad (2.4.46d)$$

$$\delta P_I = \dot{m}_{error,I} RT \frac{\delta t}{Vol_I} \quad (2.4.46e)$$

$$\delta P_{I+1} = \dot{m}_{error,I+1} RT \frac{\delta t}{Vol_{I+1}} \quad (2.4.46f)$$

Eq. 2.4.30 now becomes,

$$\left. \begin{aligned} & - \left(\frac{A_I}{(u + ec)_I} + \frac{u_I A_I}{RT} \right) \left(\frac{\delta t RT}{Vol_{I-1}} \right) \dot{m}_{error,I-1} \\ & + \left(\frac{A_{I+1}}{(u + ec)_{I+1}} + \frac{A_I}{(u + ec)_I} + \frac{u_{I+1} A_{I+1}}{RT} \right) \left(\frac{\delta t RT}{Vol_I} \right) \dot{m}_{error,I} \\ & - \left(\frac{A_{I+1}}{(u + ec)_{I+1}} \right) \left(\frac{\delta t RT}{Vol_{I+1}} \right) \dot{m}_{error,I+1} \end{aligned} \right\} = \dot{m}_{change,I} \quad (2.4.47)$$

From this equation we can see that the coefficient of $\dot{m}_{error,I}$ is always positive and so the downwind effective pressure method and the upwind effective density method both pass the simple stability criterion ($\dot{m}_{change,I}$ has the same sign as $\dot{m}_{error,I}$) for all Mach numbers. It should also be noted that the coefficients of $\dot{m}_{error,I-1}$ and $\dot{m}_{error,I+1}$ are of the opposite sign to the coefficient of $\dot{m}_{error,I}$ and it is generally of a smaller magnitude. This further assures the stability of Eq. 2.4.45.

While the pressure-density relationship of Eq. 2.4.45 is stable, testing has shown that it results in solutions with poor shock capturing. The calculated shock is spread over numerous grid points.

Fig. 2.4.3 shows the calculated and theoretical pressure distributions for a 1-D calculation using Eq. 2.4.45 with a nominal shock Mach number of 1.45.

Stability of a 3-Point Interpolation for the Effective Pressure: One of the pressure-density relations which can be used in the density update method is a three point interpolation of the density used in the ideal gas equation of state to obtain an effective pressure. If we assume that the temperature is approximately uniform, we may write the interpolation formula as

$$P_I = (\rho_{I+1} - \frac{(\rho_{I+2} - \rho_{I-1})}{3})RT \quad (2.4.48)$$

The change in pressure for one iteration is therefore

$$\delta P_I = (\delta \rho_{I+1} - \frac{\delta \rho_{I+2}}{3} + \frac{\delta \rho_{I-1}}{3})RT \quad (2.4.49)$$

Substituting this change of pressure into Eq. 2.4.30 and neglecting variations of A, u, and c with x, we obtain,

$$\left. \begin{aligned} & - \left(\frac{Ac^2}{\gamma(u+c)} \right) \left(\delta \rho_I - \frac{\delta \rho_{I+1}}{3} + \frac{\delta \rho_{I-2}}{3} \right) \\ & + \left(\frac{2Ac^2}{\gamma(u+c)} \right) \left(\delta \rho_{I+1} - \frac{\delta \rho_{I+2}}{3} + \frac{\delta \rho_{I-1}}{3} \right) - uA\delta \rho_I \\ & - \left(\frac{Ac^2}{\gamma(u+c)} \right) \left(\delta \rho_{I+2} - \frac{\delta \rho_{I+3}}{3} + \frac{\delta \rho_I}{3} \right) - uA\delta \rho_{I+1} \end{aligned} \right\} = \dot{m}_{change,I} \quad (2.4.50)$$

Collecting terms of $\delta \rho$ and substituting the Mach number, M , for u/c , we get

DENTON 1D EXAMPLE

UPWIND DENSITY

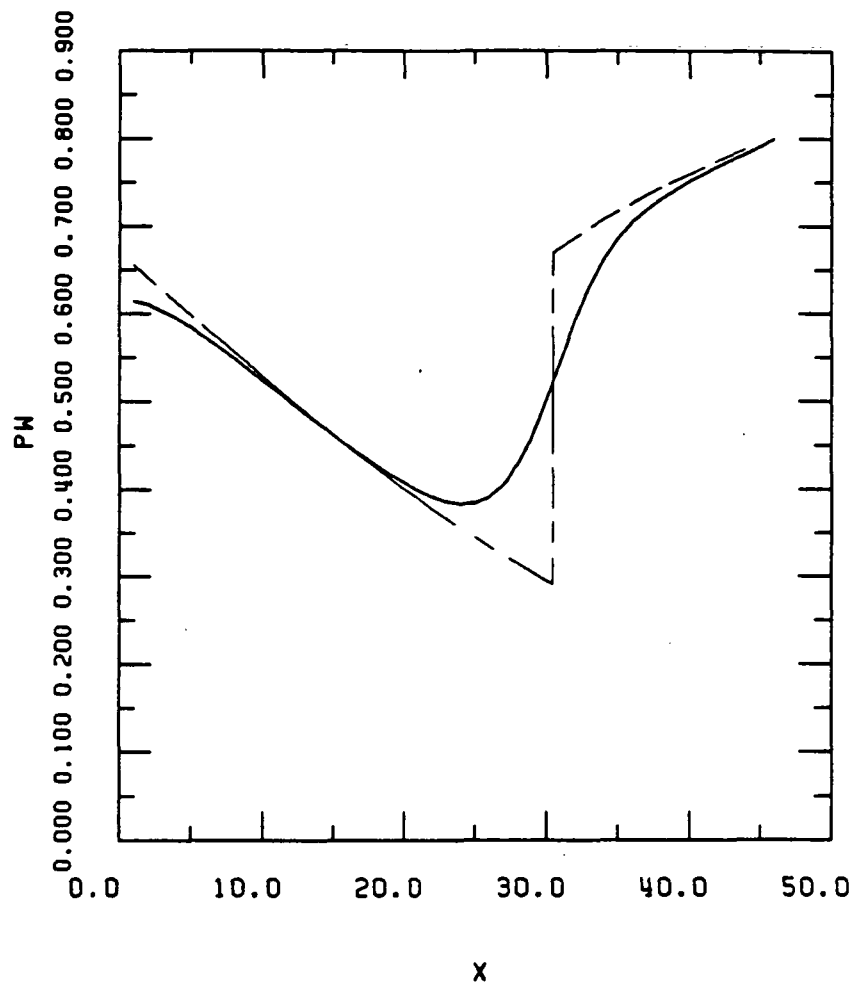


Fig. 2.4.3 Comparison of calculated and theoretical 1-D static pressure distributions, $PW = P/P_{t,inlet}$.

— theoretical;
 - - - calculated using an upwind effective density, Eq. 2.4.45.

Grid spacing, $\delta x = 1$; $P_{exit}/P_{t,inlet} = 0.80$.

$$\begin{aligned}
& + Ac/(3\gamma(M + 1)) \quad \delta\rho_{I+3} \\
& - 5Ac/(3\gamma(M + 1)) \quad \delta\rho_{I+2} \\
& + Ac(7/(3\gamma(M + 1)) + M) \quad \delta\rho_{I+1} \\
& - Ac(4/(3\gamma(M + 1)) + M) \quad \delta\rho_I \\
& + 2Ac/(3\gamma(M + 1)) \quad \delta\rho_{I-1} \\
& - Ac/(3\gamma(M + 1)) \quad \delta\rho_{I-2} \\
& = \dot{m}_{change,I}
\end{aligned} \tag{2.4.51}$$

We can see that the change in mass flow rate for the control volume between grid points I and I + 1 is now dependent upon the changes in density at 6 grid points. If there was only a mass flow rate error for control volume (I,J) the simple test for stability would be satisfied. Since the coefficient of $\delta\rho_{I+1}$ is positive for all Mach numbers the change in mass flow rate would have the same sign as the error in mass flow rate.

However, since the coefficients of $\delta\rho_{I+3}$ and $\delta\rho_{I-1}$ are also positive, a more sophisticated stability criterion is appropriate. The stability criterion that we will apply is : the center point coefficient must be greater than the sum of the other positive coefficients.

$$\Sigma(\text{centerpoint coefficient}) > \Sigma(\text{other positive coefficients}) \tag{2.4.52}$$

Applying this criterion to Eq. 2.4.51, stability requires that

$$Ac(7/(3\gamma(M + 1)) + M) > 3Ac/(3\gamma(M + 1)) \tag{2.4.53}$$

This expression is always true, therefore Eq. 2.4.48 should be stable for all Mach numbers. The experience of Denton and other users of his code confirms this.

Stability of the 3-Point Interpolation for the Effective Density: A similar analysis can be done for the pressure-update effective-density method using a three point interpolation of pressure to obtain the effective density

$$\rho_{I+1} = [P_I + \frac{(P_{I+1} - P_{I-2})}{3}] \frac{1}{RT} \quad (2.4.54)$$

For the change in density, we get

$$\delta\rho_{I+1} = (\delta P_I + \frac{(\delta P_{I+1} - \delta P_{I-2})}{3}) \frac{1}{RT} \quad (2.4.55)$$

and then substituting this change into Eq. 2.4.30, gives us

$$\begin{aligned} &+ (A/c)(-1/M + \gamma M/3) \quad \delta P_{I+1} \\ &+ (A/c)(2/M + 2\gamma M/3) \quad \delta P_I \\ &- (A/c)(1/M + \gamma M) \quad \delta P_{I-1} \\ &- (A/c)(\gamma M/3) \quad \delta P_{I-2} \\ &+ (A/c)(\gamma M/3) \quad \delta P_{I-3} \\ &= \dot{m}_{change,I} \end{aligned} \quad (2.4.56)$$

The center point coefficient is the coefficient of δP_I , since this is proportional to $\dot{m}_{error,I}$ in the pressure update method. In Eq. 2.4.56, the coefficient of δP_I is positive and greater than the sum of the other positive coefficients; therefore Eq. 2.4.54 should be stable for all Mach numbers.

Mach Number Dependent Interpolation Formula for Effective Density: From experience, it has been observed that when the Mach number is low, the pressure update method is stable with the ideal gas equation of state satisfied at each grid point. Since this is the correct pressure-density relation for ideal gases it should be used where feasible. In this section we will start with a generalized pressure interpolation equation for the effective density

$$\rho_{I+1} = [P_I + a_0(P_{I+1} - P_I) + a_1 \frac{(P_{I+1} - P_{I-1})}{2} + a_2 \frac{(P_{I+1} - P_{I-2})}{3}] \frac{1}{RT} \quad (2.4.57)$$

and seek Mach number limitations at a_0, a_1 and a_2 using criterion (Eq. 2.4.52). Comparing equations 2.4.45 and 2.4.57, the upwind effective density corresponds to $a_0 = a_1 = a_2 = 0$, the three

point interpolation, Eq. 2.4.54, corresponds to $a_0 = a_1 = 0$, $a_2 = 1$, and ideal gas to $a_0 = 1$, $a_1 = a_2 = 0$. Substituting

$$\delta p_{I+1} = [(1 - a_0)\delta P_I + (a_0 + \frac{a_1}{2} + \frac{a_2}{3})\delta P_{I+1} - \frac{a_1}{2}\delta P_{I-1} - \frac{a_2}{3}\delta P_{I-2}] \frac{1}{RT} \quad (2.4.58)$$

into Eq. 2.4.30 and rearranging in terms of the coefficients of each δP , a_0 , a_1 , and a_2 yields

$$\left. \begin{aligned} & \left(\frac{A}{c} \right) \left[(-1/M + \gamma M a_0 + (\gamma M/2)a_1 + (\gamma M/3)a_2)\delta P_{I+1} \right. \\ & \quad + (2/M + \gamma M - 2\gamma M a_0 - (\gamma M/2)a_1 - (\gamma M/3)a_2)\delta P_I \\ & \quad + (-1/M - \gamma M + \gamma M a_0 - (\gamma M/2)a_1)\delta P_{I-1} \\ & \quad + ((\gamma M/2)a_1 - (\gamma M/3)a_2)\delta P_{I-2} \\ & \quad \left. + ((\gamma M/3)a_2)\delta P_{I-3} \right] \end{aligned} \right\} = \dot{m}_{change,I} \quad (2.4.59)$$

Let us first consider the case when $a_1 = a_2 = 0$ and find limiting values of a_0 . From Eq. 2.4.57, it is obvious that we should consider only values in the range

$$0 \leq a_0 \leq 1 \quad (2.4.60)$$

The coefficient of δP_I is positive when

$$2/M + \gamma M - 2\gamma M a_0 > 0 \quad (2.4.61)$$

This gives a limit on a_0 which is a function of the Mach number and the limit is

$$a_0 < 1/(\gamma M^2) + 1/2 \quad (2.4.62)$$

But the coefficient of δP_{I+1} is positive when

$$-1/M + \gamma M a_0 > 0, \text{ or } M^2 > 1/(\gamma a_0) \quad (2.4.63)$$

In this region, from Eq. 2.4.52, we require that

$$2/M + \gamma M - 2\gamma M a_0 > -1/M + \gamma M a_0 \quad (2.4.64)$$

or

$$a_0 < 1/(\gamma M^2) + 1/3 . \quad (2.4.65)$$

Valid values of a_0 based on these criteria are shown as a function of Mach number in Fig. 2.4.4.

Let us next consider limiting values of a_1 when a_0 and a_2 are zero. From Eq. 2.4.59 the coefficient of δP_I

$$2/M + \gamma M - \gamma M a_1/2 > 0 \quad (2.4.66)$$

is positive for all Mach numbers in the range

$$0 \leq a_1 \leq 1. \quad (2.4.67)$$

The coefficient of δP_{I-2} is positive for all M and the coefficient of δP_{I+1} is positive when

$$-1/M + \gamma M a_1/2 > 0 \quad \text{or} \quad M^2 > 2/(\gamma a_1). \quad (2.4.68)$$

For $M^2 < 2/(\gamma a_1)$ we then require the coefficient of δP_I to be greater than the coefficient of δP_{I-2} ,

$$2/M + \gamma M - \gamma M a_1/2 > \gamma M a_1/2. \quad (2.4.69)$$

With $a_1 \leq 1$, this is always satisfied. For $M^2 > 2/(\gamma a_1)$ we require the coefficient of δP_I to be greater than the sum of the coefficients of δP_{I-2} and δP_{I+1} ,

$$2/M + \gamma M - \gamma M a_1/2 > \gamma M a_1 - 1/M \quad (2.4.70)$$

or

$$a_1 < 2/(\gamma M^2) + 2/3 . \quad (2.4.71)$$

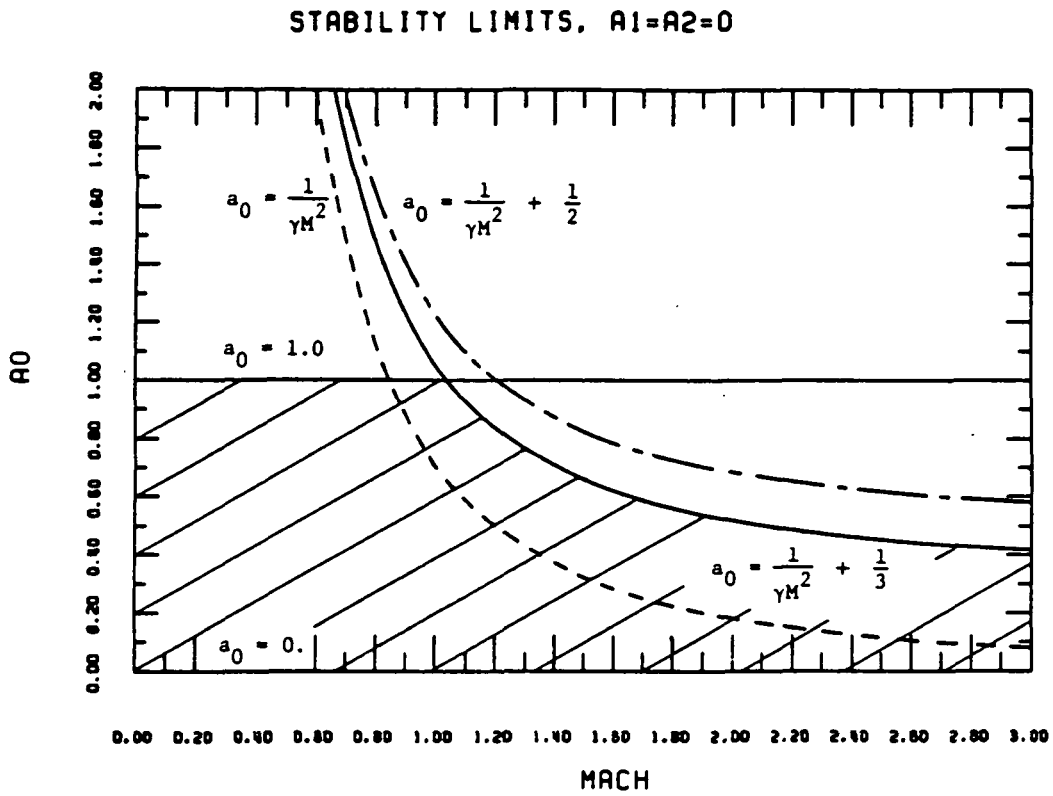


Fig. 2.4.4 Acceptable values of a_0 as a function of Mach number based on Eqs. 2.4.60, 2.4.62, 2.4.63, and 2.4.65 (for $\gamma = 1.4$).

Thus we can have $a_1 = 1$ up to $M^2 = 6/\gamma$ or up to $M = 2.07$ for $\gamma = 1.4$. Fig. 2.4.5 shows the valid range of a_1 based on these criteria.

We now consider combinations of a_0 , a_1 and a_2 . In particular if

$$a_0 + a_1 + a_2 = 1. \quad (2.4.72)$$

the interpolation scheme is second order accurate. (See Appendix A.)

For Mach numbers less than 2, $a_1 = 1$ is stable. Therefore, for $M \leq 2$, we will choose

$$\begin{aligned} a_2 &= 0 \\ a_0 + a_1 &= 1. \end{aligned} \quad (2.4.73)$$

From similar stability analyses to those already given

$$a_0 < 2/(\gamma M^2) - 1/3 \quad (2.4.74)$$

should be stable for $M \leq 2$.

For $M > 2$, we will choose

$$\begin{aligned} a_0 &= 0 \\ a_1 + a_2 &= 1. \end{aligned} \quad (2.4.75)$$

The stability analysis suggests that acceptable values of a_1 are

$$a_1 < 0.4 + 3.6/(\gamma M^2). \quad (2.4.76)$$

The stability criteria, Eqs. 2.4.74 and 2.4.76, are shown on Fig. 2.4.6.

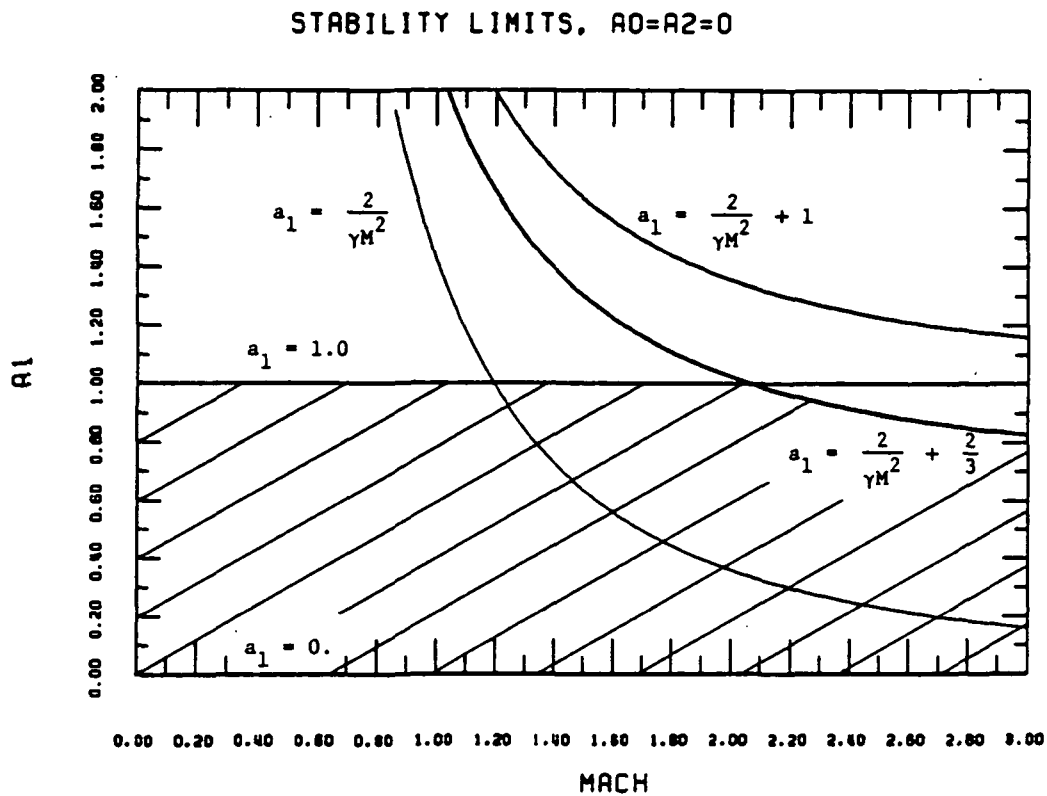


Fig. 2.4.5 Acceptable values of a_1 as a function of Mach number based on Eqs. 2.4.67, 2.4.68, 2.4.69, and 2.4.71 (for $\gamma = 1.4$).

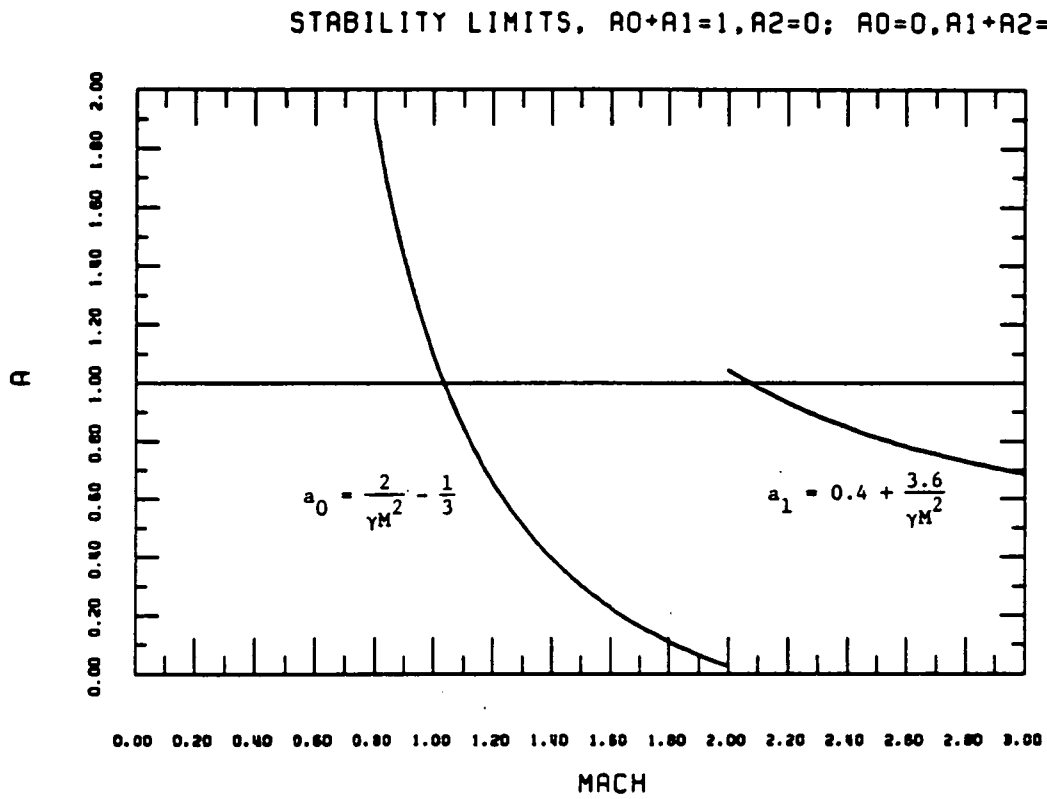


Fig. 2.4.6 Stability limits for a_0 when $a_2 = 0$ and $a_0 + a_1 = 1$,
and for a_1 when $a_0 = 0$ and $a_1 + a_2 = 1$.

A set of equations for a_0 , a_1 , and a_2 , which satisfy Eq. 2.4.72 and so give second order accurate interpolation, and which satisfy Eqs. 2.4.73-2.4.76 so that they satisfy the stability criteria, have been selected. These are:

$$\begin{aligned} a_0 &= (0.8/3)(4/M^2 - 1) \\ \text{for } M \leq 2 \quad a_1 &= 1 - a_0 \\ a_2 &= 0; \end{aligned} \tag{2.4.77}$$

$$\begin{aligned} a_0 &= 0 \\ \text{for } M > 2 \quad a_1 &= 4/M^2 \\ a_2 &= 1 - a_1. \end{aligned} \tag{2.4.78}$$

These Mach number dependent formulations for a_0 , a_1 and a_2 are shown in Fig. 2.4.7. These equations are tested in Section 3.4 where they are referred to as the M&M formula.

2.5 TIME STEPS

A unique feature of this method is the use of different time steps for the continuity and momentum equations. Previous workers who have used explicit time marching methods have used the CFL condition as a basis for determining allowable time steps which maintain stability. The general form of the CFL condition for three dimensional inviscid flow is (21),

$$(\delta t)_{CFL} \leq \left(\frac{|u|}{\delta x} + \frac{|v|}{\delta y} + \frac{|w|}{\delta z} + c \sqrt{\frac{1}{(\delta x)^2} + \frac{1}{(\delta y)^2} + \frac{1}{(\delta z)^2}} \right)^{-1} \tag{2.5.1}$$

The same time step is used for both the continuity and momentum equations and typically the governing equations are updated simultaneously rather than sequentially as is done with the current method. The CFL condition is justified by requiring that the analytical domain of influence lie

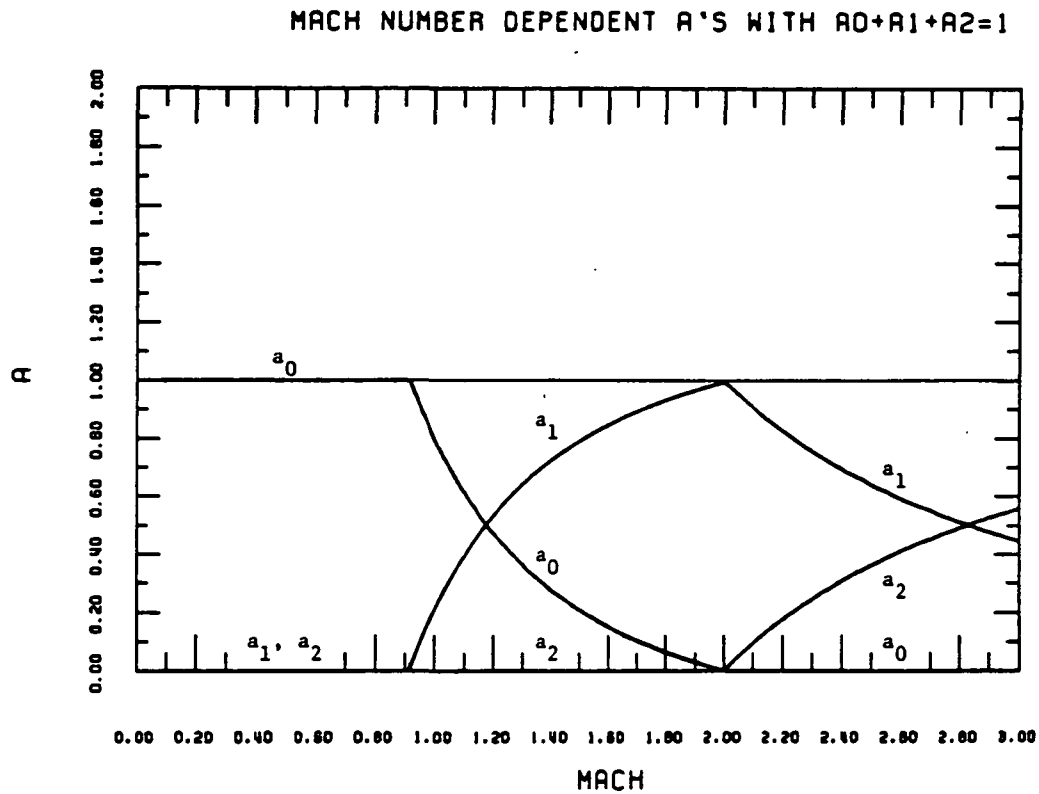


Fig. 2.4.7 M & M Mach number dependent values (Eqs. 2.4.77 and 2.4.78) for the coefficients in Eq. 2.4.57.

within the numerical domain of influence (21). The CFL condition can become very restrictive when the grid becomes highly stretched (the δy dimension is much less than the δx dimension). A highly stretched grid is needed in calculations with turbulent boundary layers.

The Denton code (13) uses a variation of the CFL condition (Eq. 2.5.1). The time steps are based upon the following,

$$\delta t \leq FT \times \frac{(\delta l)_{\min}}{\sqrt{\gamma RT_{01}}} \quad (2.5.2)$$

where FT is a time factor typically between 0.2 and 0.5, δl_{\min} is the minimum characteristic length for a given control volume, and $\sqrt{\gamma RT_{01}}$ is a reference speed of sound based upon the inlet stagnation temperature. The same time step is used in the continuity and momentum equations. The time steps can ; however, be different for each control volume if only the steady-state solution is desired. If a time accurate solution is desired then the same time step must be used everywhere in the flow and it must be based upon the control volume with the most restrictive time step.

The current method not only uses different time steps for each control volume but it also uses different time steps for the continuity equation and for the momentum equations. The advantage of using different time steps is that for flows with thin boundary layers, the allowable momentum time step can be significantly larger than that allowed by the CFL condition. These larger time steps allow the boundary layer profiles to change more rapidly and enhances the convergence rate significantly compared with a method which uses the CFL condition. To be able to have a calculation method which uses different time steps for different equations, the usual conservative form of the momentum equations cannot be used. The form of the momentum equations used for the current method is

$$\rho \frac{\partial \underline{u}}{\partial t} + \nabla \cdot \rho \underline{u} \underline{u} - \underline{u} (\nabla \cdot \rho \underline{u}) = - \nabla \cdot P \delta_{ij} + \nabla \cdot \mu \nabla \underline{u} + \nabla \cdot \mu \overline{\nabla \underline{u}}^T . \quad (2.5.3)$$

This is in contrast to the straight conservative form of the momentum equations which is

$$\frac{\partial \rho \underline{u}}{\partial t} + \nabla \cdot \rho \underline{u} \underline{u} = - \nabla \cdot P \delta_{ij} + \nabla \cdot \mu \nabla \underline{u} + \nabla \cdot \overline{\nabla \underline{u}}^T . \quad (2.5.4)$$

By using Eq. 2.5.3 instead of Eq. 2.5.4, the \underline{u} velocity vector is updated directly from the momentum error. Eq. 2.5.4 requires that you update $(\rho \underline{u})$ first and then calculate the new velocity from

$$\underline{u}^{n+1} = (\rho \underline{u})^{n+1} / \rho^{n+1} . \quad (2.5.5)$$

The time derivative of $(\rho \underline{u})$, $\frac{\partial(\rho \underline{u})}{\partial t}$ can be expanded, using the chain rule, as

$$\frac{\partial(\rho \underline{u})}{\partial t} = \rho \frac{\partial \underline{u}}{\partial t} + \underline{u} \frac{\partial \rho}{\partial t} \quad (2.5.6)$$

The term $\partial \rho / \partial t$ is also calculated from the continuity error. So to correctly update $(\rho \underline{u})$ over one time step using the conservative form, Eq. 2.5.4, the same time step must be used for both the continuity and momentum equations. However, Eq. 2.5.3 does not have that restriction. It should be noted that as the solution approaches a steady-state, $(\underline{u}(\nabla \cdot \rho \underline{u}))$ goes to zero, therefore Eq. 2.5.3 then reduces to Eq. 2.5.4. In the current method, the expressions that are used to determine the allowable time steps are , for the momentum equations

$$\delta t_m \leq \frac{1}{\left| \frac{u}{\delta x} \right| + \left| \frac{v_{eff}}{\delta y} \right| + \left| \frac{2\mu}{\rho(\delta y)^2} \right|} \quad (2.5.7)$$

and for continuity,

$$\delta t_c \leq \frac{1}{2RT \left[\frac{\delta t_m}{(\delta x)^2} + \frac{\delta t_m}{(\delta y)^2} + \left| \frac{u}{RT \delta x} \right| + \left| \frac{v_{eff}}{RT \delta y} \right| \right]} \quad (2.5.8)$$

where δt_m is the momentum time step, δt_c is the continuity time step and v_{eff} is an effective y-component of velocity. The effective velocity, v_{eff} , is determined from the following equation,

$$v_{eff} = \frac{|\text{mass flux through north face}| + |\text{mass flux through south face}|}{2\delta x \rho} \quad (2.5.9)$$

where the north and south faces for a control volume are shown in Fig. 2.5.1. These time steps are typically reduced by a factor of 2 to reflect the uncertainty of the non-linear nature of the equations and the non-uniformity of the grid. During the initial transients, a factor of up to 4 may be needed. These reductions in the time steps will be given the symbol TIMEF. In the following two subsections, the logic behind these time steps will be presented. The time steps can be derived based upon (1) the differential, or (2) the discretized form of the governing equations.

DIFFERENTIAL FORM

The x-momentum equation can be written in non-conservative form as

$$\rho \frac{\partial u}{\partial t} + \rho u \frac{\partial u}{\partial x} + \rho v \frac{\partial u}{\partial y} = - \frac{\partial P}{\partial x} + \mu \frac{\partial^2 u}{\partial y^2} \quad (2.5.10)$$

assuming that viscous stresses can be represented by the simplified form shown. For stability we require that the coefficient of the unsteady velocity be greater than the sum of the absolute value of the coefficients which involve derivatives of the u-velocity. Let us rewrite Eq. 2.5.10 in terms of changes δu , δt_m , and the dimensions δx , and, δy ,

$$\rho \frac{\delta u}{\delta t_m} + \rho u \frac{\delta u}{\delta x} + \rho v \frac{\delta u}{\delta y} = - \frac{\delta P}{\delta x} + 2\mu \frac{\delta u}{(\delta y)^2} \quad (2.5.11)$$

Now let us apply the above stability requirement to Eq. 2.5.11, and the result is

$$\frac{\rho}{\delta t_m} \geq \left| \frac{\rho u}{\delta x} \right| + \left| \frac{\rho v}{\delta y} \right| + \left| \frac{2\mu}{(\delta y)^2} \right| \quad (2.5.12)$$

or in terms of δt_m ,

$$\delta t_m \leq \frac{1}{\left| \frac{u}{\delta x} \right| + \left| \frac{v}{\delta y} \right| + \left| \frac{2\mu}{\rho(\delta y)^2} \right|} \quad (2.5.13)$$

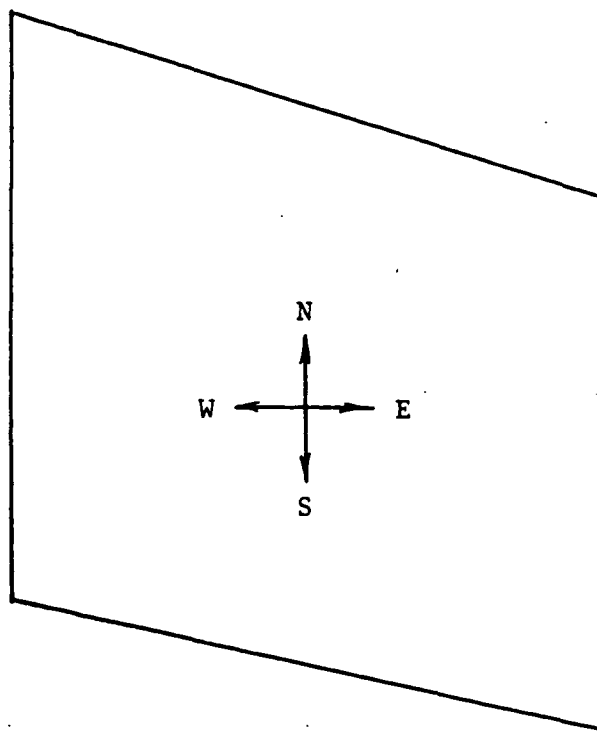


Fig. 2.5.1 Identification of Control Volume Faces

The v-velocity used in Eq. 2.5.13 should be the effective velocity which was introduced in Eq. 2.5.9.

The time step used for the continuity equation is determined using a similar procedure, but because of the sequential nature of the current method, extra care must be taken to quantify the interaction between the continuity and momentum equations. In the current method the pressure is updated because of the continuity error and this new pressure is used in the momentum equation. This pressure change must not be too large so as to upset the stability of the method. The continuity equation can be written in differential form as

$$\frac{\partial \rho}{\partial t} + \frac{\partial \rho u}{\partial x} + \frac{\partial \rho v}{\partial y} = 0 \quad . \quad (2.5.14)$$

Expanding the derivatives using the chain rule; Eq. 2.5.14 becomes

$$\frac{\partial \rho}{\partial t} + \rho \frac{\partial u}{\partial x} + u \frac{\partial \rho}{\partial x} + \rho \frac{\partial v}{\partial y} + v \frac{\partial \rho}{\partial y} = 0 \quad . \quad (2.5.15)$$

What we want to do now is to make each derivative in Eq. 2.5.15 in terms of a common variable. Because we are using a pressure update method we will choose pressure as our common variable. For our analysis we will assume that the fluid is an ideal gas and that temperature changes are small in comparison to pressure changes over one iteration. That means that a change in density, $\delta \rho$, from one iteration to the next can be related to the change in pressure using

$$\delta \rho = \frac{\delta P}{RT} \quad . \quad (2.5.16)$$

Rewriting Eq. 2.5.15 in terms of finite changes $\delta \rho$, δu , δv , and δt_c and finite dimensions δx and δy ,

$$\frac{\delta \rho}{\delta t_c} + \rho \frac{\delta u}{\delta x} + u \frac{\delta \rho}{\delta x} + \rho \frac{\delta v}{\delta y} + v \frac{\delta \rho}{\delta y} = 0 \quad . \quad (2.5.17)$$

Substituting Eq. 2.5.16 into Eq. 2.5.17, we get

$$\frac{1}{RT} \frac{\delta P}{\delta t_c} + \rho \frac{\delta u}{\delta x} + \frac{u}{RT} \frac{\delta P}{\delta x} + \rho \frac{\delta v}{\delta y} + \frac{v}{RT} \frac{\delta P}{\delta y} = 0 . \quad (2.5.18)$$

The momentum equation must be used to relate a given change in $u, \delta u$, to a change in pressure, δP . If the momentum equation, Eq. 2.5.11, is reduced to its steady form it becomes,

$$\rho u \frac{\delta u}{\delta x} + \rho v \frac{\delta u}{\delta y} = - \frac{\delta P}{\delta x} + 2\mu \frac{\delta u}{(\delta y)^2} . \quad (2.5.19)$$

Solving for δu , and using absolute values to give conservative results,

$$\delta u = \frac{\frac{\delta P}{\rho}}{[|\frac{u}{\delta x}| + |\frac{v_{eff}}{\delta y}| + |\frac{2\mu}{\rho(\delta y)^2}|] \delta x} \quad (2.5.20)$$

then using Eq. 2.5.13, Eq. 2.5.20 becomes,

$$\delta u = \frac{(\frac{\delta P}{\rho}) \delta t_m}{\delta x} . \quad (2.5.21)$$

Similarly we can obtain

$$\delta v = \frac{(\frac{\delta P}{\rho}) \delta t_m}{\delta y} . \quad (2.5.22)$$

Now we can substitute Eq. 2.5.21 and Eq. 2.5.22 into Eq. 2.5.18 and the resulting expression is

$$\frac{1}{RT} \frac{\delta P}{\delta t_c} + \frac{\rho}{\delta x} [\frac{\delta P \delta t_m}{\rho \delta x}] + \frac{u}{RT} \frac{\delta P}{\delta x} + \frac{\rho}{\delta y} [\frac{\delta P \delta t_m}{\rho \delta y}] + \frac{v}{RT} \frac{\delta P}{\delta y} = 0 . \quad (2.5.23)$$

Using the same stability requirement as was used for the momentum equations, we get

$$\frac{1}{RT} \frac{1}{\delta t_c} \geq |\frac{\delta t_m}{(\delta x)^2}| + |\frac{u}{RT \delta x}| + |\frac{\delta t_m}{(\delta y)^2}| + |\frac{v_{eff}}{RT \delta y}| \quad (2.5.24)$$

which when solved for δt_c becomes

$$\delta t_c \leq \frac{1}{RT \left[\left| \frac{\delta t_m}{(\delta x)^2} \right| + \left| \frac{\delta t_m}{(\delta y)^2} \right| + \left| \frac{u}{RT \delta x} \right| + \left| \frac{v}{RT \delta y} \right| \right]} \quad (2.5.25)$$

DISCRETIZED FORM

Another way of determining the time step limitations for the continuity and momentum equations is to analyse the discretized form of the steady momentum and continuity equations. The momentum equations will be analysed first to determine the momentum time steps.

MOMENTUM TIME STEPS: Integrating the steady flow x-momentum equation

$$\nabla \cdot \rho \underline{u} u = - \frac{\partial P}{\partial x} + \nabla \cdot \mu \nabla u \quad (2.5.26)$$

over the control volume shown in Fig. 2.5.2 and using Gauss' theorem to obtain area integrals we obtain

$$\iint \rho \underline{u} u \cdot d\underline{A} = \iint P A_x + \iint \mu \nabla u \cdot d\underline{A} \quad (2.5.27)$$

Discretizing this equation for the control volume shown in Fig. 2.5.2 and neglecting derivatives with respect to x in the viscous terms, we obtain

$$\begin{aligned} & (\dot{m}u)_{east,I,J} + (\dot{m}u)_{west,I,J} + (\dot{m}u)_{north,I,J} + (\dot{m}u)_{south,I,J} + (P_{I+1,J} - P_{I,J})\delta y \\ & - \left[\frac{\mu(u_{I+1,J+1} - u_{I+1,J})}{\delta y} - \frac{\mu(u_{I+1,J} - u_{I+1,J-1})}{\delta y} \right] \delta x = 0 \quad (2.5.28) \end{aligned}$$

The momentum fluxes, $(\dot{m}u)_{west}$ and $(\dot{m}u)_{east}$ can be represented as,

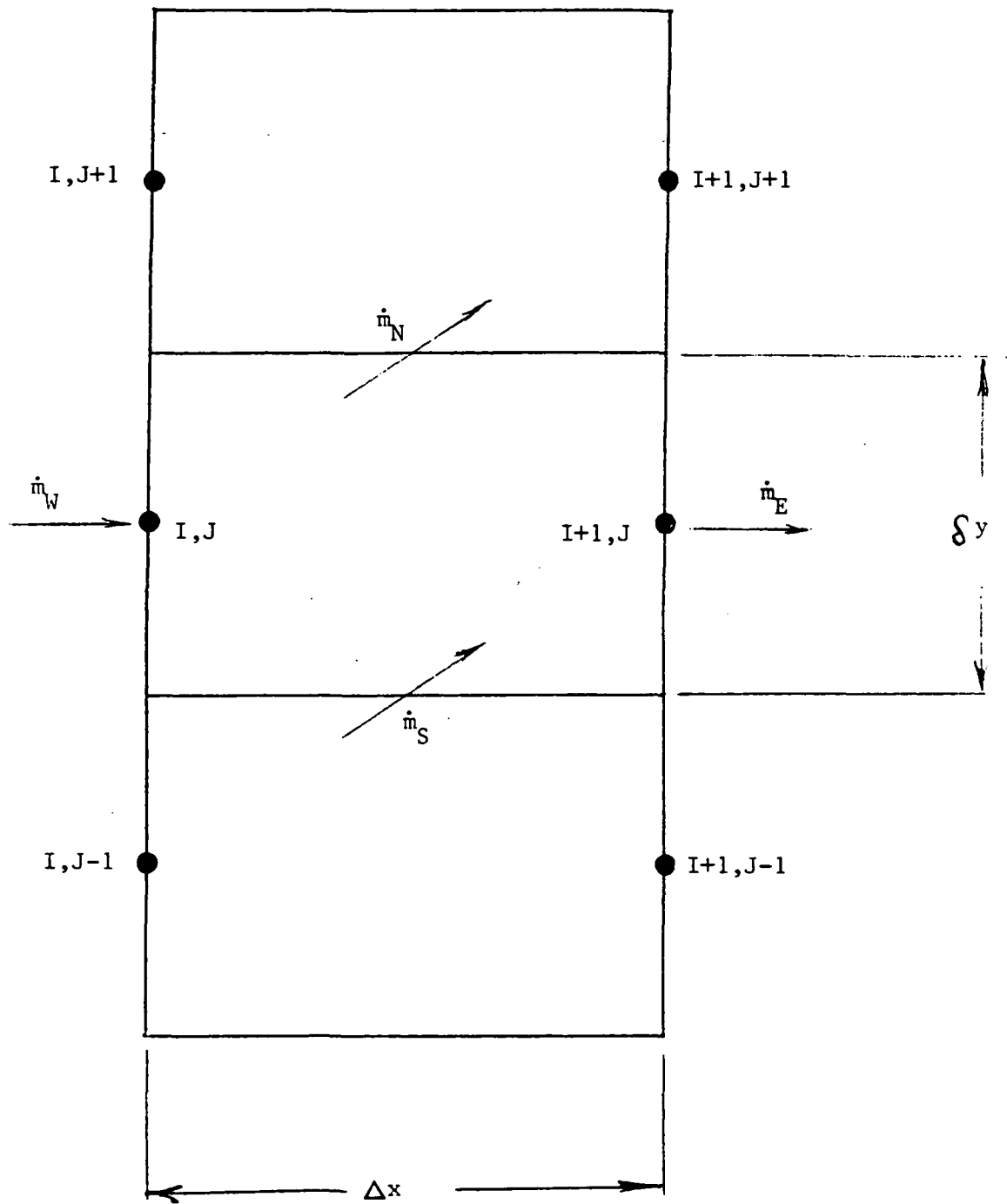


Fig. 2.5.2 Typical Flux Arrangement for a Control Volume

$$(\dot{m}u)_{west} = \dot{m}_{west} \times u_{I,J} \quad (2.5.29)$$

and

$$(\dot{m}u)_{east} = \dot{m}_{east} \times u_{I+1,J} \quad (2.5.30)$$

Assuming that the grid spacing is uniform in the y-direction, the momentum fluxes $(\dot{m}u)_{south}$ and $(\dot{m}u)_{north}$ are respectively,

$$(\dot{m}u)_{south} = 0.25 \times \dot{m}_{south} \times (u_{I,J} + u_{I+1,J} + u_{I,J-1} + u_{I+1,J-1}) \quad (2.5.31)$$

and

$$(\dot{m}u)_{north} = 0.25 \times \dot{m}_{north} \times (u_{I,J} + u_{I+1,J} + u_{I,J+1} + u_{I+1,J+1}) \quad (2.5.32)$$

Combining Eqs. 2.5.28, 2.5.29, 2.5.30, 2.5.31, and 2.5.32, we get that

$$\begin{aligned} & \dot{m}_{east} \times u_{I+1,J} + \dot{m}_{west} \times u_{I,J} + 0.25 \times \dot{m}_{north} \times (u_{I,J} + u_{I+1,J} + u_{I,J+1} + u_{I+1,J+1}) \\ & + 0.25 \times \dot{m}_{south} \times (u_{I,J} + u_{I+1,J} + u_{I,J-1} + u_{I+1,J-1}) + (P_{I+1,J} - P_{I,J})\delta y \\ & - \left[\frac{\mu(u_{I+1,J+1} - u_{I+1,J})}{\delta y} - \frac{\mu(u_{I+1,J} - u_{I+1,J-1})}{\delta y} \right] \delta x = RHS \quad (2.5.33) \end{aligned}$$

For the converged solution, the right hand side (RHS) of Eq. 2.5.33 will be zero. For intermediate solutions, the right hand side of Eq. 2.5.33 is equal to the momentum error.

The stability requirement to be applied to the discretized momentum equation (Eq. 2.5.33) is that the change in velocity for node (I+1,J), $\delta u_{I+1,J}$, for one time step be less than the momentum error divided by the sum of the coefficients associated with the centerpoint node (I+1,J), in other words,

$$\delta u_{I+1,J} \leq \frac{(\text{momentum error})}{(\text{sum of the coefficients of node } I+1,J)} . \quad (2.5.34)$$

The coefficients associated with the velocity $u_{I+1,J}$ from Eq. 2.5.33 are

$$\Sigma(\text{Coefficients}) = \dot{m}_{east} + 0.25\dot{m}_{south} + 0.25\dot{m}_{north} + 2\mu \frac{\delta x}{\delta y} . \quad (2.5.35)$$

To reflect the uncertainty of the signs of the fluxes through the transverse faces, the transverse contributions to the coefficients will be combined into a single transverse mass flux, \dot{m}_T , defined as

$$\dot{m}_T = 0.5[|\dot{m}_{south}| + |\dot{m}_{north}|] . \quad (2.5.36)$$

With this, Eq. 2.5.35 becomes

$$\Sigma(\text{Coefficients}) = \dot{m}_{east} + 0.5\dot{m}_T + 2\mu \frac{\delta x}{\delta y} . \quad (2.5.37)$$

The mass flux through the east face, \dot{m}_{east} , in terms of the fluid properties at the node point (I+1,J) is,

$$\dot{m}_{east} = \rho_{I+1,J} u_{I+1,J} \delta y . \quad (2.5.38)$$

Therefore Eq. 2.5.37 can be written as,

$$\Sigma(\text{Coefficients}) = \rho_{I+1,J} u_{I+1,J} \delta y + 0.50 \dot{m}_T + 2\mu \frac{\delta x}{\delta y} . \quad (2.5.39)$$

To put the stability requirements of Eq. 2.5.34 in terms of time marching terminology, note that from the above stability requirement that

$$\delta u_{I+1,J} \leq \frac{\text{momentum error}}{(\text{sum of the coefficients of node } I+1,J)} \quad (2.5.40)$$

and from time marching terminology that

$$\delta u_{I+1,J} = \frac{(\text{momentum error})}{\rho} \frac{\delta t_m}{Vol_{I,J}} \quad (2.5.41)$$

Combining Eqs. 2.5.40 and 2.5.41, we get for a time marching method that

$$\delta t_m \leq \frac{\rho Vol_{I,J}}{(\text{sum of the coefficients of node I+1,J})} \quad (2.5.42)$$

Substituting the value for the sum of the coefficients from Eq. 2.5.39 into Eq. 2.5.42, we get that

$$\delta t_m \leq \frac{\rho \delta x \delta y}{\rho u \delta y + 0.5 \dot{m}_T + \frac{2\mu \delta x}{\delta y}} \quad (2.5.43)$$

where $Vol_{I,J} = \delta x \delta y$ has been used. Simplifying Eq. 2.5.43, we get

$$\delta t_m \leq \frac{1}{\frac{u}{\delta x} + \frac{0.5 \dot{m}_T}{\rho \delta x \delta y} + \frac{2\mu}{\rho \delta y^2}} \quad (2.5.44)$$

Then substituting in the previously defined v_{eff} (Eq. 2.5.9), Eq. 2.5.44 becomes

$$\delta t_m \leq \frac{1}{\frac{u}{\delta x} + \frac{0.5 v_{eff}}{\delta y} + \frac{2\mu}{\rho \delta y^2}} \quad (2.5.45)$$

which can be compared with Eq. 2.5.13 derived from the differential form of the governing equations and is

$$\delta t_m \leq \frac{1}{\left| \frac{u}{\delta x} \right| + \left| \frac{v_{eff}}{\delta y} \right| + \frac{2\mu}{\rho \delta y^2}} \quad (2.5.46)$$

CONTINUITY TIME STEP: The continuity time step can also be calculated based upon the discretized form of the momentum and continuity equations. The basic stability requirement used in obtaining the continuity time step will be that over one time step that the change in mass flow rate not be greater than the error in mass flow rate as defined in section 2.4. Because the degree of complexity would be large to analyze the full form of the discretized continuity and momentum equations for a generalized control volume, a simplified analysis will be used here which analyzes the x and y- direction contributions to the continuity time step separately. The principle of superposition will then be used to develop a complete expression for the continuity time step.

In the PRESSURE INTERPOLATION SECTION (2.4), the stability characteristics of various pressure interpolation schemes were discussed. The stability of these various pressure interpolation schemes were analyzed using the discretized form of the continuity equation and the x-momentum equation in a 1-D example (see Fig. 2.5.3). One of the stability requirements introduced in this analysis was that the error in mass flow rate and the change in mass flow rate as defined in that section have the same sign.

In the pressure interpolation stability analysis, the discretized form of the steady continuity equation was represented by Eq. 2.4.11, which is

$$\rho_{I+1}A_{I+1}\delta u_{I+1} - \rho_I A_I \delta u_I + u_{I+1}A_{I+1}\delta \rho_{I+1} - u_I A_I \delta \rho_I = \dot{m}_{error,I} \quad (2.5.47)$$

where the changes $\delta()$ are differences between the correct solution and the current solution. The left hand side of this equation may also be used to evaluate the changes in net mass flow rate in one time step if the changes $\delta()$ are changes in properties in one time step. Over one time step, the changes in pressure are determined from the continuity equation and the changes in velocity are determined from the momentum equation. Changes in density are found through the ideal gas equation of state. For the one-dimensional example shown in Fig. 2.5.3, if we are using the pressure update time marching method, along with an upwind effective density, and if we assume that only control volume (I,J) has a mass flow rate error, we can say that

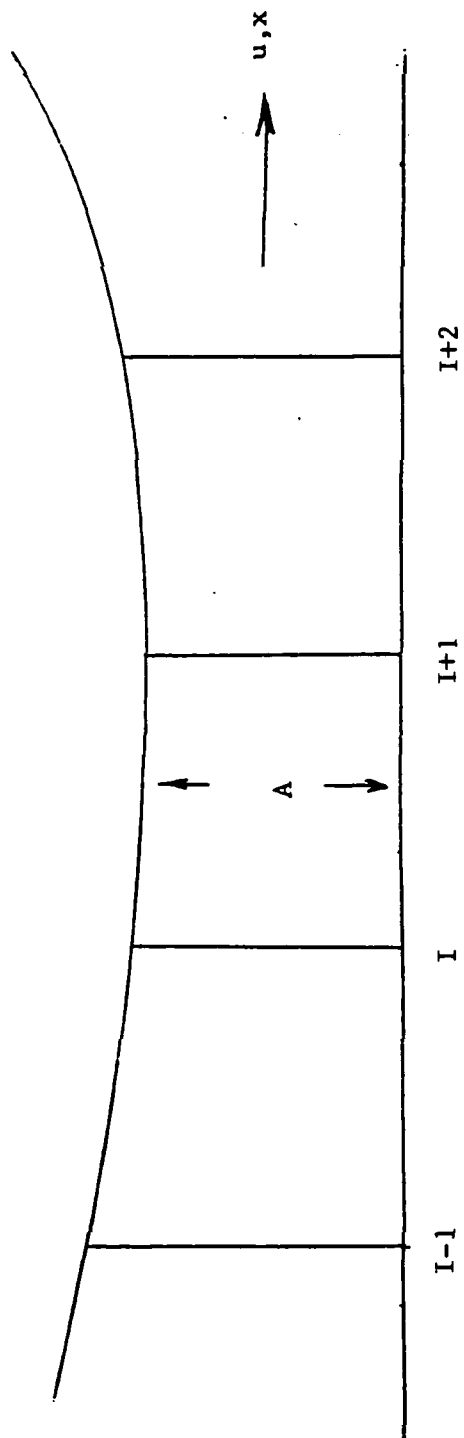


Fig. 2.5.3 1-D Geometry Used For Time Step Determination

$$\delta P_I = \dot{m}_{error,I} \delta t_c RT / Vol_I \quad (2.5.48)$$

$$\delta P_{I+1} = 0 \quad (2.5.49)$$

$$\delta \rho_I = P_{I-1} / RT = 0 \quad (2.5.50)$$

and

$$\delta \rho_{I+1} = \delta P_I / RT = \dot{m}_{error,I} \delta t_c / Vol_I \quad (2.5.51)$$

The changes in velocity are determined from the discretized form of the momentum equation. The resulting expressions for the change in velocity, δu , were found to be

$$\delta u_{I+1} = (\delta P_I - \delta P_{I+1}) \frac{\delta t_m}{\rho_{I+1} \delta x_I} = [\dot{m}_{error,I} \delta t_c \frac{RT}{Vol_I}] \frac{\delta t_m}{\rho_{I+1} \delta x_I} \quad (2.5.52)$$

and

$$\delta u_I = (\delta P_{I-1} - \delta P_I) \frac{\delta t_m}{\rho_I \delta x_{I-1}} = [-\dot{m}_{error,I} \delta t_c \frac{RT}{Vol_I}] \frac{\delta t_m}{\rho_I \delta x_{I-1}} \quad (2.5.53)$$

having assumed that at the beginning of a time step that the momentum equation is balanced except for the continuity error. Now if Eqs. 2.5.50, 2.5.51, 2.5.52, and 2.5.53 are substituted into Eq. 2.5.47, we get

$$\begin{aligned} & \rho_{I+1} A_{I+1} [\dot{m}_{error,I} \delta t_c \frac{RT}{Vol_I}] \frac{\delta t_m}{\rho_{I+1} \delta x_I} \\ & - \rho_I A_I [-\dot{m}_{error,I} \delta t_c \frac{RT}{Vol_I}] \frac{\delta t_m}{\rho_I \delta x_{I-1}} \\ & + u_{I+1} A_{I+1} \dot{m}_{error,I} \frac{\delta t_c}{Vol_I} = \dot{m}_{change} \end{aligned} \quad (2.5.54)$$

For our one-dimensional example,

$$Vol_I \cong A_I \delta x_I \quad (2.5.55)$$

$$A_{I+1} \cong A_I \quad (2.5.56)$$

$$\delta x_{I-1} \cong \delta x_I \quad (2.5.57)$$

and

$$\rho_{I+1} \cong \rho_I \quad (2.5.58)$$

Using Eqs. 2.5.55, 2.5.56, 2.5.57, and 2.5.58 and rearranging, Eq. 2.5.54 becomes,

$$\dot{m}_{change,I} = \delta t_c RT \dot{m}_{error,I} \left[\frac{2\delta t_m}{\delta x_I^2} + \frac{u_{I+1}}{\delta x_I RT} \right] \quad (2.5.59)$$

The upwinded density method ($a_0 = 0$, $a_1 = 0$, $a_2 = 0$) has been used in our analysis because it results in the most conservative time step. Eq. 2.5.59 is used in the PRESSURE INTERPOLATION SECTION to see under what conditions the error in mass flow rate has the same sign as the change in mass flow rate. Now we want to find an equation which tests under what conditions the change in mass flow rate is less than the error in mass flow rate,

$$\dot{m}_{change,I} < \dot{m}_{error,I} \quad (2.5.60)$$

Substituting Eq. 2.5.60, into Eq. 2.5.59 we get

$$1.0 \leq \left[\frac{2\delta t_m}{\delta x^2} + \frac{u}{RT\delta x} \right] RT \delta t_c \quad (2.5.61)$$

Solving Eq. 2.5.61 for the continuity time step, δt_c , we get

$$\delta t_c \leq \frac{1}{RT \left[\frac{2\delta t_m}{\delta x^2} + \frac{u}{RT\delta x} \right]} \quad (2.5.62)$$

When the differential form of the governing equations was used, we got

$$\delta t_c \leq \frac{1}{RT \left[\frac{\delta t_m}{\delta x^2} + \frac{\delta t_m}{\delta y^2} + \left| \frac{u}{RT\delta x} \right| + \left| \frac{v_{eff}}{RT\delta y} \right| \right]} \quad (2.5.63)$$

where the terms in Eq. 2.5.62 can be recognized as the x-momentum contributions to Eq. 2.5.63.

THE CFL CONDITION AND THE DENSITY UPDATE METHOD: When the density update time marching calculation procedure is used by Denton (13), the same time step, the CFL condition, is used in both the continuity and momentum equations. It will be shown using the stability criteria for the continuity time step , ($\dot{m}_{change} < \dot{m}_{error}$), that if the same time step is used in both the momentum and continuity equations, Eq. 2.5.62 gives a result close to the CFL condition. It should be noted though that the density update method is not necessarily restricted to using the same time step.

Using an analysis similar to that used in the previous section, it can be shown that if the density update method is used along with the downwind effective pressure, the resulting one dimensional relationship between changes in mass flow rate and errors in mass flow rate is

$$\left[\frac{2\delta t_m}{\delta x^2} + \frac{u}{\delta x RT} \right] \dot{m}_{error,1} \delta t_c RT = \dot{m}_{change} \quad (2.5.64)$$

which is identical to Eq. 2.5.59. Now we want to determine what the limiting stable time step is if we let $\delta t_m = \delta t_c$ and $\dot{m}_{change} < \dot{m}_{error}$. The resulting expression for the time step is

$$\delta t \leq \frac{\delta x}{4RT} \left[-u + \sqrt{u^2 + 8RT} \right] \quad (2.5.65)$$

For our one-dimensional example, the CFL condition would set the time step as

$$\delta t_{CFL} \leq \frac{\delta x}{(u + c)} . \quad (2.5.66)$$

Fig. 2.5.4 shows a comparison of the (time steps/ δx) calculated using Eqs. 2.5.65 and 2.5.66 for a Mach number range from 0.01 to 2.0. Over this range, the time steps calculated using these two equations are within $\pm 20\%$. At Mach numbers greater than 0.4, the CFL condition gives a more conservative time step than Eq. 2.5.65. Fig. 2.5.5 shows a comparison of the time steps calculated using Eqs. 2.5.65 and 2.5.66 with the different time steps for the continuity and momentum equations calculated using Eqs. 2.5.7 and 2.5.8 over the same Mach number range.

TRANSVERSE CONTRIBUTIONS TO THE CONTINUITY TIME STEP: When mass imbalances are caused by incorrect mass fluxes through the transverse faces, the pressure changes from the continuity error act through the y-momentum equation to correct these mass imbalances. An analysis, similar to that just shown for the 1-D example, will be used to show how transverse fluxes affect the continuity time step.

Fig. 2.5.6 shows four control volumes of identical dimensions at a fixed axial location. All errors in transverse fluxes are assumed to be zero except between control volumes (I,J) and (I,J-1). To the right of the control volumes, in Fig. 2.5.6, is a plot of the static pressures at the upstream nodes for the control volumes, before and after one time step. The static pressures at all nodes are assumed to be initially the same (represented as triangles in Fig. 2.5.6).

The transverse fluxes shown in Fig. 2.5.6 will cause the pressure (represented as squares in Fig. 2.5.6) to increase at node (I,J-1) and to decrease at node (I,J) through the mass flow rate errors for control volumes (I,J-1) and (I,J) respectively. These changes in pressure at nodes (I,J) and (I,J-1) will induce pressure gradients in the transverse direction (represented by the dashed line in Fig. 2.5.6) which will cause the mass imbalance to correct itself. The pressure changes ; however, must

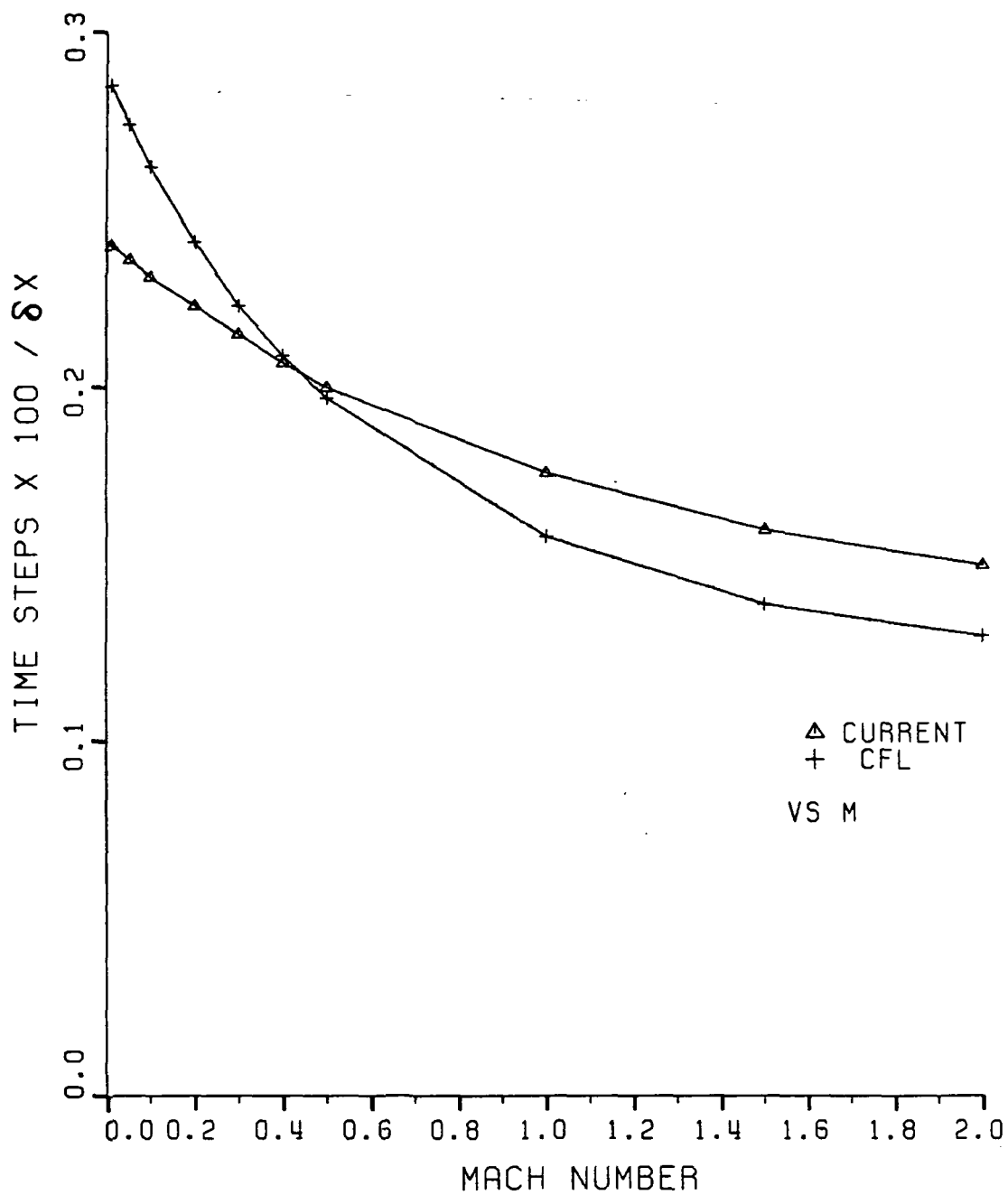


Fig. 2.5.4 Time Steps Using CFL Condition and Current Stability Method Applied With $\delta t_m = \delta t_c$.

C - 2

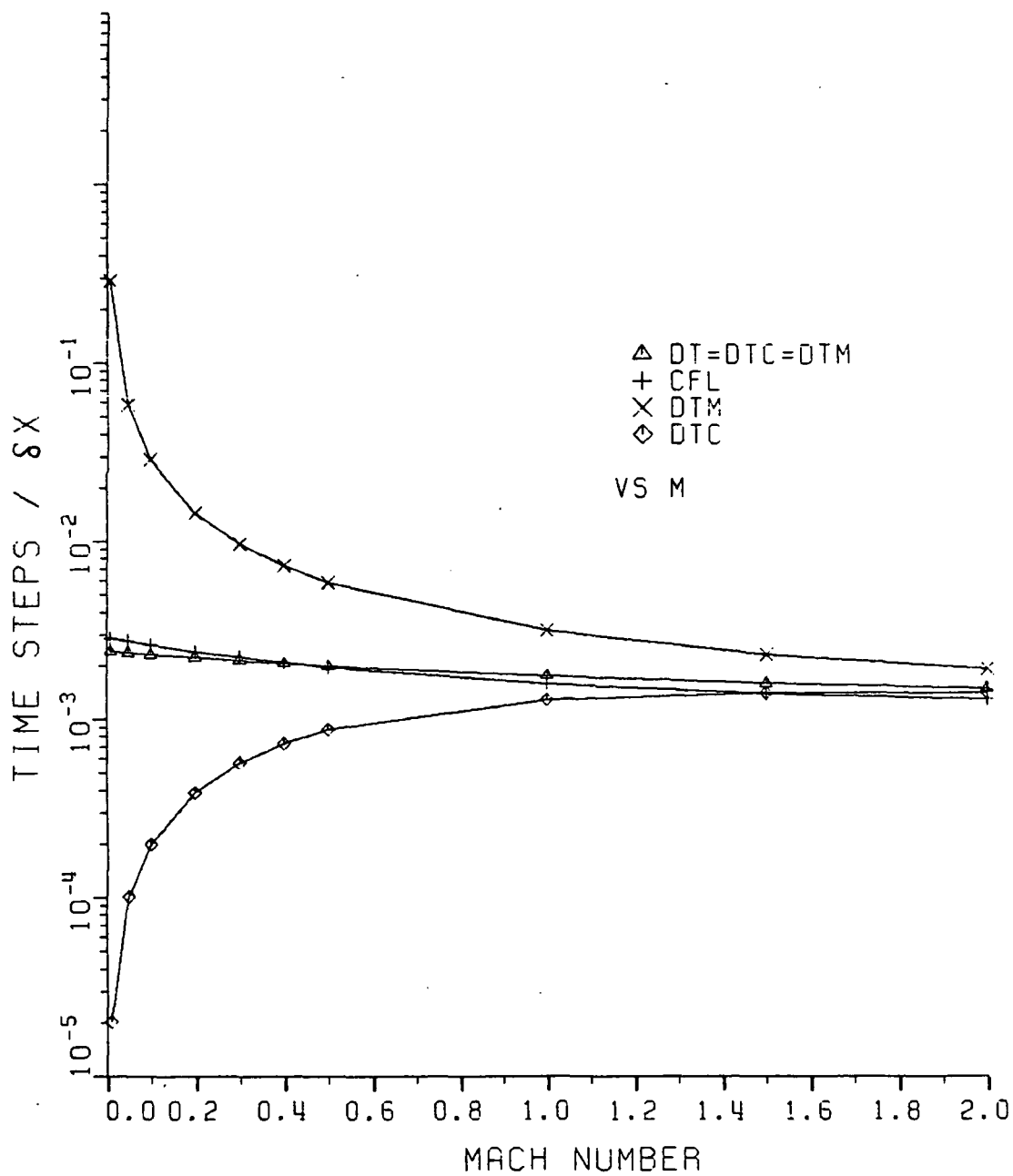


Fig. 2.5.5 Time Steps Comparison

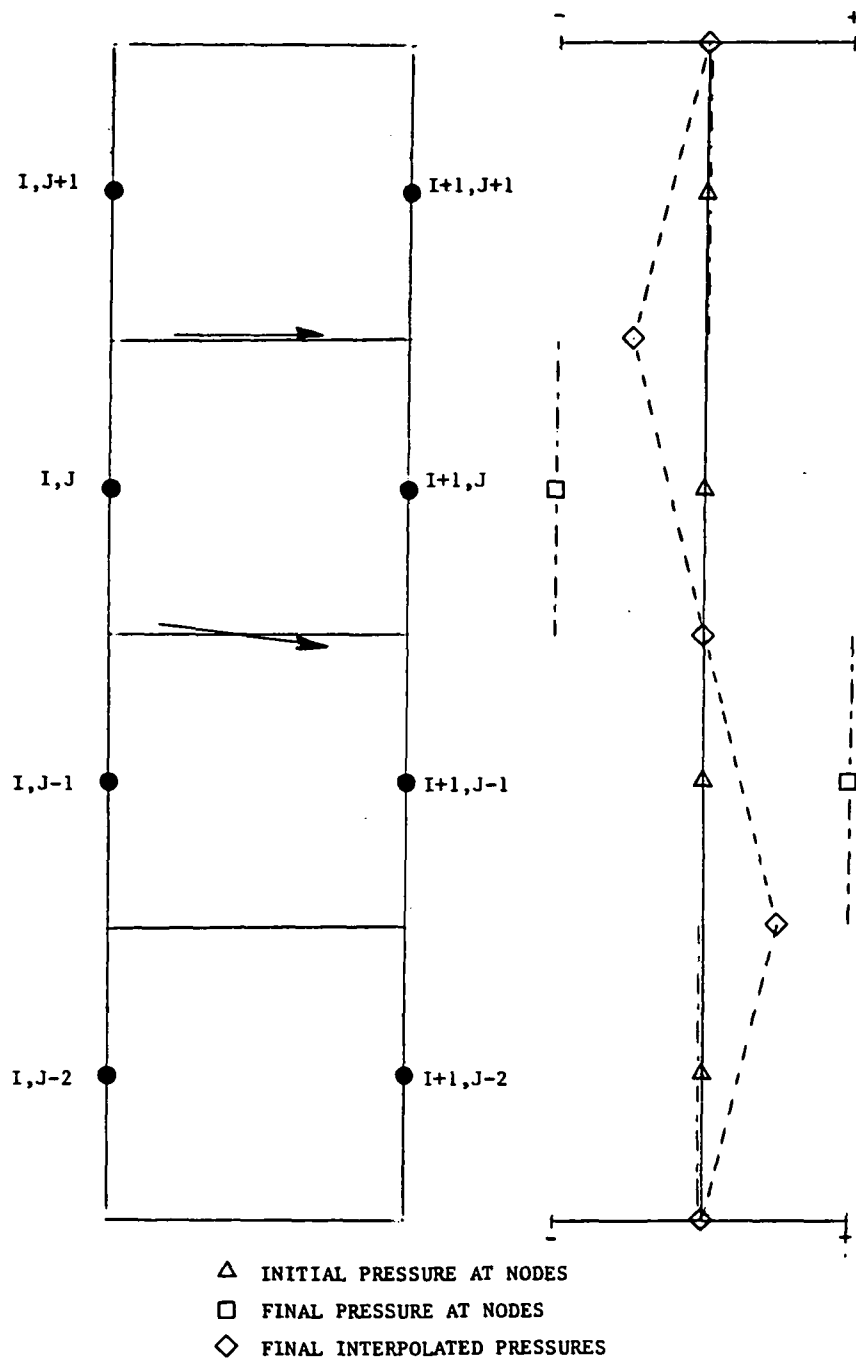


Fig. 2.5.6 Simplified Geometry For Determination of Y-Momentum Equation Contribution to Time Step

not be so great so as to violate our stability requirement that the change in mass flow rate be less than the error in mass flow rate.

Several simplifying assumptions are made throughout this part of the analysis to reduce its complexity. Just as in the analysis in the PRESSURE INTERPOLATION SECTION, we will assume here that the momentum equation is balanced initially for each control volume except for the continuity error. In Section 2.4, the x-momentum equation reduced to Eq. 2.4.24

$$\delta u_{I+1} = (\delta P_I - \delta P_{I+1})\delta t/(\rho_{I+1}\delta x_I) \quad (2.5.67)$$

when the momentum equation is balanced initially except for the continuity error. For the case where the transverse fluxes cause the imbalance, the equivalent y-momentum equation is

$$\begin{aligned} \delta v_{I+1,J} = & 0.25 \times (\delta P_{I,J} + \delta P_{I+1,J} + \delta P_{I,J-1} + \delta P_{I+1,J-1}) \\ & - 0.25 \times (\delta P_{I,J} + \delta P_{I+1,J} + \delta P_{I,J+1} + \delta P_{I+1,J+1}) \frac{\delta t_m}{(\rho_{I+1,J}\delta y_{I,J})} . \end{aligned} \quad (2.5.68)$$

Eq. 2.5.68 can be simplified for this uniform grid to

$$\delta v_{I+1,J} = [0.25 \times (\delta P_{I,J-1} + \delta P_{I+1,J-1}) - 0.25 \times (\delta P_{I,J+1} + \delta P_{I+1,J+1})] \frac{\delta t_m}{\rho_{I+1,J}\delta y_{I,J}} \quad (2.5.69)$$

For the case that we are investigating,

$$\delta P_{I,J-1} = -\dot{m}_{error,I,J}\delta t_c RT/Vol_I \quad (2.5.70)$$

$$\delta P_{I+1,J-1} = 0 \quad (2.5.71)$$

$$\delta P_{I,J+1} = 0 \quad (2.5.72)$$

$$\delta P_{I+1,J+1} = 0 . \quad (2.5.73)$$

Therefore, in this case, Eq. 2.5.69 becomes

$$\delta v_{I+1,J} = (- \dot{m}_{error} \times 0.25 \times \frac{\delta t_c RT}{Vol_I}) \frac{\delta t_m}{\rho_{I+1,J} \delta y_I} . \quad (2.5.74)$$

The same procedure can be applied to control volumes (I,J-1) and (I,J+1) and the resulting expressions for changes in v are

$$\delta v_{I+1,J-1} = (- \dot{m}_{error} \times 0.25 \times \frac{\delta t_c RT}{Vol_I}) \frac{\delta t_m}{\rho_{I+1,J-1} \delta y_I} \quad (2.5.75)$$

and

$$\delta v_{I+1,J+1} = (\dot{m}_{error,I,J} \times 0.25 \times \frac{\delta t_c RT}{Vol_{I,J}}) \frac{\delta t_m}{\rho_{I+1,J+1} \delta y_I} . \quad (2.5.76)$$

The change in mass flow rate due to the changes in v for control volume (I,J) is determined from the continuity equation using the y-contribution equivalent to Eq. 2.4.11 in Section 2.4, which would be

$$\dot{m}_{change} = (\rho A \delta v)_{north} - (\rho A \delta v)_{south} + (v A \delta \rho)_{north} - (v A \delta \rho)_{south} . \quad (2.5.77)$$

The change in mass flow rate for one iteration for our uniform grid is therefore,

$$\begin{aligned} \dot{m}_{change} = & \rho \times 0.25 \times \delta x_I \times (\delta v_{I,J} + \delta v_{I+1,J} + \delta v_{I,J+1} + \delta v_{I+1,J+1}) \\ & - \rho \times 0.25 \times \delta x_I \times (\delta v_{I,J} + \delta v_{I+1,J} + \delta v_{I,J-1} + \delta v_{I+1,J-1}) \\ & + v \times 0.25 \times \delta x_I \times (\delta \rho_{I,J} + \delta \rho_{I+1,J} + \delta \rho_{I,J+1} + \delta \rho_{I+1,J+1}) \\ & - v \times 0.25 \times \delta x_I \times (\delta \rho_{I,J} + \delta \rho_{I+1,J} + \delta \rho_{I,J-1} + \delta \rho_{I+1,J-1}) \end{aligned} \quad (2.5.78)$$

assuming mean values for the density and v-velocity. The density changes for one iteration are

$$\delta \rho_{I,J} = \dot{m}_{error,I,J} \delta t_c / Vol_I \quad (2.5.79)$$

$$\delta \rho_{I,J-1} = - \dot{m}_{error,I,J} \delta t_c / Vol_I . \quad (2.5.80)$$

Substituting Eqs. 2.5.74, 2.5.75, 2.5.76, 2.5.79, and 2.5.80 into Eq. 2.5.78, we get

$$\begin{aligned} \dot{m}_{change} = & \left[\rho \left(\dot{m}_{error} \delta t_c \frac{RT}{Vol_I} \right) - \rho \left(- \dot{m}_{error} \delta t_c \frac{RT}{Vol_I} \right) \right] \frac{\delta t_m \delta x_I}{\rho \delta y_I} \times 0.25^2 \\ & - v \delta x_I \left(- 0.25 \dot{m}_{error, I, J} \frac{\delta t_c}{Vol_I} \right) . \end{aligned} \quad (2.5.81)$$

If Eq. 2.5.81 is rearranged, we get

$$\dot{m}_{change} = \frac{0.25 \times \dot{m}_{error} \delta t_c RT}{Vol_I} \left[\frac{0.5 \delta t_m \delta x_I}{\delta y_I} + \frac{v \delta x_I}{RT} \right] . \quad (2.5.82)$$

For the control volumes used in this analysis,

$$Vol_I = \delta x_I \delta y_I . \quad (2.5.83)$$

Applying the stability criteria, $\dot{m}_{change} < \dot{m}_{error}$, and using Eq. 2.5.83, Eq. 2.5.82 becomes,

$$1.0 \geq \delta t_c RT \left[\frac{0.125 \delta t_m}{\delta y_I^2} + \frac{0.25 v}{RT \delta x_I} \right] . \quad (2.5.84)$$

When Eq. 2.5.84 is solved for the continuity time step, δt_c , we get

$$\delta t_c \leq 1/RT \left[\frac{0.125 \delta t_m}{\delta y_I^2} + \frac{0.25 v}{RT \delta x_I} \right] . \quad (2.5.85)$$

The mass flow rate error through the transverse face of control volume (I, J) causes the pressure to change at node (I, J). This pressure change will also act through the x-momentum equation in exactly the same manner as previously outlined in Eqs. 2.5.47-2.5.63. When both the x and y contributions to the continuity time step (Eqs. 2.5.62 and 2.5.85) are combined together we get that

$$\delta t_c \leq \frac{1}{RT \left[\frac{2\delta t_m}{\delta x^2} + \frac{.125\delta t_m}{\delta y^2} + \frac{u}{RT\delta x} + \frac{0.25v}{RT\delta y} \right]} \quad (2.5.86)$$

To insure that the time step we choose will result in a stable calculation procedure, the time step that has been calculated using the differential form of the governing equations (Eq. 2.5.25) and the time step derived from the discretized form of the governing equations (Eq. 2.5.86) have been combined together and symmetry has been invoked and the resulting equation is Eq. 2.5.8 presented earlier,

$$\delta t_c \leq \frac{1}{2RT \left[\frac{\delta t_m}{\delta x^2} + \frac{\delta t_m}{\delta y^2} + \frac{u}{RT\delta x} + \frac{v_{eff}}{RT\delta y} \right]} \quad (2.5.87)$$

2.6 BOUNDARY CONDITIONS AND INITIAL GUESS

BOUNDARY CONDITIONS

Along the upstream boundary, the total temperature, total pressure, and v-velocity are specified for inviscid flow. Along the downstream boundary the static pressure is specified. For viscous flow, at the upstream boundary, the total temperature, freestream total pressure, inlet boundary layer velocity profile, and flow angle are specified.

Pressures along the solid boundaries are determined from linear extrapolation. There is no mass flux across element faces which coincide with the solid boundaries. For viscous flow, the values of the x-component and y-component of velocity are set equal to zero at solid walls.

For flow through cascades, the additional boundary condition of periodicity must be considered. Fig. 2.6.1 shows a two dimensional projection of a typical grid system up to the leading edge of a cascade blade. Note that a grid point is not located along the periodic boundary when the new control volumes are used. The computational domain extends from the lower periodic boundary to the upper periodic boundary. The missing calculation points outside the computational domain are replaced by the corresponding points adjacent to the other periodic boundary.

INITIAL GUESS

The initial guess for the inviscid part of the flow field is determined from a 1-D inviscid solution. A boundary layer is then added along the wall using a constant ratio of boundary layer thickness to duct height throughout the duct. The velocity profile used in the boundary layer is the inlet velocity profile. For certain geometries, an estimate of the blockage effect of the boundary layer is used to specify an effective geometry for the calculation of the initial solution.

2.7 CALCULATION OF VISCOUS FORCES

The momentum equation for unsteady flow in differential form is

$$\frac{\partial \rho \underline{u}}{\partial t} + \nabla \rho \cdot \underline{u} \underline{u} = - \nabla P + \nabla \cdot \mu \nabla \underline{u} + \nabla \cdot \mu \overline{\nabla \underline{u}}^T + \nabla \cdot \delta_{ij} \lambda \frac{\partial u_k}{\partial x_k} . \quad (2.7.1)$$

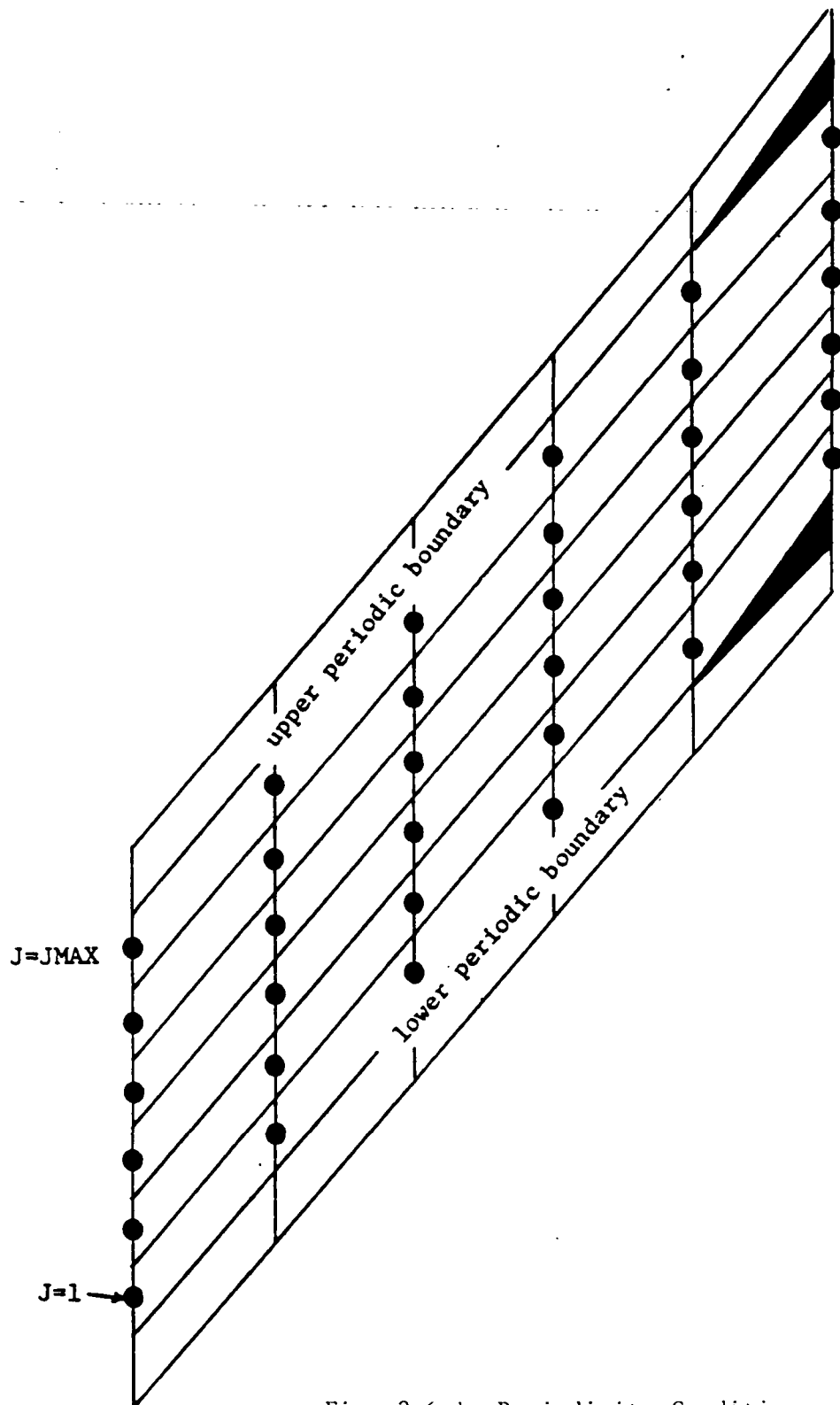


Fig. 2.6.1 Periodicity Condition

The normal stresses associated with second coefficient of viscosity, λ , will be neglected in this analysis and in any subsequent calculations. We will be concerned in this section with how the viscous terms ($\nabla \cdot \mu \nabla \underline{u}$ and $\nabla \cdot \mu \nabla \underline{u}^T$) are evaluated using the non-orthogonal, physical mesh system that is incorporated in the present method.

In a control volume analysis of a flow field, we are interested in the actual forces which act upon the control surfaces and the components of these force in the coordinate directions (x, y , and z) rather than the derivatives of the shear stresses as seen in Eq. 2.7.1. To transform the governing equations from differential form (Eq. 2.7.1) into an integral form, we use Gauss' theorem. In terms of some arbitrary vector, Φ , Gauss' theorem says,

$$\iiint \nabla \cdot \Phi \, dVol = \iint \Phi \cdot d\mathbf{A} \quad (2.7.2)$$

The viscous terms ($\nabla \cdot \mu \nabla \underline{u}$ and $\nabla \cdot \mu \nabla \underline{u}^T$) in Eq. 2.7.1, are converted from differential form to control volume form using Eq. 2.7.2 and the result is,

$$\iiint (\nabla \cdot \mu \nabla \underline{u} + \nabla \cdot \mu \nabla \underline{u}^T) dVol = \iint (\mu \nabla \underline{u} \cdot d\mathbf{A} + \mu \nabla \underline{u}^T \cdot d\mathbf{A}) \quad (2.7.3)$$

The current two-dimensional scheme uses control volumes which are made up of four straight line segments (see Fig. 2.7.1). The surface integral in Eq. 2.7.3 is simplified into a summation over the four sides of the control volume. The integral over the surface in Eq. 2.7.3 can therefore be represented as

$$\begin{aligned} \iint (\mu \nabla \underline{u} \cdot d\mathbf{A} + \mu \nabla \underline{u}^T \cdot d\mathbf{A}) = \\ \sum_{K=1}^4 (\mathbf{A}_K \cdot \mu \nabla \underline{u} + \mathbf{A}_K \cdot \mu \nabla \underline{u}^T) \end{aligned} \quad (2.7.4)$$

Each area vector in Eq. 2.7.4 is assigned a magnitude equal to the area of the face in question and a direction which points in the outward normal direction. The evaluation of Eq. 2.7.4 results in the net viscous forces in the x and y directions for a control volume.

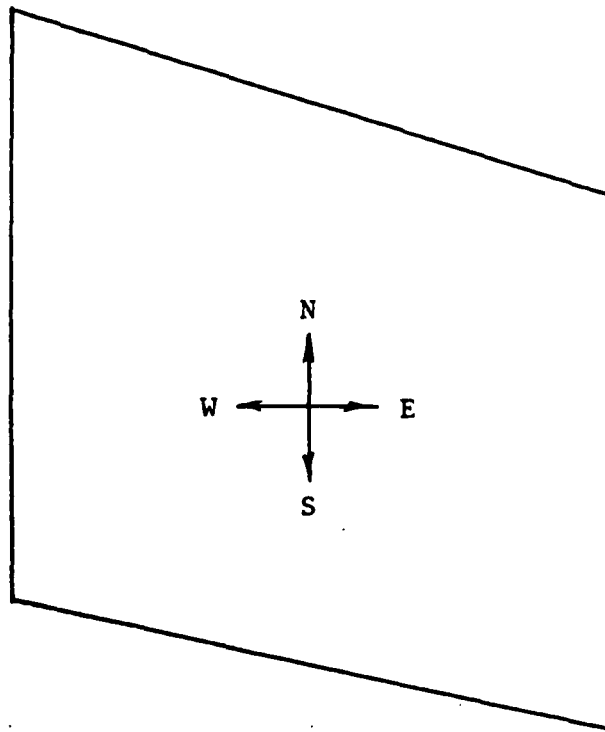


Fig. 2.7.1 Typical Control Volume

For laminar flow, the absolute viscosity, μ , is used in Eq. 2.7.4 to evaluate the shear forces. For turbulent flow, an effective viscosity is used in Eq. 2.7.4. The effective viscosity that is used is the sum of the absolute viscosity and an apparent eddy viscosity. The current method uses a Prandtl mixing length model to evaluate this eddy viscosity. This mixing length model is outlined in Table 2.7.1.

The details of this mixing length calculation will be presented later in this section.

The velocity gradients, ∇u_L , needed in Eq. 2.7.4 can be determined within a non-orthogonal grid by using,

$$\nabla u_L = \frac{\underline{D}_J \times \underline{D}_K}{\underline{D}_I \cdot (\underline{D}_J \times \underline{D}_K)} \frac{\partial u_L}{\partial I} + \frac{\underline{D}_K \times \underline{D}_I}{\underline{D}_J \cdot (\underline{D}_K \times \underline{D}_I)} \frac{\partial u_L}{\partial J} + \frac{\underline{D}_I \times \underline{D}_J}{\underline{D}_K \cdot (\underline{D}_I \times \underline{D}_J)} \frac{\partial u_L}{\partial K} \quad (2.7.5)$$

where \underline{D}_I , \underline{D}_J , and \underline{D}_K are directional vectors along the grid directions (I, J, and K), see Appendix B. For the two-dimensional case, $\partial u_L / \partial K = 0$ and \underline{D}_K is a vector spanning the height of the duct (in the direction $\underline{D}_I \times \underline{D}_J$). Two typical two dimensional control volumes are shown in Fig. 2.7.2. The directional vectors (\underline{D}_I and \underline{D}_J) are identified in Fig. 2.7.2. The magnitudes of the vectors are dependent upon the grid spacing as can be seen in Fig. 2.7.2. The directional vectors that are shown in Fig. 2.7.2 would be used to calculate the velocity gradients applicable to the boundary common to both of the control volumes.

The derivatives of the velocities in Eq. 2.7.5 are taken with respect to the grid indices, in other words,

$$\frac{\partial u_L}{\partial I} = (u_L)_{I+1} - (u_L)_I \quad (2.7.6)$$

where $(u_L)_I$ is the velocity at the beginning of vector \underline{D}_I and $(u_L)_{I+1}$ is the velocity at the end of vector \underline{D}_I . For the geometries and boundary conditions investigated in the present work, the gradients in properties in the I direction are much smaller than gradients in the J direction. As a

Table 2.7.1 Prandtl Mixing Length Model

$$\mu_{eff} = \mu_l + \mu_t \quad (1)$$

$$\mu_t = \rho L^2 \frac{du}{dy} \quad (2)$$

L is the smaller of

0.08 times the width of the boundary layer

0.41 times the distance to the nearest wall

Van Driest Correction

$$L = 0.41 y^+ (1 - \exp[-y^+ \sqrt{\rho \tau} / 26 \mu_l]) \quad (3)$$

Near Wall Correction

$$\mu_{eff} = \sqrt{\mu_l(\mu_l + \mu_t)} \quad (4)$$

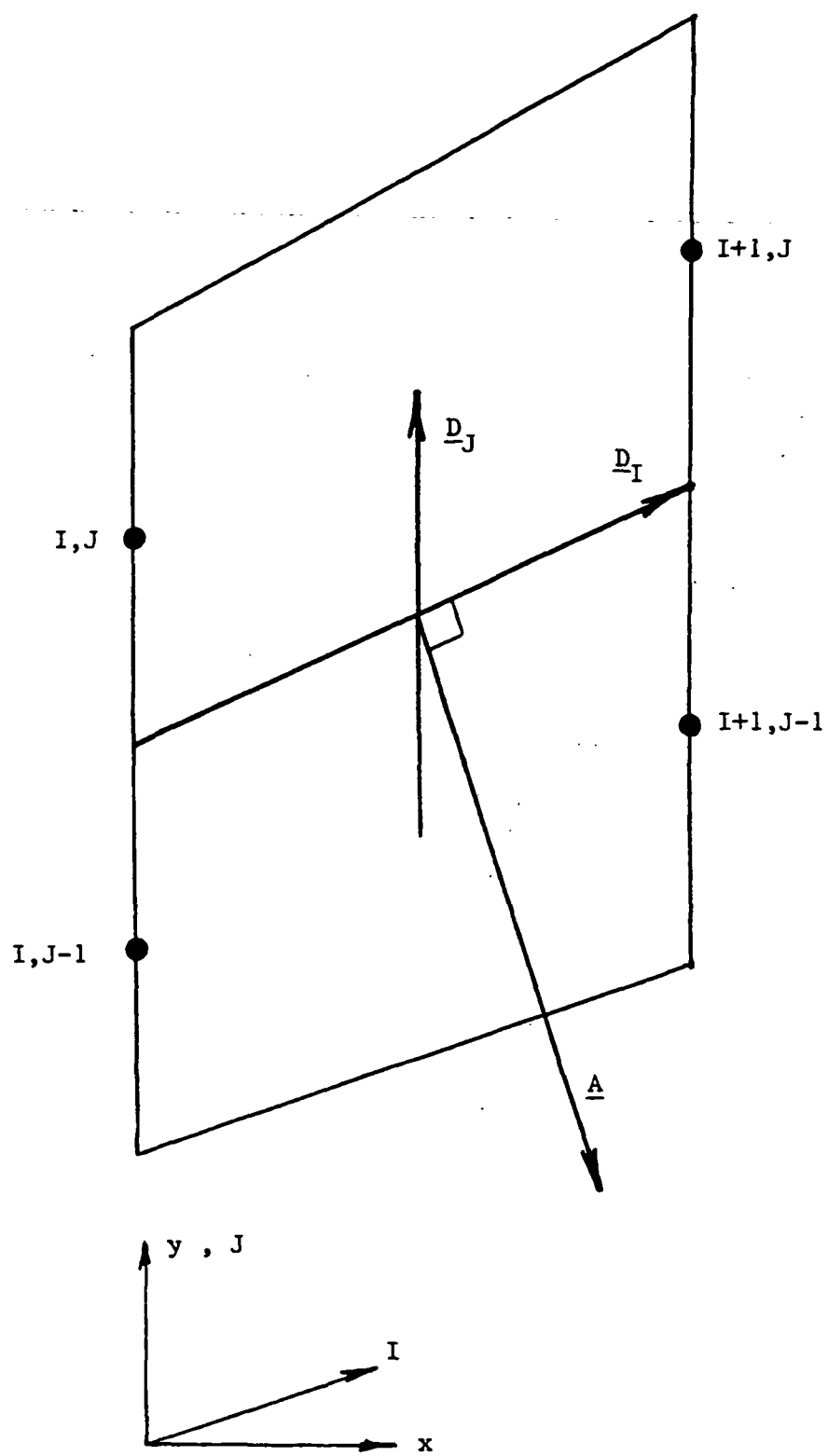


Fig. 2.7.2 Two Typical Control Volumes

consequence, only the J derivative contributions to Eq. 2.7.5 will be considered in the present work. This is equivalent to using the thin-layer Navier-Stokes formulation.

FORCES ON THE SOUTH FACE OF A CONTROL VOLUME

In the actual calculations, for a non-uniform , non-orthogonal grid, the directional vectors are slightly different than those shown in Fig. 2.7.2. For the south face of a control volume, the area and directional vectors actually used are shown in Fig. 2.7.3. The directional vector \underline{D}_s , and the velocity change are evaluated using the downstream nodal values because their use strengthens the centerpoint coefficient of the matrix of unknown variables. The directional vector \underline{D}_s , is located midway between the four nodes rather than at the boundary surface. This is because the viscosity and velocity gradient used in calculating the shear forces on the south face are evaluated midway between the two nodes. The shear stress is known to vary less through the boundary layer than the velocity gradient or the mixing length squared. Therefore, it is preferable to calculate the shear stress using a velocity gradient and mixing length midway between the grid points in the J-direction and then assign the resulting shear force to the face of the control volume between the points. The upper wall and lower wall control volumes are shown in Figs. 2.7.4 and 2.7.5 , respectively with the directional vectors identified. The shear stresses are evaluated midway between the wall and the near wall point and then the shear forces are assigned to the wall surface. The effective viscosity used to evaluate these wall shear forces is a combination of the laminar and turbulent viscosities given by

$$\mu_{eff} = \sqrt{\mu_l(\mu_l + \mu_t)} \quad . \quad (2.7.7)$$

This relationship is used only at the wall and has been shown (Ref. 22) to allow a good calculation of wall shear stress with a near wall point further away from the wall than is typically required.

Symmetry is used to calculate the forces on the north face of a control volume, in other words,

$$\vec{F}_{north,I,J} = - \vec{F}_{south,I,J+1} \quad (2.7.8)$$

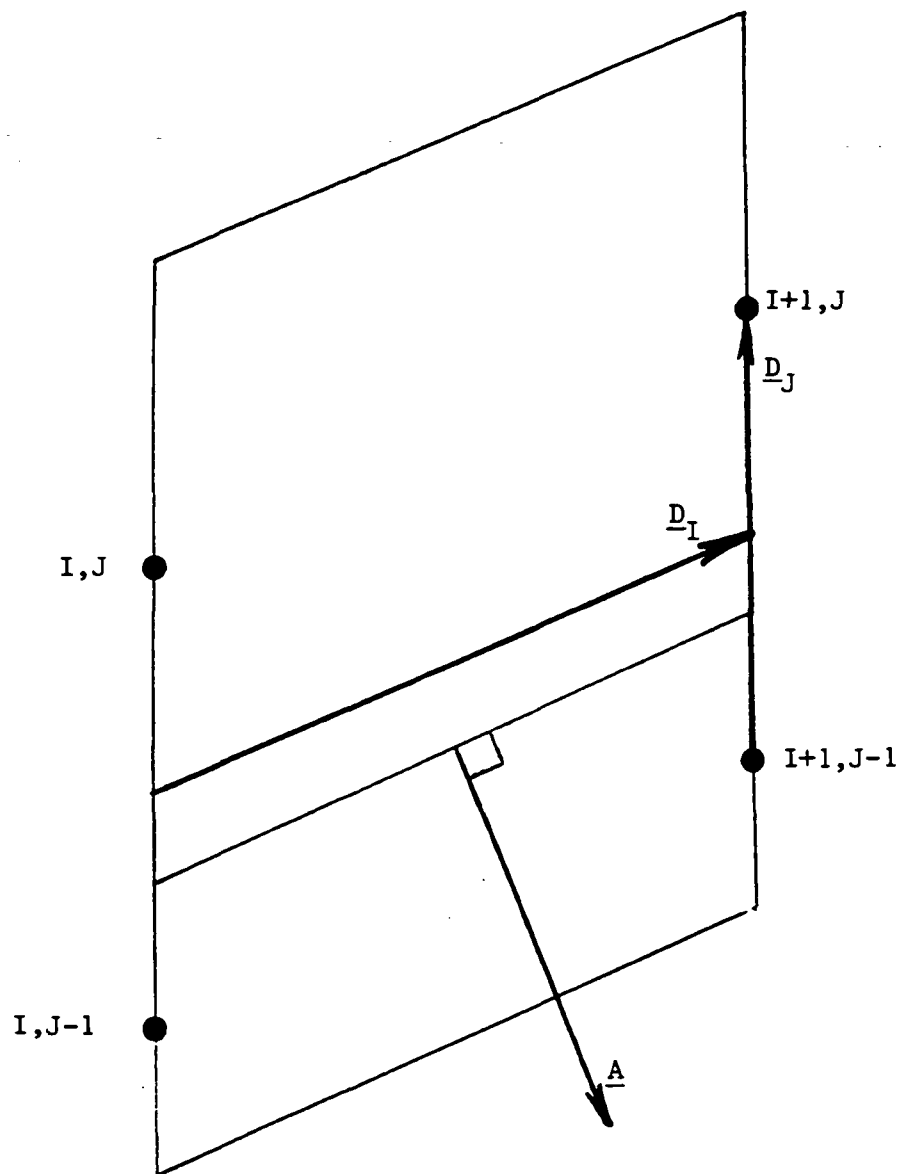


Fig. 2.7.3 Two Typical Control Volumes With Directional Vectors Identified For South Face

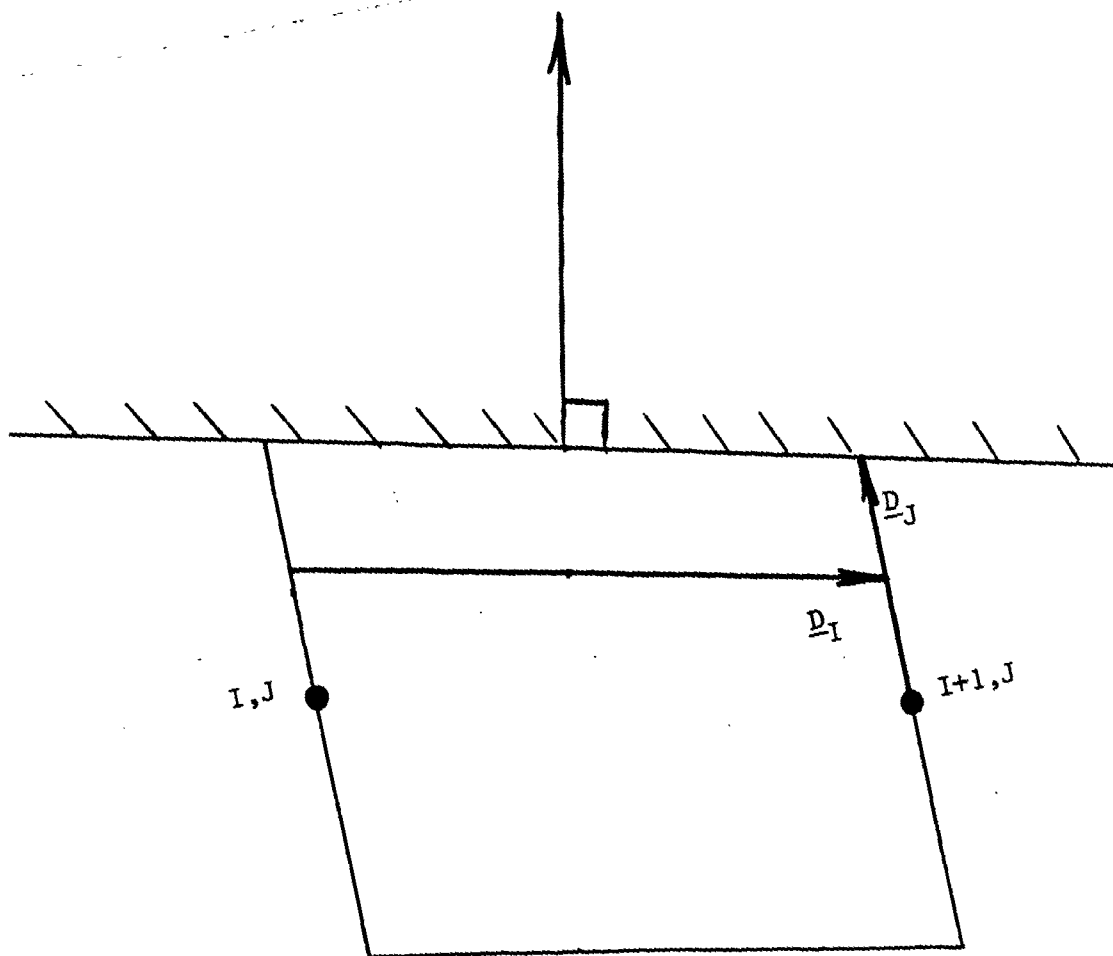


Fig. 2.7.4 Upper Wall Control Volumes

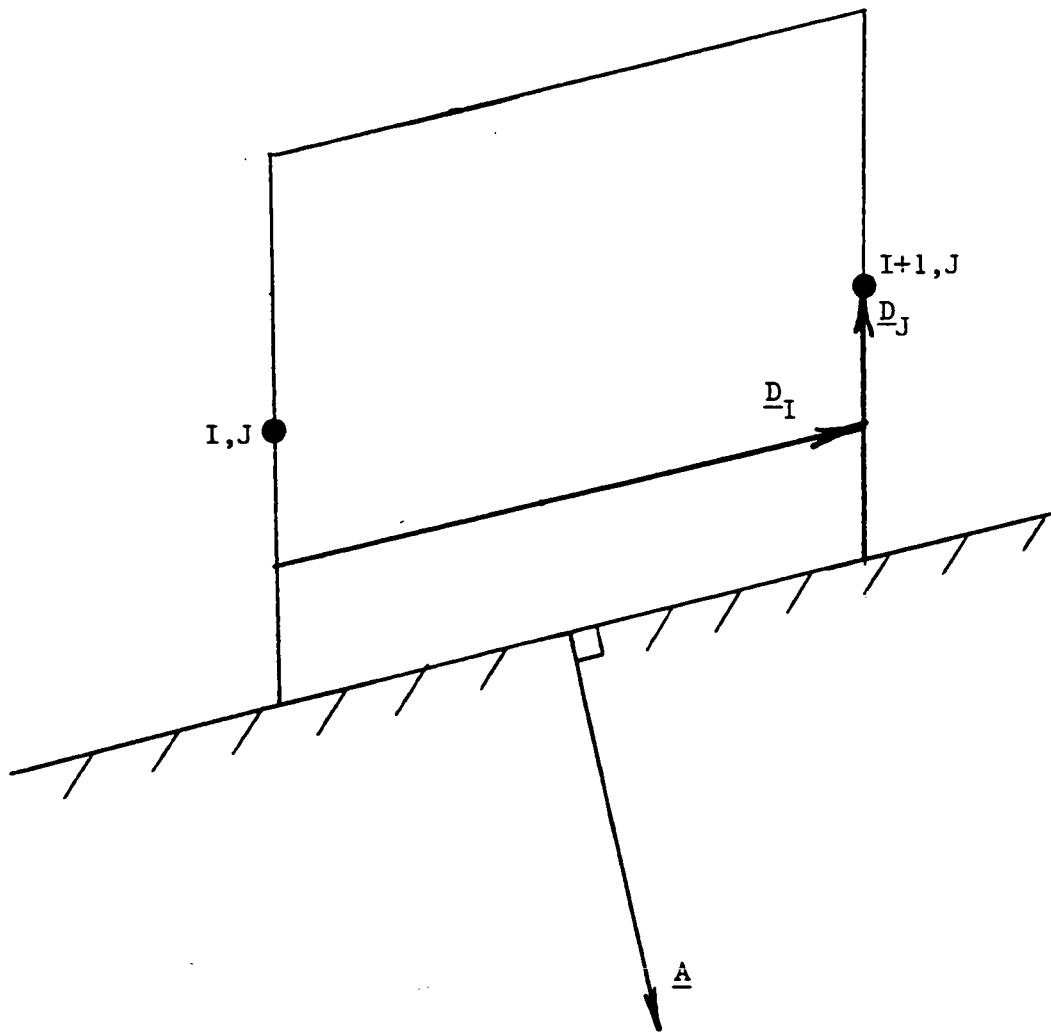


Fig. 2.7.5 Lower Wall Control Volumes

where \vec{F}_{north} and \vec{F}_{south} are the shear forces on the north and south faces of the control volume respectively.

FORCES ON THE WEST FACES OF A CONTROL VOLUME

The forces on the west face of the control volume are calculated by scalar multiplying an interpolated shear stress with the west face area vector (see Eq. 2.7.4). Referring to Fig. 2.7.6, for a node point (I,J) which is located on the west face of control volume (I,J), first the velocity gradient and viscosity are calculated at the western edge of surfaces A and B which are midway between the node points (I,J) and (I,J-1) and node points (I,J+1) and (I,J), respectively. The west sides of surfaces A and B are also the locations where the shear stresses are calculated for the north and south faces of the control volume (I-1,J). The product of the velocity gradient and viscosity at node (I,J) is determined by linearly interpolating using the following interpolation formula,

$$\phi_{I,J} = \phi_A + \frac{(y_A/2)}{(\frac{y_B}{2} + \frac{y_A}{2})} (\phi_B - \phi_A) \quad (2.7.9)$$

where ϕ_A and ϕ_B are the products of the velocity gradient and the viscosity at the west sides of surfaces A and B respectively. Once these interpolated values have been calculated, Eq. 2.7.4 can be used to calculate the components of the shear forces on the west face. The shear stress is interpolated to node I,J rather than interpolating the velocity gradient since the shear stress varies less through the boundary layer than the velocity gradient. Similarly for the east face we have

$$\vec{F}_{east,I,J} = - \vec{F}_{west,I+1,J} \quad (2.7.10)$$

CALCULATION OF MIXING LENGTH AND VISCOSITY

When the mixing length model of Table 2.7.1 is used in the 0.41y region, a distance normal to the wall, "y", must be determined to calculate the mixing length. For a flat wall, the distance to the wall from a point is, of course, measured along a line perpendicular to the wall. However, with the

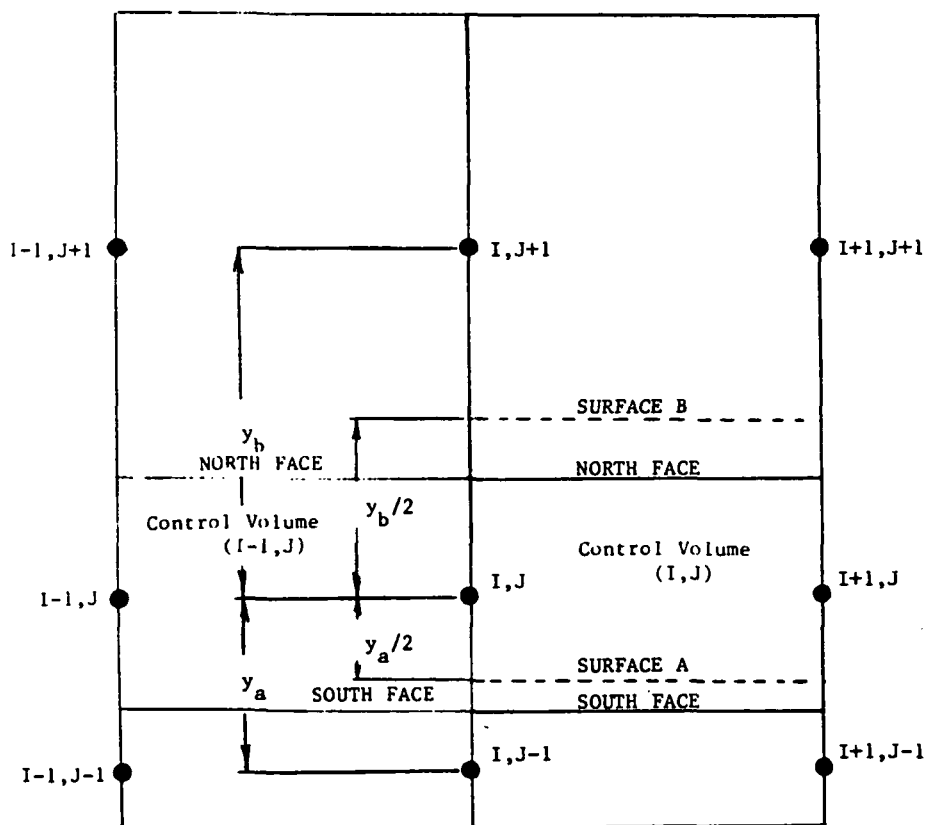


Fig. 2.7.6 Control Volume Arrangement for West Face Force Evaluation

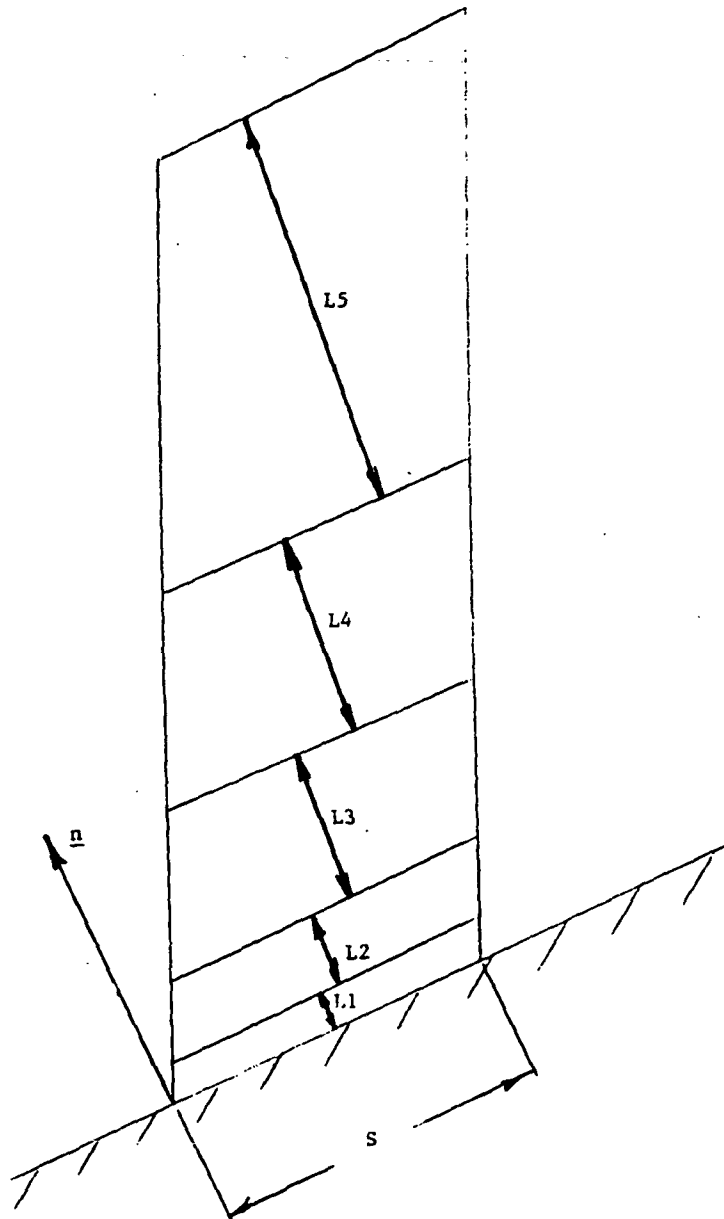


Fig. 2.7.7 Distances Normal to the Wall

current grid system, grid lines and lines orthogonal to the wall are not coincident (see Fig. 2.7.7). Fig. 2.7.7 shows 5 adjacent control volumes. The normal distance (L) between the north and south faces of a control volume is equal to the volume of the control volume divided by the distance (S) between the east and west faces of the control volume measured in the I grid direction. The total normal distance from the wall to the node point on the west face of a control volume (L_{west}) is equal to the sum of all previous normal distances between that control volume and the nearest wall plus one half of the normal distance for that control volume. We can represent that distance as

$$L_{west} = \sum_{k=1}^{n-1} L_k + 0.5 \times L_n \quad (2.7.11)$$

where n is the number of control volumes from the wall.

The total normal distance needed for calculating the mixing length for the south face of a control volume (L_{south}) is equal to the sum of all previous normal distances to the previous node ($L_{west,n-1}$) plus the equivalent normal distance half way between the two grid points in question. The procedure used to calculate this length is shown in Fig. 2.7.8. We can represent this total distance as

$$L_{south,n} = L_{west,n-1} + \frac{(L_{n-1} + L_n)}{4} \quad (2.7.12)$$

To determine the mixing length in the outer part of the boundary layer, the boundary layer thickness measured normal to the wall must also be determined. The lengths that were calculated above can also be used in calculating the boundary layer thickness. The edge of the boundary layer is determined by using the magnitude of the normalized local total pressure gradient as a measure of its location. The normalized total pressure gradient used here is

$$\text{normalized total pressure gradient} = \frac{\Delta P_t}{\Delta y} \frac{1}{0.5 \rho_e u_e^2} \quad (2.7.13)$$

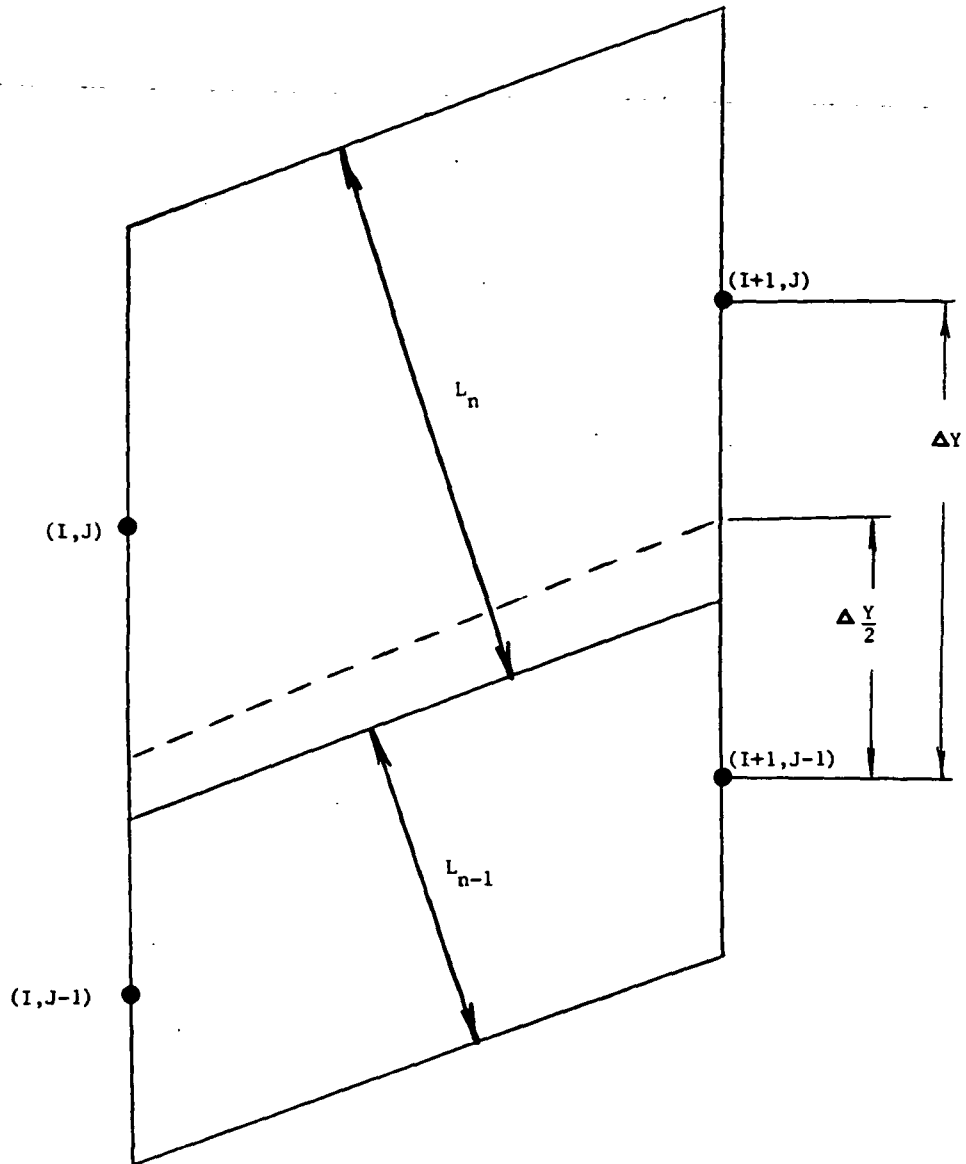


Fig. 2.7.8 Normal Distance to the South Face of the Control Volume

where " Δy " is the normal distance between two grid points. The local freestream values of density and velocity are used in Eq. 2.7.13. The grid line that is considered the freestream is input into the method. Starting from the freestream the normalized total pressure gradient (Eq. 2.7.13) is calculated between grid points and is compared with a characteristic normalized total pressure gradient. The edge of the boundary layer is defined as where the magnitude of the calculated gradient is equal to the characteristic gradient. The exact distance is determined using interpolation and is based upon the distances normal to the wall. The characteristic normalized total pressure gradient is determined by

$$\frac{\Delta P_{t, char}}{\Delta y} \frac{1}{0.5 \rho_e u_e^2} = \frac{1}{CL} \quad (2.7.14)$$

where CL is some characteristic length of the flow field, typically the duct width.

Once the mixing length has been calculated, the apparent eddy viscosity is calculated using Eq. 1 in Table 2.7.1. The velocity gradient used in the eddy viscosity calculation is determined using the following expression,

$$\frac{du}{dy} = \sqrt{\left[\frac{\mathbf{A} \cdot \nabla u}{|\mathbf{A}|} \right]^2 + \left[\frac{\mathbf{A} \cdot \nabla v}{|\mathbf{A}|} \right]^2} \quad (2.7.15)$$

where \mathbf{A} is the area vector on the south side of the control volume. This formula gives the magnitude of the total velocity gradient reflecting the non-orthogonality of the grid.

2.8 MULTI-VOLUME METHOD FOR PRESSURE CHANGES

Preliminary calculations of boundary layer flows using the density update method (with non-uniform grid spacing) resulted in solutions which became unstable after only a small number of iteration steps. After a detailed investigation of the nature of this instability, the cause could be attributed to effects resulting from the large aspect ratio of the control volumes near the wall and the large variation of properties in the boundary layer. The first contributing factor was the use of different time steps for each control volume and for each equation. Near the walls where the control volumes were very thin and the velocities were low, the continuity time steps that were used for calculating the changes in density were small. The ratio of the momentum and continuity time steps there was also very large. The pressure in the outer part of the boundary layer was changing much more rapidly than it was near the wall. This induced large transverse pressure gradients and then large transverse velocities followed resulting in an unstable calculation procedure. It was felt that to stabilize this calculation procedure, the changes in pressure through the boundary layer must be coupled in some manner and that the changes in pressure be only dependent on the continuity error and not on both the density change through the continuity error and the temperature change through the momentum error and its resulting velocity change. We wanted to minimize transverse pressure gradients in the intermediate solution to enhance stability.

The above realizations resulted in two changes. One change altered the way that the continuity error is used to update the flow properties (see Section 2.3 DISTRIBUTION OF PROPERTIES). Previously (12), errors in continuity were used to update the density at the node points. The pressure was then calculated from the equation of state. An alternative procedure has been developed which updates the pressure directly from the continuity error. The density is then evaluated using the equation of state.

The second change is to group control volumes in the boundary layer to form a larger global control volume. The continuity error is calculated for this global control volume and changes in pressure are assigned equally to each of the upstream nodes for each control volume making up the global control volume. Initially the global control volume extends from the wall to the edge of the boundary layer. Then the global control volume is made successively smaller towards the wall. This is shown schematically in Fig. 2.8.1. The entire pressure change for one iteration at each node within the multi-volume region is determined by adding together all the pressure changes assigned to that node. If a non-uniform grid is used, the continuity time step for each global control volume may be based upon the continuity time step for the largest control volume within the global control volume. A non-uniform grid is preferred for this multi-volume method so that pressure changes for successively smaller global control volumes become smaller.

The multi-volume method propagates pressure changes rapidly through the boundary layer and minimizes large transverse pressure gradients in the intermediate solution. The above changes allow the calculation of boundary layer flows where the control volumes near the wall can have aspect ratios (length/height) of over 1000. Without the multi-volume method these aspect ratios could not be used. The stability and convergence properties of various multi-volume approaches are investigated in section 3.5.

2.9 TRANSVERSE UPWIND DIFFERENCING

When the control volumes become long and thin near the wall of the duct, the fluxes through the top and bottom faces of the control volume become more significant in comparison to the fluxes through the streamwise faces. Because the nodes of the control volumes are located in the middle of these streamwise faces, the predominant flow direction must be in the streamwise direction for the discretization method used here to properly reflect the convective nature of the flow. When the

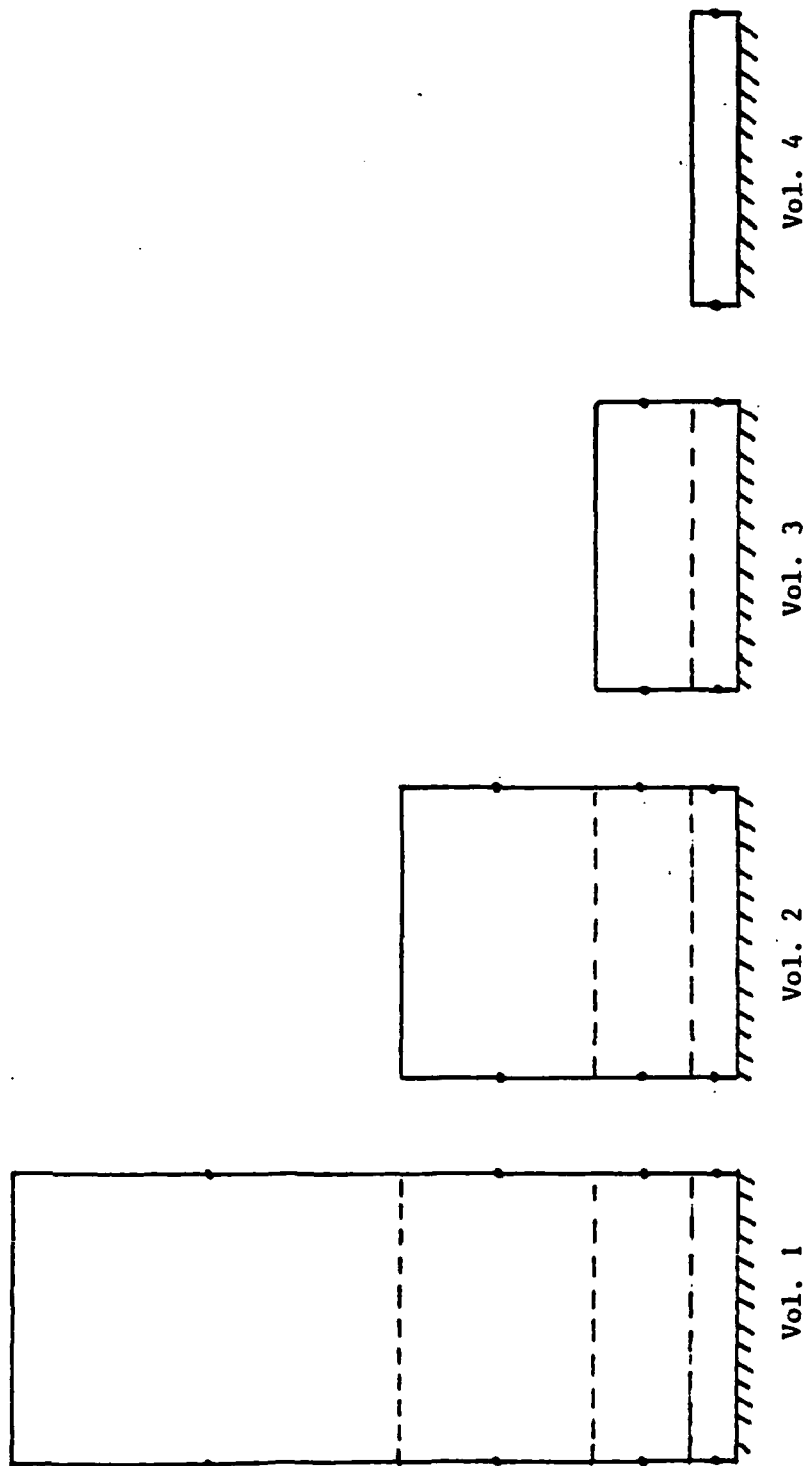


Fig. 2.8.1 Multi-Volume Method For Pressure Changes in the Boundary Layer
Using Successively Smaller Control Volumes

fluxes in the transverse direction become significant, the solution procedure may become unstable because the diagonal terms in the coefficient matrix become smaller as the transverse fluxes increase. This is because the velocities at the corners of the nodes are determined from interpolation. To strengthen the diagonal dominance of the coefficient matrix, the momentum fluxes through the transverse faces may be calculated using interpolated velocities upstream in the transverse direction rather than the actual interpolated values. These velocities are multiplied by the mass fluxes through the sides of the control volumes to get the total momentum flux. The direction and magnitude of the upwinding is determined from a criterion based upon the magnitude of the flux ratio, FRATIO. FRATIO is the ratio of the mass flux through the transverse face divided by the mass flux through the streamwise face. A criterion for upwinding is derived next.

The criterion for upwinding is based upon an analysis of the convective terms in the momentum equations and how the discretization affects the dominance of the centerpoint coefficient. The momentum equations for unsteady flow are

$$\frac{\partial \rho \underline{u}}{\partial t} + \nabla \cdot \rho \underline{u} \underline{u} = - \nabla \cdot P \delta_{ij} + \nabla \cdot \mu \nabla \underline{u} + \nabla \cdot \mu \overline{\nabla \underline{u}}^T . \quad (2.9.1)$$

When Gauss' theorem is applied to the steady convective terms of Eq. 2.9.1 to transform the governing equations from differential to integral form, we get

$$\iiint \nabla \cdot \rho \underline{u} \underline{u} d(Vol) = \iint \rho \underline{u} \underline{u} \cdot d\underline{A} . \quad (2.9.2)$$

The convective terms in Eq. 2.9.2 can be rewritten as

$$B = \rho \frac{\partial \underline{u}}{\partial t} + \nabla \cdot \rho \underline{u} \underline{u} - \underline{u} \nabla \cdot \rho \underline{u} . \quad (2.9.3)$$

When Gauss' theorem is applied to the steady portion of Eq. 2.9.3, we get

$$C \equiv \iiint (\nabla \cdot \rho \underline{u} \underline{u} - \underline{u} \nabla \cdot \rho \underline{u}) dVol = \iint \rho \underline{u} \underline{u} \cdot d\underline{A} - \bar{u} \iint \rho \underline{u} \cdot d\underline{A} \quad (2.9.4)$$

where \bar{u} is an average velocity for the control volume. The second term on the right hand side of Eq. 2.9.4 can be recognized as the continuity error contribution to the momentum equation. We use Eq. 2.9.4 in the current method, to evaluate the momentum fluxes.

If our computational domain is discretized into finite quadrilateral control volumes, the convective momentum fluxes can be identified as those associated with the north, south, east, and west faces of the control volume (see Fig. 2.9.1). These momentum fluxes can be further classified into those associated with the x-momentum equation ($(\dot{m}u)_{north}, (\dot{m}u)_{south}, (\dot{m}u)_{west},$ and $(\dot{m}u)_{east}$) and those associated with the y-momentum equation ($(\dot{m}v)_{north}, (\dot{m}v)_{south}, (\dot{m}v)_{west},$ and $(\dot{m}v)_{east}$) . For example, the momentum flux contribution to the x-momentum equation through the north face of the control volume is

$$(\dot{m}u)_{north} = \int_N u \rho \underline{u} \cdot d\underline{A} \quad (2.9.5)$$

where \underline{A} is an outward normal vector. A typical control volume with the x-momentum fluxes identified is shown in Fig. 2.9.1.

The mass fluxes through the north, south, east, and west faces of a control volume are $\dot{m}_{north}, \dot{m}_{south}, \dot{m}_{east},$ and $\dot{m}_{west},$ respectively. The mass flux through the north face of the control volume out of the control volume is

$$\dot{m}_{north} = \int_N \rho \underline{u} \cdot d\underline{A} \quad (2.9.6)$$

where positive mass flux is defined here as a flux directed outward from the control volume. The continuity error, $\dot{m}_{error},$ for a control volume (I,J) is

$$\dot{m}_{error} = - \dot{m}_{north,I,J} - \dot{m}_{south,I,J} - \dot{m}_{west,I,J} - \dot{m}_{east,I,J} . \quad (2.9.7)$$

From symmetry, we can note that

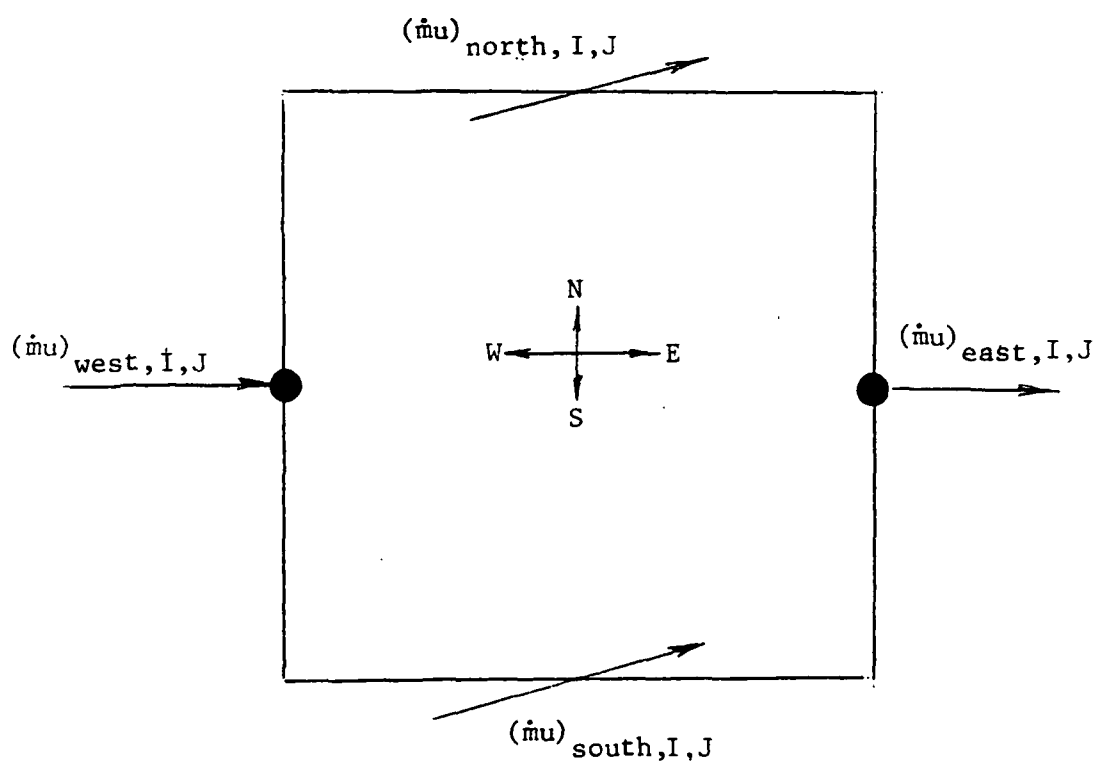


Fig. 2.9.1 Convective Momentum Fluxes for a Control Volume

$$\dot{m}_{north,I,J} = - \dot{m}_{south,I,J+1} \quad (2.9.8)$$

and

$$\dot{m}_{east,I,J} = - \dot{m}_{west,I+1,J} \quad (2.9.9)$$

Substituting Eqs. 2.9.8 and 2.9.9 into Eq. 2.9.7, we get

$$\dot{m}_{error,I,J} = \dot{m}_{south,I,J+1} - \dot{m}_{south,I,J} + \dot{m}_{west,I+1,J} - \dot{m}_{west,I,J} \quad (2.9.10)$$

From the momentum balance, the convective contributions to the x-momentum equation (see Eq. 2.9.4) for a finite control volume are

$$C = (\dot{m}u)_{north,I,J} + (\dot{m}u)_{south,I,J} + (\dot{m}u)_{east,I,J} + (\dot{m}u)_{west,I,J} + (u_E \dot{m}_{error})_{I,J} \quad (2.9.11)$$

where $(u_E \dot{m}_{error})_{I,J}$ is the continuity error contribution to the momentum error. The corrections to the momentum error, $(u_E \dot{m}_{error})_{I,J}$ and $(v_E \dot{m}_{error})_{I,J}$, due to the continuity error are

$$(u_E \dot{m}_{error})_{I,J} = - \bar{u} \iint \rho \underline{u} \cdot d\underline{A} \quad (2.9.12)$$

and

$$(v_E \dot{m}_{error})_{I,J} = - \bar{v} \iint \rho \underline{u} \cdot d\underline{A} \quad (2.9.13)$$

where u_E and v_E are effective velocities for a control volume and \bar{u} and \bar{v} are average velocities for a control volume. The effective velocities may be different from the average velocities to improve the stability of the method.

The momentum flux $(\dot{m}u)_{north}$ is ,

$$= (\rho u \cdot \Delta)_{north,I,J} u_{north,I,J}$$

$$(\dot{m}u)_{north,I,J} = \dot{m}_{north,I,J} u_{north,I,J}$$

$$= - \dot{m}_{south,I,J+1} u_{north,I,J} \quad (2.9.14)$$

Using a four point interpolation for u_{north}

$$(\dot{m}u)_{north,I,J} = - \dot{m}_{south,I,J+1} \times$$

$$0.5[(u_{I,J} + u_{I+1,J}) \times (1 - g_N) + (u_{I,J+1} + u_{I+1,J+1}) \times g_N] \quad (2.9.15)$$

where $0 \leq g_N \leq 1$. Similarly,

$$(\dot{m}u)_{south,I,J} = \dot{m}_{south,I,J} \times 0.5[(u_{I,J-1} + u_{I+1,J-1}) \times (1 - g_S) + (u_{I,J} + u_{I+1,J}) \times g_S] \quad (2.9.16)$$

$$(\dot{m}u)_{west,I,J} = \dot{m}_{west,I,J} \times u_{I,J} \quad (2.9.17)$$

$$(\dot{m}u)_{east,I,J} = - (\dot{m}u)_{west,I+1,J} = - \dot{m}_{west,I+1,J} \times u_{I+1,J} \quad (2.9.18)$$

where g_N and g_S are interpolation parameters for the north and south faces of the control volume respectively. The interpolation parameters, g_N and g_S , are usually calculated from the position of the control volume face relative to the two node points adjacent to that face (see 2.2 CONTROL VOLUMES). We will call this the geometric interpolation parameter, g_{int} . However when the transverse fluxes become large enough in comparison to the streamwise fluxes, the centerpoint coefficient will not be dominant if these geometric interpolation parameters are used. Other more stable interpolation parameters must be determined.

Now substituting Eqs. 2.9.10, 2.9.15, 2.9.16, 2.9.17, and 2.9.18 into Eq. 2.9.11, and grouping coefficients with common velocities, we get

$$\begin{aligned}
C = & u_{I+1,J} \times [- \dot{m}_{south,I,J+1} \times 0.5 \times (1 - g_N) + \dot{m}_{south,I,J} \times 0.5 \times g_S - \dot{m}_{west,I+1,J}] \\
& + u_{I,J} \times [- \dot{m}_{south,I,J+1} \times 0.5 \times (1 - g_N) + \dot{m}_{south,I,J} \times 0.5 \times g_S + \dot{m}_{west,I,J}] \\
& + u_{I,J+1} \times [- \dot{m}_{south,I,J+1} \times 0.5 \times g_N] \\
& + u_{I+1,J+1} \times [- \dot{m}_{south,I,J+1} \times 0.5 \times g_N] \\
& + u_{I,J-1} \times [\dot{m}_{south,I,J} \times 0.5 \times (1 - g_S)] \\
& + u_{I+1,J-1} \times [\dot{m}_{south,I,J} \times 0.5 \times (1 - g_S)] \\
& + u_E \times [+ \dot{m}_{south,I,J+1} - \dot{m}_{south,I,J} + \dot{m}_{west,I+1,J} - \dot{m}_{west,I,J}] .
\end{aligned} \tag{2.9.19}$$

The value of u_E in Eq. 2.9.19 will depend upon the sign of the continuity error and its influence on the strength of the centerpoint coefficient.

The last term in Eq. 2.9.19 is

$$\begin{aligned}
& + u_E \times [+ \dot{m}_{south,I,J+1} - \dot{m}_{south,I,J} + \dot{m}_{west,I+1,J} - \dot{m}_{west,I,J}] \\
& = + u_E \times [\dot{m}_{error}] .
\end{aligned} \tag{2.9.20}$$

If the continuity error, \dot{m}_{error} , is negative we will let

$$u_E = u_{I,J} \tag{2.9.21}$$

which reduces the magnitude of the non-centerpoint coefficients. If the continuity error, \dot{m}_{error} , is positive we will let

$$u_E = u_{I+1,J} \tag{2.9.22}$$

which will strengthen the centerpoint coefficient. Both these decisions enhance the stability of the method. It can be shown for forward flow and with this choice of the effective velocity, u_E , that the coefficient of $u_{I,J}$ is always negative if either $\dot{m}_{south,I,J} = 0$ or $\dot{m}_{south,I,J+1} = 0$. As will be seen, the contribution of node I,J to the sum of the non-centerpoint coefficients will not need to be considered further in this analysis. Also because of this choice of u_E , the magnitude of the mass flux, $\dot{m}_{west,I,J}$, does not detrimentally affect the stability of the scheme in forward flow.

To arrive at interpolation parameters which will probably result in a stable calculation procedure, we will investigate the stability of two simple examples. These examples assume 1) that the mass flux through the north face of the control volume is zero and 2) that the mass flux through the south face of the control volume is zero. Finally, more conservative interpolation parameters will be determined which will take into account the possibility of arbitrary combinations of north and south fluxes. This will be accomplished by using only 1/2 of the flux, $\dot{m}_{west,I+1,J}$, in the calculation of the interpolation parameters which satisfy the stability criteria.

CASE # 1

For this case, we have assumed that the mass flux through the north face of the control volume is zero. This test case is shown schematically in Fig. 2.9.2. When the mass balance is applied we get,

$$\dot{m}_{error,I,J} = -\dot{m}_{south,I,J} - \dot{m}_{west,I,J} + \dot{m}_{west,I+1,J} \quad (2.9.23)$$

If the mass flux through the south face is positive and the continuity error is negative because of this flux, then Eq. 2.9.19 becomes

$$C = u_{I+1,J} \times [0.5 \times g_S \times \dot{m}_{south,I,J} - \dot{m}_{west,I+1,J} + \dot{m}_{error}]$$

$$+ u_{I,J} \times [0.5 \times g_S \times \dot{m}_{south,I,J} + \dot{m}_{west,I,J}]$$

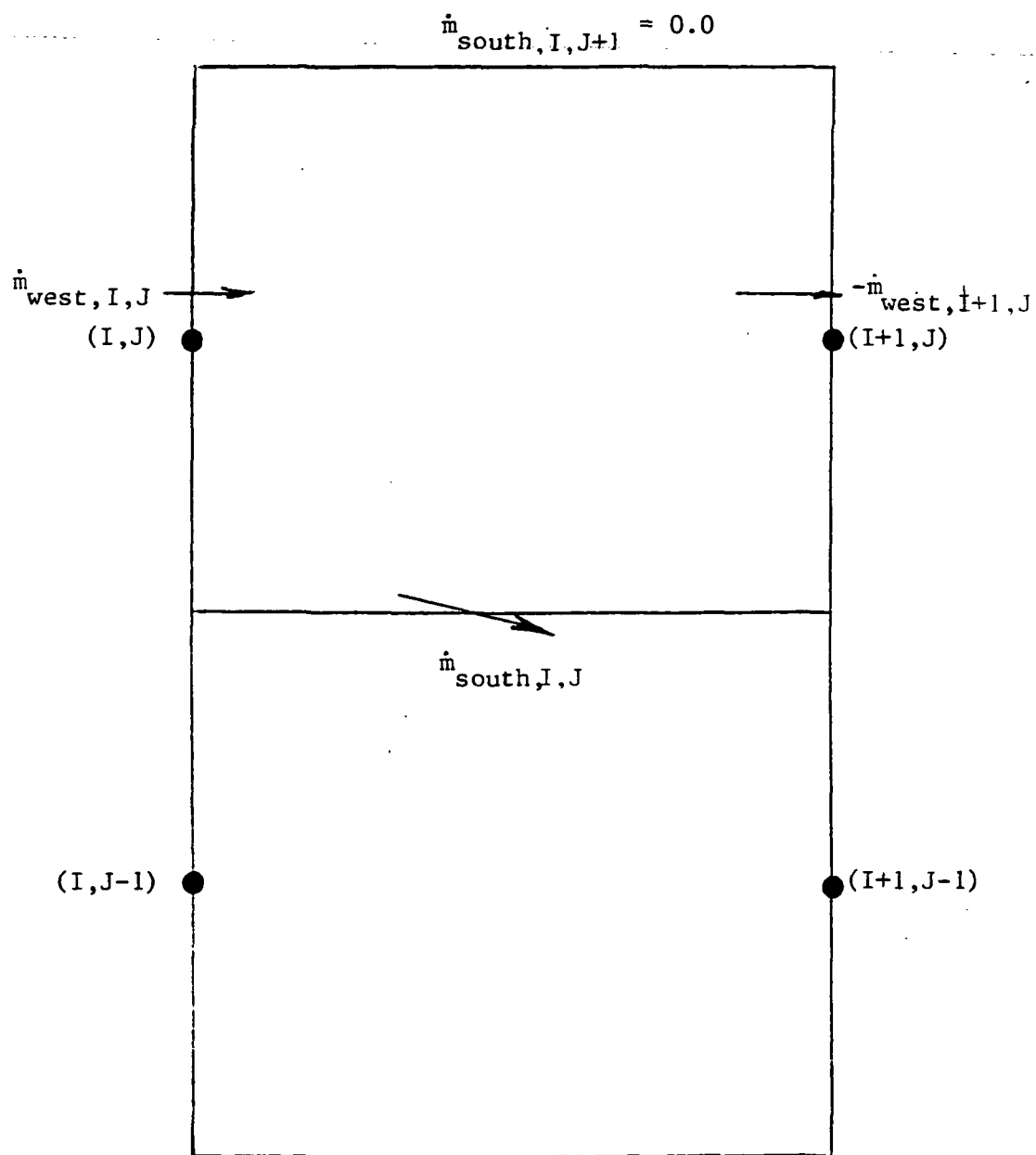


Fig. 2.9.2 Schematic of Case #1

$$\begin{aligned}
& + u_{I,J-1} \times [0.5 \times \dot{m}_{south,I,J} \times (1 - g_S)] \\
& + u_{I+1,J-1} \times [0.5 \times \dot{m}_{south,I,J} \times (1 - g_S)] .
\end{aligned} \tag{2.9.24}$$

All non-centerpoint coefficients are negative; therefore, the requirement for stability is

$$0.5 \times g_S \times \dot{m}_{south,I,J} - \dot{m}_{west,I+1,J} + \dot{m}_{error} \geq 0 \tag{2.9.25}$$

$$0.5 \times g_S \times \dot{m}_{south,I,J} - \dot{m}_{west,I,J} - \dot{m}_{south,I,J} \geq 0 . \tag{2.9.26}$$

This will be satisfied for any value of g_S .

For positive $\dot{m}_{south,I,J}$ and a corresponding negative continuity error, Eq. 2.9.19 becomes

$$\begin{aligned}
C &= u_{I+1,J} \times [0.5 \times g_S \times \dot{m}_{south,I,J} - \dot{m}_{west,I+1,J}] \\
& + u_{I,J} \times [0.5 \times g_S \times \dot{m}_{south,I,J} + \dot{m}_{west,I,J} + \dot{m}_{error}] \\
& + u_{I,J-1} \times [0.5 \times \dot{m}_{south,I,J} \times (1 - g_S)] \\
& + u_{I+1,J-1} \times [0.5 \times \dot{m}_{south,I,J} \times (1 - g_S)] .
\end{aligned} \tag{2.9.27}$$

The requirement for stability is, therefore,

$$0.5 \times g_S \times \dot{m}_{south,I,J} - \dot{m}_{west,I+1,J} \geq \dot{m}_{south,I,J} \times (1 - g_S) . \tag{2.9.28}$$

In terms of FRATIO, $\dot{m}_{south,I,J}/\dot{m}_{west,I+1,J}$, and g_S , Eq. 2.9.28 becomes

$$g_S \geq \frac{1 + FRATIO}{1.5FRATIO} . \tag{2.9.29}$$

CASE # 2

For this case, we have assumed that the mass flux through the south face of the control volume is zero. When the mass balance is applied we get,

$$\dot{m}_{error,I,J} = + \dot{m}_{south,I,J+1} - \dot{m}_{west,I,J} + \dot{m}_{west,I+1,J} . \quad (2.9.30)$$

If the mass flux through the north face is positive, in other words, if $\dot{m}_{south,I,J+1} < 0$ and $\dot{m}_{error,I,J}$ is negative then Eq. 2.9.19 becomes

$$\begin{aligned} C = & u_{I+1,J} \times [- \dot{m}_{south,I,J+1} \times 0.5 \times (1 - g_N) - \dot{m}_{west,I+1,J}] \\ & + u_{I,J} \times [- \dot{m}_{south,I,J+1} \times 0.5 \times (1 - g_N) + \dot{m}_{west,I,J} + \dot{m}_{error}] \\ & + u_{I,J+1} \times [- g_N \times 0.5 \times \dot{m}_{south,I,J+1}] \\ & + u_{I+1,J+1} \times [- g_N \times 0.5 \times \dot{m}_{south,I,J+1}] . \end{aligned} \quad (2.9.31)$$

The requirement for stability is,

$$- \dot{m}_{south,I,J+1} \times 0.5 \times (1 - g_N) - \dot{m}_{west,I+1,J} \geq - g_N \times \dot{m}_{south,I,J+1} . \quad (2.9.32)$$

In terms of FRATIO and g_N , we get

$$g_N \leq \frac{1 + 0.5 \times FRATIO}{1.5FRATIO} \quad (2.9.33)$$

where in this case,

$$FRATIO = \frac{\dot{m}_{south,I,J+1}}{\dot{m}_{west,I+1,J}} . \quad (2.9.34)$$

If the mass flux through the north face is negative, in other words, if $\dot{m}_{south,I,J+1} > 0$ and $\dot{m}_{error,I,J}$ is positive, then Eq. 2.9.19 becomes

$$\begin{aligned}
C = & u_{I+1,J} \times [- \dot{m}_{south,I,J+1} \times 0.5 \times (1 - g_N) - \dot{m}_{west,I+1,J} + \dot{m}_{error}] \\
& + u_{I,J} \times [- \dot{m}_{south,I,J+1} \times 0.5 \times (1 - g_N) + \dot{m}_{west,I,J}] \\
& + u_{I,J+1} \times [- g_N \times 0.5 \times \dot{m}_{south,I,J+1}] \\
& + u_{I+1,J+1} \times [- g_N \times 0.5 \times \dot{m}_{south,I,J+1}] .
\end{aligned} \tag{2.9.35}$$

The requirement for stability is,

$$- \dot{m}_{south,I,J+1} \times 0.5 \times (1 - g_N) - \dot{m}_{west,I+1,J} + \dot{m}_{error} \geq 0 \tag{2.9.36}$$

$$- \dot{m}_{south,I,J+1} \times 0.5 \times (1 - g_N) - \dot{m}_{west,I,J} + \dot{m}_{south,I,J+1} \geq 0 . \tag{2.9.37}$$

This result is always satisfied for all values of g_N .

Since the north face of one control volume is the south face of another control volume, $g_{S,J+1} = g_{N,J}$. The most conservative value for the interpolation parameter is chosen from Eqs. 2.9.29 and 2.9.33 so that we use a consistent interpolation scheme for a given face. If the geometric interpolation parameter, g_{INT} , is more conservative than those specified in Eqs. 2.9.29 and 2.9.33, then it should, of course, be used.

ANY COMBINATION OF NORTH AND SOUTH FLUXES

If only 1/2 the mass flux, $\dot{m}_{west,I,J+1}$, is used in the determination of the interpolation parameters, g_N and g_S , it can easily be seen (looking at Eqs. 2.9.28 and 2.9.32) that the corresponding interpolation parameters become more conservative and are

$$g_s \geq \frac{0.5 + FRATIO}{1.5FRATIO} \tag{2.9.38}$$

$$g_n \leq \frac{0.5 + 0.5FRATIO}{1.5FRATIO} \quad (2.9.39)$$

This is equivalent to using twice the FRATIO in Eqs. 2.9.29 and 2.9.33. The criteria for the interpolation parameters, g_s and g_n , are summarized in Table 2.9.1. The above interpolation parameters are not assured to provide stable discretization for all possible combinations of mass fluxes ; however, these interpolation parameters have resulted in stable solutions for all the test cases investigated in this dissertation. However, some of the solutions were unstable before this upwinding was used. For all the test cases in this dissertation, upwinding was only needed in the transient solution and at the steady state the geometric interpolation parameters were used.

2.10 ENERGY EQUATION

For most of the calculations which are to be used as test cases in the present work, the assumption of constant total temperature will be a sufficient representation of the energy equation in the flow fields. By assuming constant total temperature, the computations are less expensive to run and the computer storage requirements are less. An assumption of constant total temperature is satisfactory because of these reasons:

1. an adiabatic wall is assumed in the calculations.
2. no work is done on the fluid at the solid boundaries.
3. the Mach numbers in the flow fields that are investigated are low enough that total temperature gradients within the boundary layer are small.

Table 2.9.1 Upwinded Interpolation Parameters

SOUTH FACE

If $\dot{m}_{\text{south},i,j} < 0$ no restriction on g_s

If $\dot{m}_{\text{south},i,j} > 0$ $g_s \geq \frac{0.5 + \text{FRATIO}}{1.5 \text{FRATIO}}$

where $\text{FRATIO} = \frac{\dot{m}_{\text{south},i,j}}{\dot{m}_{\text{west},i+1,j}}$

NORTH FACE

If $\dot{m}_{\text{south},i,j+1} < 0$ $g_n \leq \frac{0.5 + 0.5 \text{FRATIO}}{1.5 \text{FRATIO}}$

If $\dot{m}_{\text{south},i,j+1} > 0$ no restriction on g_n

where $\text{FRATIO} = \frac{\dot{m}_{\text{south},i,j+1}}{\dot{m}_{\text{west},i+1,j}}$

- noting that for consistency g_n for control volume j must equal g_s for control volume $j+1$
- reflecting symmetry and the geometric interpolation parameters, the most conservative value is chosen

4. the turbulent Prandtl number of air is approximately 0.9. For a Prandtl number of 1.0, the assumption of constant total temperature is valid, therefore a solution with a Prandtl number of 0.9 should not deviate greatly from the constant total temperature assumption.

However, it was felt that the methodology required to include the energy equation in the governing equations should be developed and simple test cases should be used to demonstrate its success. Later in this dissertation, four test cases will be presented which use the full energy equation in their calculations. These test cases will be

1. turbulent boundary layer flow in an adverse pressure gradient with an inlet freestream Mach number of 0.55.
2. flat plate turbulent boundary layer with a freestream Mach number of 0.95.
3. Sajben's diffuser (23) including the full energy equation.
4. flat plate turbulent boundary layer with a freestream Mach number of 2.8.

Unless otherwise noted, the laminar Prandtl number for the calculations will be .73 and the turbulent Prandtl number will be 0.9. For the moment, the integral form of the energy equation incorporated into this finite volume method will be presented.

The energy equation in differential form is

$$\frac{\partial E_t}{\partial t} + \nabla \cdot E_t \underline{u} = - \nabla \cdot \underline{q} + \nabla \cdot [\underline{u} \cdot (\mu \nabla \underline{u} + \mu \overline{\nabla \underline{u}^T})] - \nabla \cdot P \underline{u} \quad (2.10.1)$$

where the total energy per unit volume, E_t , is

$$E_t = \rho(e + \frac{1}{2}(u^2 + v^2)) = \rho e_t \quad (2.10.2)$$

The left hand side of Eq. 2.10.1 can be rewritten as

$$\frac{\partial E_t}{\partial t} + \nabla \cdot E_t \underline{u} = \frac{\partial(\rho e_t)}{\partial t} + \nabla \cdot \rho e_t \underline{u} \quad (2.10.3)$$

and

$$\frac{\partial(\rho e_t)}{\partial t} + \nabla \cdot (\rho e_t) \underline{u} = \rho \frac{\partial e_t}{\partial t} + \rho \underline{u} \cdot \nabla e_t \quad (2.10.4)$$

and then expanding the right hand side of Eq. 2.10.4, we get,

$$\rho \frac{\partial e_t}{\partial t} + \rho \underline{u} \cdot \nabla e_t = \rho \frac{\partial e_t}{\partial t} + \nabla \cdot \rho \underline{u} e_t - e_t (\nabla \cdot \rho \underline{u}) \quad (2.10.5)$$

The procedure just outlined is identical to what was done to the unsteady and convective terms in the momentum equations (see section 2.1).

The heat flux vector q , can be represented as

$$q = -k \nabla T \quad (2.10.6)$$

Substituting Eqs. 2.10.3-2.10.6 into Eq. 2.10.1 , we get

$$\begin{aligned} \rho \frac{\partial e_t}{\partial t} = & - \nabla \cdot \rho \underline{u} e_t + e_t (\nabla \cdot \rho \underline{u}) - \nabla \cdot (-k \nabla T) \\ & + \nabla \cdot [\underline{u} \cdot (\mu \nabla \underline{u} + \mu \overline{\nabla \underline{u}^T})] - \nabla \cdot P \underline{u} \quad (2.10.7) \end{aligned}$$

Applying Gauss' theorem to convert to the integral form of the energy equation we get

$$\begin{aligned} \rho \frac{\partial e_t}{\partial t} \times \delta Vol = & - \iint \rho \underline{u} e_t \cdot d\underline{A} + \bar{e}_t \iint \rho \underline{u} \cdot d\underline{A} - \iint -k \nabla T \cdot d\underline{A} \\ & + \iint [\underline{u} \cdot (\mu \nabla \underline{u} + \mu \overline{\nabla \underline{u}^T})] \cdot d\underline{A} - \iint P \underline{u} \cdot d\underline{A} \quad (2.10.8) \end{aligned}$$

where \bar{e} is an average value for the control volume. As with the momentum equations, Eq. 2.10.8 has a term, $\bar{e}_i \oint \rho \underline{u} \cdot d\underline{A}$, which removes the continuity error contribution to the energy error.

To enhance stability, the energy equation of Eq. 2.10.8 is not used from the initial solution. The first 500 iterations of the calculation use the assumption of constant total temperature. After 500 iterations, the energy equation is added. Initially there are large errors in continuity and momentum and these large errors act through the energy equation to cause errors in the total energy for a control volume. This interaction is destabilizing therefore we let the calculation proceed until continuity and momentum are reasonably satisfied before the energy equation is added.

The appropriate boundary conditions to be used with the energy equation in our calculations are:

1. Adiabatic wall, meaning that the heat flux through the solid walls is zero.
2. There is no work done on the control volumes at the solid boundary due to viscous forces. This is because the velocity at the wall is zero.

Because the energy equation has the same general form as the momentum equations, approximately the same time step is used in the energy equation as is used in the momentum equations. More will be said about this later in this section. The addition of the energy equation does destabilize the solution somewhat when compared with the assumption of constant total temperature. For this reason, the time step used for the energy equation is usually reduced by a factor of 2 compared to the momentum equation time step. Transverse upwind differencing is also used for the specific total energy, e_t , in the energy equation in exactly the same manner as it was used for velocities in the momentum equations.

An alternative form of the energy equation has also been used and will be derived here. This alternative form has enhanced convergence properties when compared with the above formulation. Briefly, the energy equation is reformulated so that changes in total enthalpy, h_t , are calculated over one time step rather than changes in total energy, e_t , which was done previously (Eq. 2.10.7). Also,

the energy error due to the continuity error and the momentum error are removed using this alternative formulation.

The total enthalpy can be defined in terms of the total energy and the static temperature by starting with the definition of total enthalpy

$$h_t = h + \frac{V^2}{2} = e + \frac{P}{\rho} + \frac{V^2}{2} = e_t + \frac{P}{\rho} \quad (2.10.9)$$

and for an ideal gas,

$$\frac{P}{\rho} = RT \quad (2.10.10)$$

so that

$$h_t = e_t + RT \quad (2.10.11)$$

Taking the derivative of both sides of Eq. 2.10.11 with respect to time , t , and multiplying by the density, we get

$$\rho \frac{\partial h_t}{\partial t} = \rho \frac{\partial e_t}{\partial t} + \rho R \frac{\partial T}{\partial t} \quad (2.10.12)$$

The static temperature T can be represented in terms of the total enthalpy and the absolute velocity as

$$T = \frac{h_t}{C_p} - \frac{V^2}{2C_p} \quad (2.10.13)$$

therefore

$$\frac{\partial T}{\partial t} = \frac{1}{C_p} \frac{\partial h_t}{\partial t} - \frac{V}{C_p} \frac{\partial V}{\partial t} \quad (2.10.14)$$

Therefore Eq. 2.10.12 can be rewritten as

$$\rho \frac{\partial h_t}{\partial t} = \rho \frac{\partial e_t}{\partial t} + \rho R \left[\frac{1}{C_p} \frac{\partial h_t}{\partial t} - \frac{V}{C_p} \frac{\partial V}{\partial t} \right] \quad (2.10.15)$$

Now if we solve for the time derivative of the total enthalpy, we get

$$\rho \frac{\partial h_t}{\partial t} = \rho \gamma \frac{\partial e_t}{\partial t} - \frac{\rho R}{C_v} V \frac{\partial V}{\partial t} \quad (2.10.16)$$

where γ is the ratio of specific heats and V is the magnitude of the velocity vector. The second term on the right hand side of Eq. 2.10.16 is the momentum error contribution to the total enthalpy error. Substituting $\rho \frac{\partial e_t}{\partial t}$ from Eq. 2.10.7 into Eq. 2.10.16, we get

$$\begin{aligned} \rho \frac{\partial h_t}{\partial t} = & \gamma \quad - \nabla \cdot \rho \underline{u} e_t + e_t (\nabla \cdot \rho \underline{u}) - \nabla \cdot (-k \nabla T) \\ & + \nabla \cdot [\underline{u} \cdot (\mu \nabla \underline{u} + \mu \overline{\nabla \underline{u}^T})] - \nabla \cdot P \underline{u} - \frac{\rho R}{C_v} V \frac{\partial V}{\partial t} . \end{aligned} \quad (2.10.17)$$

This equation may be rewritten, by using $h_t = e_t + P/\rho$, as

$$\begin{aligned} \rho \frac{\partial h_t}{\partial t} = & \gamma \quad - \nabla \cdot \rho \underline{u} h_t + h_t (\nabla \cdot \rho \underline{u}) - \nabla \cdot (-k \nabla T) \\ & + \nabla \cdot [\underline{u} \cdot (\mu \nabla \underline{u} + \mu \overline{\nabla \underline{u}^T})] - \frac{P}{\rho} \nabla \cdot \rho \underline{u} - \frac{\rho R}{C_v} V \frac{\partial V}{\partial t} . \end{aligned} \quad (2.10.18)$$

By noting that $\nabla \cdot \rho \underline{u} = \partial \rho / \partial t$, the last two terms of Eq. 2.10.18 are of the form,

$$M = l \frac{\partial \rho}{\partial t} + m \frac{\partial V}{\partial t} . \quad (2.10.19)$$

At the steady state, Eq. 2.10.18 becomes

$$0 = \gamma \quad [- \nabla \cdot \rho \underline{u} h_t - \nabla \cdot (-k \nabla T) + \nabla \cdot [\underline{u} \cdot (\mu \nabla \underline{u} + \mu \overline{\nabla \underline{u}^T})]] . \quad (2.10.20)$$

Therefore, we may arbitrarily alter the variables l and m and the steady form of the energy equation, Eq. 2.10.20, will be obtained for converged solutions. The transient behavior of h_t is improved in the calculation procedure by choosing $l = m = 0$ so that the transient energy equation used for each time step is,

$$\rho \frac{\partial h_t}{\partial t} = \gamma - \nabla \cdot \rho \underline{u} h_t + h_t (\nabla \cdot \rho \underline{u}) - \nabla \cdot (-k \nabla T) + \nabla \cdot [\underline{u} \cdot (\mu \nabla \underline{u} + \mu \overline{\nabla \underline{u}^T})] \quad (2.10.21)$$

By setting $l = m = 0$, we remove the influence of the continuity and momentum errors to the energy equation during transients in the solution. Applying Gauss' theorem to Eq. 2.10.21 we get the integral form of the energy equation,

$$\rho \frac{\delta h_t}{\delta t} \times \delta Vol = \gamma - \iint \rho \underline{u} h_t \cdot d\underline{A} + \bar{h}_t \iint \rho \underline{u} \cdot d\underline{A} - \iint -k \nabla T \cdot d\underline{A} + \iint [\underline{u} \cdot (\mu \nabla \underline{u} + \mu \overline{\nabla \underline{u}^T})] \cdot d\underline{A} \quad (2.10.22)$$

where \bar{h}_t and \bar{P} are average values for the control volume. The time step used in Eq. 2.10.22 must be reduced by a factor of γ compared with that used in Eq. 2.10.8. This reduced time step is needed to ensure the stability of the new formulation since the coefficient of the steady terms in the energy equation have increased by a factor of γ in the new formulation (see section 2.5).

It was found to be important in the implementation of the energy equation, that the heat flux term and the work done due to shear forces term were evaluated consistently. This means that the work due to shear forces should be evaluated midway between the node points and not at the control volume faces because the heat flux calculation by the nature of its discretization is valid at the midpoint between the node points.

An interesting observation can be made from this form of the energy equation about boundary layer flow over a flat plate with a Prandtl number of 1. For steady flow, Eq. 2.10.22 becomes

$$\begin{aligned}
0 = & - \iint \rho \underline{u} h_i \cdot d\underline{A} - \iint -k \nabla T \cdot d\underline{A} \\
& + \iint [\underline{u} \cdot (\mu \nabla \underline{u} + \mu \overline{\nabla \underline{u}^T})] \cdot d\underline{A} .
\end{aligned} \tag{2.10.23}$$

In addition, the viscous terms are simplified using the boundary layer approximation by noting that

$$\underline{u} \cdot (\mu \nabla \underline{u} + \mu \overline{\nabla \underline{u}^T}) \cong u \mu \frac{\partial u}{\partial y} = \mu \frac{\partial u^2/2}{\partial y} \tag{2.10.24}$$

and therefore

$$\iint [\underline{u} \cdot (\mu \nabla \underline{u} + \mu \overline{\nabla \underline{u}^T})] \cdot d\underline{A} \cong \iint \mu \frac{\partial u^2/2}{\partial y} dA_y . \tag{2.10.25}$$

For an ideal gas with constant specific heats,

$$T = \frac{h}{C_p} \tag{2.10.26}$$

and the Prandtl number is defined as,

$$Pr = \frac{\mu C_p}{k} \tag{2.10.27}$$

therefore,

$$- \iint -k \nabla T \cdot d\underline{A} = \iint \frac{\mu}{Pr} \nabla h \cdot d\underline{A} . \tag{2.10.28}$$

Also if gradients in enthalpy in the x-direction are small compared to gradients in the y-direction, then

$$\iint \frac{\mu}{Pr} \nabla h \cdot d\underline{A} \cong \iint \frac{\mu}{Pr} \frac{\partial h}{\partial y} dA_y . \tag{2.10.29}$$

Substituting Eqs. 2.10.24, 2.10.25, 2.10.28, and 2.10.29 into Eq. 2.10.23, we get

$$0 = - \iint \rho \underline{u} h_t \cdot d\underline{A} + \iint \frac{\mu}{Pr} \frac{\partial h}{\partial y} dA_y + \iint \mu \frac{\partial u^2/2}{\partial y} dA_y . \quad (2.10.30)$$

The last two terms of Eq. 2.10.30 can be combined if the Prandtl number is taken as 1. The resulting equation is

$$0 = - \iint \rho \underline{u} h_t \cdot d\underline{A} + \iint \mu \frac{\partial h_t}{\partial y} dA_y . \quad (2.10.31)$$

If the total enthalpy is constant in the flow, $\nabla h_t = 0$, therefore

$$\iint \mu \frac{\partial h_t}{\partial y} dA_y = 0 \quad (2.10.32)$$

and

$$- \iint \rho \underline{u} h_t \cdot d\underline{A} = - h_t \iint \rho \underline{u} \cdot d\underline{A} = 0 . \quad (2.10.33)$$

at the steady state. Therefore the specification of constant total enthalpy in the flow field is a solution to the energy equation for flow over a flat plate when the Prandtl number is 1. It should be noted also that the term, $\iint \mu \frac{\partial h_t}{\partial y} dA_y$, is a diffusion term in terms of the total enthalpy, h_t . The energy equation and the momentum equation are therefore similar enough to justify the use of approximately the same time steps for both the energy and momentum equations.

3.0 RESULTS

3.1 FLAT PLATE BOUNDARY LAYER

A laminar boundary layer was calculated in a constant height duct. The boundary layer thickness at the inlet was 15 % of the duct height. The freestream Mach number was 0.43. The inlet velocity profile was the Blasius profile. The absolute viscosity was 0.01 kg/m s. The duct height as 44 mm and the duct length was 112 mm. The geometry and the grid are shown in Fig. 3.1.1. The Reynolds number based upon x varies from 5070 to 11840 along the duct. The duct is 17 inlet boundary layer thicknesses long. Fig. 3.1.2 shows that the development of the velocity profile compares very well with that predicted by theory.

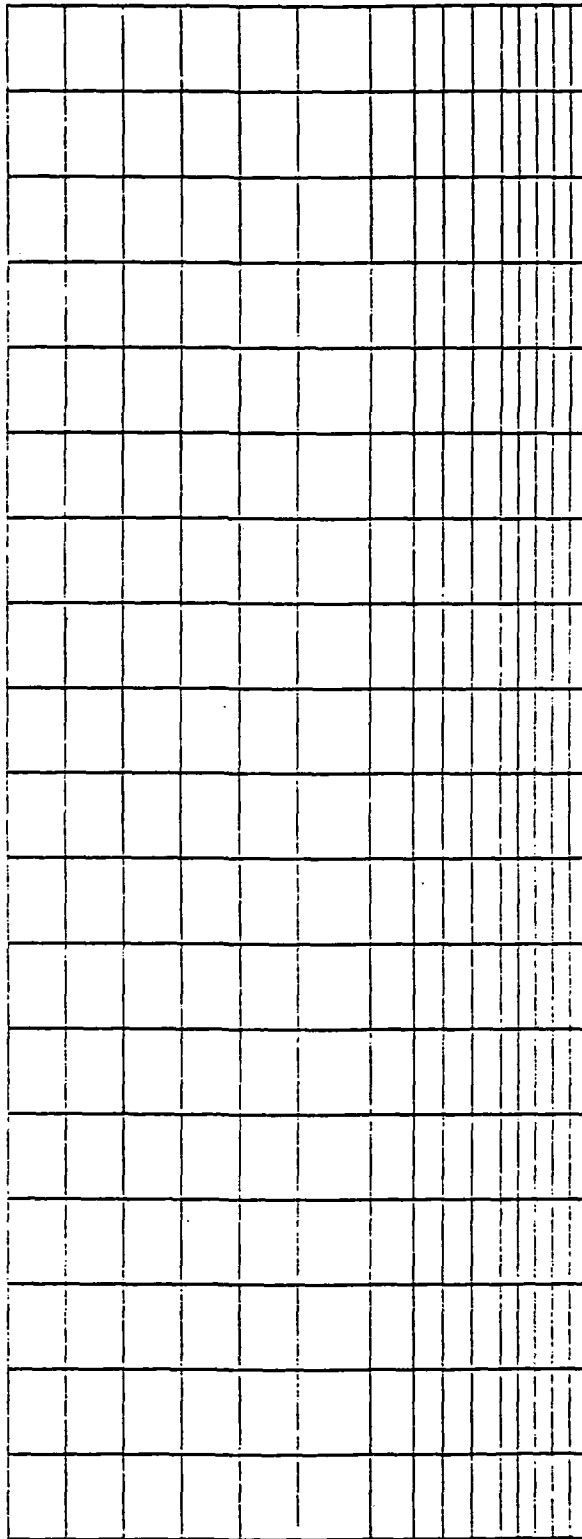


Fig. 3.1.1 Geometry and Grid For Flat Plate Laminar Boundary Layer Calculation

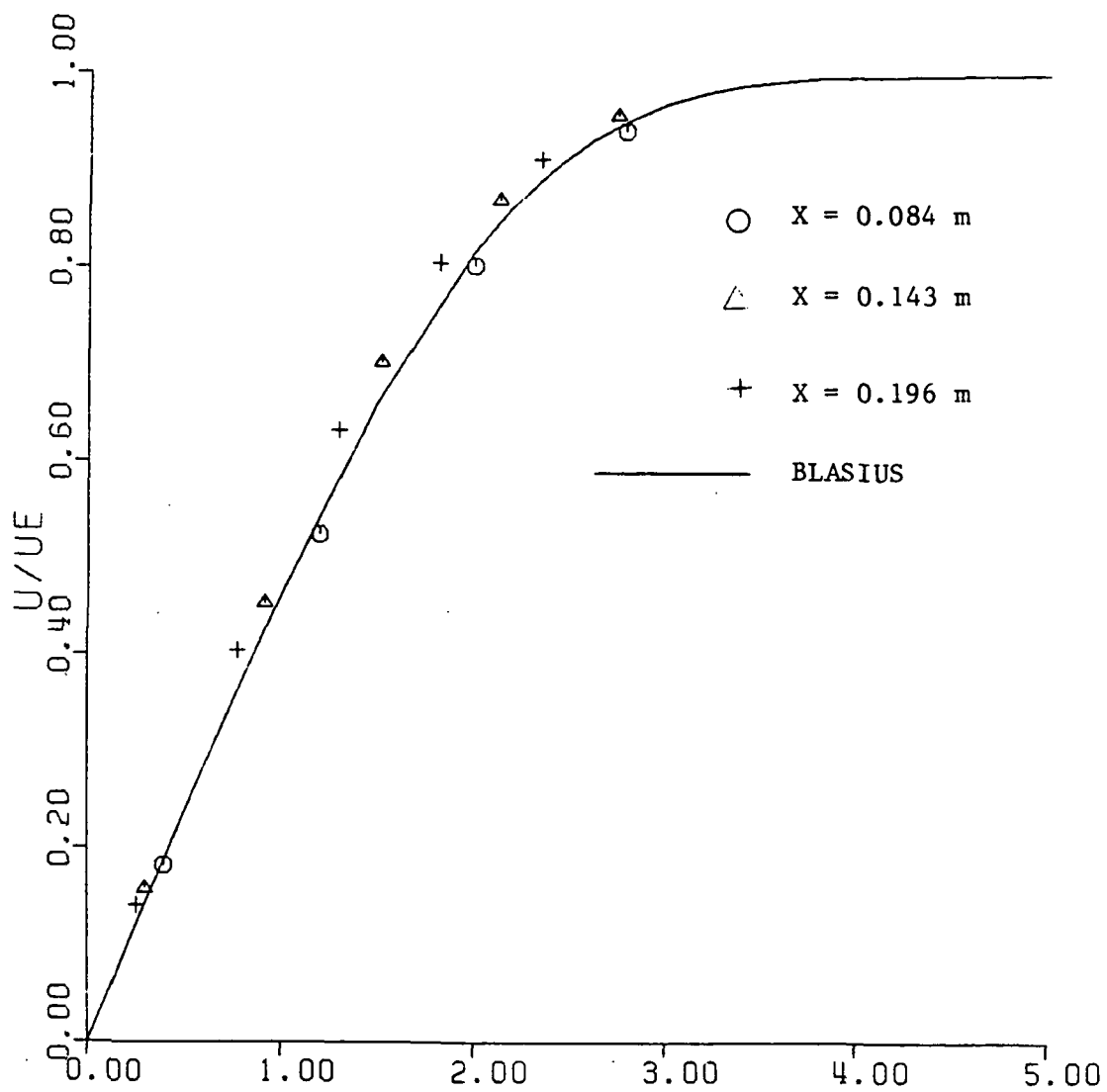


Fig. 3.1.2 Flat Plate Laminar Boundary Layer Velocity Profile

3.2 INVISCID CALCULATIONS OF SAJBEN'S DIFFUSER

Sajben's diffuser (23) will be used here as a test case to illustrate the difference in the results obtained using the effective pressure and effective density methods (see section 2.4). Remember that an effective pressure or an effective density is needed to stabilize the solution procedure for the density update and the pressure update methods, respectively. The calculations in this section were made using a three dimensional finite-volume code derived from the Denton finite volume code (13) now in use at NASA Lewis Research Center. This new code uses the current control volumes (see section 2.2) in a three dimensional configuration.

The geometry and grid used in the calculations are shown in Fig. 3.2.1. There were 34 axial grid points and 10 equally spaced radial grid points. The current calculations are made essentially two dimensional by inputting the coordinates of the diffuser at a very large radius (900 m) in x-r coordinates. The calculations begin at $x/h = -3.6$ and end at $x/h = 7.9$, where h is the throat height. The inlet total pressure is 135 kPa and the inlet total temperature is 300 K. The exit static pressure is 108 kPa. This gives a $P_{exit}/P_{t,inlet} = 0.800$. With these conditions, one dimensional isentropic flow gives a shock with an upstream Mach number of 1.495 at the location marked in Fig. 3.2.1. Multigriding (13) is used to improve the convergence speed.

Fig. 3.2.2 shows a comparison of the effective pressure and the thermodynamic pressure for this test case when the density update method was used. In regions where the flows varies smoothly, the effective pressure and thermodynamic pressure are essentially equal but in regions of the flow where there are large gradients in properties they can be substantially different (up to 10 %). Fig. 3.2.3 shows a comparison of the total pressure through the diffuser calculated using the thermodynamic pressure and the effective pressure. The total pressure calculated from the effective pressure is in much better agreement with the theoretical solution; however, current practice is to

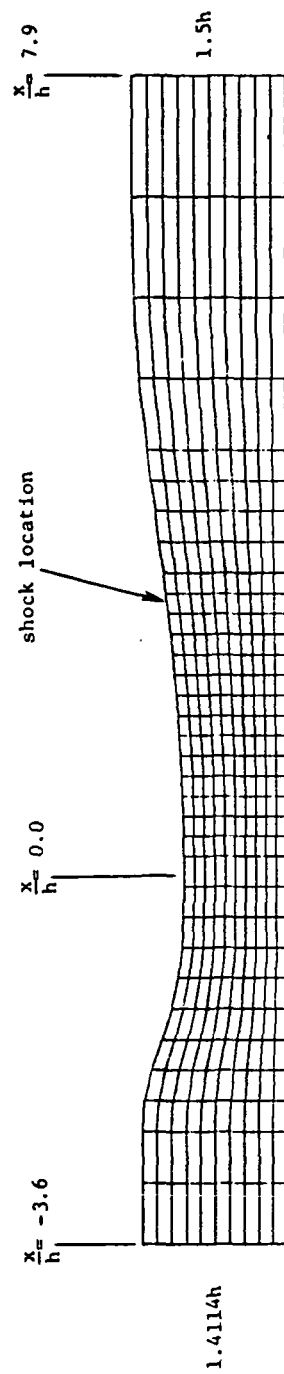


Fig. 3.2.1 Geometry and Grid for Inviscid Calculations of Sajben's Diffuser

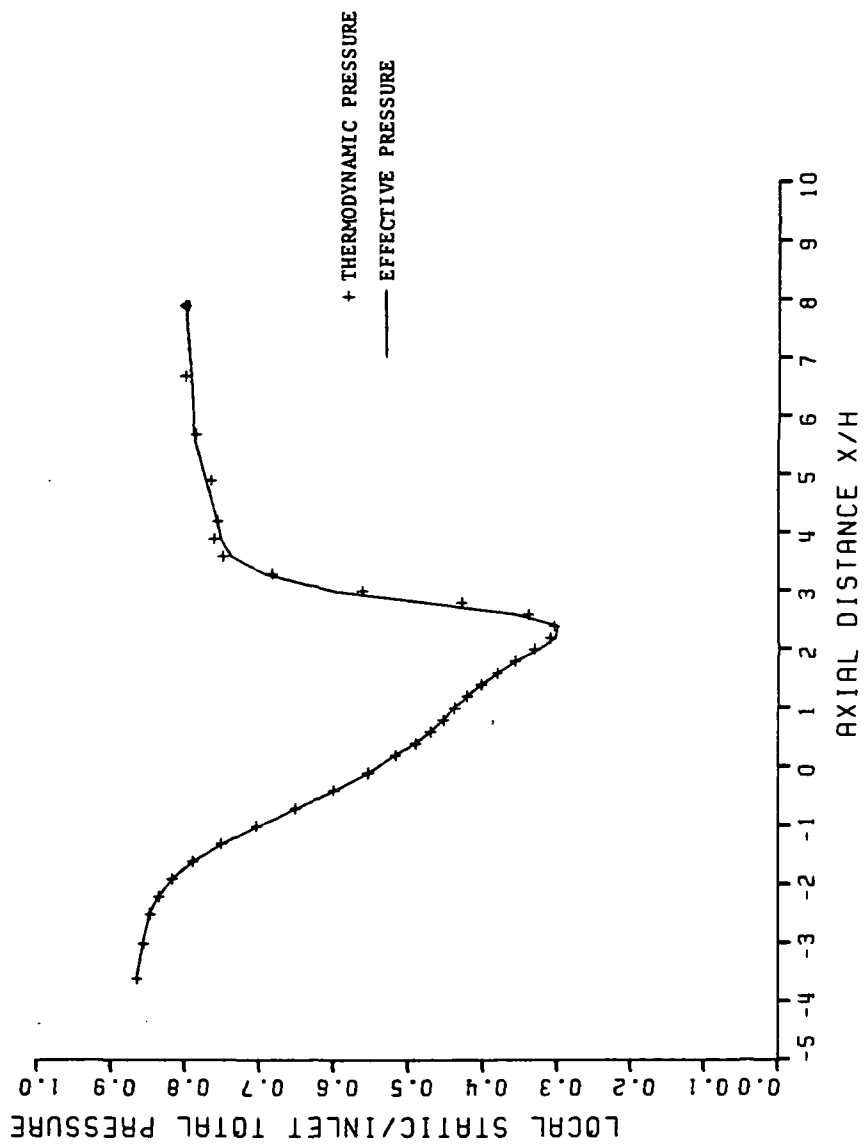


Fig. 3.2.2 Comparison of Static Pressure With Effective Pressure
For Sajben's Diffuser

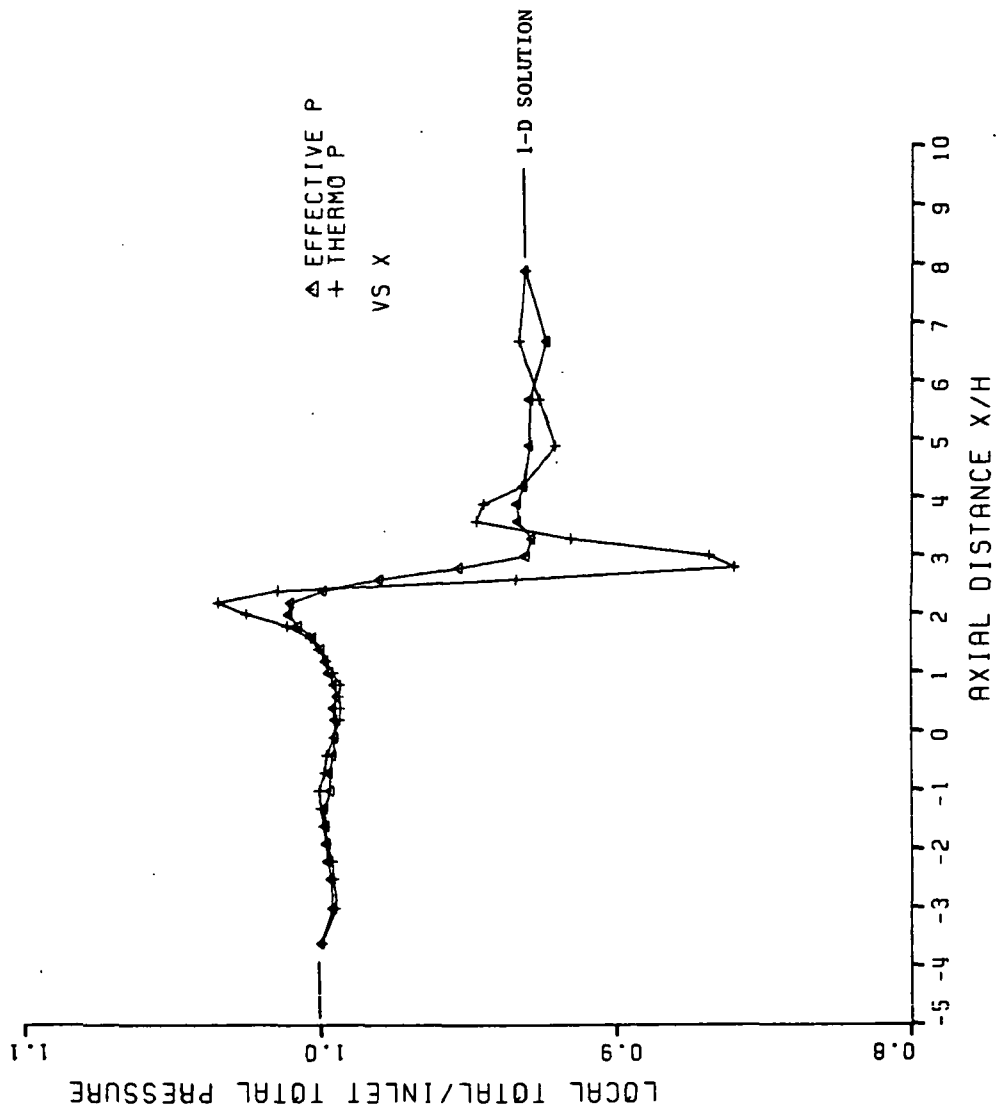


Fig. 3.2.3 Comparison of Total Pressures Calculated Using Thermodynamic and Effective Pressures For Sajben's Diffuser

print out the total pressure calculated from the thermodynamic pressure. The exit $P_{t,exit}/P_{t,inlet}$ is calculated to be .931 for both cases and it agrees well with the one dimensional analytical value of .9304.

Fig. 3.2.4 compares the bottom flat wall static pressures for calculations of transonic flow in Sajben's diffuser using the effective pressure method and the effective density method with the same boundary conditions as specified above. The pressure shown in Fig. 3.2.4 from the density update method is the effective pressure. Fig. 3.2.5 compares the total pressure for these two cases. The effective density method gives a much more uniform total pressure upstream and downstream of the shock; there are no overshoots in total pressure when the effective density method is used

In summary, much better total pressure distributions through shocks are obtained when the interpolated effective pressure, needed to stabilize the density update solution procedure, is used to calculate the total pressure. This simple change largely eliminates the undershoot in total pressure downstream of a shock. Overshoots and undershoots in total pressure can then be further reduced by a factor of 10 by adopting the effective density method rather than the effective pressure method.

3.3 THE INFLUENCE OF TRANSVERSE SMOOTHING ON A STEP PROFILE IN A STRAIGHT DUCT

Transverse smoothing is required in Denton's method with the control volumes shown in Fig. 2.1.2 because there are more grid points across the duct (unknowns) than there are control volumes (equations). Smoothing formulae are used to add non-physical "extra equations". Two forms of transverse smoothing are used in the Denton code; these are linear smoothing, described in Table

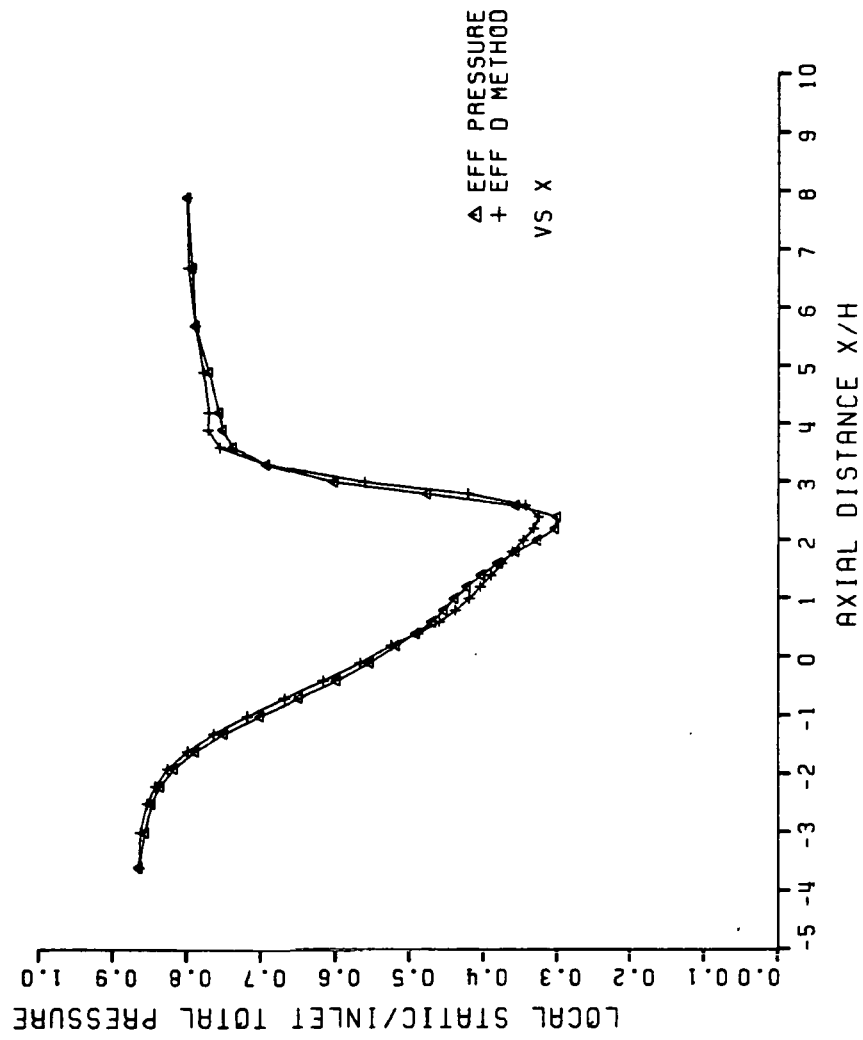


Fig. 3.2.4 Comparison of Static Pressures Calculated Using The Effective Pressure and Effective Density Method's for Sajben's Diffuser

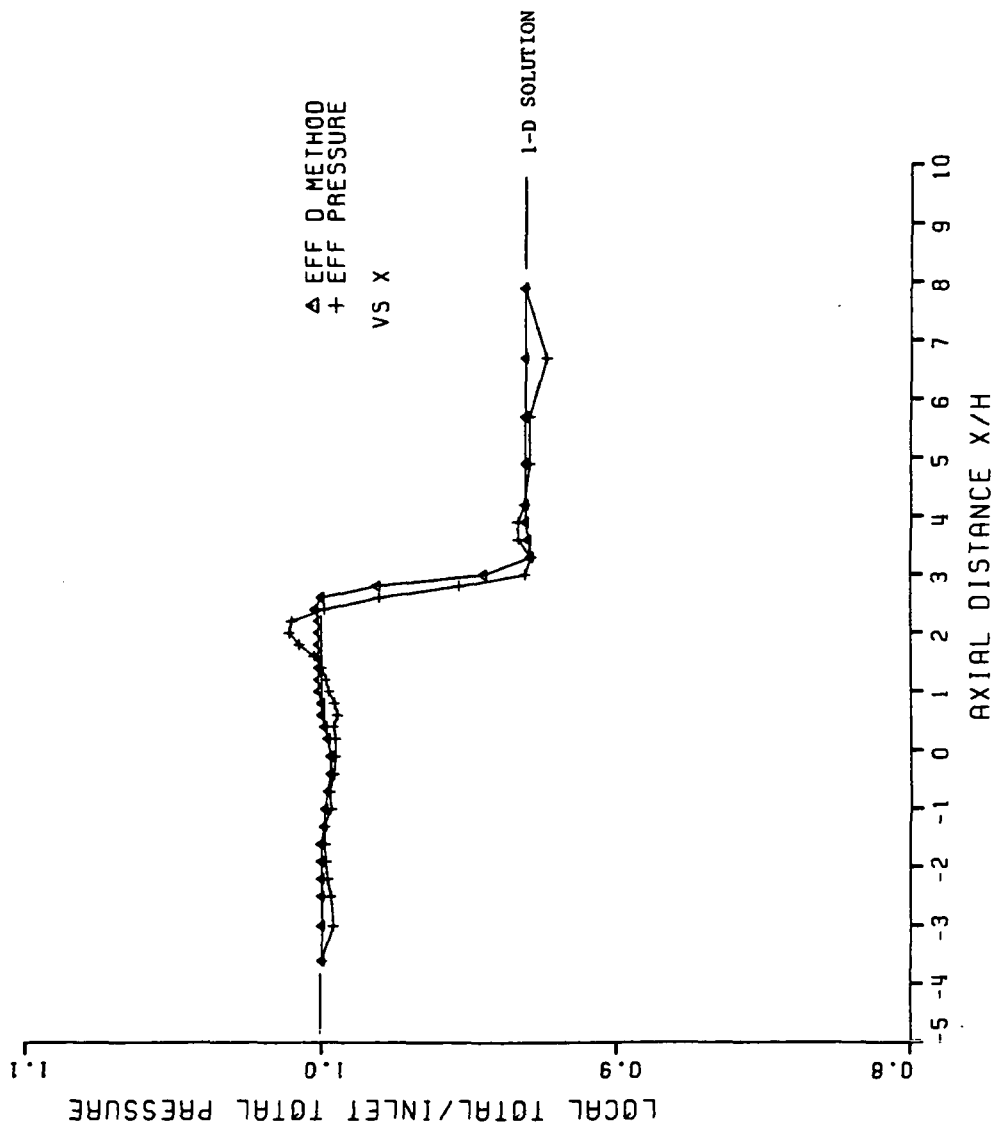


Fig. 3.2.5 Comparison of Total Pressures Calculated Using The Effective Pressure and Effective Density Methods for Sajben's Diffuser

3.3.1, and non-linear smoothing, described in Table 3.3.2 and Fig. 3.3.1. This transverse smoothing of properties cause numerical viscosity to be introduced into the solution when large gradients in the properties are seen across the duct.

For calculations where the gradients across the duct are small, little numerical viscosity would be expected. However, in the boundary layer region of a viscous flow the gradients in properties can be large and this smoothing could cause large numerical viscosity. As a severe test case, calculations were made for a step profile in inlet properties in a straight duct. Both the control volumes used by Denton and the control volumes used in the present work were used in the calculations. The geometry can be seen in Fig. 3.3.2. A step inlet profile of total pressure is specified. The total pressure at the centerline is 135 kPa and the total pressure is reduced to 120 kPa ($P_{t,side}/P_{t,centerline} = 0.889$) at the sides (see Fig. 3.3.3). The exit static pressure in the duct is 108 kPa ($0.8P_{t,centerline}$).

Fig. 3.3.4 shows Mach number profiles at three axial locations along the duct for the case where linear smoothing was used (with $SF = 0.02$). The inlet step profile ($x = 0.0$ m) is quickly altered into a parabolic type profile ($x = 4.0$ m). This parabolic profile then changes relatively little until the end of the duct ($x = 21.0$). Fig. 3.3.5 presents the total pressure distribution along the duct. The step profile causes an almost step change in the total pressure at the beginning of the duct and then the total pressure decreases as in a viscous flow. Fig. 3.3.6 compares the Mach number profiles at the end of the duct for calculations using linear smoothing ($SF = 0.02$) and non-linear smoothing ($SF = 0.02$). Non-linear smoothing did not improve the profile.

Additional calculations were made using the same boundary conditions as above but using the new control volumes and no smoothing. Fig. 3.3.7 compares the inlet Mach number and exit Mach number profiles for this test case. The improvement over the previous results is dramatic. The total pressure distribution has also improved especially along the centerline of the duct as can be seen in Fig. 3.3.8. These results show conclusively that the numerical scheme used to calculate flows with

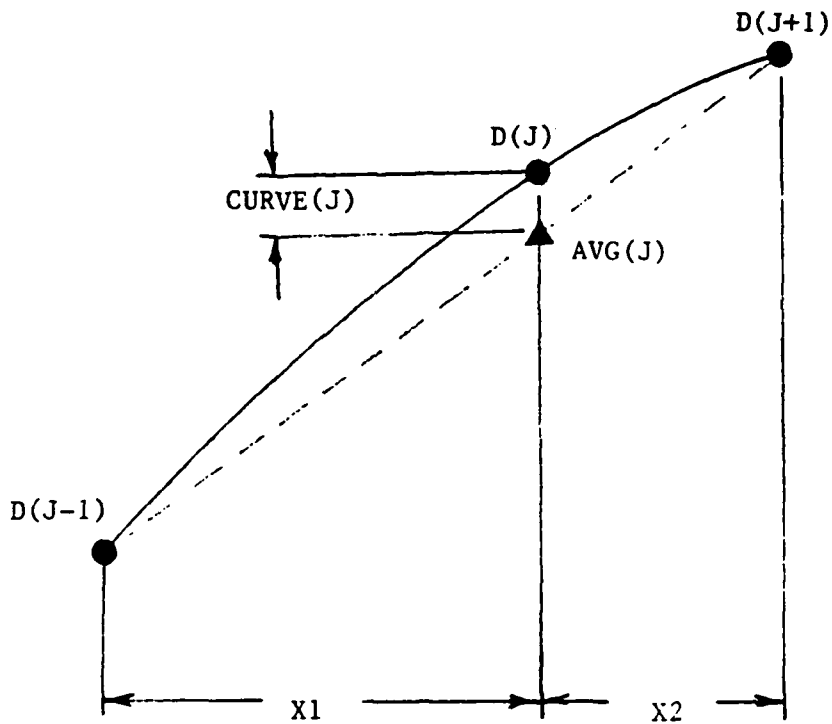
Table 3.3.1 Linear Smoothing of Flow Properties

$$D(J) = (1.-SF) * D(J) + \frac{SF}{2} * (D(J+1) + D(J-1))$$

the variable D at node J is smoothed using this equation. The smoothing factor is SF, typically 0.01 - 0.02. The variables are updated and then smoothed. The variables that are smoothed are ρ , ρ^V_x , ρ^V_r , ρ^V_{θ} , and ρ_e .

Table 3.3.2 Procedure for Non-Linear Smoothing

- 1) an average value of a property D is determined from the neighboring nodes using linear interpolation.
AVG(J) (see Eq. 1 Fig. 3.3.1)
- 2) the difference between the actual and average value of a property D at a node is determined and assigned the variable name CURVE(J). (see Eq. 2 Fig. 3.3.1)
- 3) a variable SCURVE is determined from the average of the variable CURVE from the neighboring nodes.
(see Eq. 3 Fig. 3.3.1)
- 4) the variable D at node I is smoothed using equation 4 in Fig. 3.3.1. The smoothing factor is SF, typically 0.01 - 0.02.
- 5) this non-linear smoothing procedure results in no smoothing added to linearly or parabolically varying properties.



$$FU(J) = X2 / (X1 + X2)$$

$$FD(J) = X1 / (X1 + X2)$$

- 1) $AVG(J) = FD(J) * D(J+1) + FU(J) * D(J-1)$
- 2) $CURVE(J) = D(J) - AVG(J)$
- 3) $SCURVE(J) = FU(J) * CURVE(J-1) + FD(J) * CURVE(J+1)$
- 4) $D(J) = (1 - SF) * D(J) + SF * (AVG(J) + SCURVE(J))$

Fig. 3.3.1 Non-Linear Smoothing

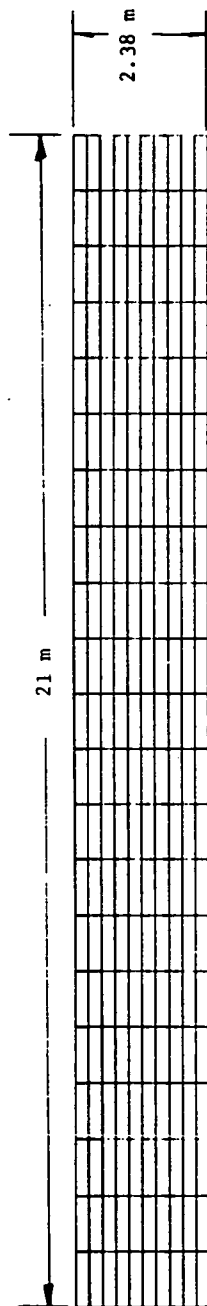


Fig. 3.3.2 Geometry and Grid Used For Step Profile

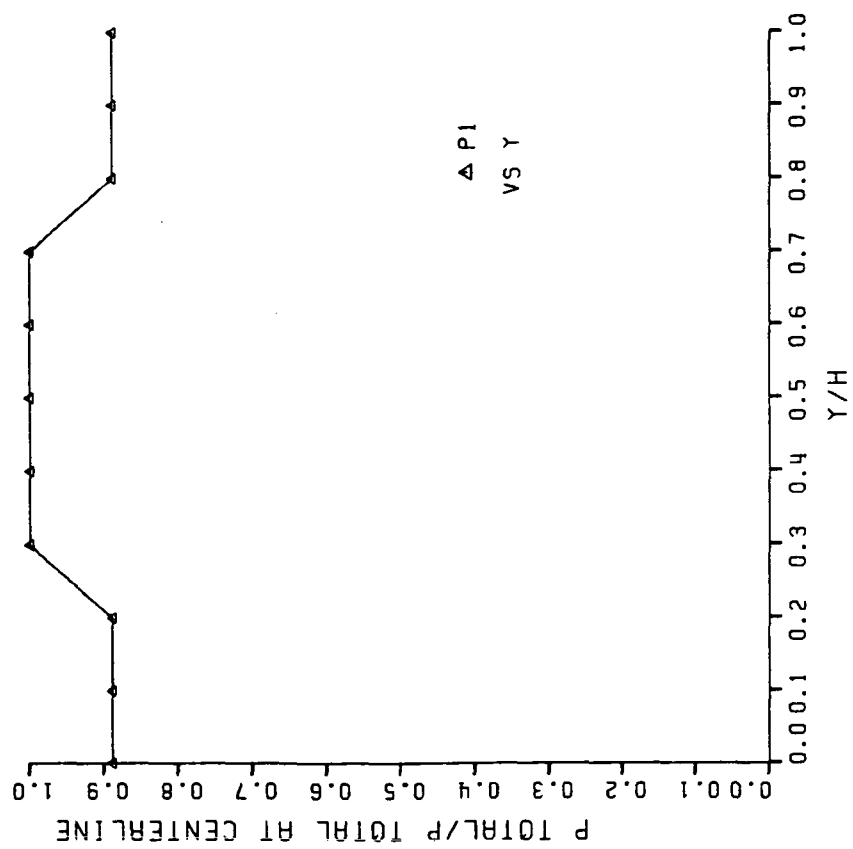


Fig. 3.3.3 Inlet Total Pressure Profile

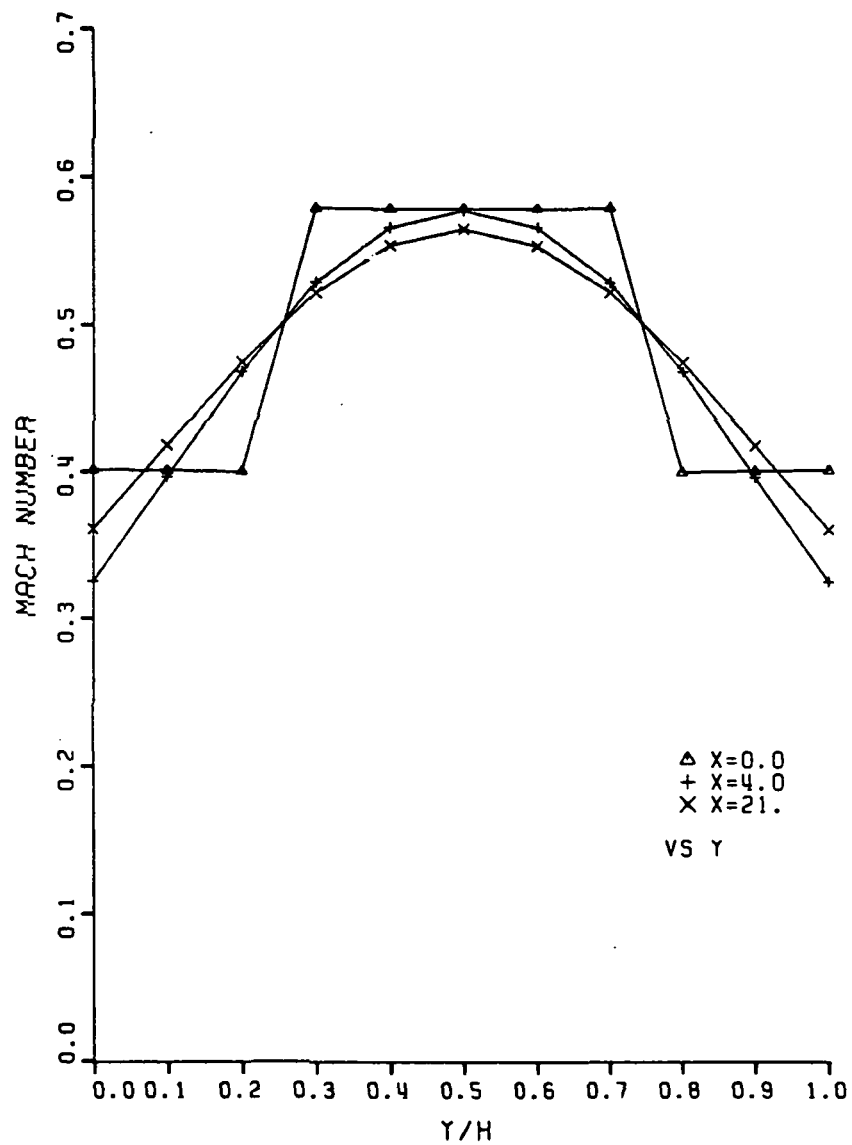


Fig. 3.3.4 Mach Number Profiles At Different Axial Locations With Linear Smoothing

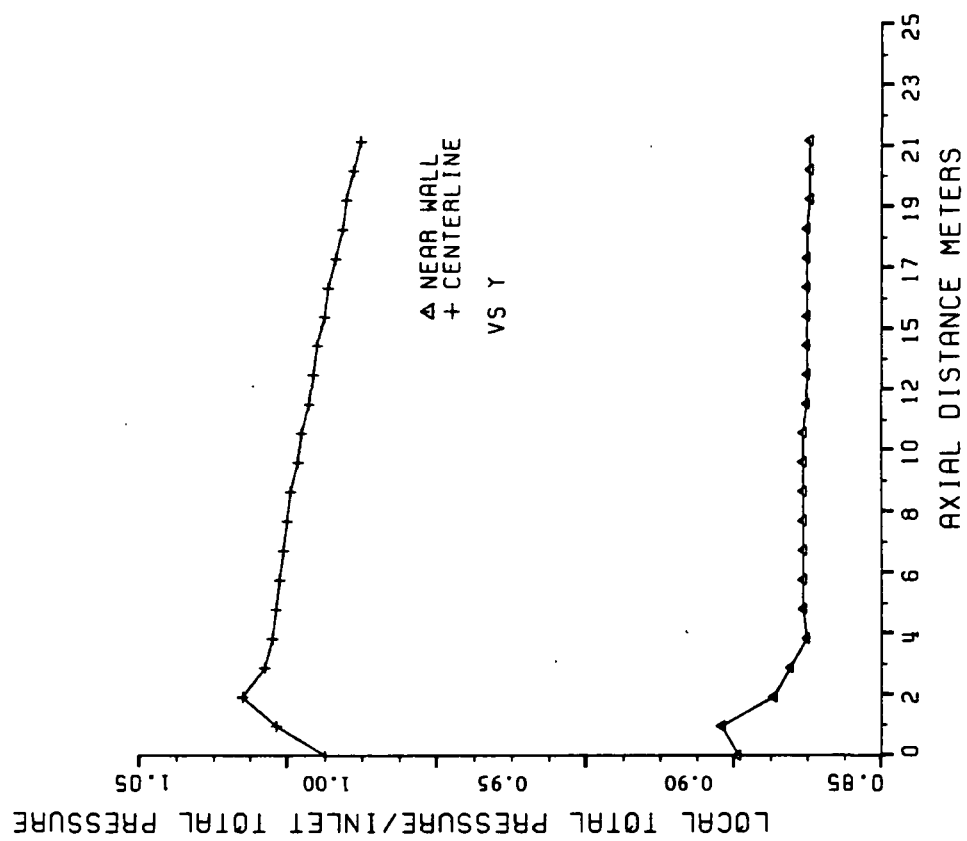


Fig. 3.3.5 Total Pressure Along Grid Lines
With Linear Smoothing

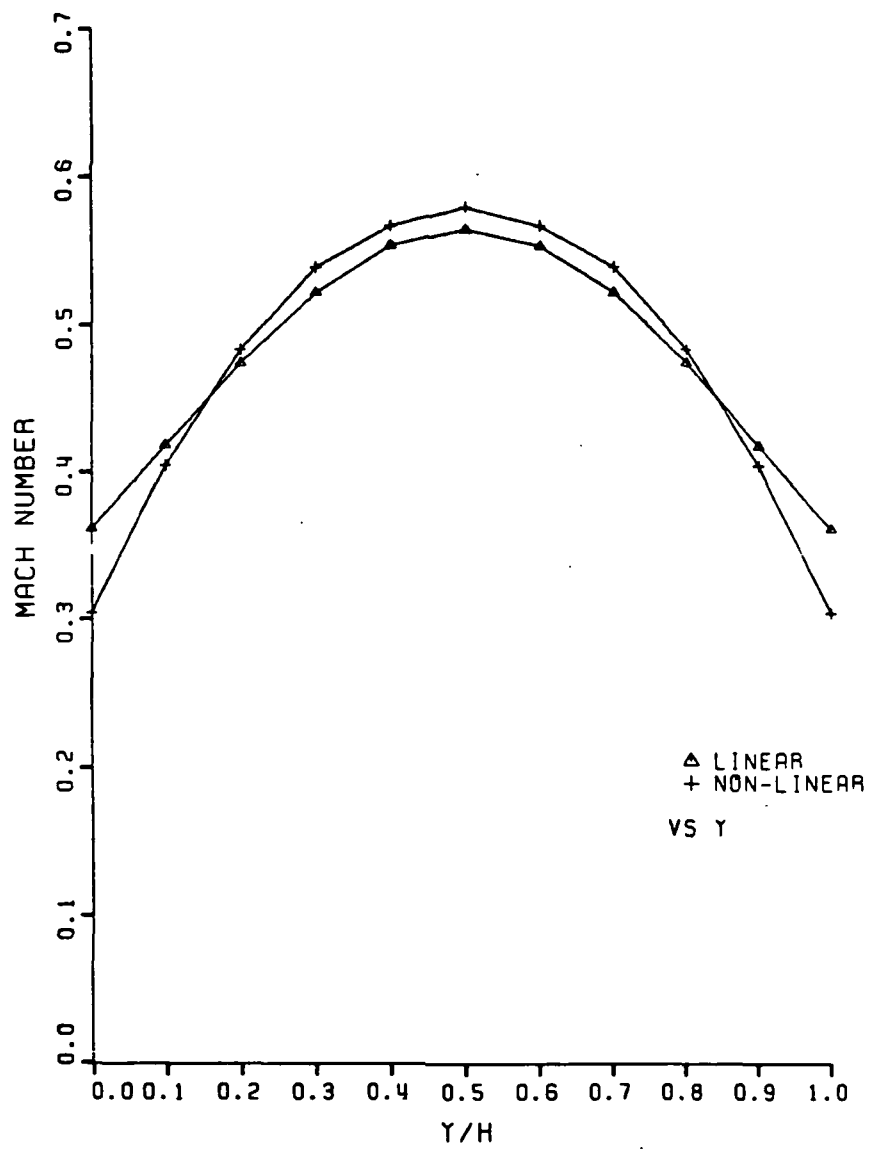


Fig. 3.3.6 Exit Mach Number Profile Comparison
Non-Linear and Linear Smoothing

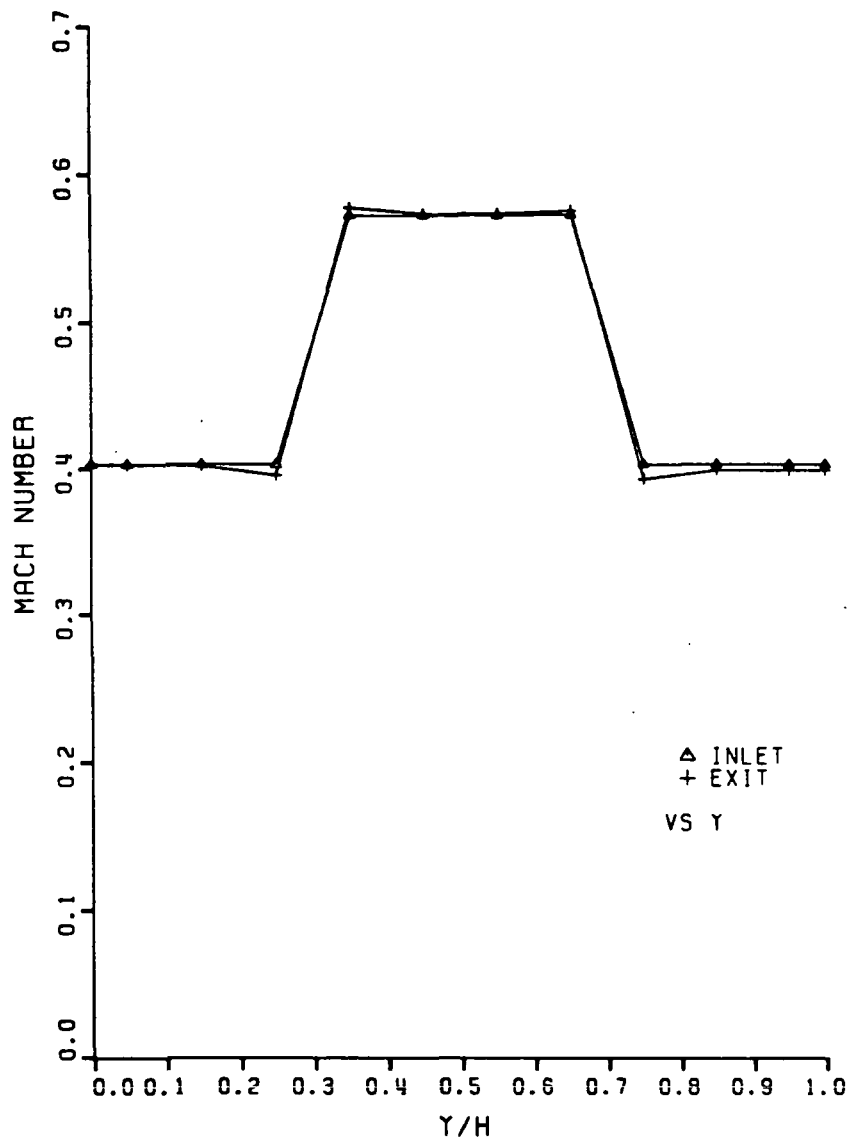


Fig. 3.3.7 Mach Number Profiles At Inlet and Exit
No Smoothing - New Control Volumes

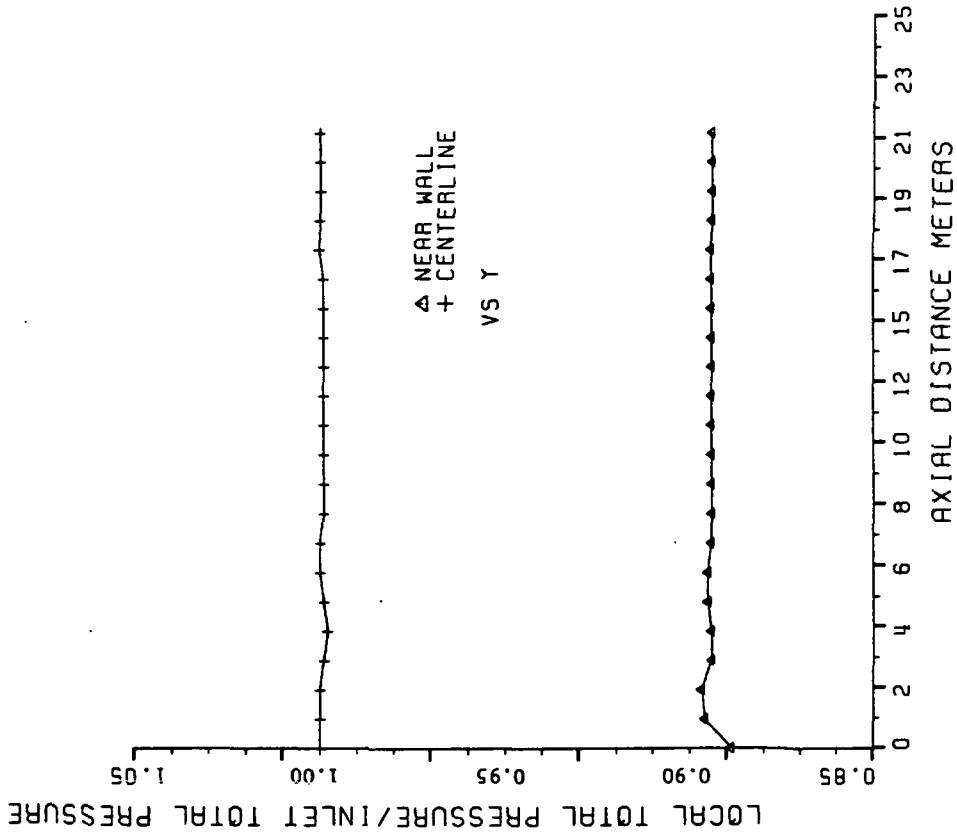


Fig. 3.3.8 Total Pressure Along Grid Lines
No Smoothing - New Control Volumes

large transverse gradients in properties , like those seen in turbulent boundary layers, must not have smoothing of properties in the transverse direction.

3.4 1-D COMPUTATIONAL TESTS OF SHOCK CAPTURING USING PRESSURE INTERPOLATION FORMULAE TO CALCULATE EFFECTIVE DENSITY

DENTON'S 1-D NOZZLE FOR TESTING SHOCK CAPTURING

Denton (12) has tested shock capturing with his finite-volume method in a convergent-divergent nozzle (see Fig. 3.4.1) designed to produce a linear variation of Mach number with distance for 1-D isentropic flow. The equation for the Mach number variation with distance is

$$x = 10. + 45.(M - 1) . \quad (3.4.1)$$

Denton considered flow which began at $x = 1$, where the Mach number was 0.8 and ended at $x = 46$, where the Mach number was 1.8. The throat ($M = 1.0$) was located at $x = 10$. He used three back pressures with $P_{exit}/P_{t,inlet} = 0.85, 0.80$, and 0.75 , respectively. The theoretical 1-D solutions for these flows are shown in Fig. 3.4.2. The maximum Mach numbers, just upstream of the shock , are 1.268, 1.455, and 1.578, respectively. This is a range of shock Mach numbers typical of turbomachinery flows.

These three pressure ratios are used with Denton's 1-D nozzle to test shock capturing with three of the pressure interpolation methods discussed in Section 2.4 (Pressure Interpolation).

DENTON 1D EXAMPLE

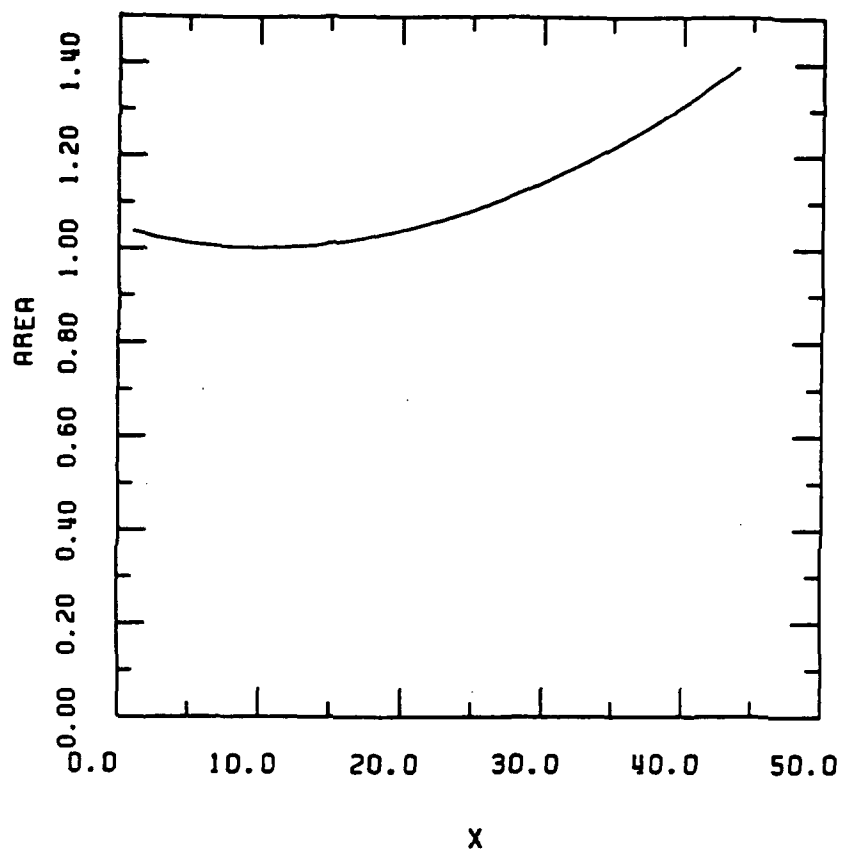


Fig. 3.4.1 Denton's Convergent-Divergent Nozzle With a Linear Variation of Mach Number With Distance

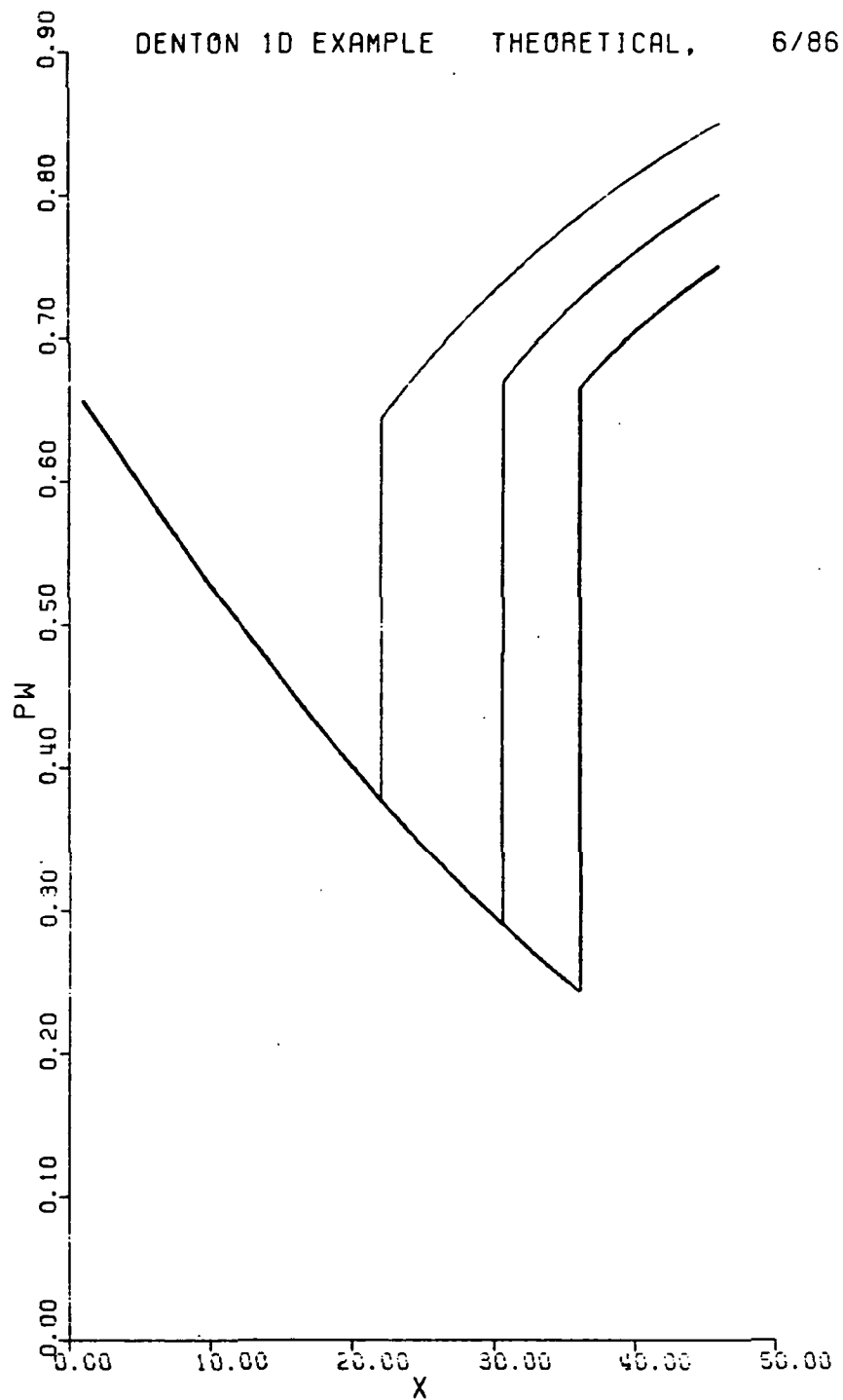


Fig. 3.4.2 Theoretical 1-D solutions for Denton's nozzle
for three exit static pressures at $x = 46.$,
 $P_{\text{exit}}/P_{t,\text{inlet}} = 0.85, 0.80, \text{ and } 0.75.$

Fig. 3.4.2a $PW = P/P_{t,\text{inlet}}$.

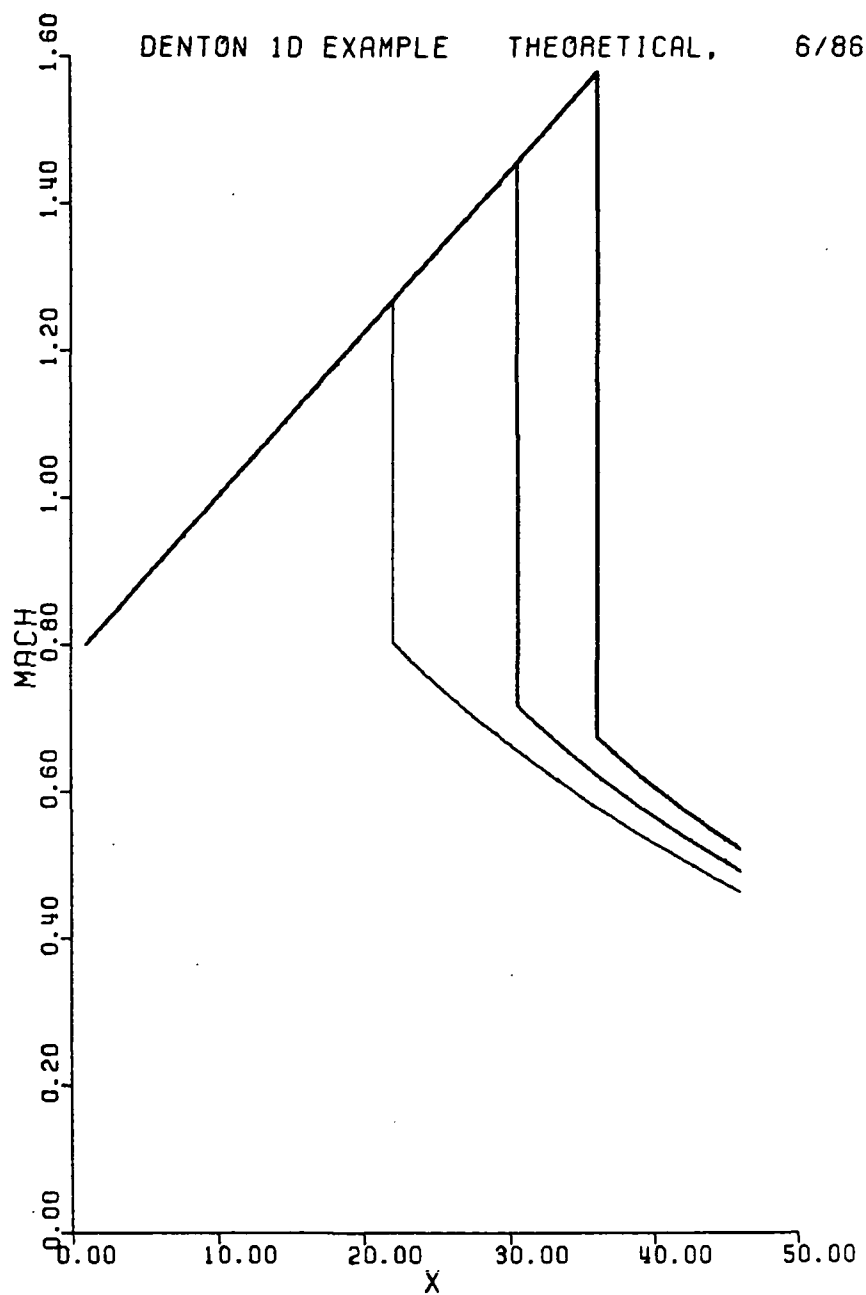


Fig. 3.4.2b Mach Number

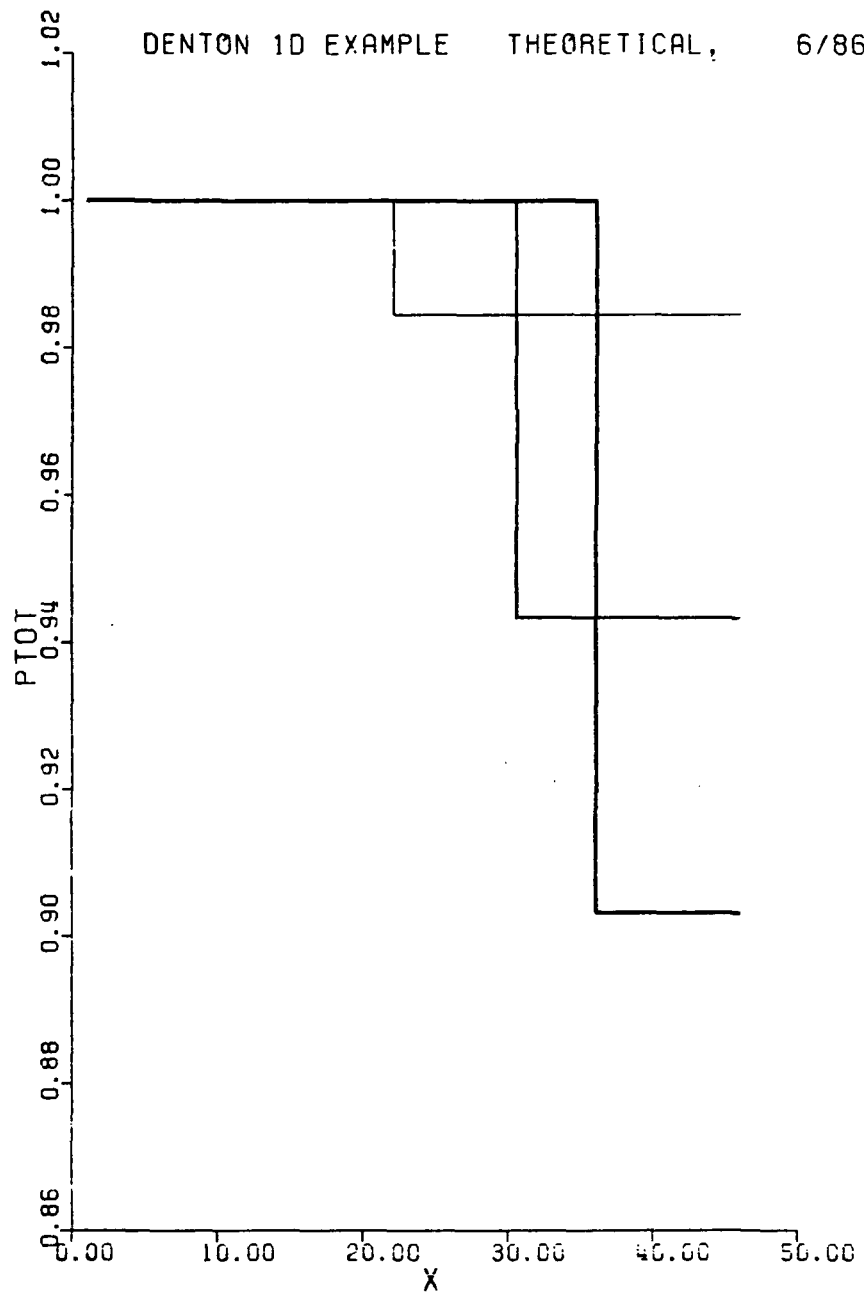


Fig. 3.4.2c $PTOT = P_t / P_{t,inlet}$

PRESSURE INTERPOLATION SCHEMES

The effective density method used in the current work uses an interpolated approximation for the pressure in the evaluation of the density. A general form of the interpolation formula considered in this thesis is

$$P_{i+1}^e = P_i + a_0(P_{i+1} - P_i) + \frac{a_1}{2}(P_{i+1} - P_{i-1}) + \frac{a_2}{3}(P_{i+1} - P_{i-2}) \quad (3.4.2)$$

and this is used to evaluate the density as

$$\rho_{i+1} = \frac{P_{i+1}^e}{RT_{i+1}} \quad (3.4.3)$$

This general form is a linear combination of a single-point interpolation, $P_{i+1} - P_i$, a 2 - point interpolation, $P_{i+1} - P_{i-1}$, and a 3 - point interpolation, $P_{i+1} - P_{i-2}$. The single-point interpolation, of course, really gives the correct perfect gas equation and involves no approximation.

The coefficients a_0 , a_1 , and a_2 are here taken to be constants or functions of Mach number. Combinations, including individual terms or pairs of terms, for which the sum of the coefficients

$$a_0 + a_1 + a_2 = 1$$

are second order accurate, as shown in Appendix A.

Correct Perfect Gas Equation ($a_1 = 0$, $a_2 = 0$, and $a_3 = 0$)

This scheme has the advantage that it involves no interpolation or approximation for the pressure. Experience has shown that it is stable for subsonic flow. But the stability analysis of Section 2.4 shows that for Mach numbers above about 1.2 this scheme becomes unstable. Thus it could not be used for the test cases of Denton's 1-D nozzle.

These observations about the use of the correct perfect gas equation are in agreement with Denton's findings for his scheme B (12). In that method changes in density were sent to the upstream corners of the element, which is equivalent to our sending pressure changes upstream. The method "proved stable, without any correction factors or damping, at low Mach numbers but instability was found to develop at Mach numbers around unity and above."

2-Point Interpolation ($a_0 = 0, a_1 = 1, a_2 = 0$)

The stability analysis presented in Section 2.4 shows the 2-point scheme to be stable for Mach numbers up to about 2.0. Use of a 2-point scheme or a 3-point scheme has been suggested by Denton in his recent ASME and AGARD Lecture Notes (13,14).

3-Point Interpolation ($a_0 = 0, a_1 = 0, a_2 = 1$)

3-point schemes have been shown in Section 2.4 to be the most conservative (in terms of stability) of the schemes considered in this thesis. Perhaps for this reason, such a method is used to stabilize the current NASA version of the Denton code. Both 2-point and 3-point schemes provide second order accuracy for a continuously changing pressure; they give correct interpolation values for linear variations in pressure (assuming equally spaced grid points).

M&M Mach Number Dependent Interpolation

The advantages of the three schemes just considered are :

1. the accuracy and stability of the perfect gas equation for subsonic flow;
2. the stability of the 3-point interpolation at Mach numbers greater than 2.0;
3. the stability and reduced smearing of properties of the 2-point interpolation at supersonic Mach numbers up to 2.0.

These advantages have been combined in a single Mach number dependent interpolation scheme in Section 2.4.

In this method

$$a_0 = \frac{0.8}{3} \left(\frac{4}{M^2} - 1 \right)$$

$$a_1 = 1 - a_0 \quad M < 2.0$$

$$a_2 = 0$$

$$a_0 = 0$$

$$a_1 = \frac{4}{M^2} \quad M \geq 2.0$$

$$a_2 = 1 - a_1 \quad (3.4.4)$$

The values of the three coefficients are shown graphically in Fig. 3.4.3. Note, once again, that the sum of the coefficients is equal to one for all Mach numbers, so that this scheme is also second order accurate. For the calculations presented here M was taken as the larger of M on the upstream and downstream side of the control volume.

COMPUTATIONAL TESTS OF THREE PRESSURE INTERPOLATION SCHEMES

Of the four schemes just considered, three are stable in the Mach number range 1.0 to 2.0. These are the 2-point, 3-point, and M&M interpolation methods. In this section, results of shock capturing with these three methods are presented and compared for Denton's 1-D nozzle.

The one-dimensional calculations were performed with 46 axial grid points with an equal axial spacing between grid points of 1 unit. The inlet Mach number was 0.8. The ratio of specific heats,

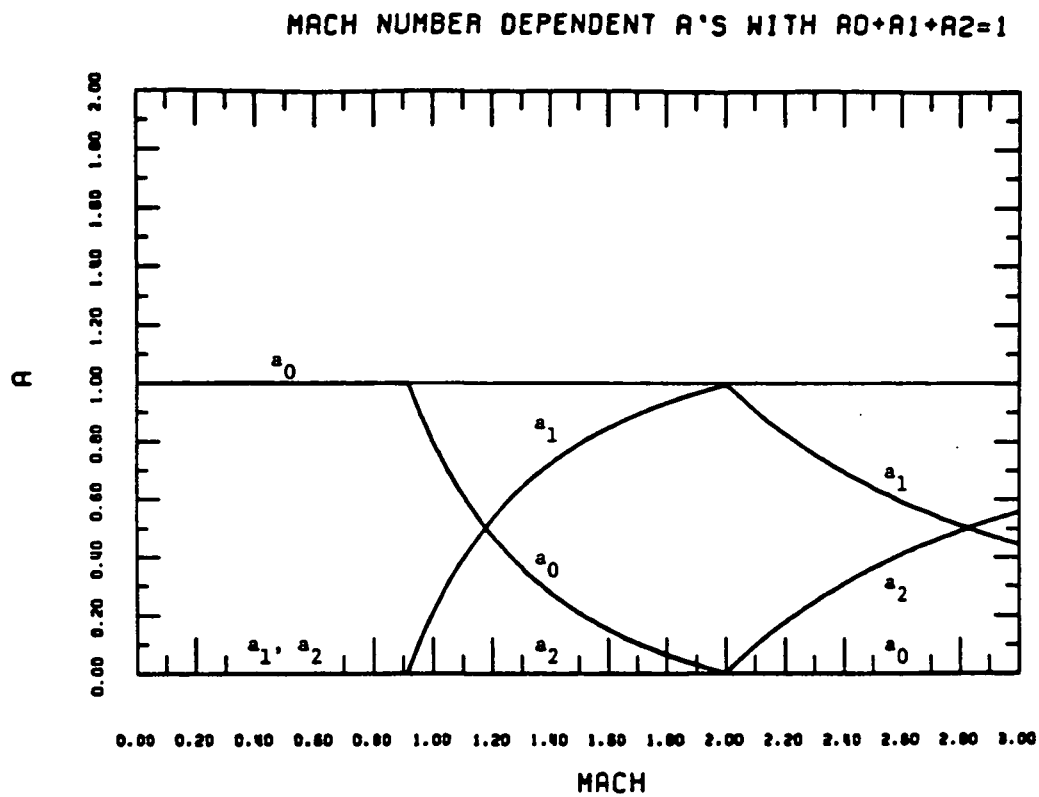


Fig. 3.4.3 M&M Mach Number Dependent Values For The Coefficients in Eq. 3.4.2.

γ , was 1.4 and the gas constant , R , was 287. J/kg K. Calculations were made with $P_{exit}/P_{t,inlet}$ of 0.85, 0.80, and 0.75.

The variations of static pressure , Mach number, and total pressure are plotted for each interpolation scheme using the same scales as for the theoretical solutions which can be seen in Fig. 3.4.2. Fig. 3.4.4 shows the results for the 3-point scheme, Fig. 3.4.5 for the 2-point scheme, and Fig. 3.4.6 for the M&M method. The results from the 3-point and M&M schemes are shown together with the theoretical solution on Fig. 3.4.7 for the pressure ratio of 0.80.

The calculated values of maximum Mach numbers upstream of the shock and total pressure ratios are compared with the values from the theoretical 1-D solutions in Table 3.4.1.

The total pressure ratios across the shocks are well calculated by all three interpolation formulae as shown in Table 2b. This is in spite of the fact that the calculated values for the maximum Mach number upstream of the shocks are significantly different from the theoretical values. For example, at the lowest back pressure, the theoretical Mach number upstream of the shock is 1.578 while the 3-point interpolation formula gives 1.501, the 2-point formula gives 1.526, and the M&M formula gives 1.533. For this case the calculated values of total pressure ratio are 0.9029, compared with the theoretical value of 0.9032. In general the M&M formula gives the closest agreement with the upstream Mach number while the 3-point formula gives the worst results. Based on the maximum calculated upstream Mach number for these cases , the M&M formula would give shock losses from 16 to 41 percent too small, while the 3-point formula would give values from 27 to 67 percent too small. Interestingly the agreement for shock losses based on maximum upstream Mach number improves (for all three formulae) as the Mach number increases. However, these results show that the peak calculated Mach number should not be used to predict shock losses and that the calculated total pressure loss across the shock is accurate to better than 0.1% and it should be used.

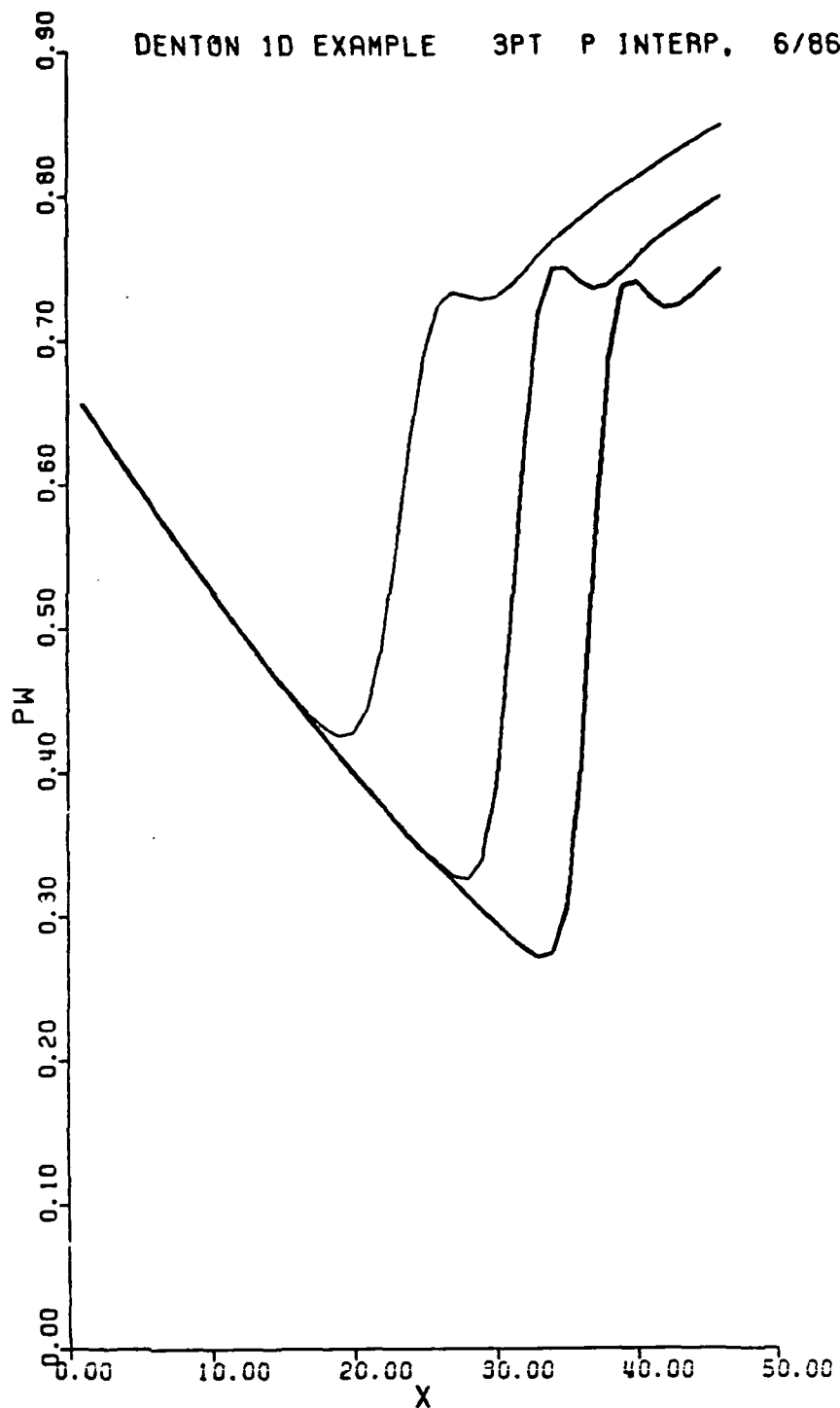


Fig. 3.4.4 Calculated 1-D Solution for Denton's Nozzle
Using 3-Point Interpolation, Eq. 3.4.2 With
 $a_0 = a_1 = 0$ and $a_2 = 1$.
Calculations For Three Exit Static Pressures at
 $x=46.$, $P_{\text{exit}}/P_{t,\text{inlet}} = 0.85, 0.80, \text{ and } 0.75$.

Fig. 3.4.4a $PW = P/P_{t,\text{inlet}}$

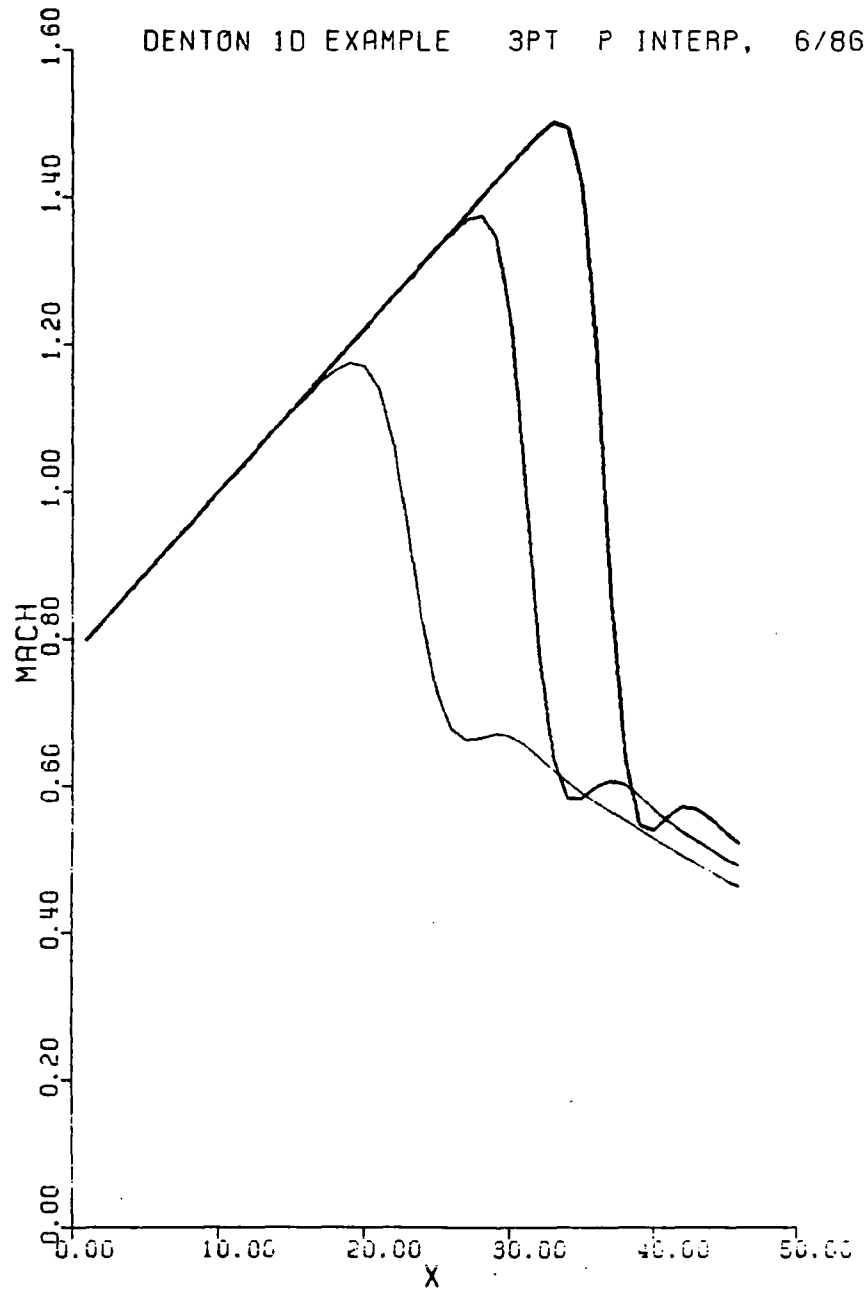


Fig. 3.4.4b Mach number.

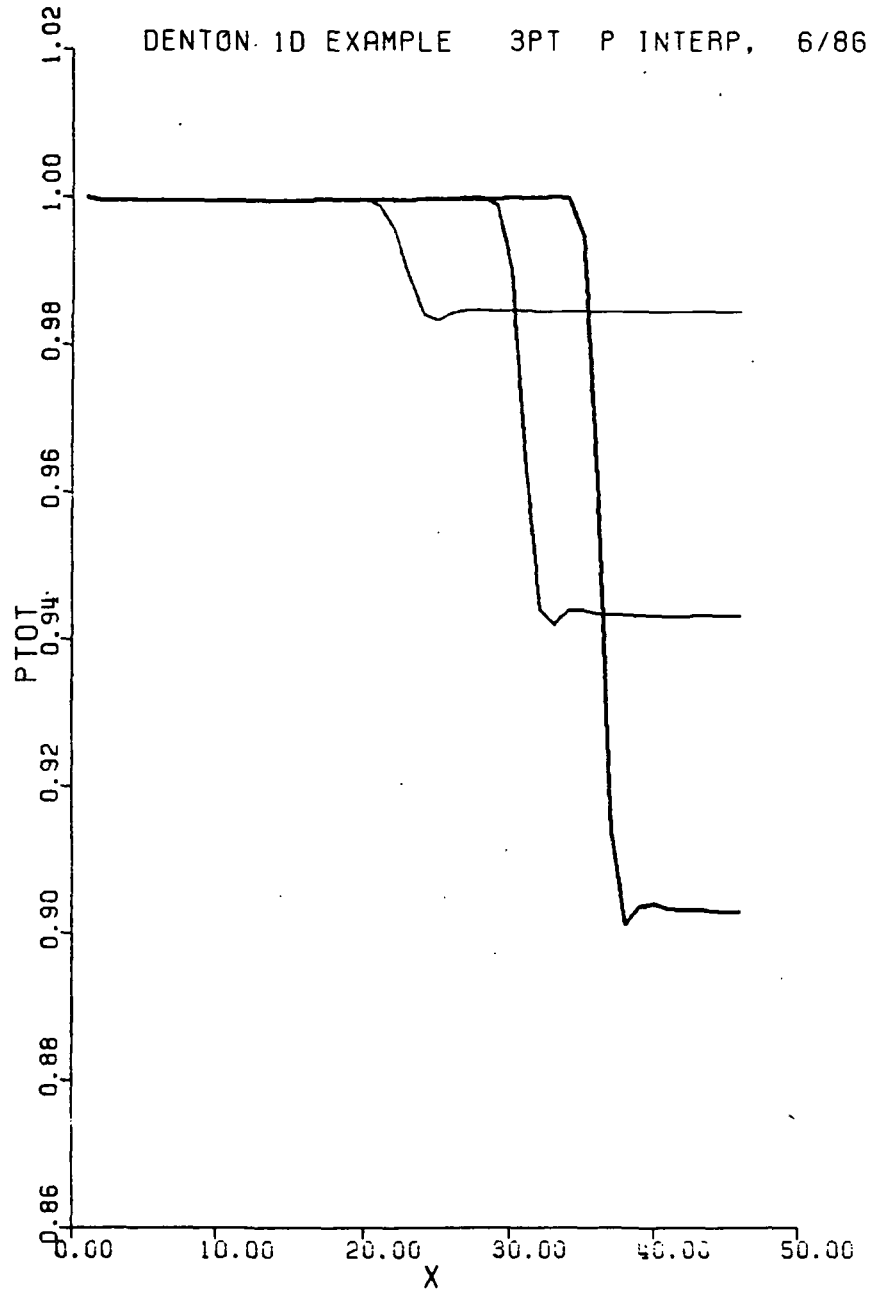


Fig. 3.4.4c $PTOT = P_t / P_{t,inlet}$

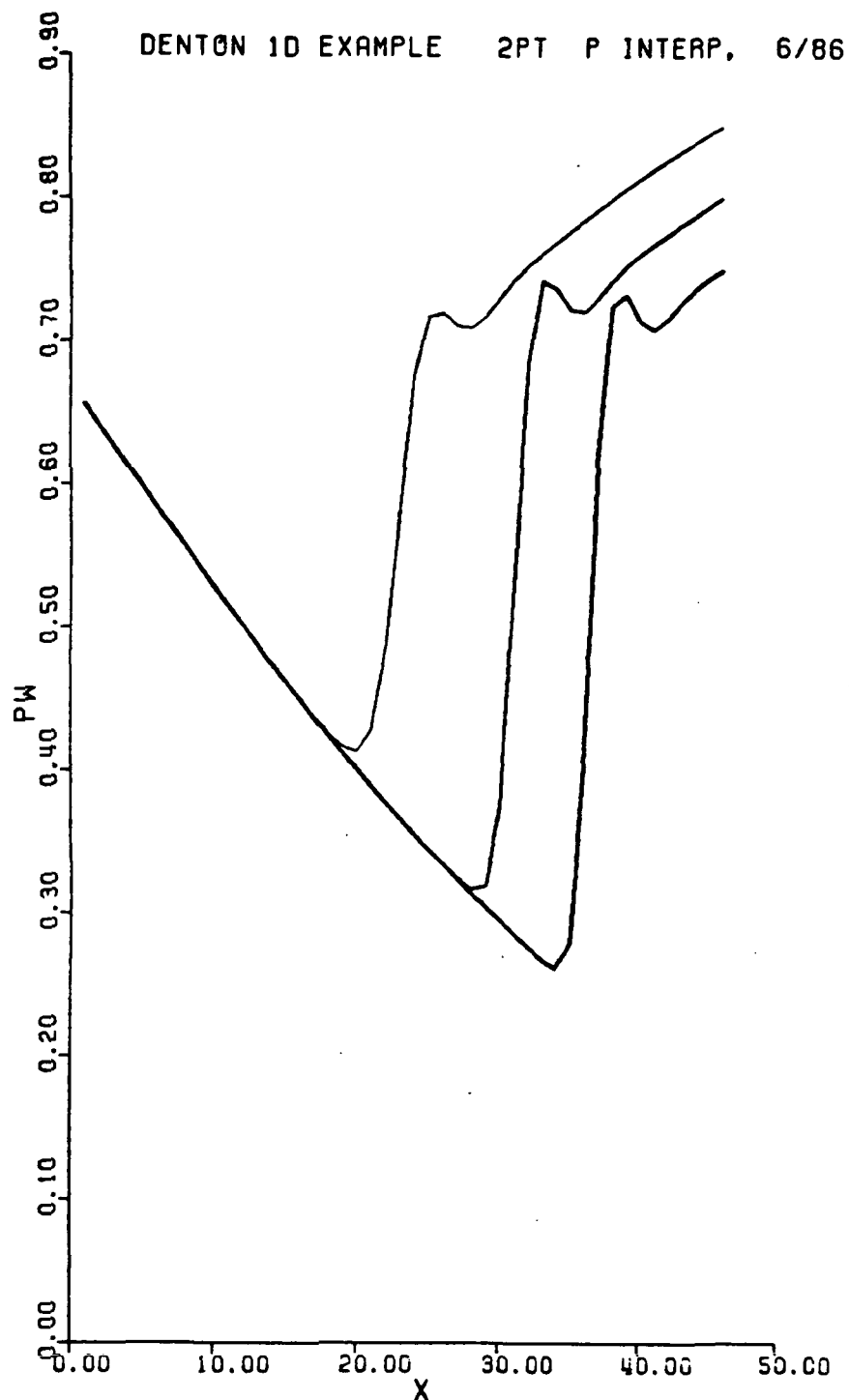


Fig. 3.4.5 Calculated 1-D Solution For Denton's Nozzle
Using 2-Point Interpolation, Eq. 3.4.2 with
 $a_0 = a_2 = 0$ and $a_1 = 1$.
Calculations For Three Exit Static Pressures At
 $x=46.$, $P_{\text{exit}}/P_{t,\text{inlet}} = 0.85, 0.80, \text{ and } 0.75$.

Fig. 3.4.5a $PW = P/P_{t,\text{inlet}}$

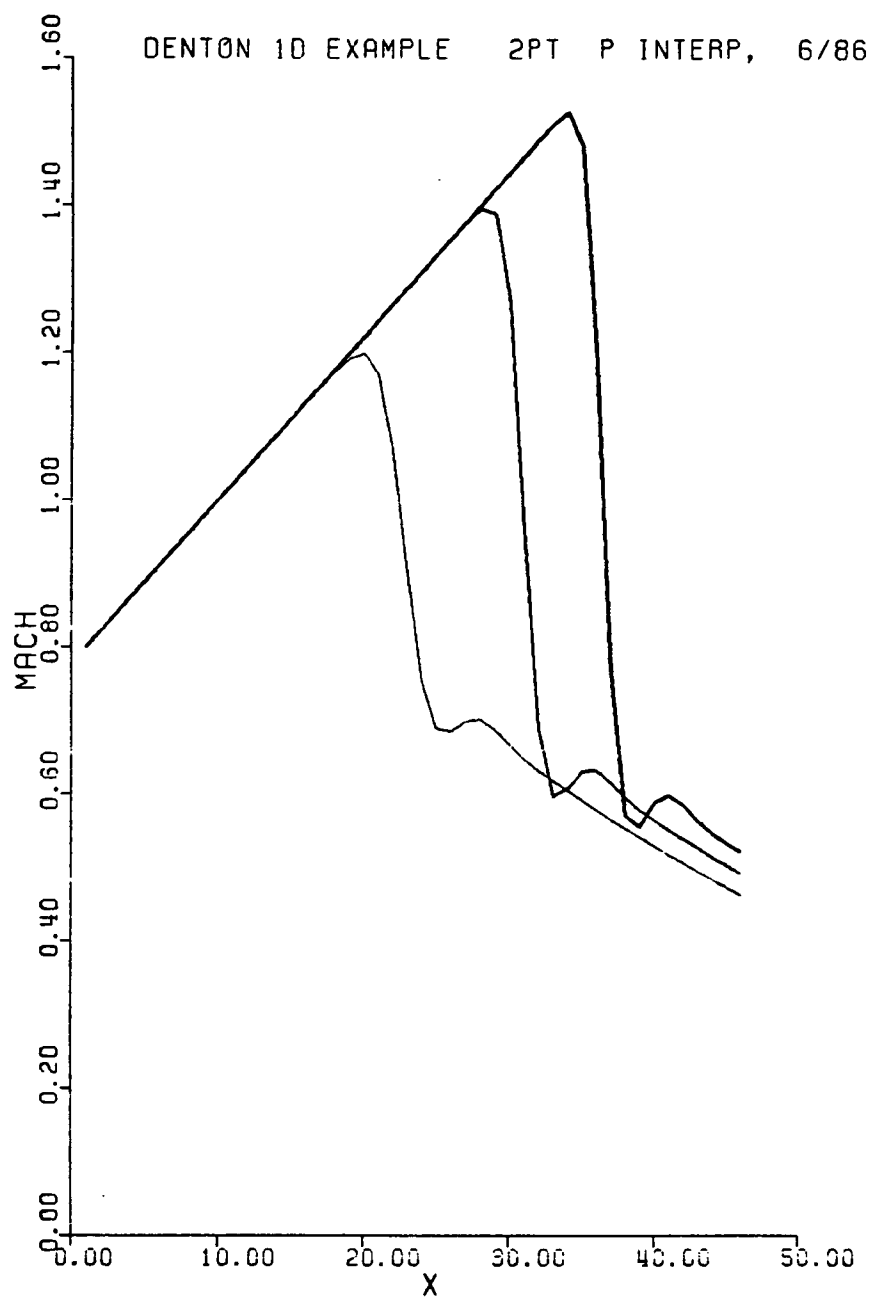


Fig. 3.4.5b Mach number.

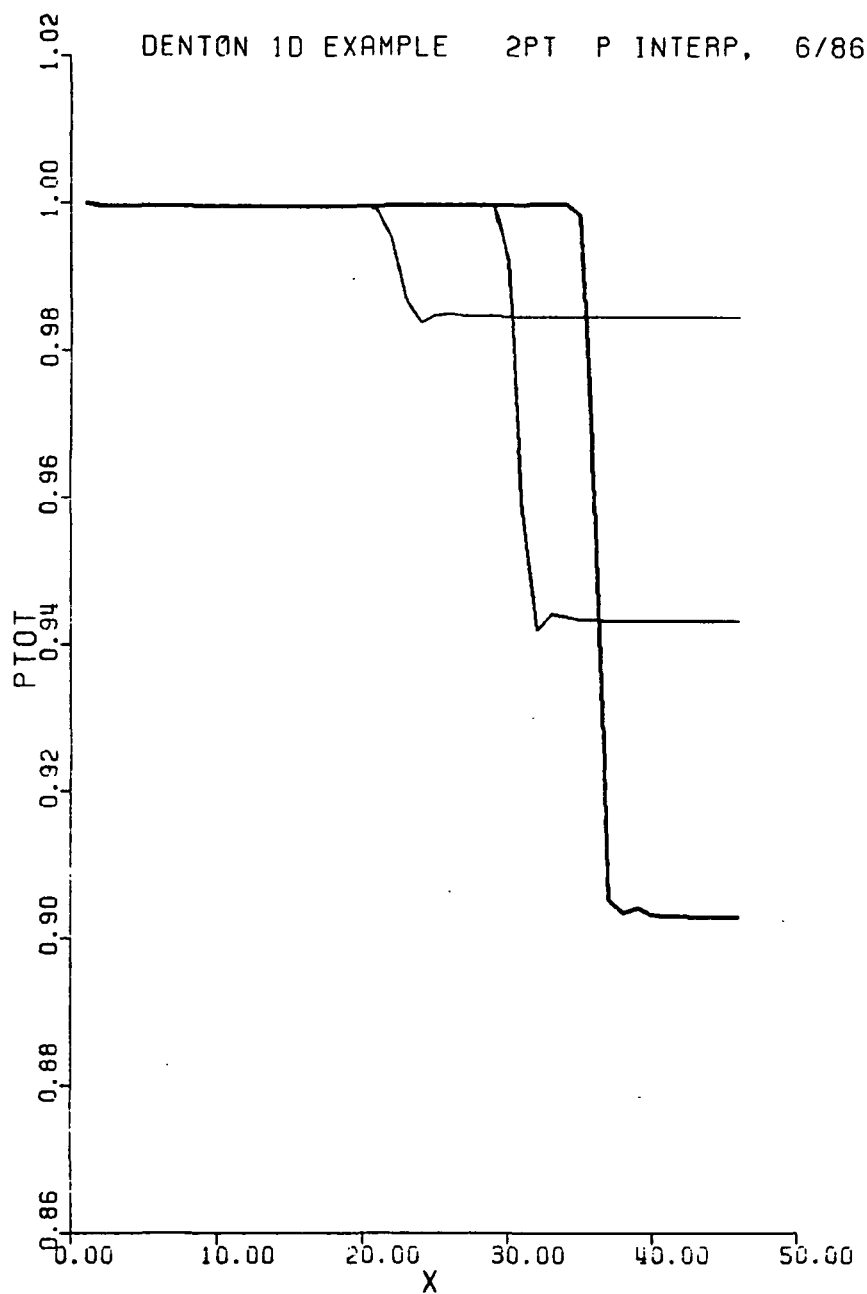


Fig. 3.4.5c $PTOT = P_t / P_{t,inlet}$

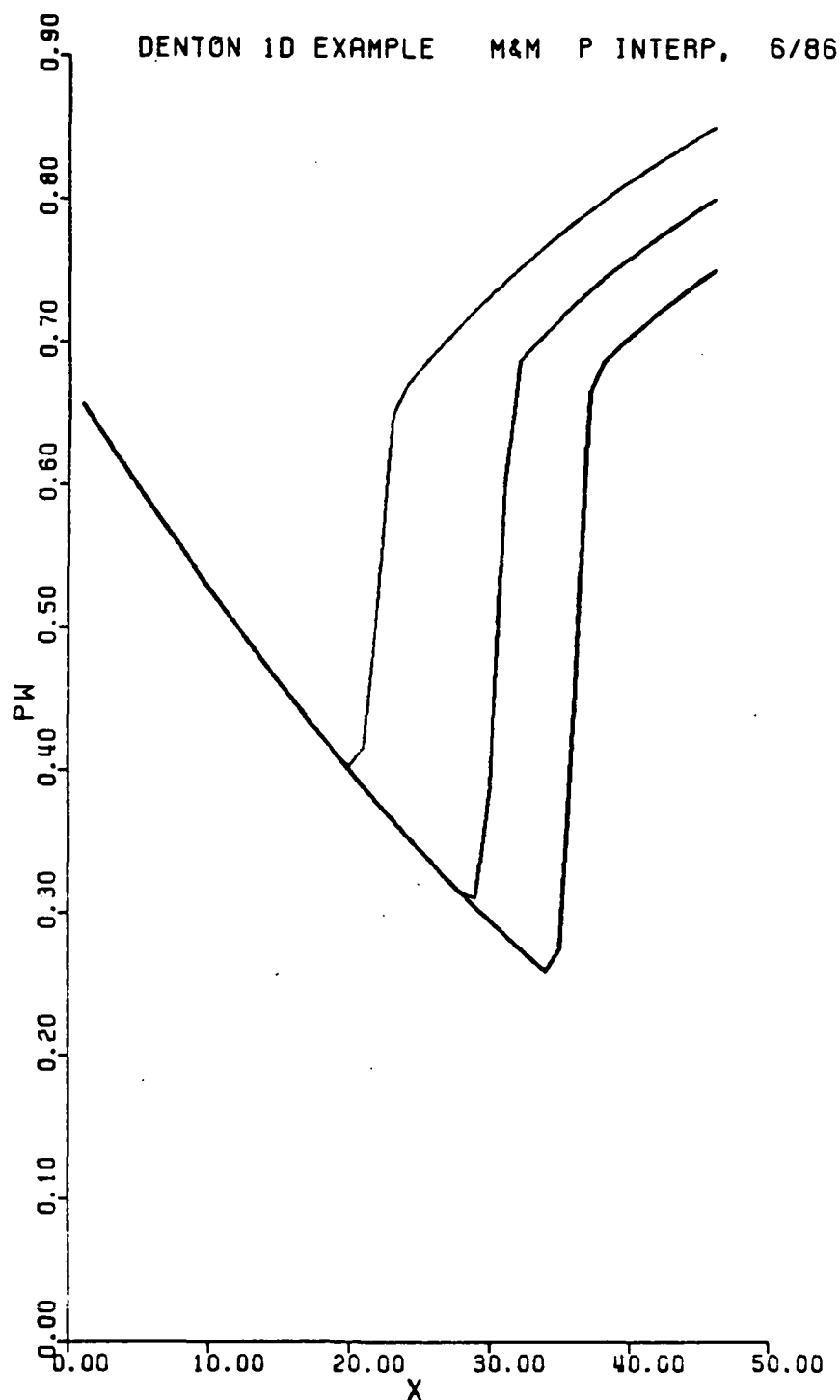


Fig. 3.4.6 Calculated 1-D Solution For Denton's Nozzle
 Using M & M Formula, Eq. 3.4.4.
 Calculations For Three Exit Static Pressures at
 $x = 46.$, $P_{\text{exit}}/P_{t,\text{inlet}} = 0.85, 0.80, \text{ and } 0.75.$

Fig. 3.4.6a $PW = P/P_{t,\text{inlet}}$

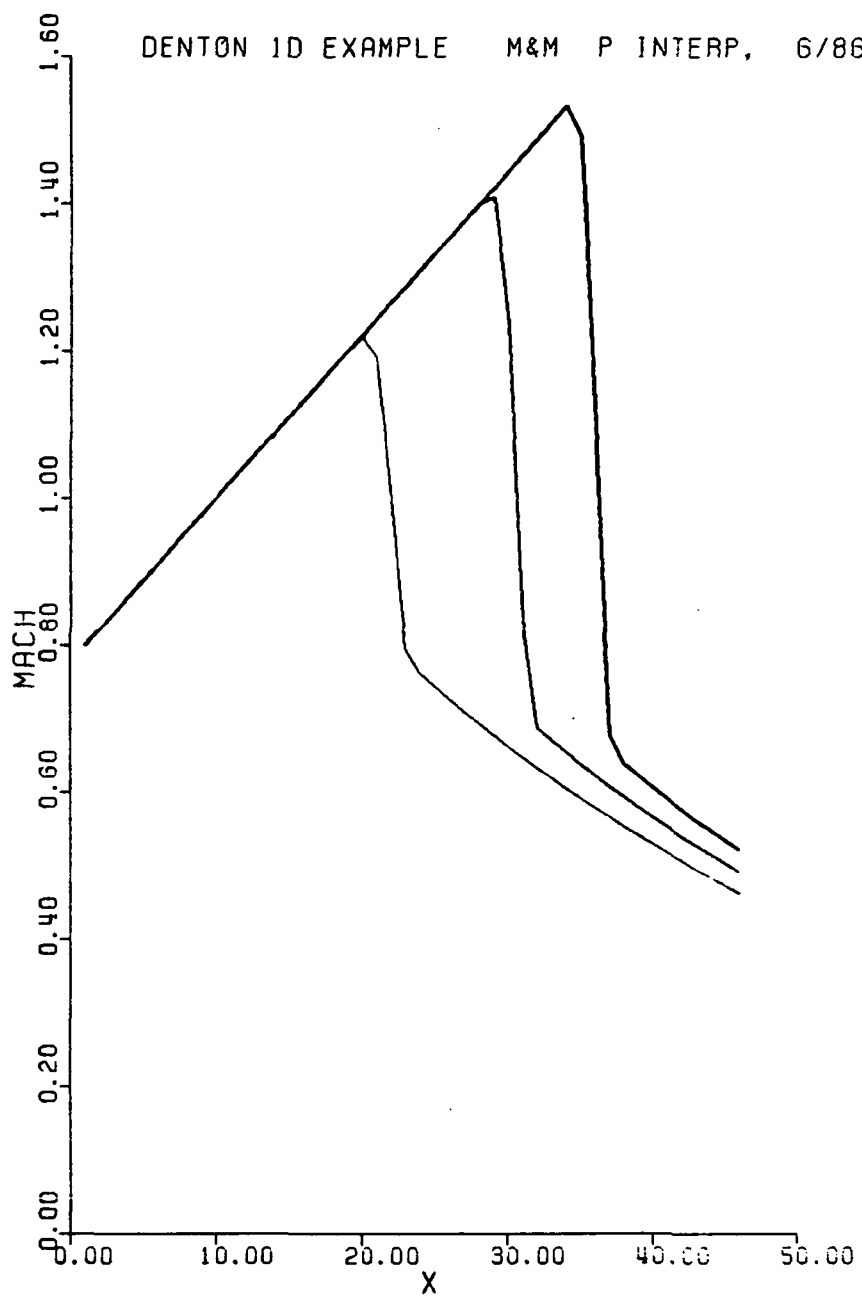


Fig. 3.4.6b Mach number.

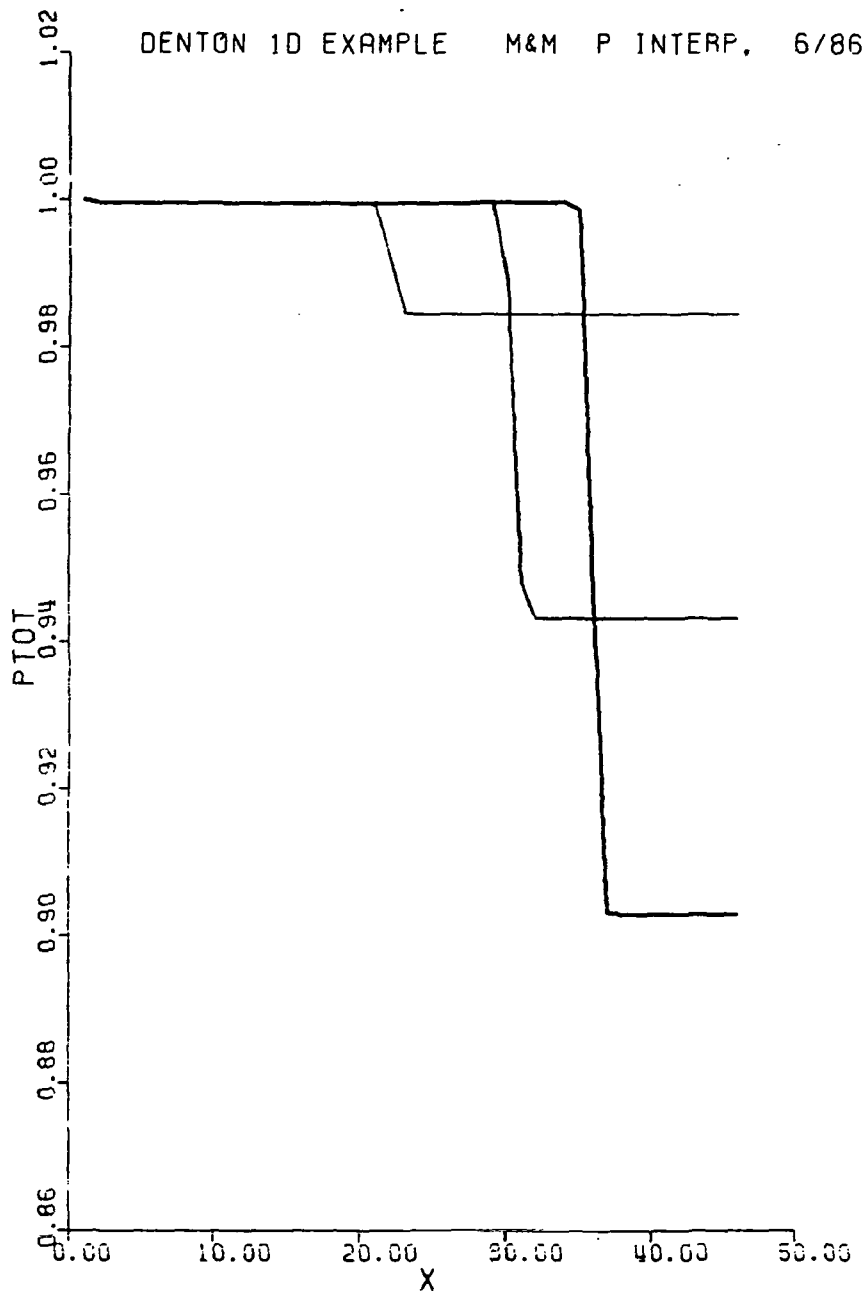


Fig. 3.4.6c $PTOT = P_t / P_{t,inlet}$.

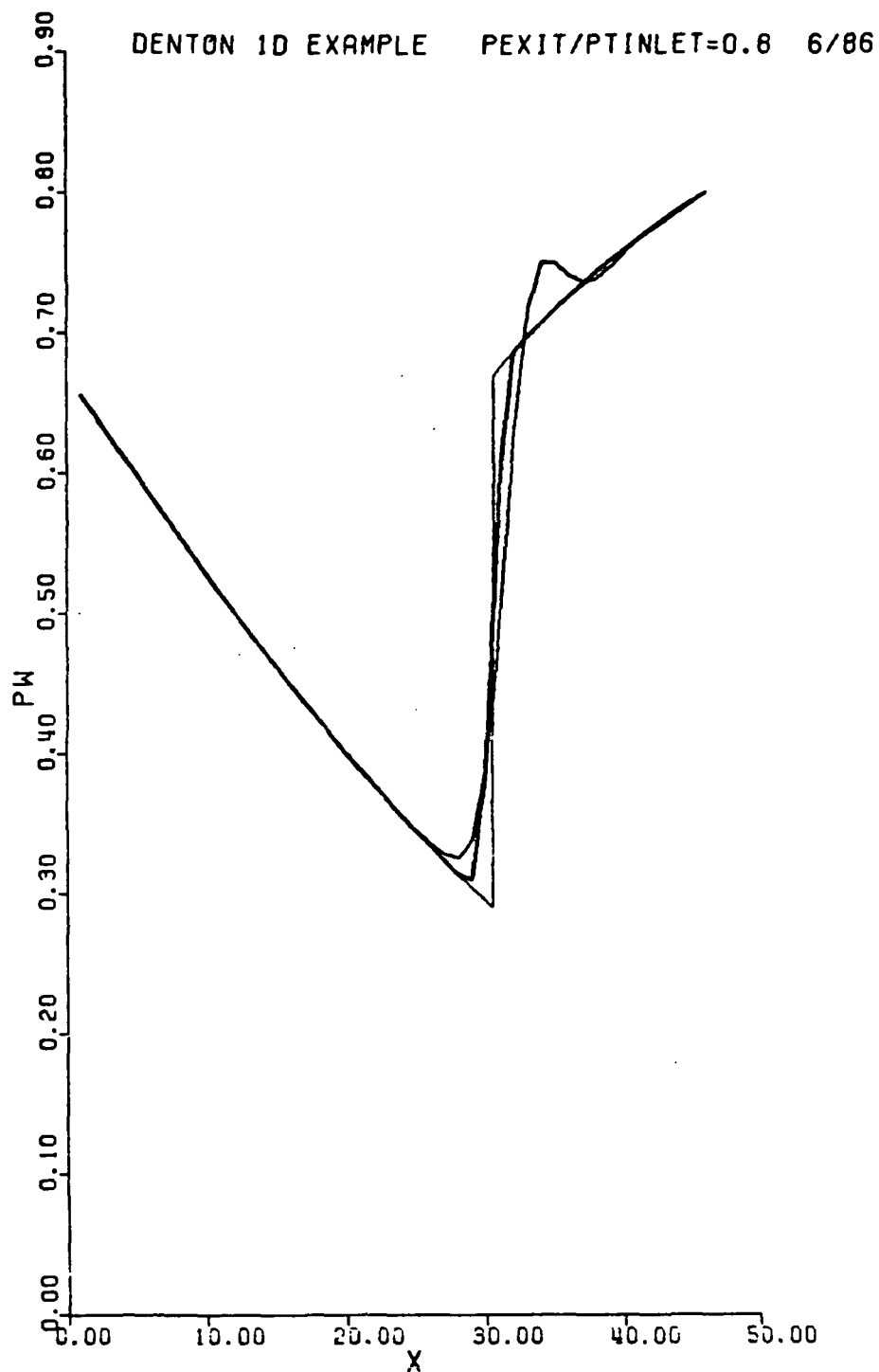


Fig. 3.4.7 Comparison of Calculated Results With The Theoretical
 1-D Solution For $P_{\text{exit}}/P_{t,\text{inlet}} = 0.80$
 Thin line - theoretical solution:
 Medium line - calculated using 3-point interpolation:
 Thick line - calculated using M & M formula.

Fig. 3.4.7a $PW = P/P_{t,\text{inlet}}$.

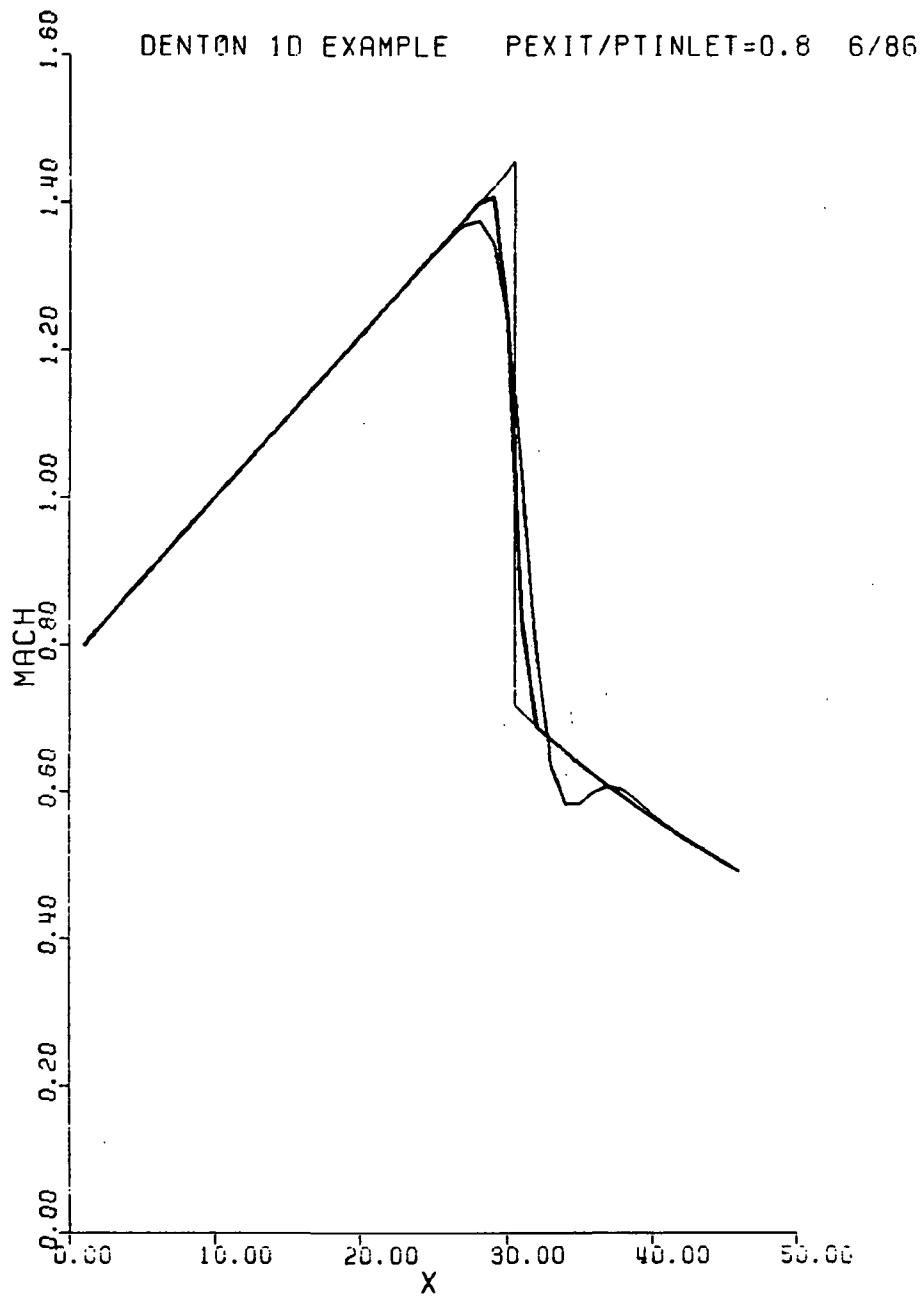


Fig. 3.4.7b Mach number.

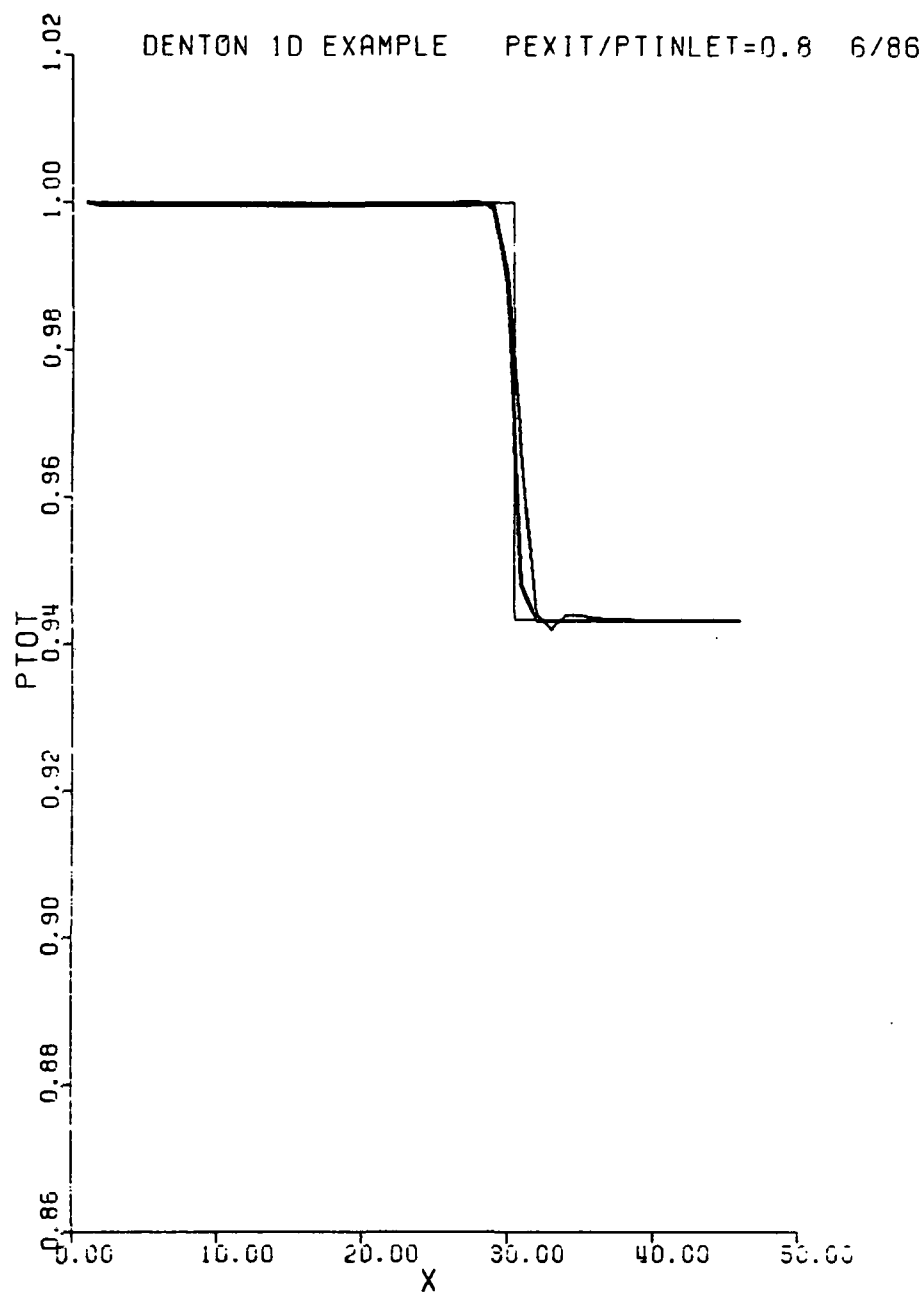


Fig. 3.4.7c $PTOT = P_t / P_{t,inlet}$

Table 3.4.1. Results of Calculations for Denton' 1-D Nozzle.

Table 3.4.1a: Maximum Mach number upstream of shock

Interpolation Formula

$\frac{P_{\text{exit}}}{P_{t \text{ inlet}}}$	Theoretical	3-Point	2-Point	Mach Number Dependent
0.85	1.268	1.175	1.198	1.218
0.80	1.455	1.374	1.395	1.408
0.75	1.578	1.501	1.526	1.533

Table 3.4.1b: Total pressure ratio, $P_{t \text{ exit}}/P_{t \text{ inlet}}$

Interpolation Formula

$\frac{P_{\text{exit}}}{P_{t \text{ inlet}}}$	Theoretical	3-Point	2-Point	Mach Number Dependent
0.85	0.9846	0.9845	0.9845	0.9845
0.80	0.9433	0.9431	0.9432	0.9432
0.75	0.9032	0.9029	0.9029	0.9029

The results in Figs. 3.4.4, 3.4.5, and 3.4.6 show that the interpolation formulae all act to smooth properties upstream of the shocks. The smoothing is most noticeable in the static pressure and Mach number distributions, especially with the 3-point interpolation scheme. The 2-point scheme gives less smoothing while the M&M formula gives the sharpest and most accurate distributions.

Both the 3-point and 2-point interpolation schemes give overshoots in static pressure and undershoots in Mach number downstream of the shocks. Only the M&M interpolation formula shows no noticeable overshoots and undershoots and this is because it has a better formulation for subsonic flow; in fact, from Eq. 3.4.4, it can be seen that the M&M formula reduces to the correct perfect gas equation for Mach numbers less than 0.918.

The M&M formula captures the shocks over about four grid points centered around the theoretical shock location. This is seen for the pressure ratio of 0.8 in Fig. 3.4.7. In contrast, Fig. 3.4.7 shows the 3-point scheme smearing the shock over about ten grid points with the shock displaced slightly downstream due to inadequate resolution of the subsonic flow. Once again the 2-point scheme gives results intermediate between those of the M&M and 3-point schemes.

3.5 LAMINAR BOUNDARY LAYER IN TWO CONVERGING DUCTS

A laminar boundary layer is calculated on the curved wall of two converging ducts. The other wall is straight and was treated as inviscid in the calculations. In all the calculations, the inlet boundary layer thickness is 5% of the inlet duct height. The inlet velocity profile is the Blasius profile. The inlet height of the duct is 44 mm and the exit height is 31 mm. The length of the duct is 180.4 mm. The absolute viscosity is .001 kg/m s. The inlet freestream Mach number is 0.10.

Two geometries are investigated with the basic dimensions given above. For one geometry, the curved wall radius is determined using a sine wave formulation. This geometry has a smooth transition from the inlet to the exit sections. The second geometry is essentially the same except that the radius is not determined using an analytical function and the second derivative of the wall radius is discontinuous. Both uniform and non-uniform grids are used in the boundary layer region. Figures 3.5.1 through 3.5.3 show the grid and geometry for the 3 arrangements to be investigated. The arrangements are

1. Smooth geometry using non-uniform grid (Fig. 3.5.1)
2. Smooth geometry using uniform grid (Fig. 3.5.2)
3. Non-smooth geometry using uniform grid (Fig. 3.5.3)

A plot of the 2nd derivative of the wall radius as a function of axial position for the non-smooth and smooth geometries is seen in Fig. 3.5.4. The location of the discontinuity is also identified in Fig. 3.5.3.

The specific ideas which are to be illustrated using this test case are,

1. Comparison of skin friction coefficients calculated using the finite volume method with those calculated using Thwaites method.
2. Comparison of skin friction coefficients calculated using uniform and non-uniform grids.
3. Comparison of skin friction coefficients calculated using smooth and non-smooth geometries.
4. Investigation of pressure variations across the duct comparing the uniform and non-uniform grids results, and non-smooth geometry results.
5. Investigation of inlet and exit boundary condition specifications.

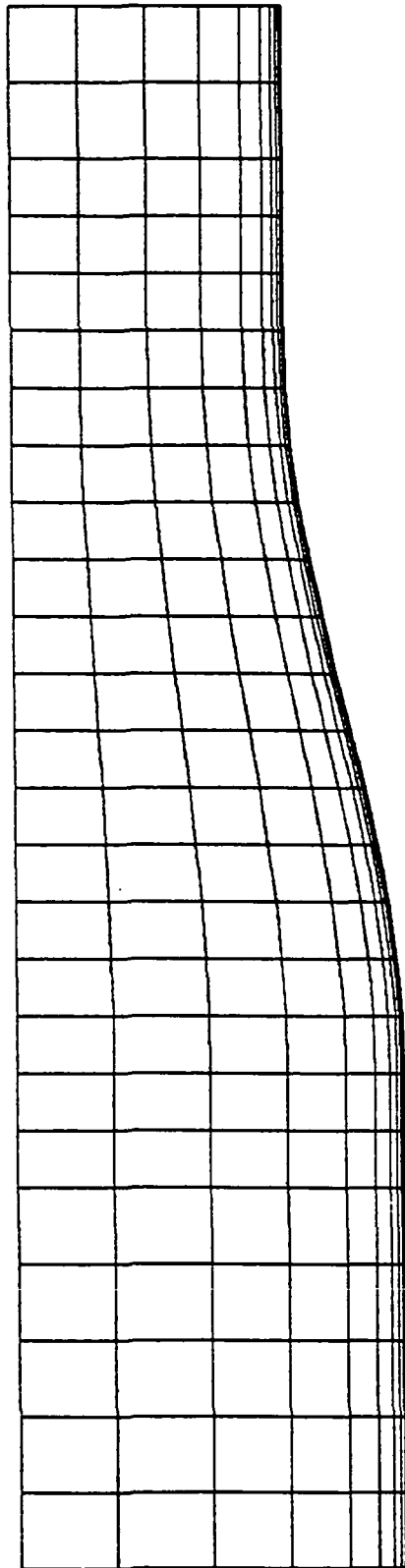


Fig. 3.5.1 Smooth Geometry Using Non-Uniform Grid

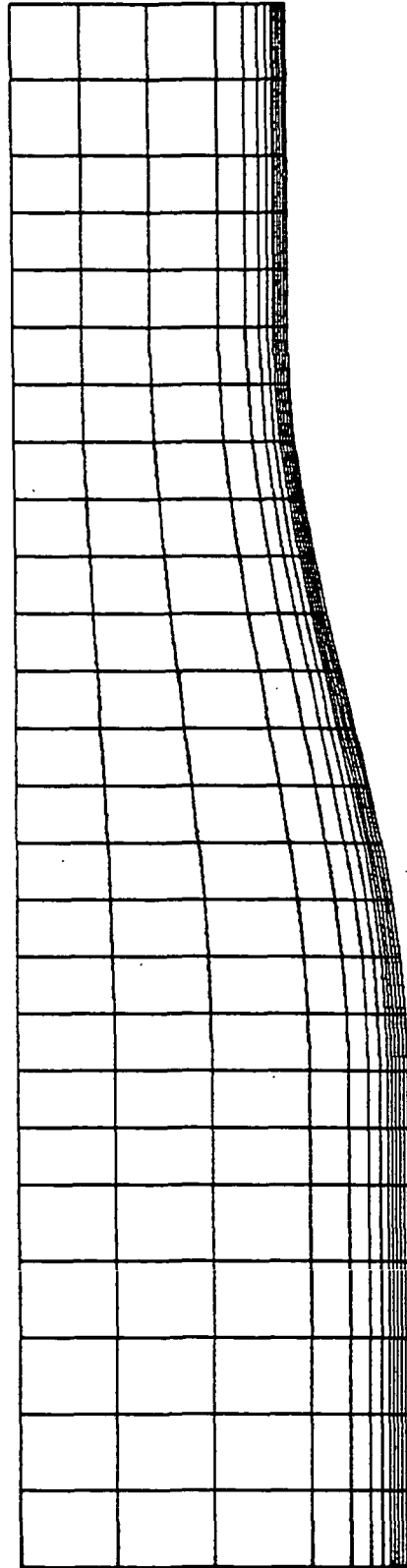


Fig. 3.5.2 Smooth Geometry Using Uniform Grid

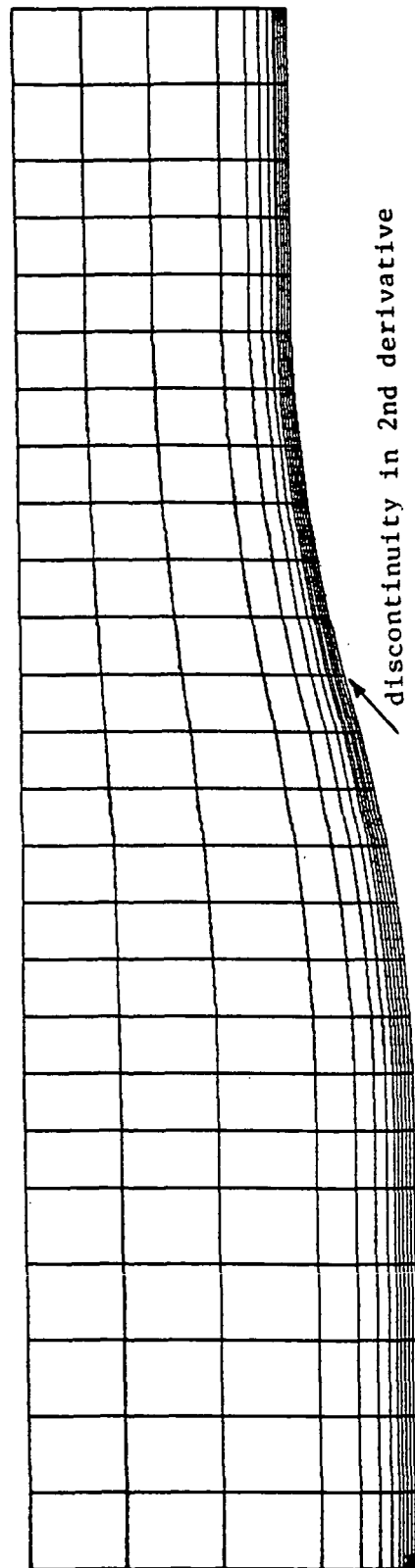


Fig. 3.5.3 Non-Smooth Geometry Using Uniform Grid

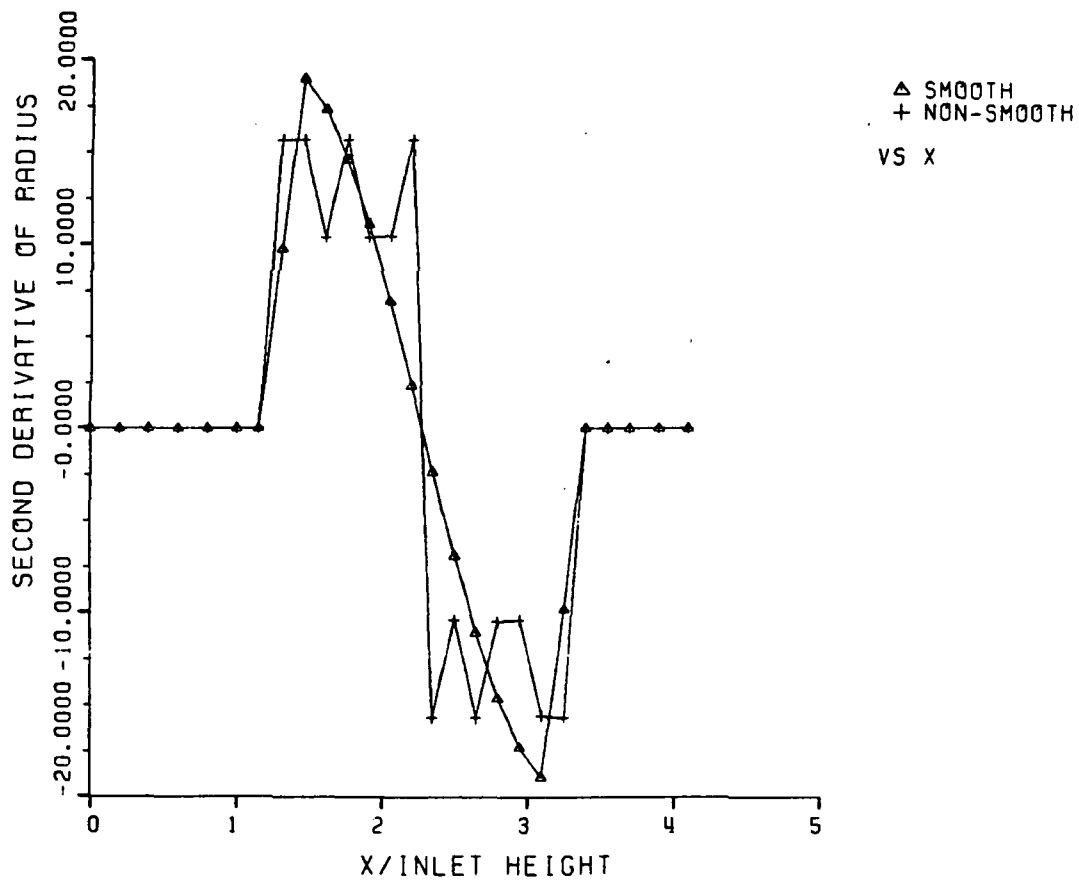


Fig. 3.5.4 Second Derivative of Radius For Converging Duct

6. Investigation of the convergence properties of uniform vs non-uniform grids, coarse vs fine grids, and different multi-volume approaches.

The radial distribution of grid points for the coarse, uniform and non-uniform grids and the fine non-uniform grid are tabulated in Table 3.5.1.

For the smooth geometry in Fig. 3.5.1, the skin friction coefficient along the duct was calculated using the finite volume method and using the method of Thwaites (25). A coarse non-uniform grid was used for the finite volume calculations. Thwaites method is an integral method used to calculate the development of laminar boundary layers in incompressible flow. Using the wall static pressure distribution from the finite volume calculation as a boundary condition, the skin friction coefficient was calculated with Thwaites method. Fig. 3.5.5 compares the skin friction coefficients obtained from the finite volume calculations with those obtained using Thwaites method. The agreement is good for most of the flow ;however, near the exit of the duct there is a discrepancy. This discrepancy may be due to the fact that the boundary layer has grown to over 25% of the duct height at the exit.

The skin friction coefficients calculated with the finite volume method using uniform and non-uniform grids are shown in Fig. 3.5.6. The agreement is excellent and it is concluded that grid spacing does not affect the prediction of the skin friction coefficient for this laminar flow.

The skin friction coefficients for the flow through the smooth and non-smooth geometries are shown in Fig. 3.5.7. Superficially, the geometries in Figs. 3.5.2 and 3.5.3 look almost identical ; however, for the non-smooth geometry the second derivative of the lower wall radius of curvature is discontinuous (see Fig. 3.5.4) causing the solution to be erratic at the discontinuity. To ensure smooth calculations, geometries input into this program should have continuous second derivatives.

The cause for the rapid increase in the skin friction coefficient at the discontinuity can be seen in Fig. 3.5.8. Fig. 3.5.8 is a plot of a transverse pressure coefficient which is defined as

Table 3.5.1 Transverse Distribution of Grid Points
for Laminar Calculations

	<u>Uniform Grid Coarse</u>	<u>Non-Uniform Grid Coarse</u>	<u>Non-Uniform Grid Fine</u>
	y/h	y/h	y/h
P1	.005	.0024	.0004
P2	.015	.0071	.00115
P3	.025	.0142	.00225
P4	.035	.0283	.0040
P5	.045	.0563	.0075
P6	.060	.1125	.0150
P7	.085	.225	.0300
P8	.125	.400	.0575
P9	.200	.625	.1125
P10	.375	.875	.225
P11	.625	-	.400
P12	.875	-	.625
P13	-	-	.875

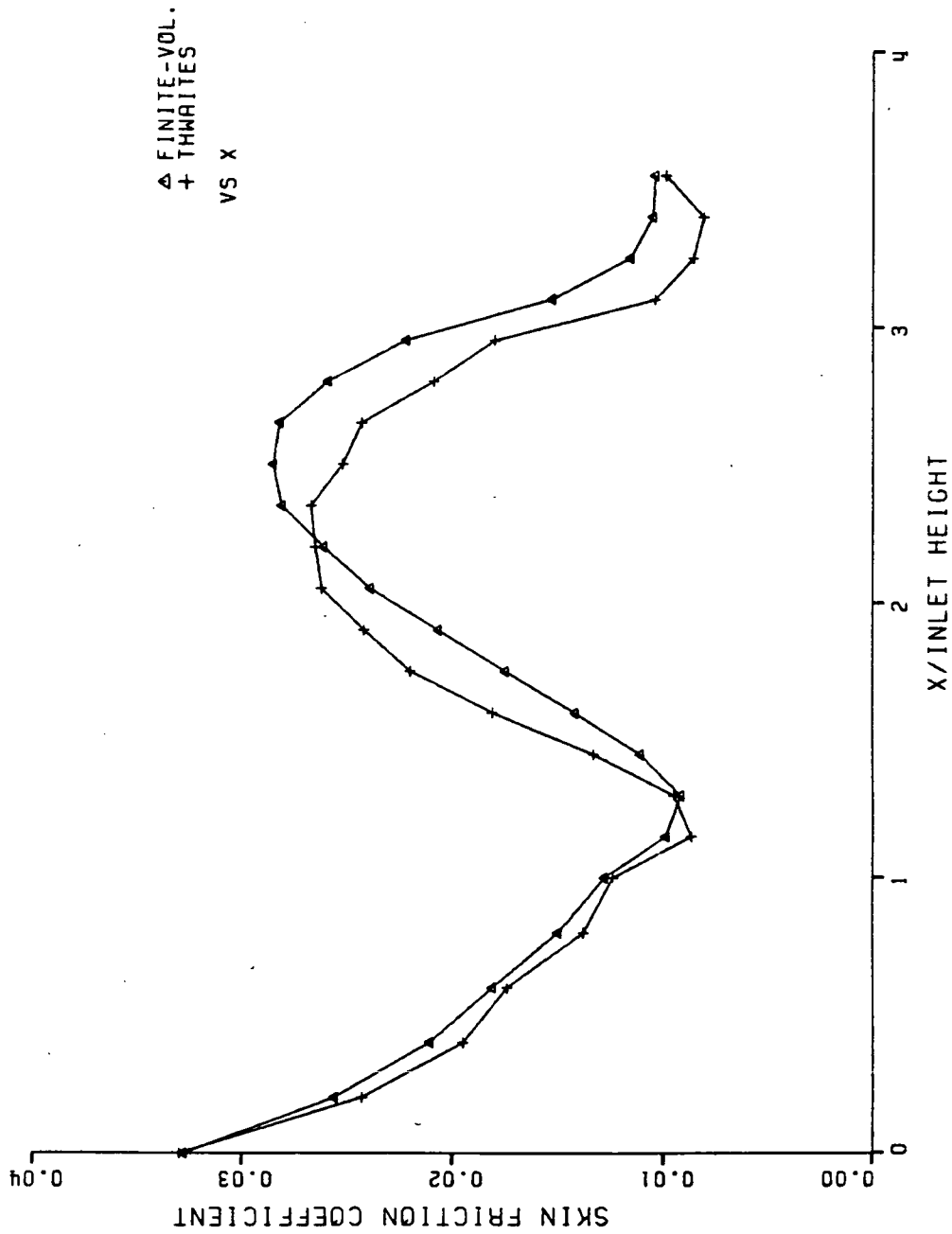


Fig. 3.5.5 Skin Friction Coefficient Finite Volume Method Vs Thwaites Method

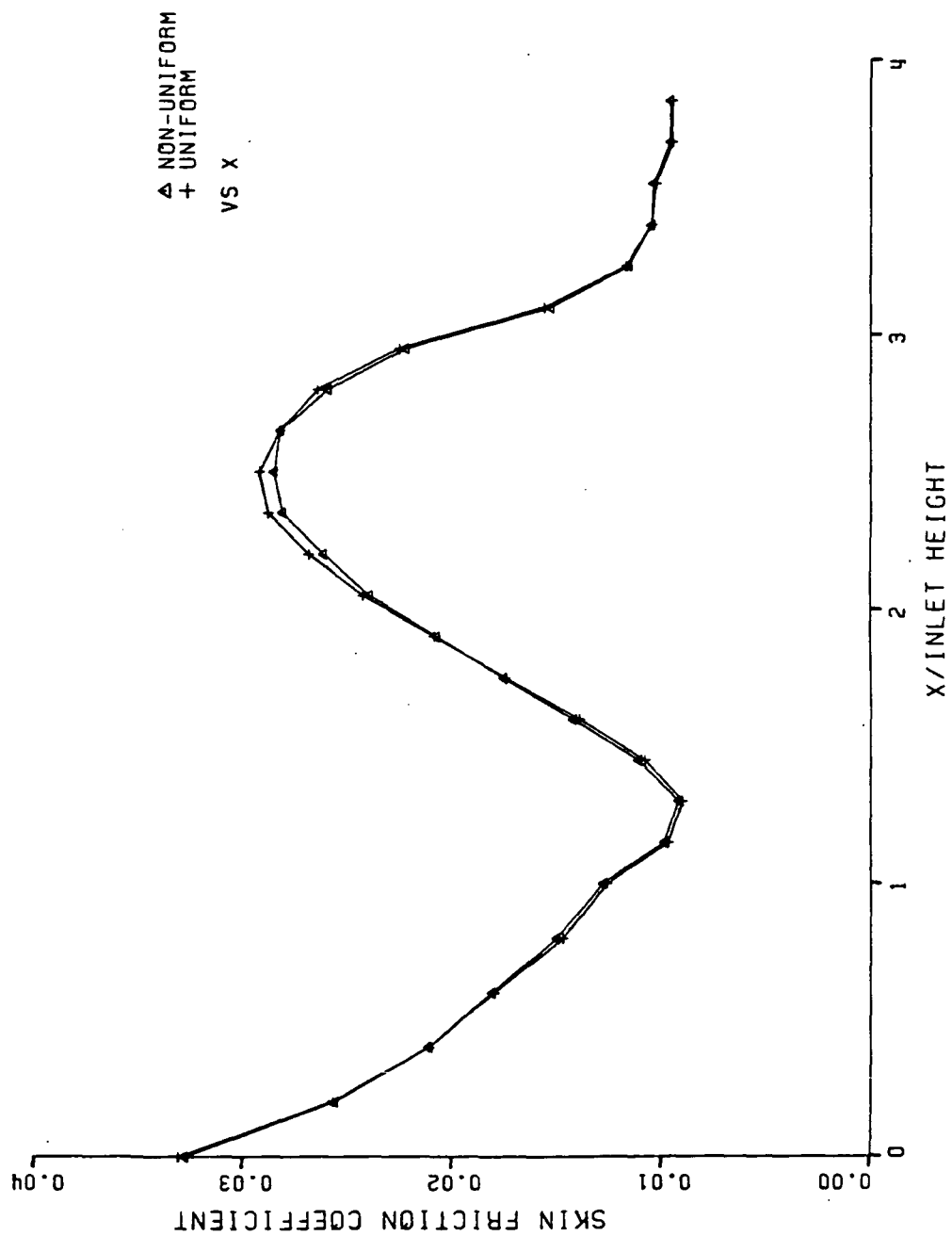


Fig. 3.5.6 Skin Friction Coefficient Finite Volume Method
Non-Uniform Vs Uniform Gridding

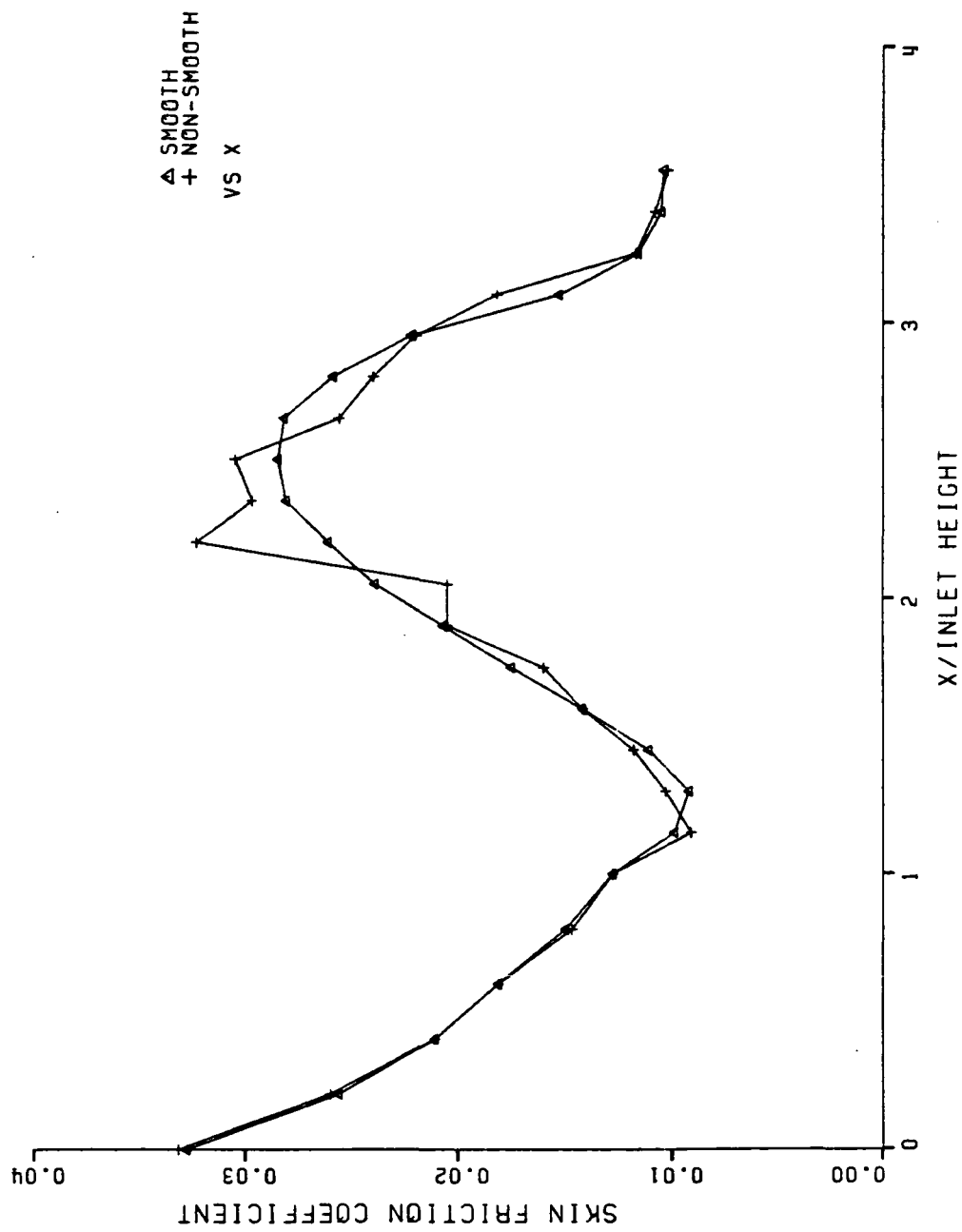


Fig. 3.5.7 Skin Friction Coefficient Smooth Geometry Vs Non-Smooth Geometry

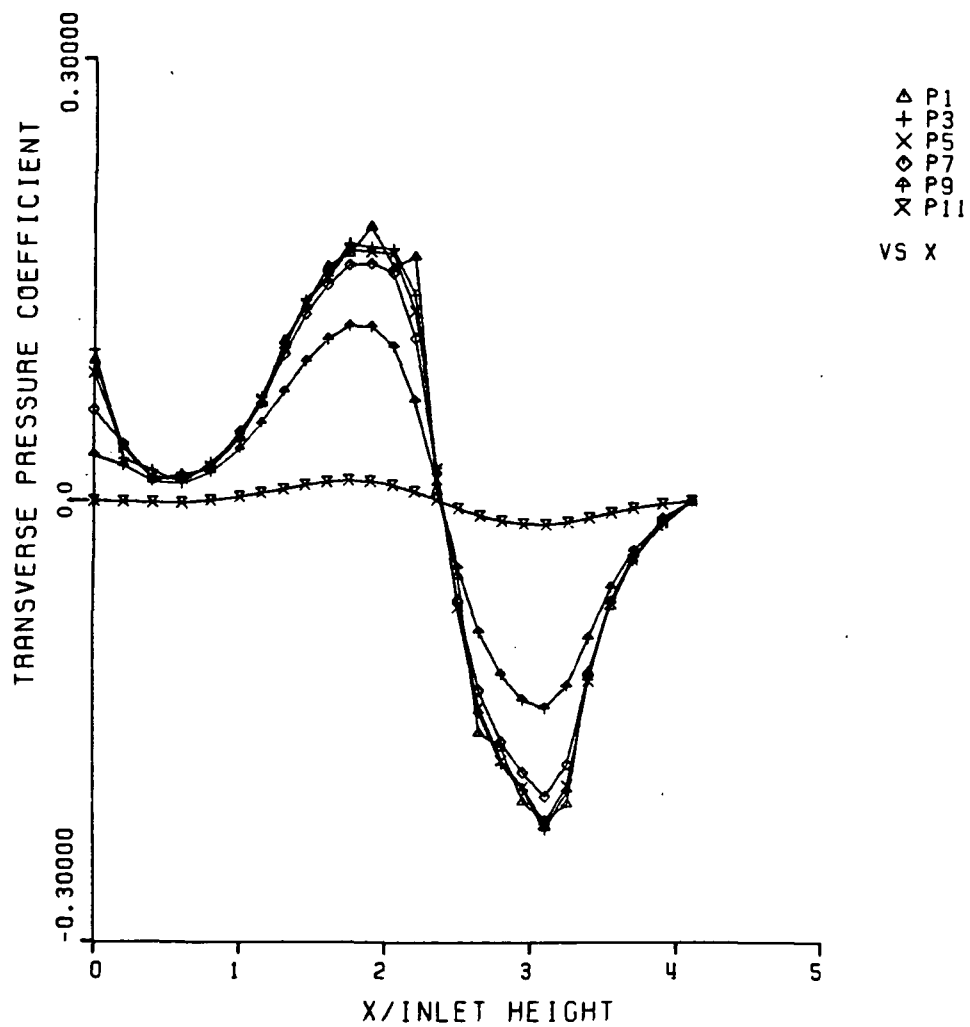


Fig. 3.5.8 Transverse Pressure Coefficient
Non-Smooth Geometry Uniform Grid

$$C_{Pt} = \frac{p - p_{fs}}{0.5\rho u^2} \quad (3.5.1)$$

where p is the local static pressure at an axial location, p_{fs} is the freestream static pressure at this axial location, and $0.5\rho u^2$ is the dynamic pressure at the inlet to the nozzle. The different curves in Fig. 3.5.8 represent the pressure coefficient at every other grid line from the wall to the freestream. Because of curvature, the pressure gradient across the duct first rises and then falls. The wall pressure (p_1) is seen to change very rapidly at the point of the discontinuity. This large axial pressure gradient results in a large change in velocity at the discontinuity and thus the large change in skin friction coefficient that was seen in Fig. 3.5.7.

For the smooth geometry the transverse pressure coefficient is shown in Fig. 3.5.9. The pressure changes are smooth throughout the entire length of the duct. The pressure coefficients shown in Fig. 3.5.9 are from calculations using a non-uniform grid. Fig. 3.5.10 shows identical results for calculations made using a uniform grid in the boundary layer.

In Figs. 3.5.8, 3.5.9, and 3.5.10, a small transverse pressure gradient can be observed at the inlet to the duct. This small transverse pressure gradient is a result of specifying the inlet v -velocity to be equal to zero. This boundary condition would be typical of inviscid calculations; however, the boundary layer in this viscous flow does have a finite v -velocity as a result of the growth of the boundary layer. The growth of the boundary layer for this test case is large because of the high absolute viscosity used. An additional calculation was made by modifying the boundary condition on the inlet v -velocity. From a previous calculation, the flow angles at the second axial station were recorded. These flow angles were then used as the inlet boundary condition for the inlet flow angle in a subsequent calculation. The transverse pressure coefficients for this case are shown in Fig. 3.5.11. The inlet transverse pressure coefficient is reduced considerably when compared with the pressure coefficient shown in Fig. 3.5.9. When the Blasius solution was used to calculate the inlet v -velocity distribution, the solution over compensated and the transverse pressure gradient was in the opposite direction to that calculated when a zero v -velocity was specified.

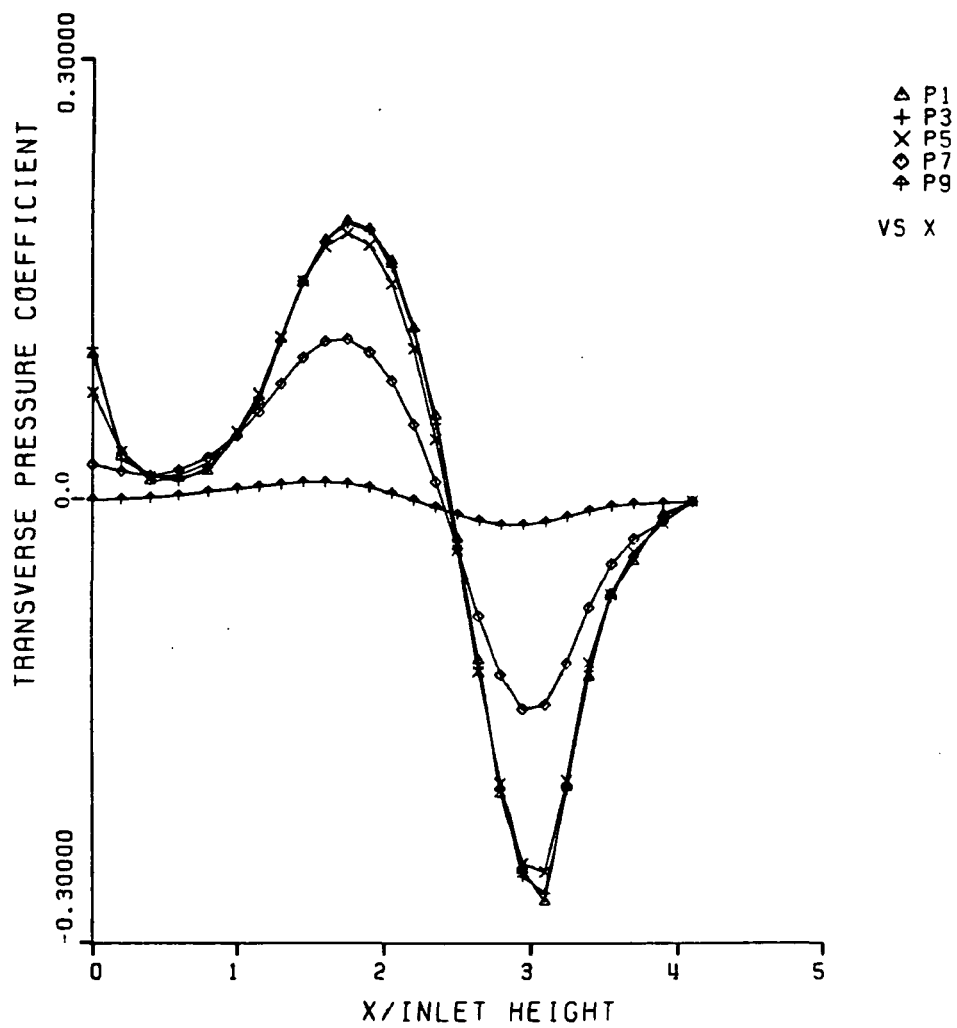


Fig. 3.5.9 Transverse Pressure Coefficient
Smooth Geometry Non-Uniform Grid

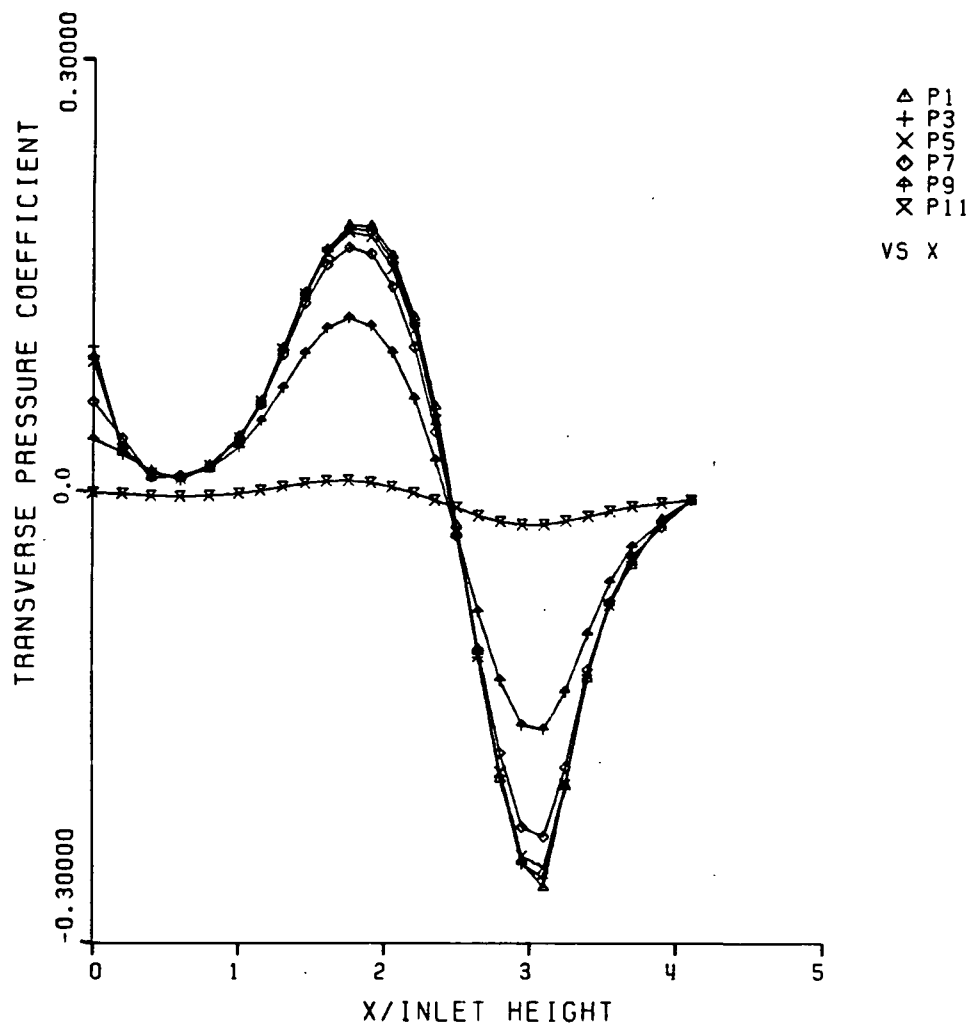


Fig. 3.5.10 Transverse Pressure Coefficient
Smooth Geometry Uniform Grid

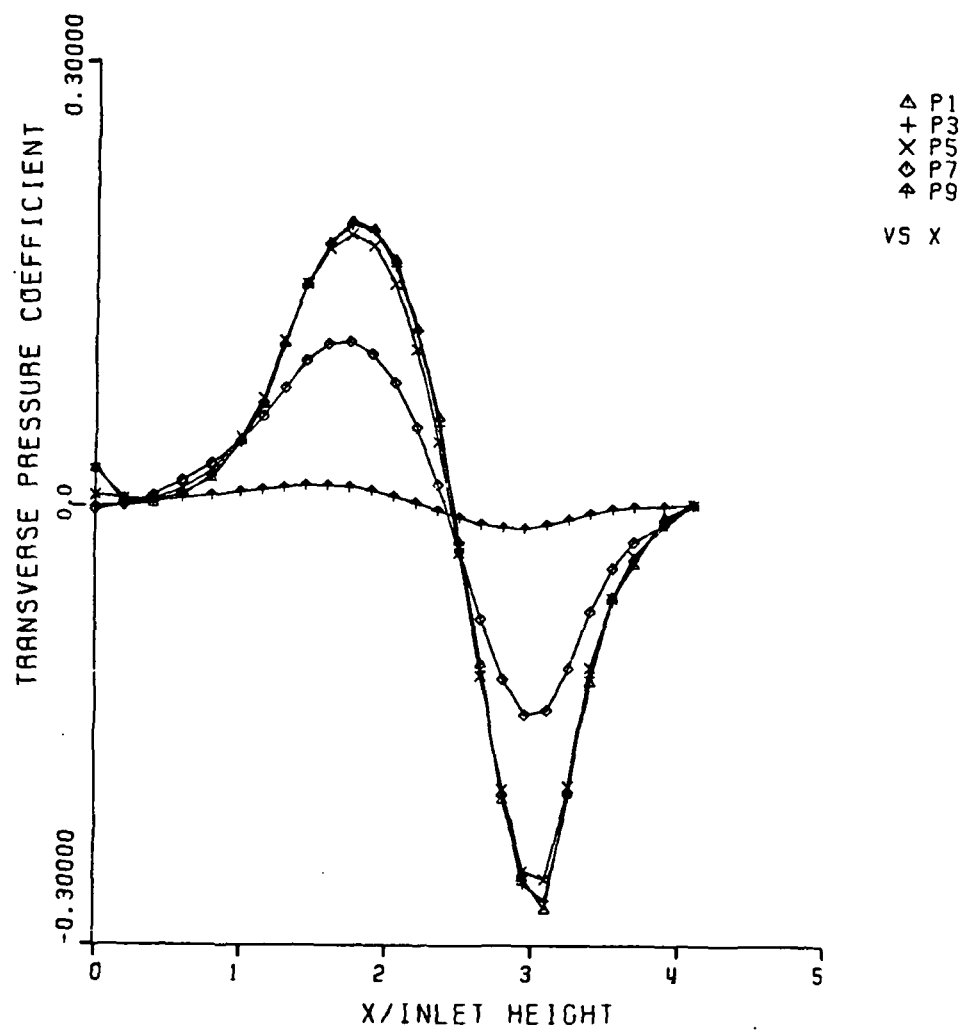


Fig. 3.5.11 Transverse Pressure Coefficient
Non-Uniform Grid Inlet v-Velocity Specified

It was also found to be important that the inlet and exit lengths of the straight portions of the duct were long enough. Oscillations in the static pressure would occur at the inlet and exit if these lengths were too short.

An additional pressure coefficient was calculated for each of the cases described above. The pressure coefficient is defined as

$$C_p = \frac{p_{01} - p}{0.5\rho u^2} \quad (3.5.2)$$

where p_{01} is the freestream total pressure, p is the local static pressure, and $0.5\rho u^2$ is the inlet dynamic pressure. This pressure coefficient again shows the effect of curvature on the pressure through the boundary layer but it also shows the relative acceleration of the flow through the nozzle. The plots are

1. non-smooth geometry with uniform grid (Fig. 3.5.12)
2. smooth geometry with non-uniform grid (Fig. 3.5.13)
3. smooth geometry with uniform grid (Fig. 3.5.14)
4. inlet flow angle specified with non-uniform grid (Fig. 3.5.15)

This test case also provided us with an opportunity to investigate the stability and convergence properties of various multi-volume approaches (see section 2.8) within the boundary layer. The various strategies are

1. [MV1] no multi-volume used in a uniform grid

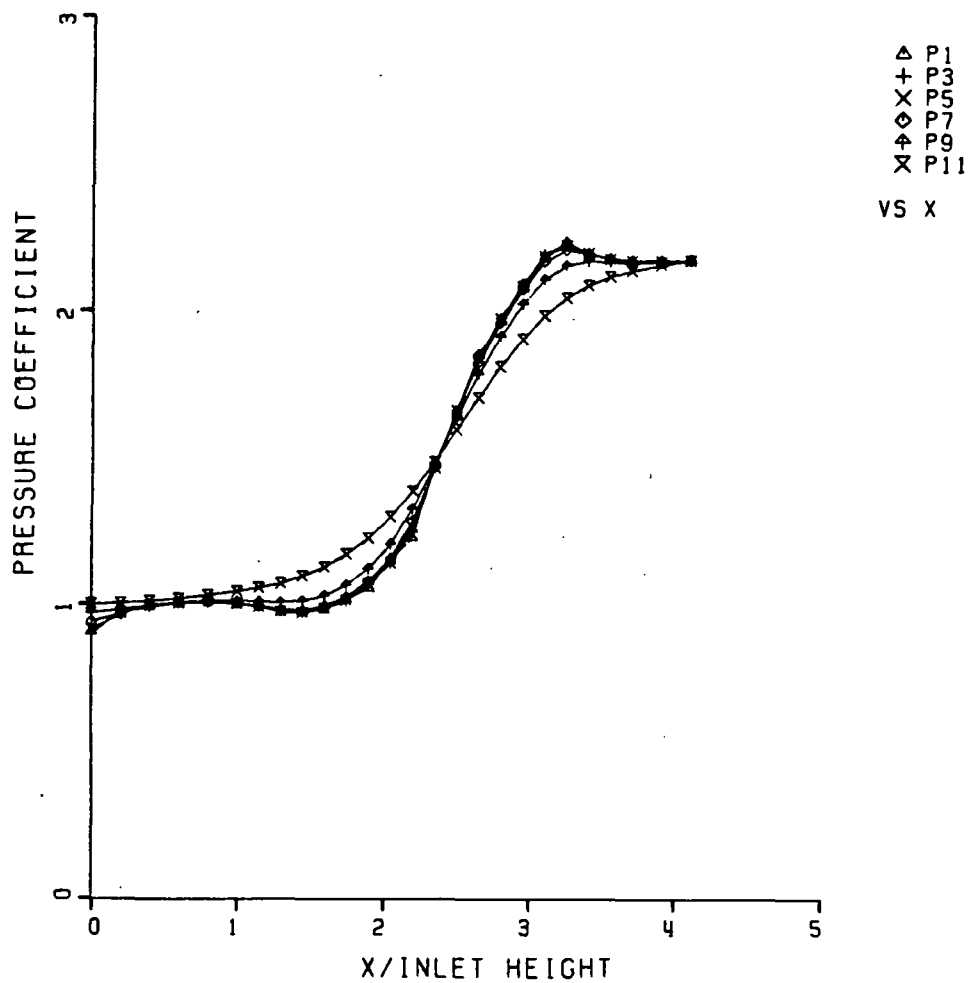


Fig. 3.5.12 Pressure Coefficient
Non-Smooth Geometry Uniform Grid

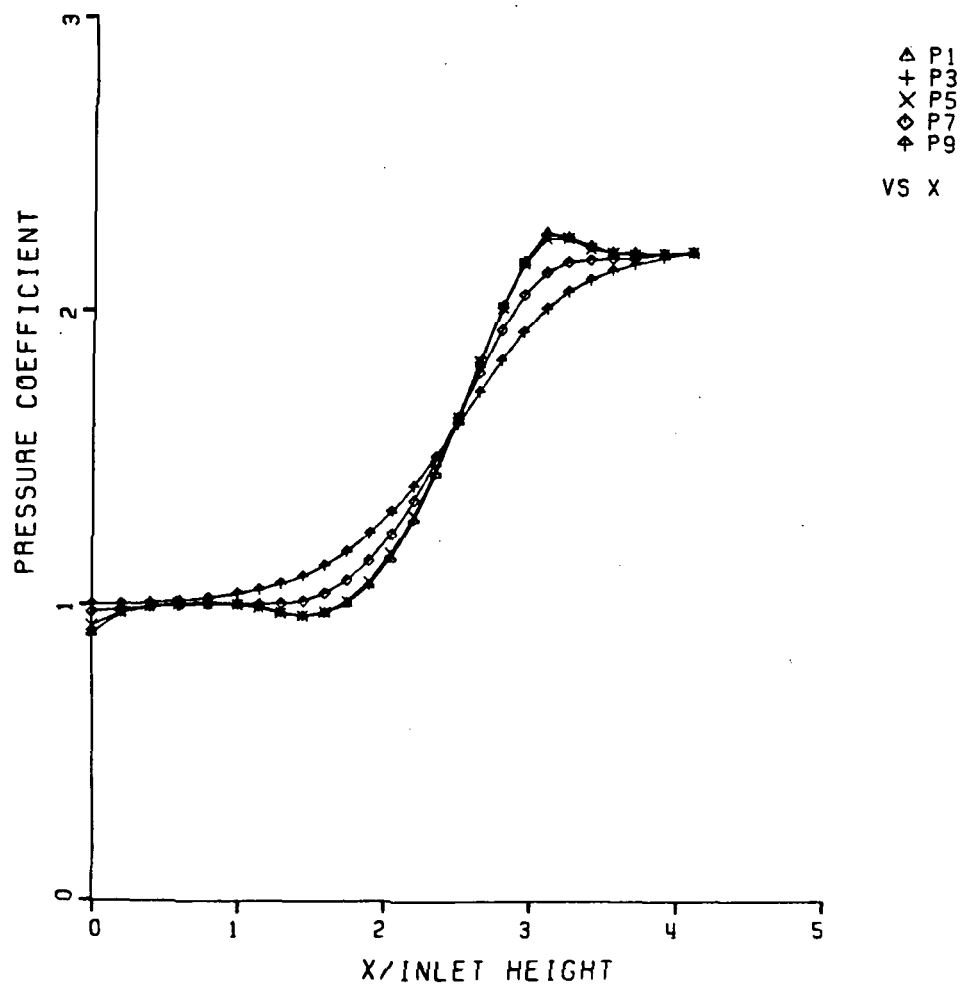


Fig. 3.5.13 Pressure Coefficient
Smooth Geometry Non-Uniform Grid

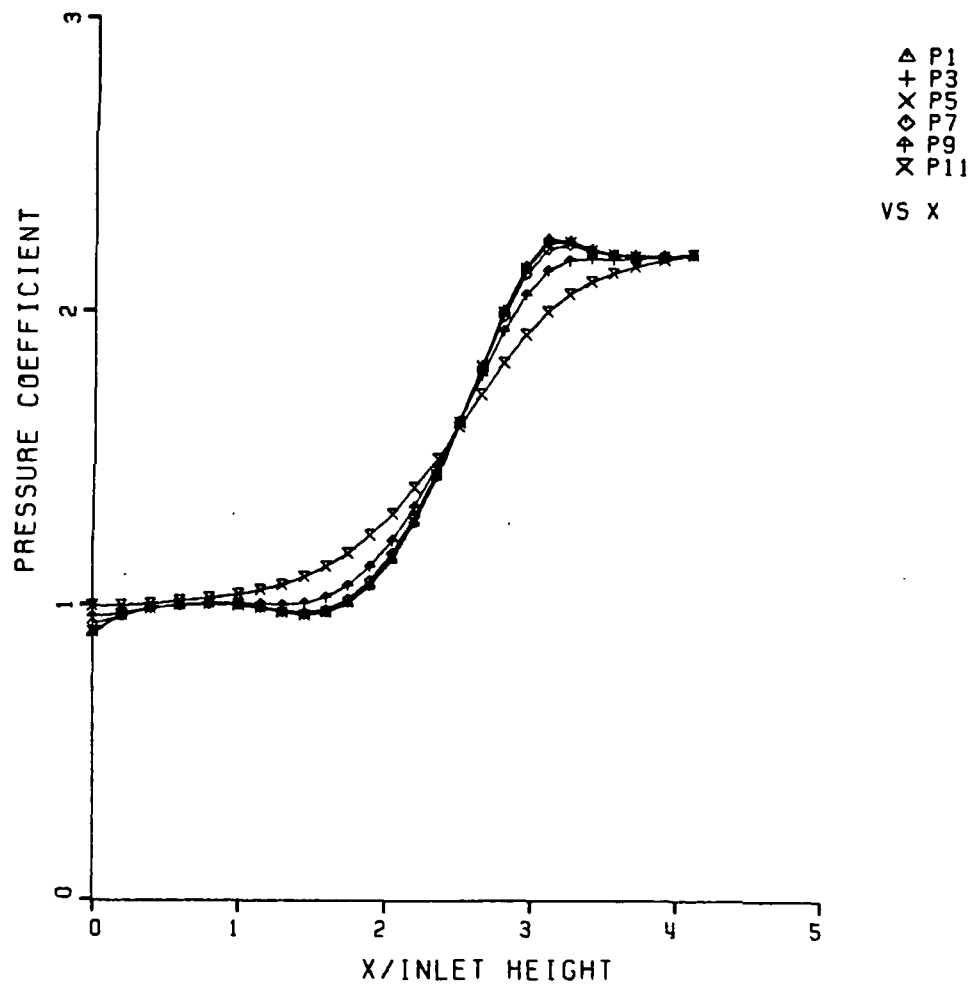


Fig. 3.5.14 Pressure Coefficient
Smooth Geometry Uniform Grid

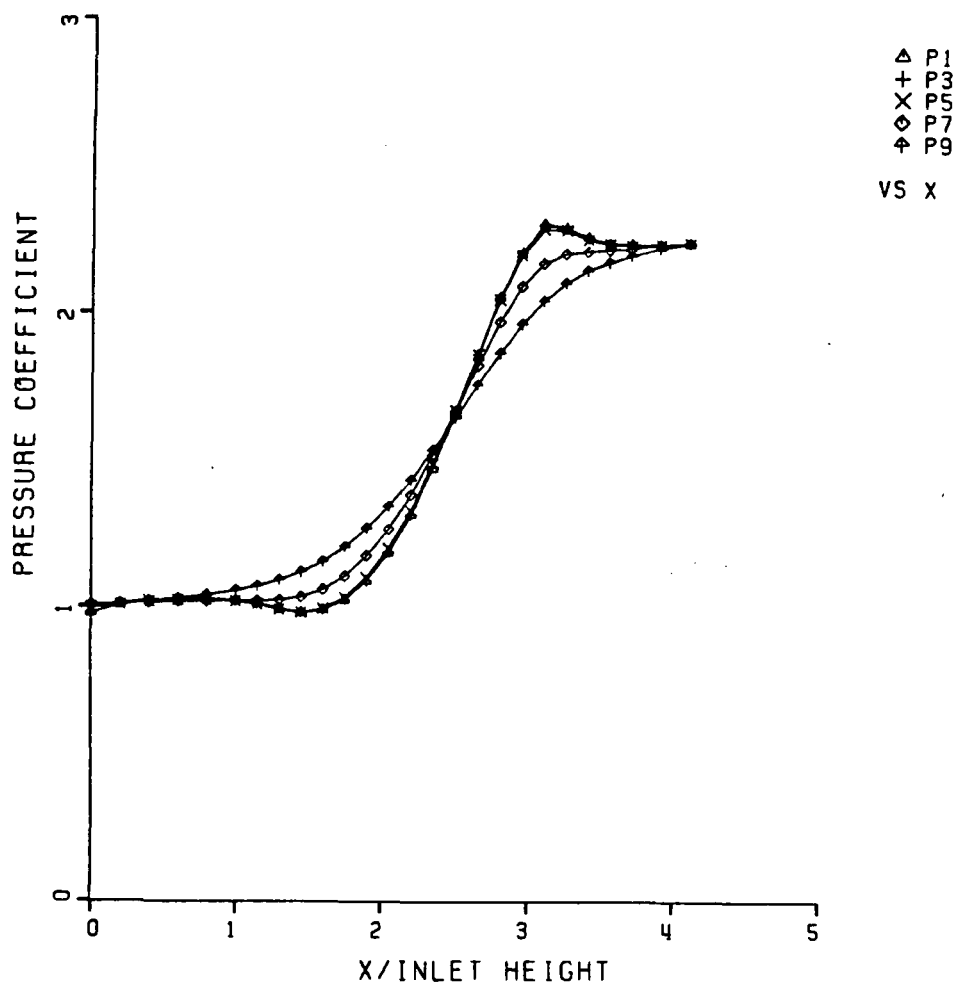


Fig. 3.5.15 Pressure Coefficient
Non-Uniform Grid Inlet v-Velocity Specified

2. [MV2] multi-volume used in a uniform grid with time steps based upon properties for the individual control volume farthest away from the wall.
3. [MV3] multi-volume used in a uniform grid with time steps based upon average properties for the entire multi-volume region.
4. [MV4] multi-volume used in a non-uniform grid with time steps based upon properties for the individual control volume farthest away from the wall.
5. [MV5] multi-volume used in a non-uniform grid with time steps based upon average properties for the entire multi-volume region.

For the uniform and non-uniform grids, the multivolume approach was used for the 6 control volumes nearest to the wall.

Two measures of convergence will be used in the following analysis. The maximum change in velocity in the flow field for one iteration divided by an average velocity for the flow field all multiplied by the time factor used in the time step determination will be our momentum residual, in other words,

$$\text{momentum residual} = \frac{(u^{n+1} - u^n)_{\max}}{u_{\text{avg}}} \times \text{TIMEF} \quad (3.5.3)$$

The time factor, TIMEF, is included so that calculations using different time factors in the time step determination can be judged on a common basis. A time factor of 4.0 was used for all of the laminar calculations. The mass flow rate error is defined as

$$\text{mass flow error} = \left| \frac{\dot{m}_{\text{local}} - \dot{m}_{\text{in}}}{\dot{m}_{\text{in}}} \right|_{\max} \times 100 \quad (3.5.4)$$

The momentum residual for multi-volume approaches 1 through 4 are shown in Fig. 3.5.16. The mass flow error for approaches 1 through 4 are shown in Fig. 3.5.17. The non-uniform grid shows

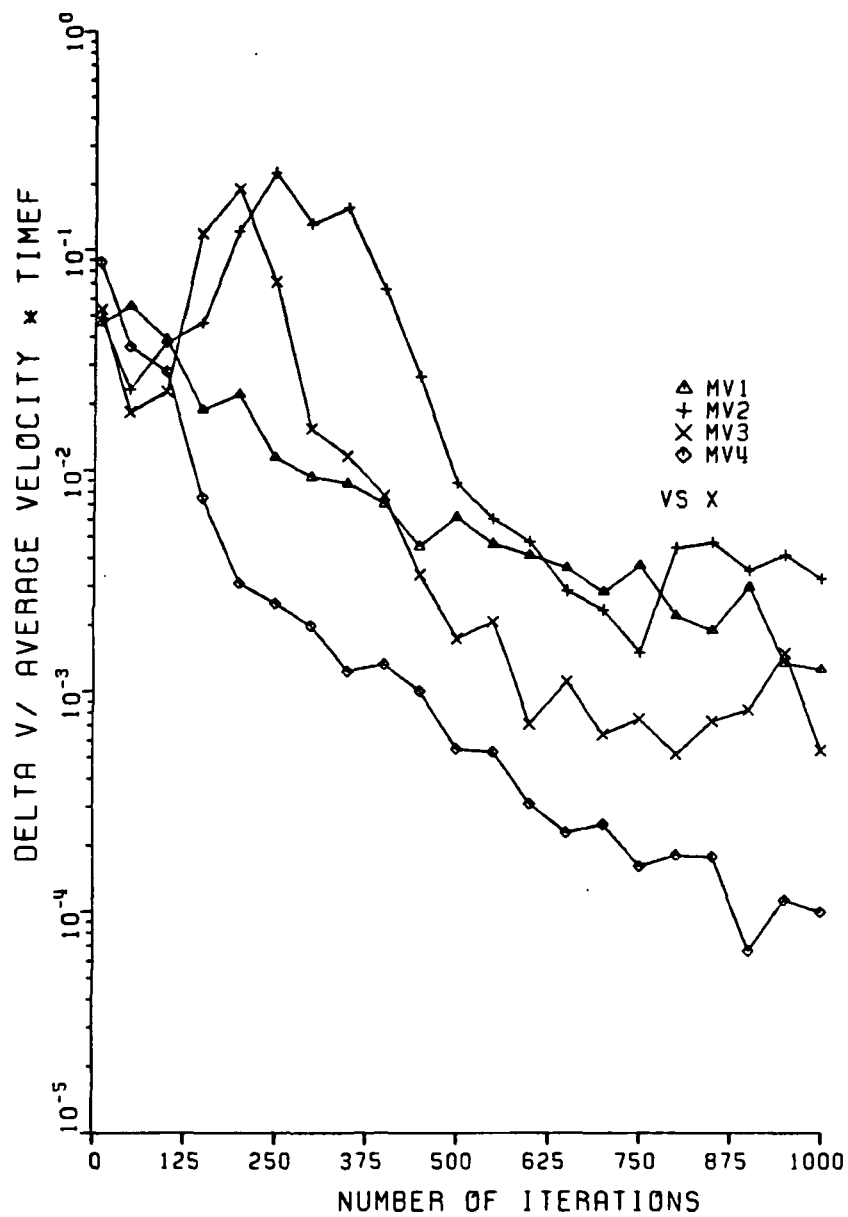


Fig. 3.5.16 Momentum Residual For Laminar Boundary Layer Calculations

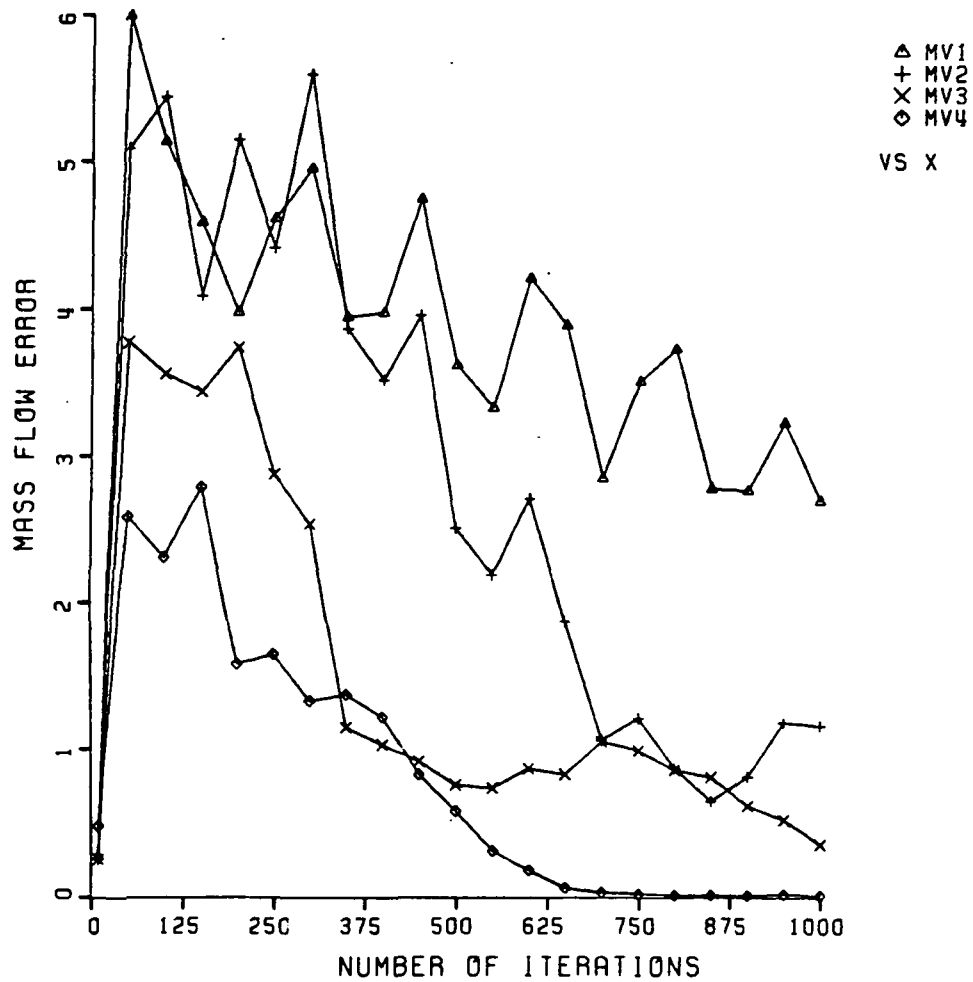


Fig. 3.5.17 Mass Flow Error For Laminar Boundary Layer Calculations

superior convergence properties when compared with the uniform grid results. When the uniform grid is used, approach MV3 is the best.

When the momentum residual and mass flow error for the non-uniform grid approaches MV4 and MV5 are compared in Figs. 3.5.18 and 3.5.19, the results are very similar. This agreement justifies the use of the simpler multi-volume approach (MV4) for the non-uniform grid. The simpler multi-volume approach uses less computer time in the multi-volume part of the program.

When a finer grid was used with the non-uniform grid arrangement in the boundary layer region (twice as many control volumes), the skin friction coefficients were identical to those calculated from the coarse grid (5 points in the boundary layer). The momentum residual and the mass flow error for the coarse and fine grids are compared in Figs. 3.5.20 and 3.5.21 respectively. The convergence properties are very similar.

The following conclusions can be reached from the above test case:

1. the geometries should be inspected for discontinuities in the second derivative to ensure smooth solutions.
2. uniform and non-uniform grids give essentially identical results for this laminar boundary layer.
3. the non-uniform grid (with a factor of 2 change in spacing) has superior convergence properties.
4. the simple form of the multi-volume used with the non-uniform grid (MV4) is preferred because of the reduced computational effort required.

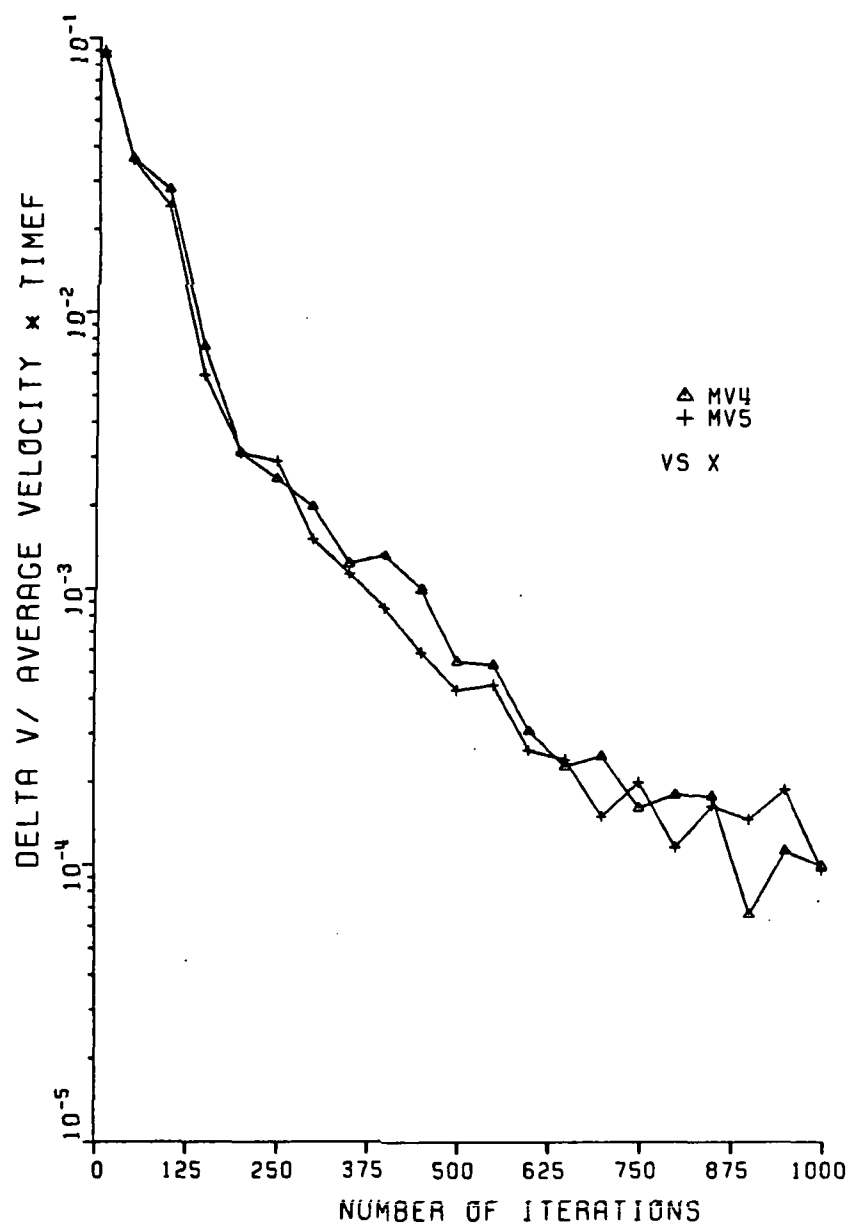


Fig. 3.5.18 Momentum Residual For Laminar Boundary Layer Calculation Local Vs Global Time Steps

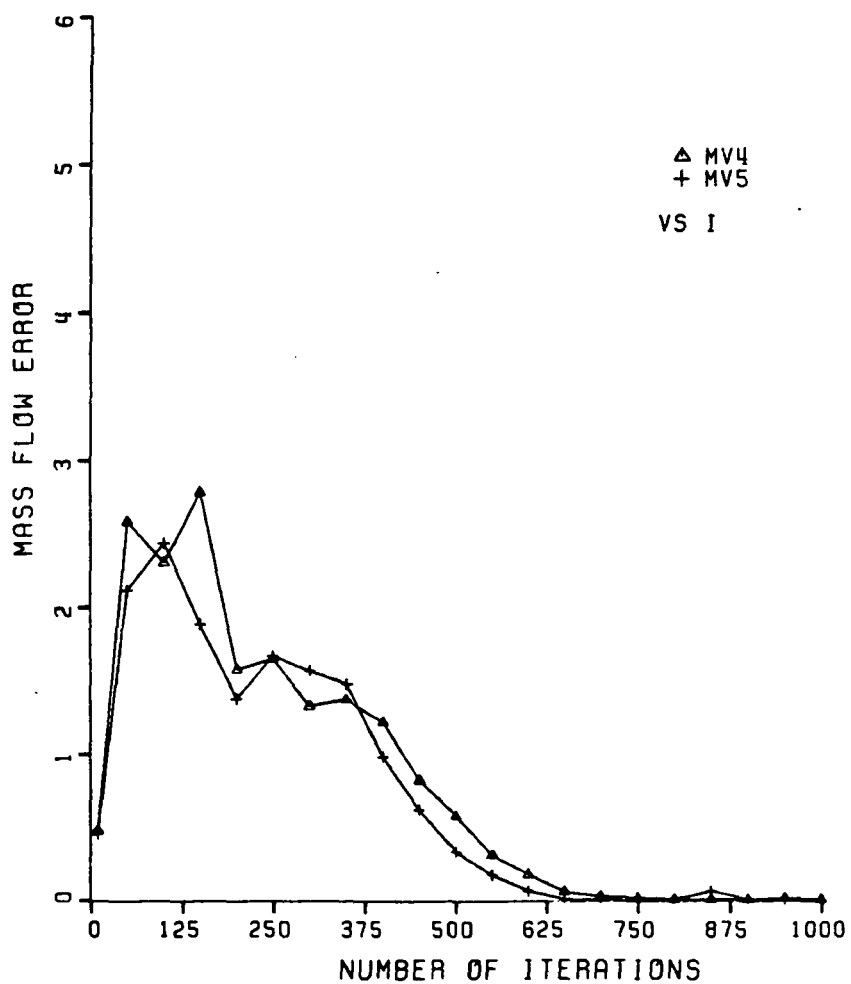


Fig. 3.5.19 Mass Flow Error For Laminar Boundary Layer Calculations Local Vs Global Time Steps

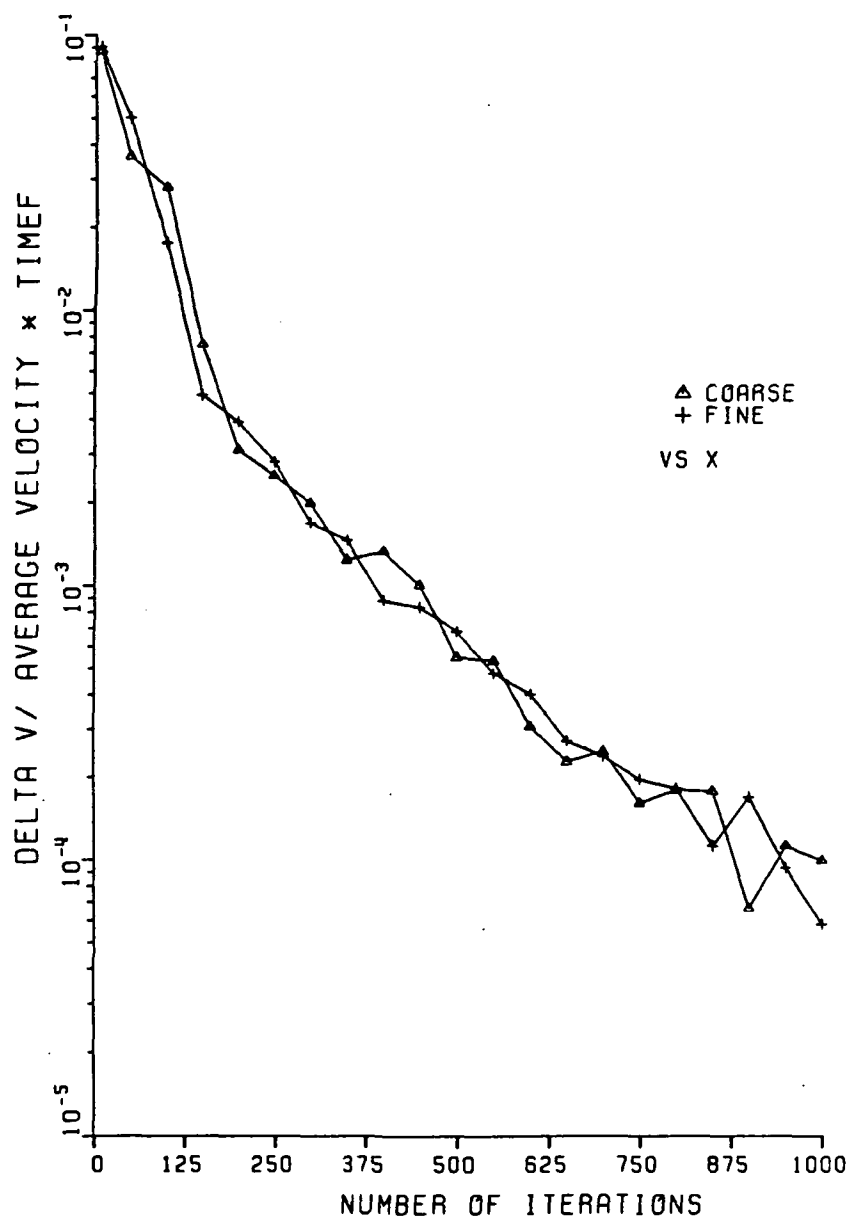


Fig. 3.5.20 Momentum Residual For Laminar Boundary Layer Calculations Coarse Vs Fine Grid

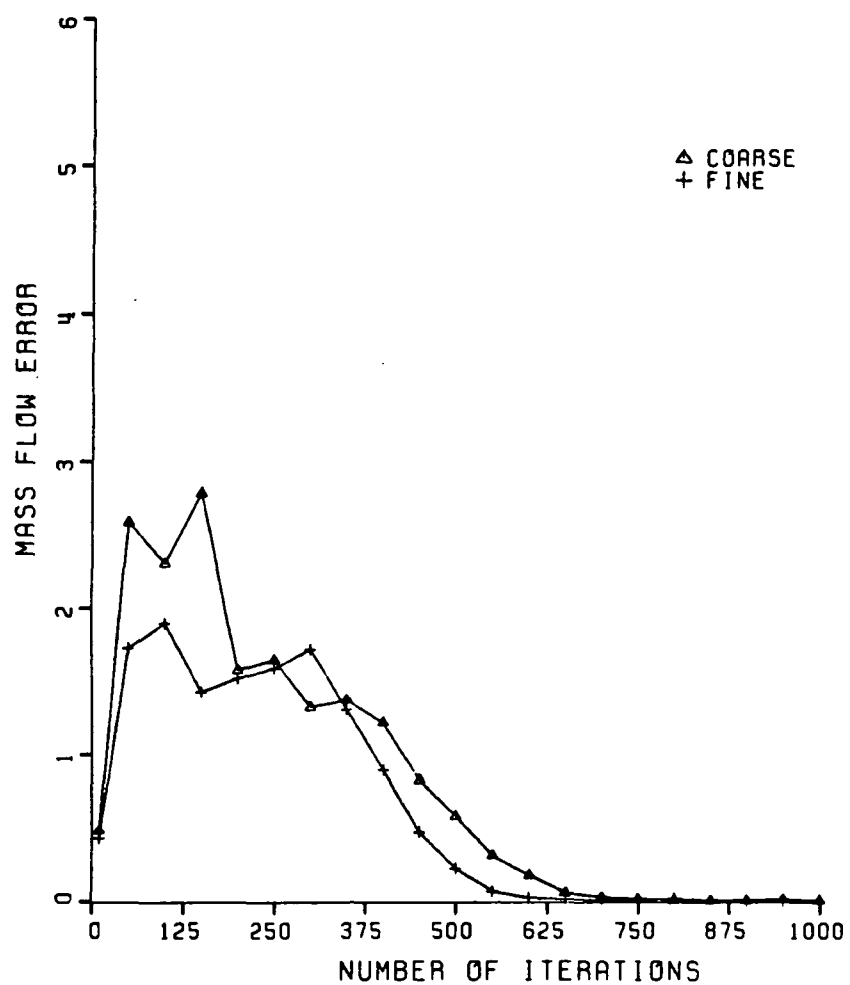


Fig. 3.5.21 Mass Flow Error For Laminar Boundary Layer Calculations Coarse Vs Fine Grid

3.6 SAMUEL AND JOUBERT INCOMPRESSIBLE TURBULENT BOUNDARY LAYER

Incompressible turbulent boundary layer flow in a diverging duct was calculated for test case 0141 of the Stanford Conference (Samuel and Joubert) (26). The geometry used by Moore (27) and the grid used in the present calculations are shown in Fig. 3.6.1. With this geometry, the top wall is treated as inviscid in the calculations. The inlet velocity is 26 m/s. The absolute viscosity is 0.000018 kg/ m s.

The duct height is 1 m at the inlet plane ($x = 0.85$ m). The length of the duct from the inlet to the exit plane is 3.3 m. The distribution of grid points across the duct and the inlet velocity profile are presented in Table 3.6.1. In the present calculations, the inlet total pressure is 102 kPa and the inlet total temperature is 300 K. The exit static pressure was chosen to be 100 kPa so that the inlet velocity in the freestream would be approximately 26 m/s.

Fig. 3.6.2 shows a comparison of the calculated skin friction coefficient with the experimental results and with the results from the Moore cascade flow program. The agreement is excellent. The skin friction coefficient, defined here as

$$C_f = \frac{\tau_w}{0.5\rho U_{ref}^2} , \quad (3.6.1)$$

uses a reference velocity , U_{ref} of 27 m/s in its evaluation.

A comparison of the calculated turbulent shear stress distribution , $\overline{u'v'}$, with the experimental results is shown in Figs. 3.6.3 and 3.6.4. The shear stresses are normalized with respect to the local freestream velocity. The agreement is very good.

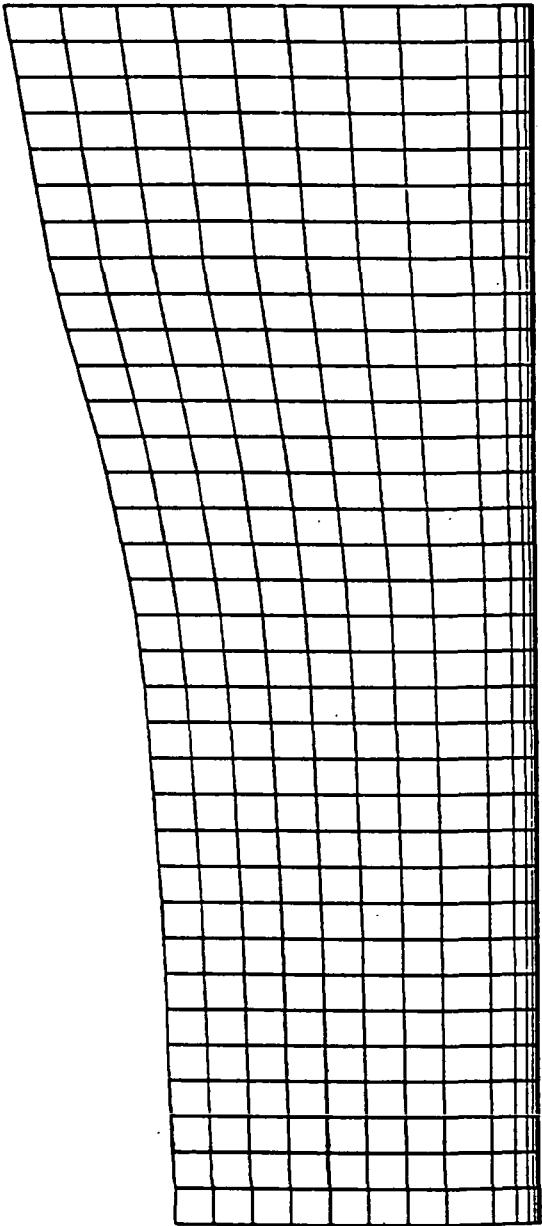


Fig. 3.6.1 Geometry and Grid For Samuel and Joubert

Table 3.6.1 Node Distribution and Inlet
Velocity Profile for Samuel and Joubert

y	$\frac{u}{u_e}$
0.000165	0.406
0.000665	0.574
0.00200	0.674
0.00500	0.760
0.0110	0.880
0.0230	0.990
0.0470	1.00
0.0950	-
0.1910	-
0.3080	-
0.4145	-
0.5120	-
0.6275	-
0.7340	-
0.8405	-
0.9470	-

PLOT 1 CASE 0141 FILE 4

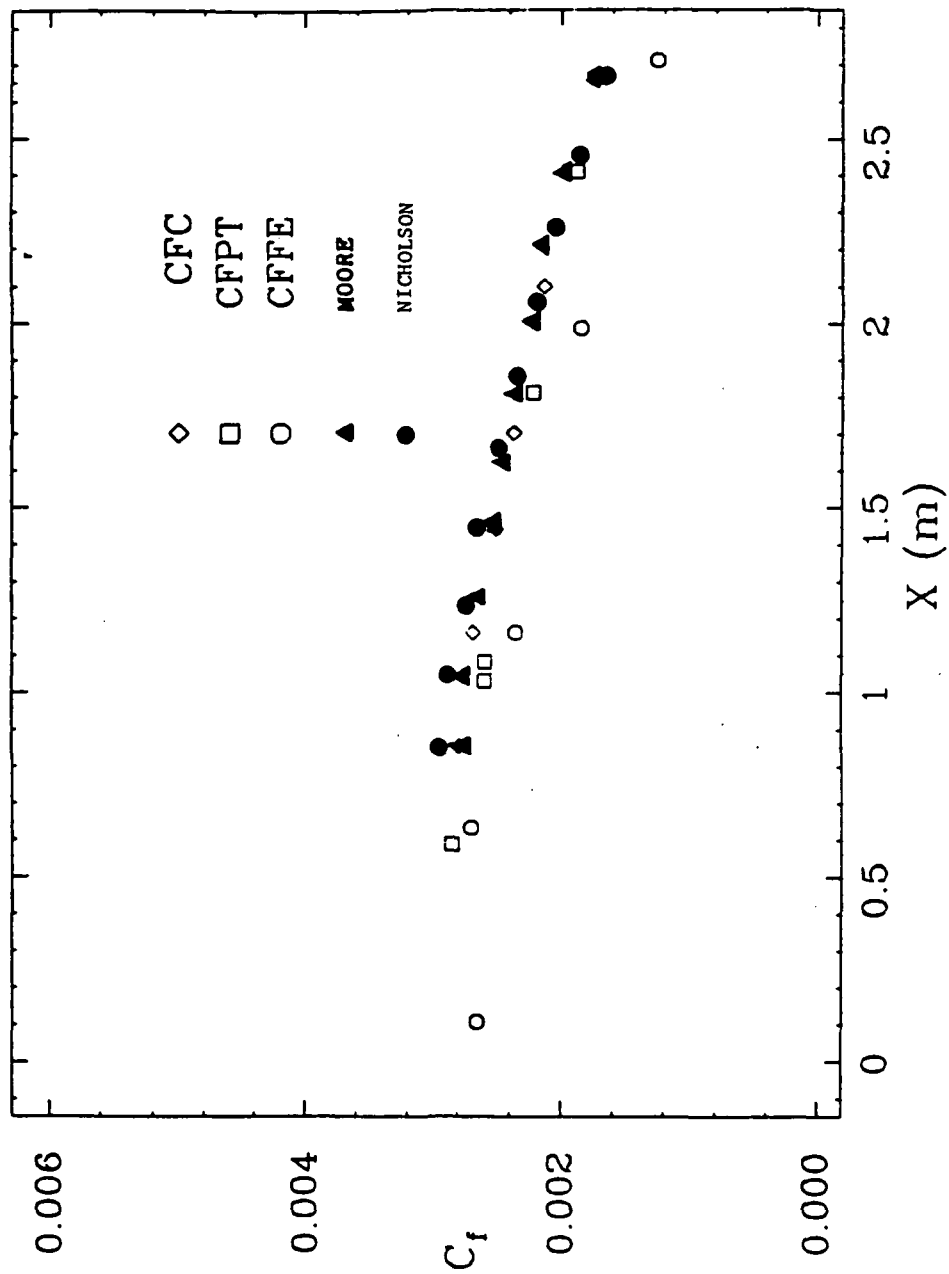
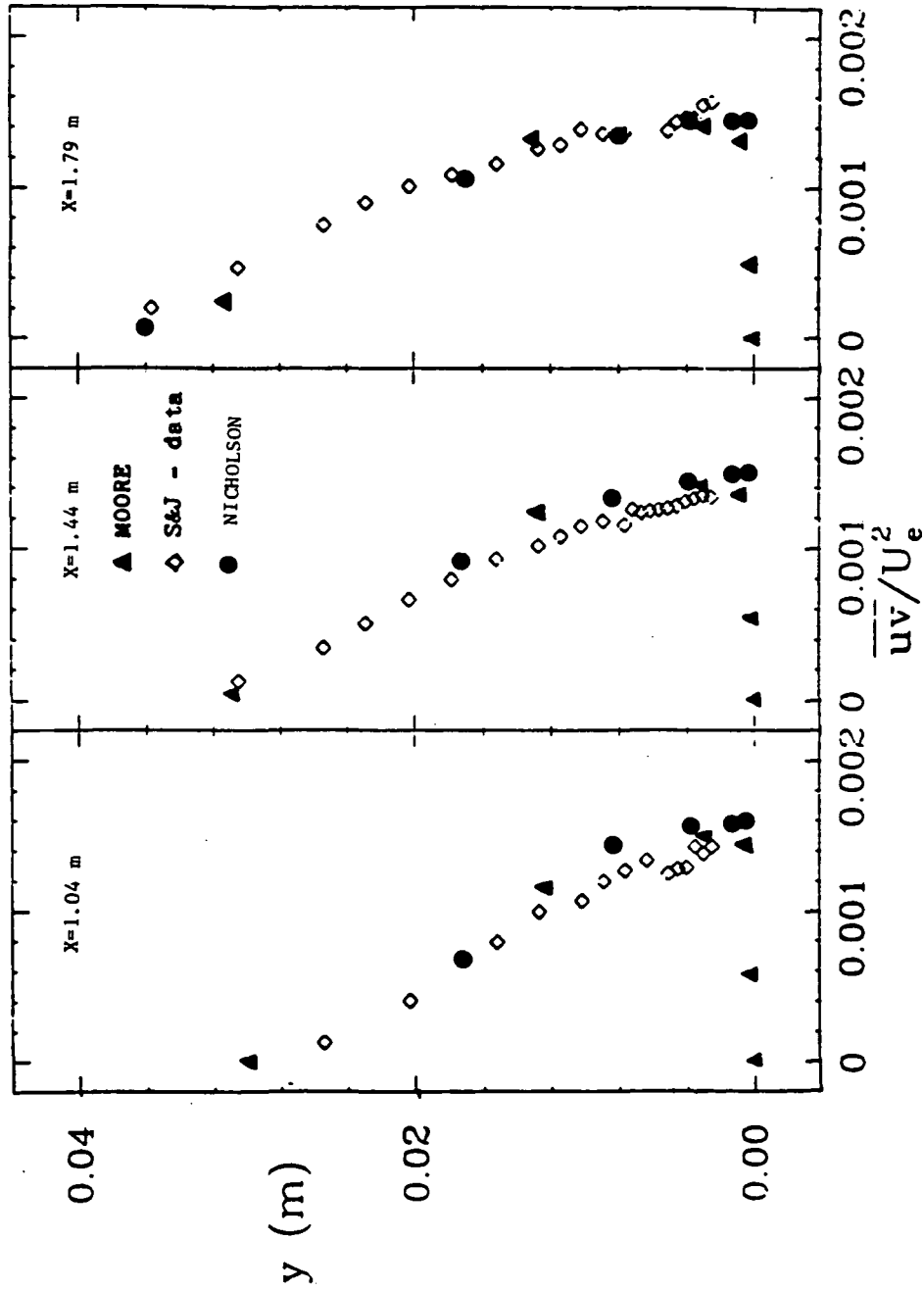
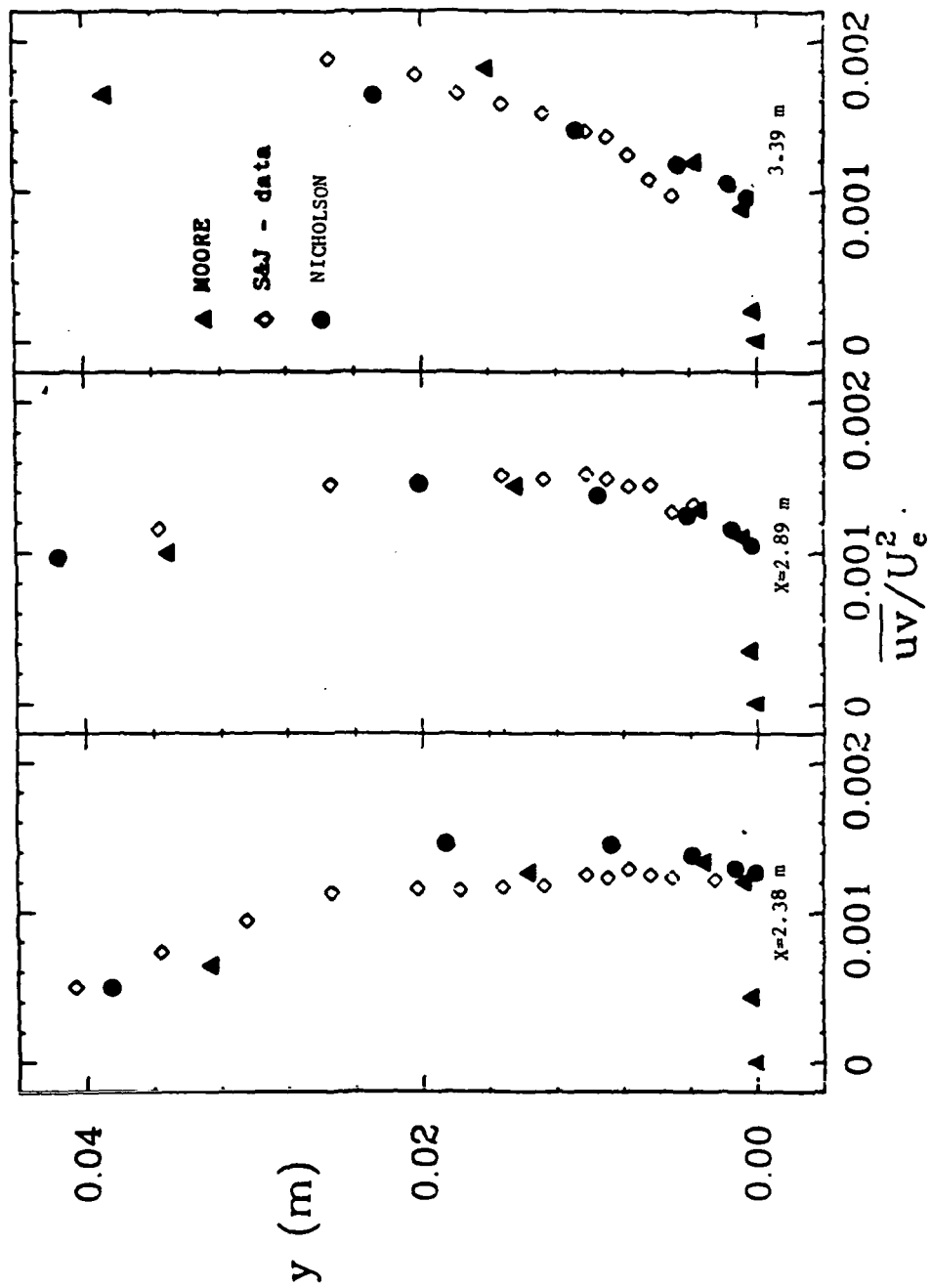


Fig. 3.6.2 Skin Friction Coefficient for Samuel and Joubert

PLOT 2 CASE 0141 FILE 25,26,27

Fig. 3.6.3 Shear Stress Distributions at $x = 1.04$ m, $x = 1.44$ m, and $x = 1.79$ m

PLOT 3 CASE 0141 FILE 28,29,30

Fig. 3.6.4 Shear Stress Distributions at $x = 2.38\text{m}$, $x = 2.89\text{m}$, and $x = 3.39\text{m}$

PLOT 4 CASE 0141 FILES 14,16

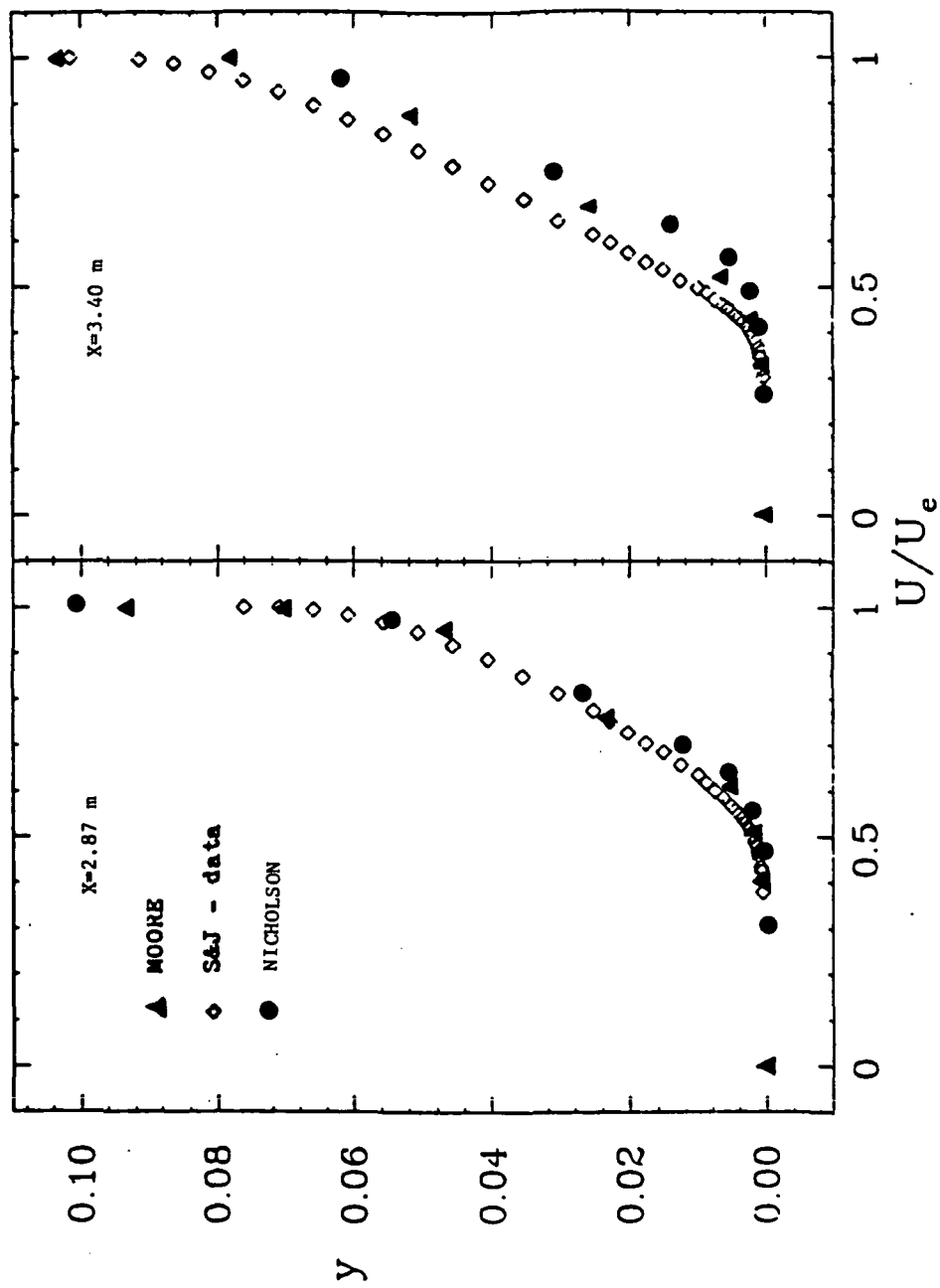


Fig. 3.6.5 Velocity Profiles for Samuel and Joubert Calculations

Fig. 3.6.5 shows a comparison of the calculated and measured velocity profiles at two locations in the duct. The agreement is good at $x = 2.87$ m, however, the calculated boundary layer at $x = 3.40$ m is thinner than the measurements. It is noteworthy that the program has been able to calculate an essentially incompressible flow ($M < 0.075$).

3.7 SAJBEN'S DIFFUSER CALCULATIONS

The diffuser geometry (Model G) (23) is shown in Fig. 3.7.1; the throat height ,h, was 44 mm and the ratio of the exit height to throat height was 1.513. The calculations begin at $x/h = -3.6$ and end at $x/h = 8.2$. Fig. 3.7.1 also shows the computational grid used which had 87 grid points in the axial direction and 20 points across the flow. The radial distribution of grid points used is shown in Table 3.7.1. The development of a turbulent boundary layer was modeled on both the curved and the flat walls. The inlet boundary layer thicknesses were specified as 9 % and 4.5 % of the inlet diffuser height for the curved and flat wall boundary layers, respectively. An absolute viscosity of 0.000018 kg/ m s was used. The inlet total pressure was 135 kPa and the inlet total temperature was 300 K.

For this calculation, the ratio of the exit static pressure to the inlet total pressure was 0.826. This computational exit static pressure is equal to the experimental exit static pressure plus a correction in pressure for the side wall boundary layer blockage. Suction slots upstream of the throat and downstream of the exit plane reduce the side wall boundary layer blockage and improve the two-dimensionality of the flow. However, the side wall boundary layers do affect the effective flow area of the diffuser and the two dimensional computations must reflect this when a suitable exit static pressure is chosen. Therefore the exit static pressure of 0.826 is 1.5 % greater than the experimental static pressure because of the blockage effect of the side wall boundary layers. In the experiment, this test point results in transonic flow in the diverging portion of the duct with a Mach number

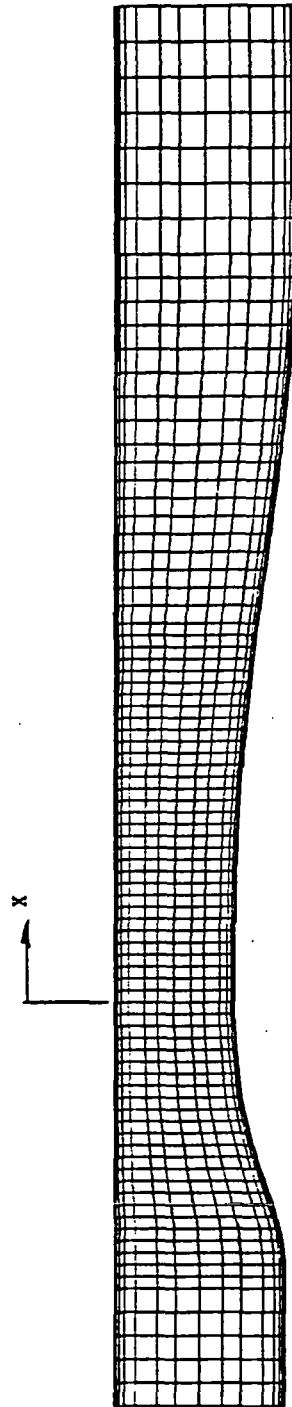


Fig. 3.7.1 Geometry and Grid For Sajben's Diffuser Calculations

Table 3.7.1 Transverse Distribution of Grid Points

1	0.0005
2	0.0020
3	0.0050
4	0.0110
5	0.0230
6	0.0470
7	0.0950
8	0.1910
9	0.3080
10	0.4305
11	0.5695
12	0.6920
13	0.8090
14	0.9050
15	0.9530
16	0.9770
17	0.9890
18	0.9950
19	0.9980
20	0.9995

of approximately 1.235 upstream of a nearly normal shock, and the flow remained fully-attached throughout the diffuser at this test condition.

A plot of static pressure contours is shown in Fig. 3.7.2. The shock can be seen in the diverging portion of the duct. The shock is well defined as illustrated by the high clustering of contours at the shock. The M&M formula (see section 2.4) is used to calculate the interpolated pressure which is used in the calculation of the effective density. Fig. 3.7.3 shows a Mach number contour plot for the calculations. The extent of the boundary layer can be seen from this figure.

The calculated and measured curved wall static pressures are compared in Fig. 3.7.4. The shock is very well defined and no overshoot occurs in the static pressure. The static pressures do not agree so well downstream of the shock because the 2-D calculations do not reflect the rapid increase in the side wall boundary layer thickness and its effective blockage. The point of minimum static pressure in the calculations is located at $x/h = 1.5$. This is taken to be the location of shock. The Mach number upstream of the shock was determined to be 1.256 from the calculated total pressure ratio across the shock in the freestream.

The computed and measured shock locations on the curved wall are compared in Fig. 3.7.5. The variable $x_{\sigma u}$ is the shock location on the curved wall and $x_{\sigma m}$ is the shock location in the middle of the duct. The Mach number upstream of the shock, determined from static pressure measurements, is represented by $M_{\sigma u}$ in Fig. 3.7.5.

The Mach number distribution through the nozzle at a fixed y/h of 0.0905 is shown in Fig. 3.7.6. This grid line was chosen because the maximum Mach number is located along it. The shock is sharp and no overshoots or undershoots occur.

Comparisons of calculated and measured velocity profiles (see Ref. 24) at four axial locations along the duct are shown in Figs. 3.7.7, 3.7.8, 3.7.9, and 3.7.10. The axial locations are $x/h = 2.31, 4.03, 6.34$, and 8.2 respectively. The agreement is good especially at the two downstream stations. The

5000 ITERATIONS PB=111.5 KPA
P AT C = 1.00

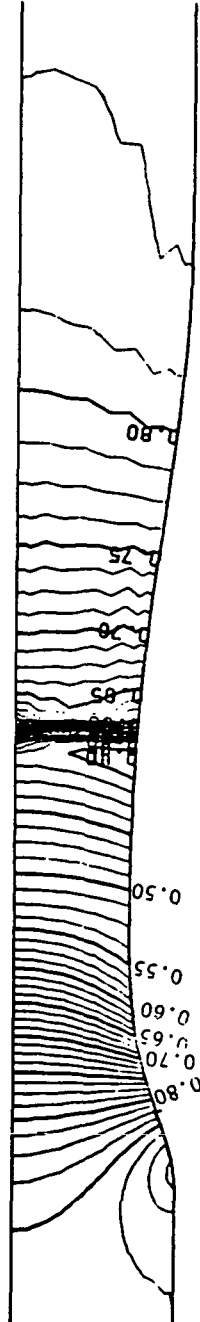


Fig. 3.7.2 Static Pressure Contours For Sajben's Diffuser

5000 ITERATIONS PB=111.5 KPA
MACH AT C = 1.00

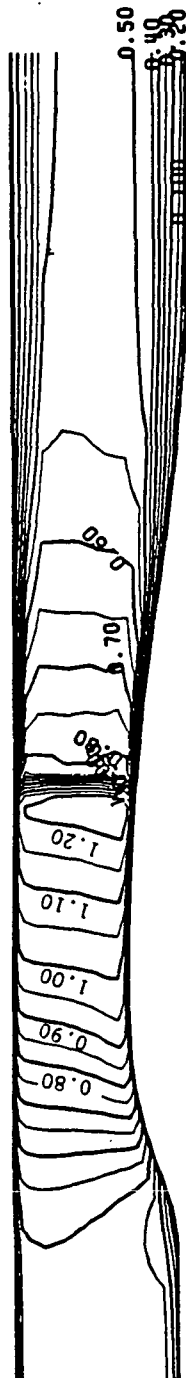


Fig. 3.7.3 Mach Number Contours For Sajben's Diffuser

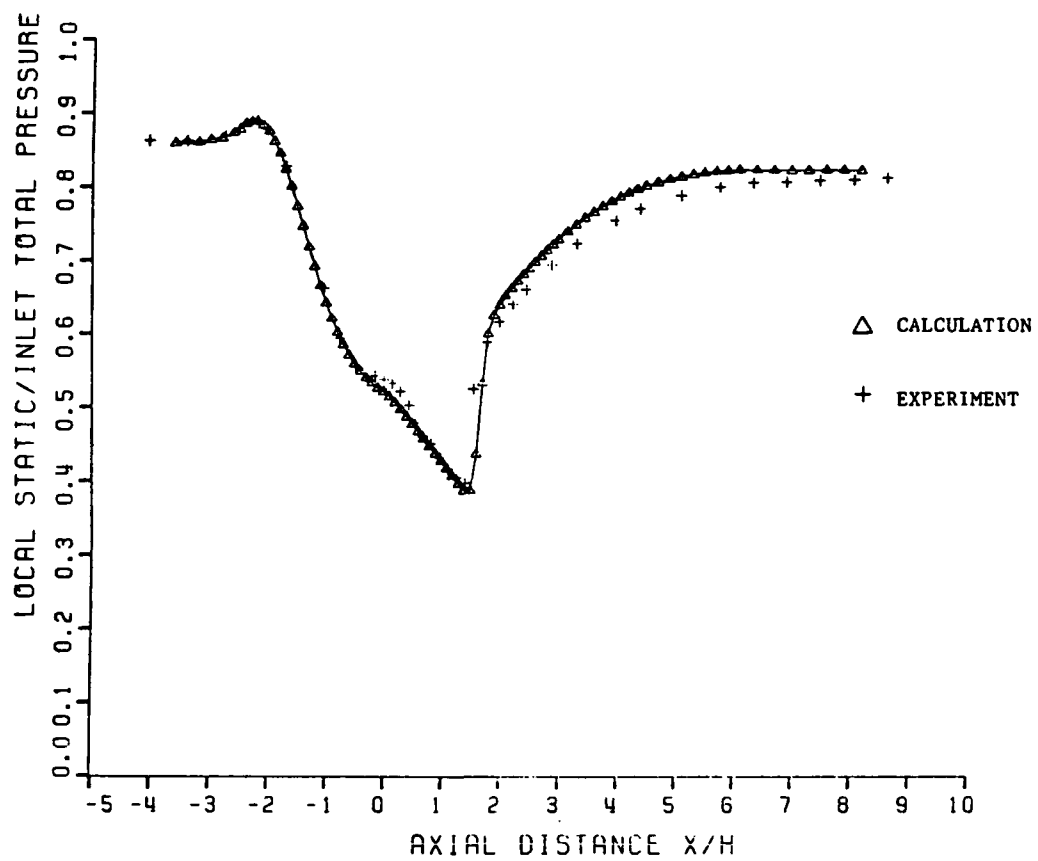


Fig. 3.7.4 Curved Wall Static Pressure For Sajben's Diffuser

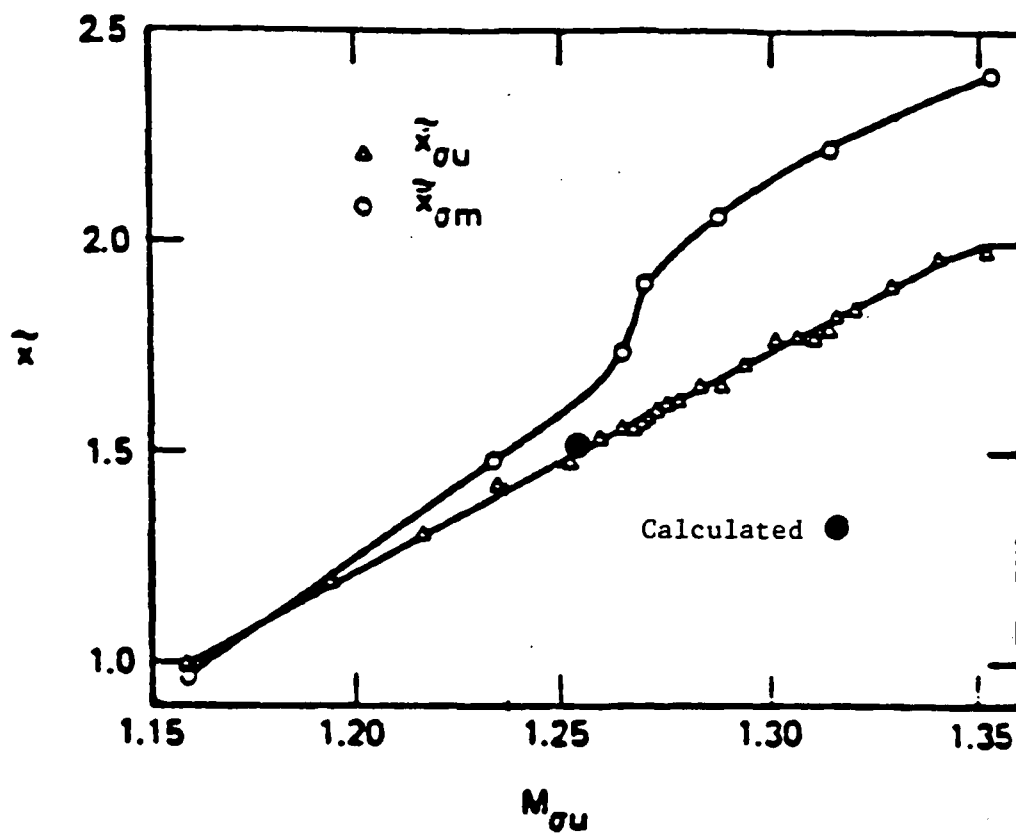


Fig. 3.7.5 Comparison of Computed and Measured Shock Position

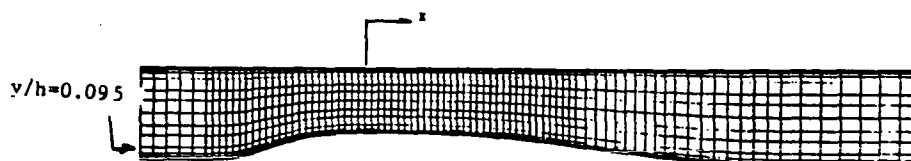
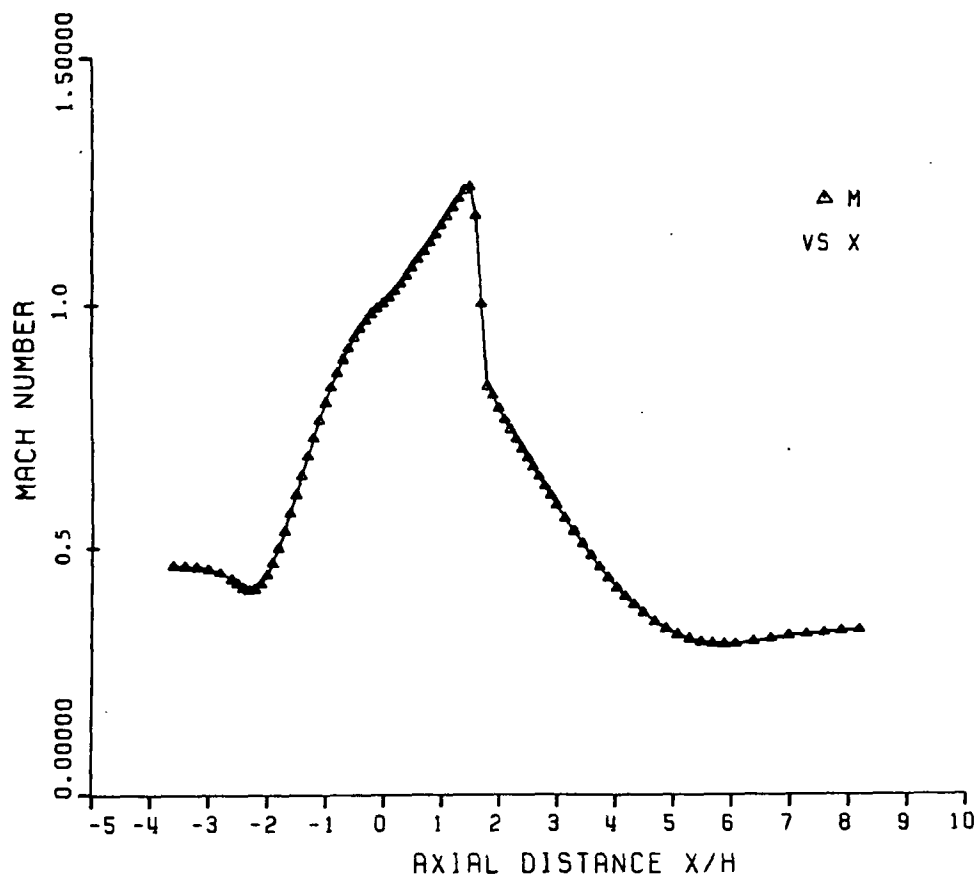


Fig. 3.7.6 Mach Number Along Grid Line at $y/h = 0.0950$

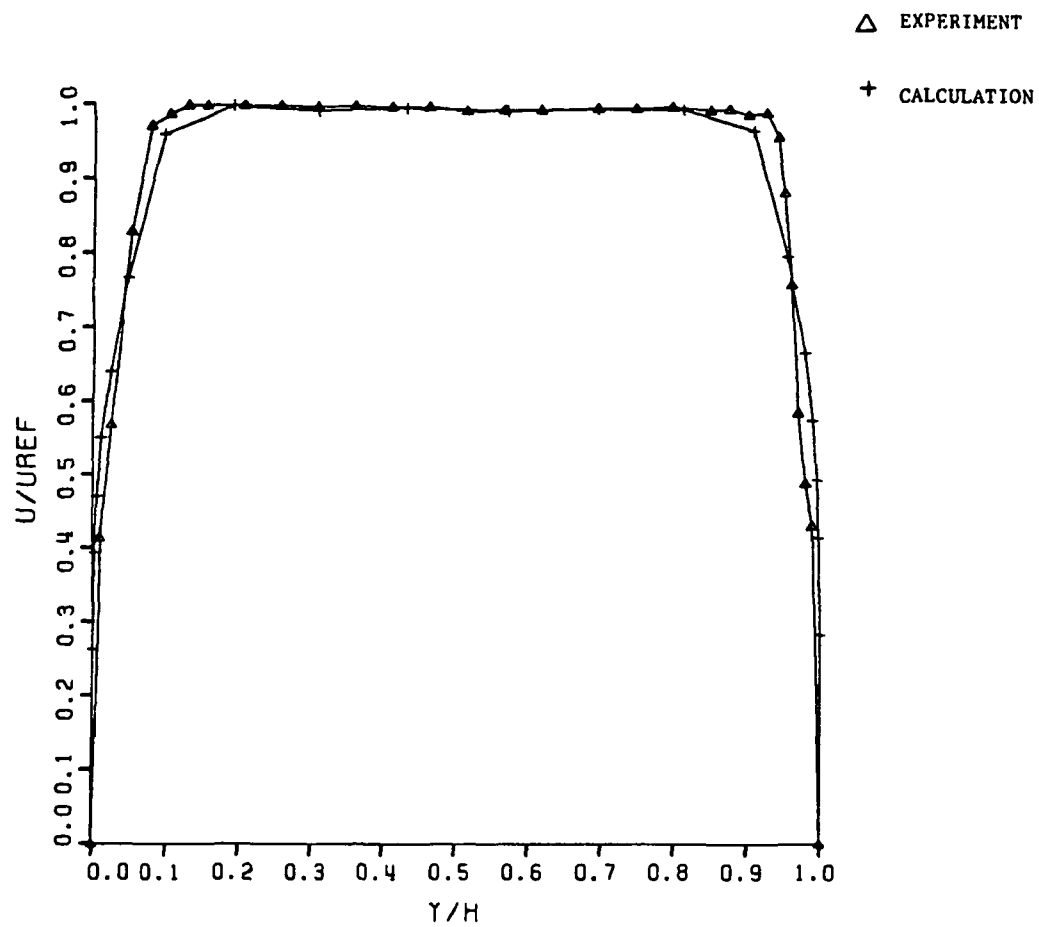


Fig. 3.7.7 Velocity Profile at $x/h = 2.31$

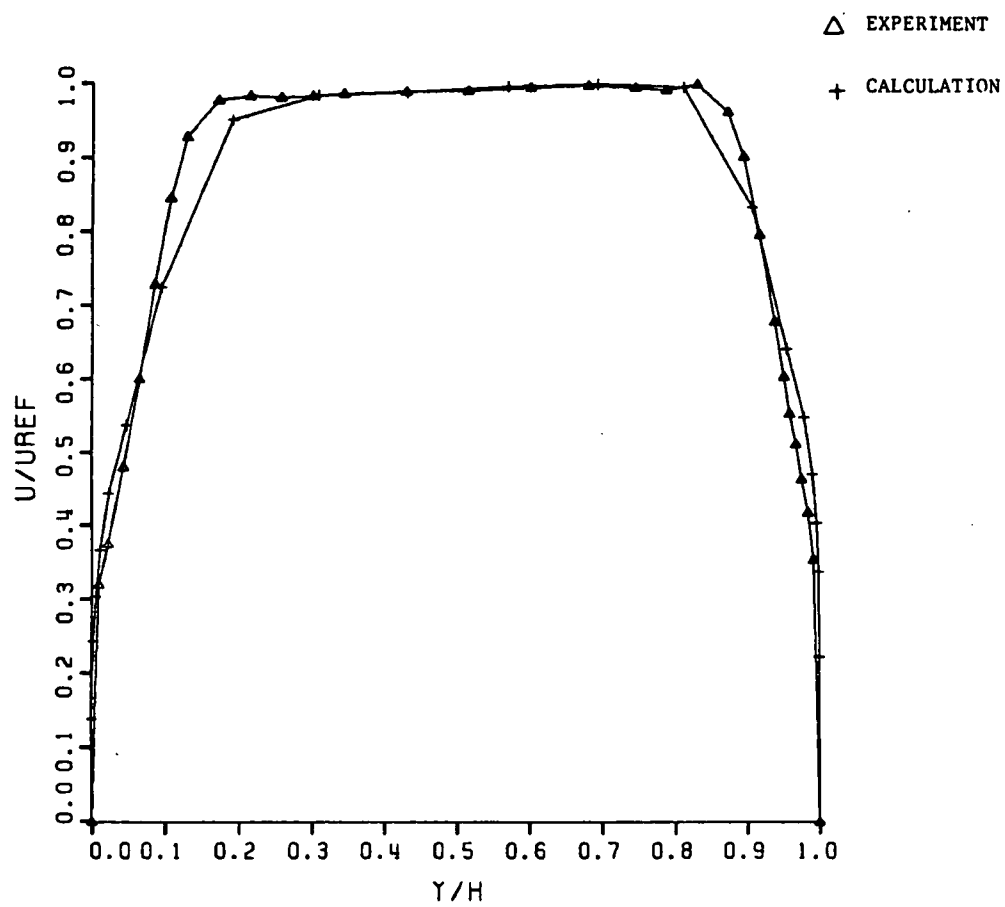


Fig. 3.7.8 Velocity Profile at $x/h = 4.03$

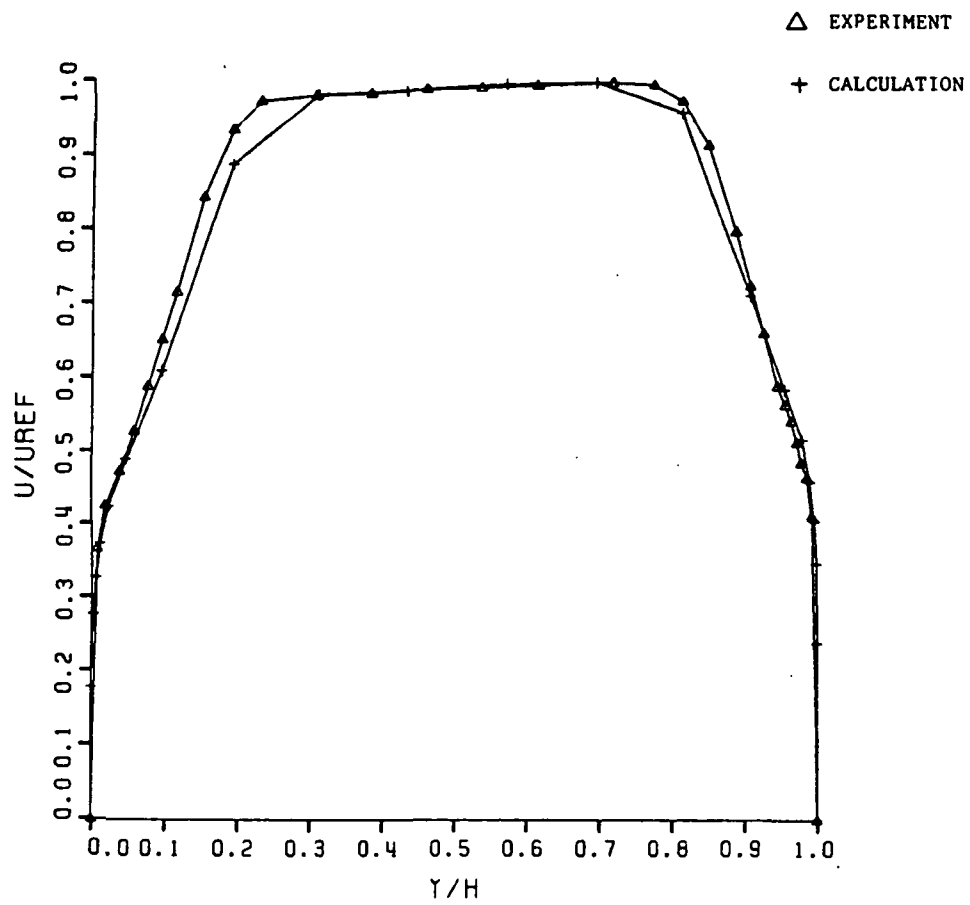


Fig. 3.7.9 Velocity Profile at $x/h = 6.34$

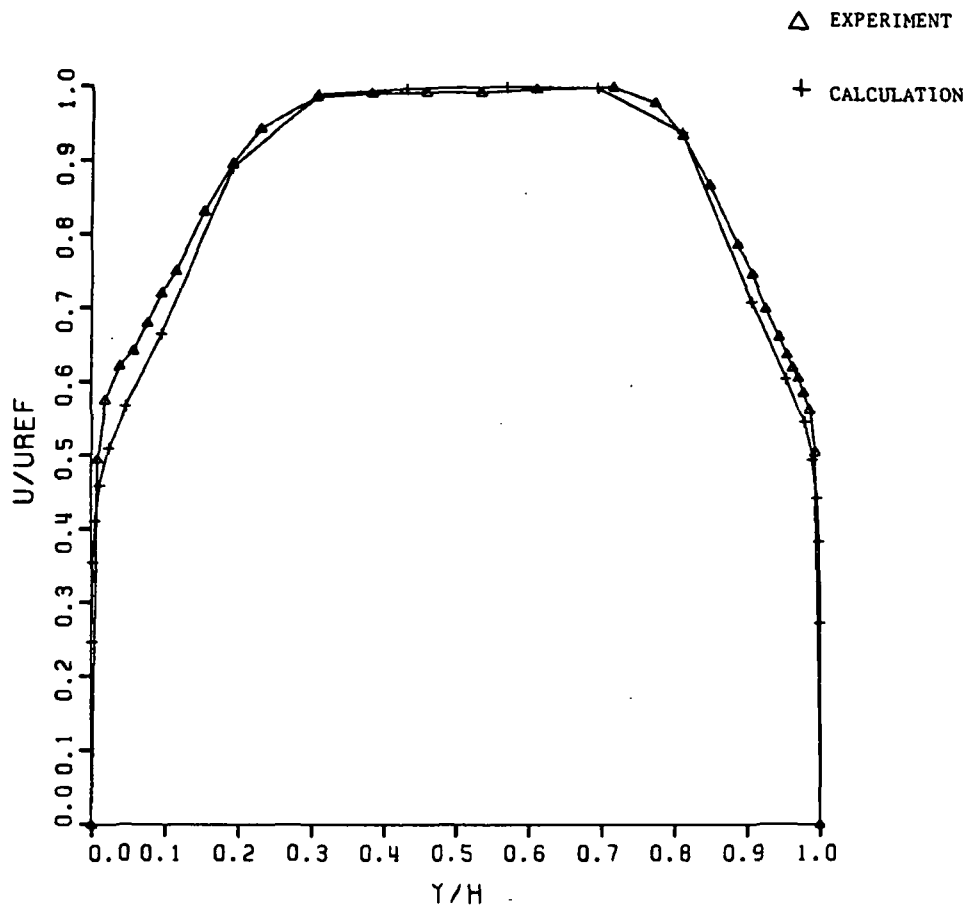


Fig. 3.7.10 Velocity Profile at $x/h = 8.20$

velocities in Figs. 3.7.7-3.7.10 are normalized with respect to the maximum computed or measured velocity in the duct at that axial location, which ever is applicable. In the calculations, the edge of the boundary layer is located where the normalized total pressure gradient is 25.0. It may be noted that the present calculations give much better agreement with the measured velocity profiles than the calculations of Liou, Coakley, and Bergmann of Reference 28 (see Fig. 3.7.17). Other investigators who have used Sajben's diffuser as a test case have not shown a comparison of their computed velocity profiles with the measurements of Ref. 24.

Fig. 3.7.11 shows static pressure contours for calculations which were made using the three-point scheme for the interpolated pressure. The shock resolution is not nearly as well defined as that obtained when the M&M formula is used. Fig. 3.7.12 shows the corresponding Mach number contour plot when the three point interpolation scheme is used.

The distribution of loss generation in the diffuser will be presented in three ways. First, the losses due to the curved wall boundary layer, the flat wall boundary layer, and the shock loss in the freestream are compared in Fig. 3.7.13. These losses were determined by first calculating the mass flow rates in the boundary layers and the freestream at the diffuser exit using the calculated boundary layer thicknesses as the boundaries between regions. Then the mass averaged total pressure loss at each axial location was calculated by integrating the total pressure loss out to these fixed mass flow rate values and then normalizing these losses with respect to the inlet freestream total pressure (see Table 3.7.2). All three losses are approximately the same. The curved wall (bottom wall) boundary layer contributes the largest proportion to the total losses because the boundary layer is thicker there.

The total pressure loss along an inviscid streamline is compared with the mass averaged total pressure loss for the entire cross-section of the diffuser in Fig. 3.7.14. This figure allows another means of comparing the shock and total losses. The total pressure loss through the shock is very well defined. The mass averaged total pressure loss through the shock is approximately 30% greater than the shock loss alone.

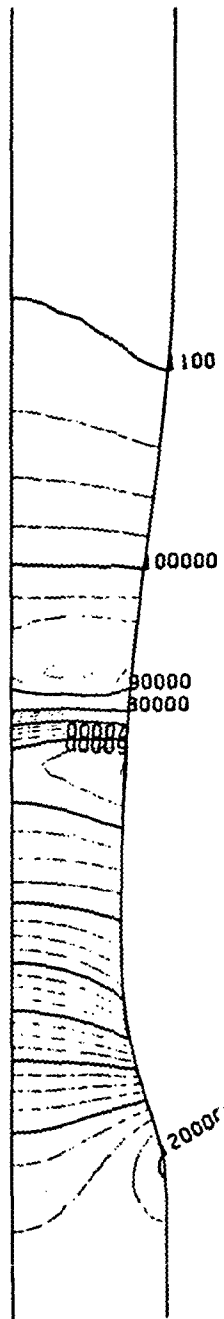


Fig. 3.7.11 Static Pressure Contours for Sajben's Diffuser Using Three Point Interpolation

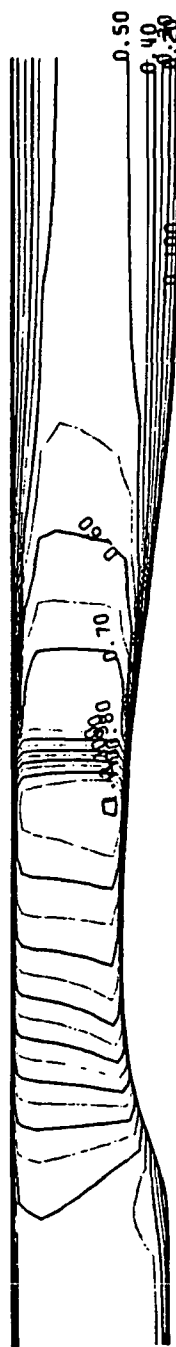


Fig. 3.7.12 Mach Number Contours for Sajben's Diffuser Using
Three Point Interpolation Scheme

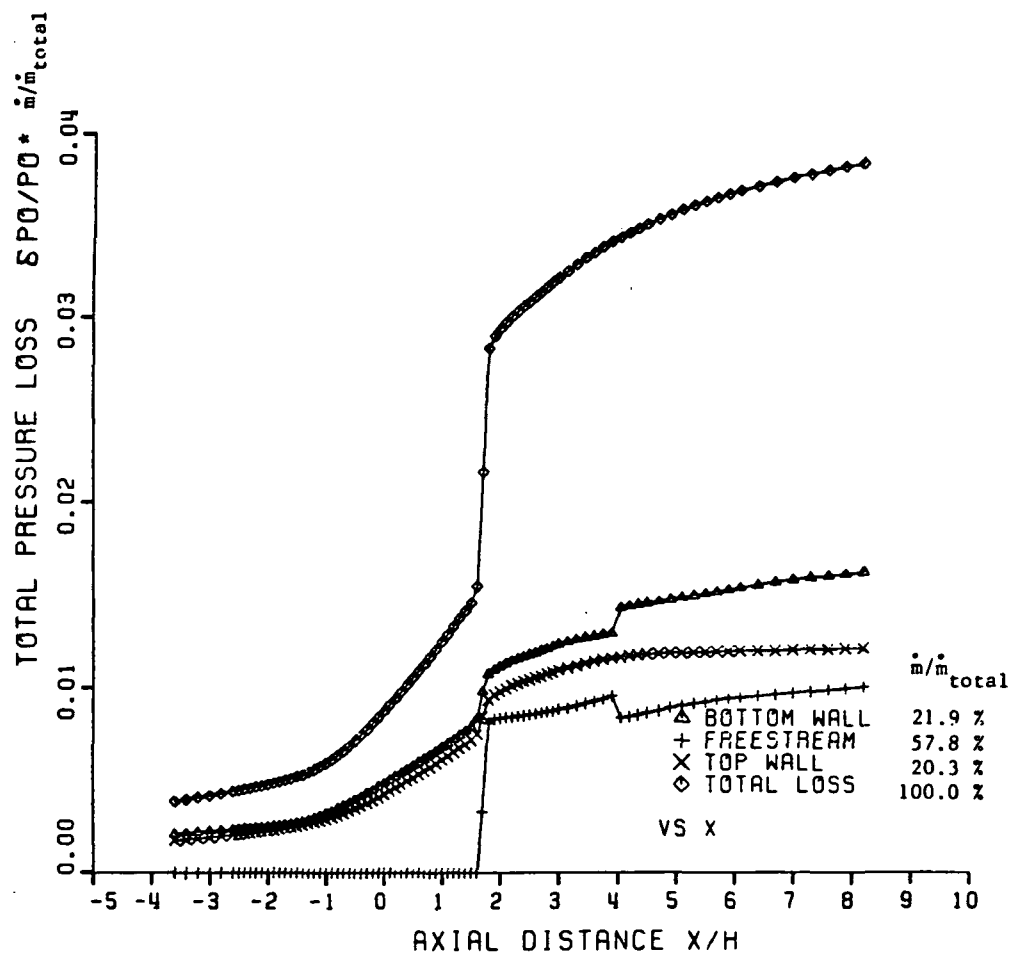


Fig. 3.7.13 Mass-Averaged Total Pressure Losses For Boundary Layer and Shock

Table 3.7.2 Example Calculation of Total Pressure
Loss for a Boundary Layer

$$\bar{P}_{t-\text{losses}} = \frac{\int_0^{\dot{m}_s} (P_{t-\text{inlet}} - P_{t-\text{local}}) \cdot d\dot{m}}{\dot{m}_{\text{total}}}$$

- * where \dot{m}_{total} is the total mass flow rate through a given cross-section of the diffuser, and \dot{m}_s is the mass flow rate in the boundary layer at the exit.

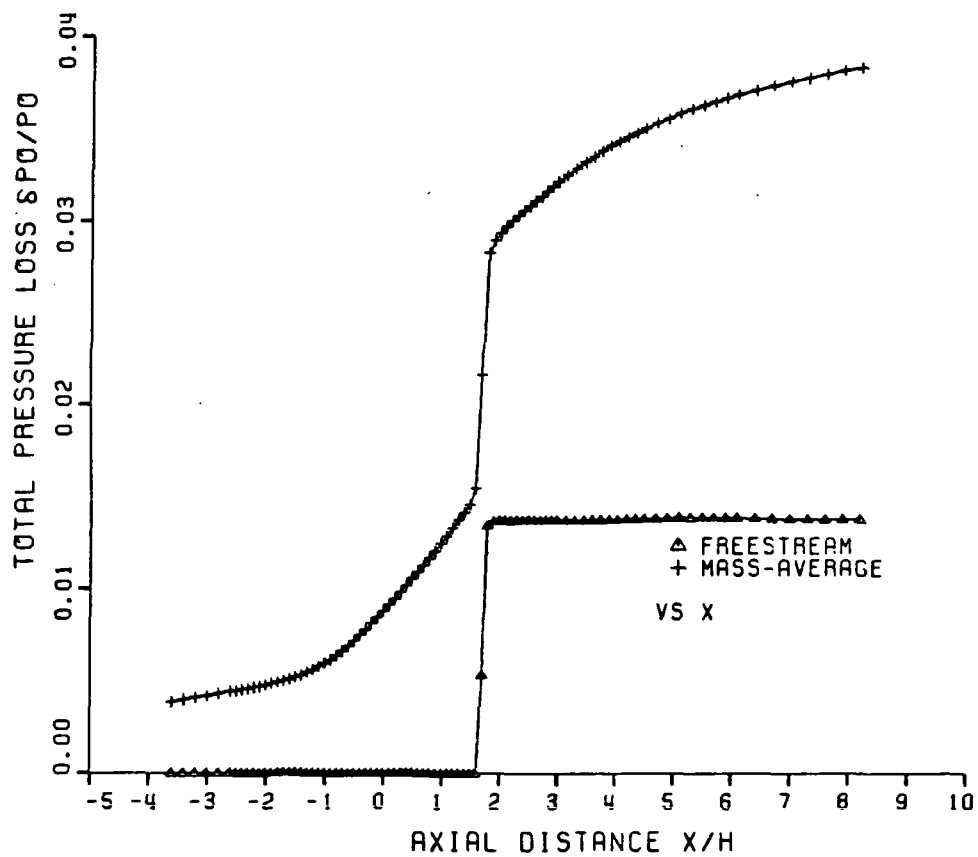


Fig. 3.7.14 Total Pressure Loss For Sajben's Diffuser Shock Vs Total Loss

The mass averaged total pressure divided by the inlet freestream total pressure at the diffuser exit is calculated from the numerical results to be 0.9615. From data given to us by M. Sajben and T. Bogar, the mass averaged total pressure calculated from the experimentally measured data is 0.965. The experimental data used for this calculation was measured midway between the side walls. The agreement is good.

The measured maximum Mach number in the exit plane of 0.51 agrees well with the calculated value of .511. The boundary layer thicknesses are measured to be approximately 25% of the duct height on the curved wall and 23 % of the duct height on the flat wall. The calculations determined the boundary layer thickness on the curved wall to be 25% of the duct height and 23% of the duct height of the flat wall.

The above calculations are after 5000 iterations using a TIMEF of 4.0. It may have been possible to run the calculation with a TIMEF of 2.0 after the initial transients but because of computer cost this option was not attempted for this test case. The momentum residual for this calculation is presented in Fig. 3.7.15. The continuity error after 5000 iterations was less than .1%. The unusual behavior observed between 3000-4000 iterations in Fig. 3.7.15 appears to be typical of the method in general when transonic flow is calculated. The same general convergence behavior is seen for the 1-D nozzle (Ref. 12) in Fig. 3.7.16. A time factor of 2.0 was used for these 1-D calculations but the same behavior is seen here on a smaller time scale. The total CPU time for the Sajben calculations was approximately 35 minutes on the IBM 3031.

A number of other workers have used this test case to verify the accuracy of their computational methods (28, 29, and 30). Liou, Coakley, and Bergmann's (28) calculations were made using a MacCormack type scheme in conjunction with a two-equation model for the turbulent stress predictions. For the weak shock case, they used an exit static pressure of $0.8 \times P_{t,inlet}$. There was good agreement between their computed and measured wall static pressures. However, the calculated velocity profiles were not in good agreement with the experimental data. Fig. 3.7.17 shows a sample of their results.

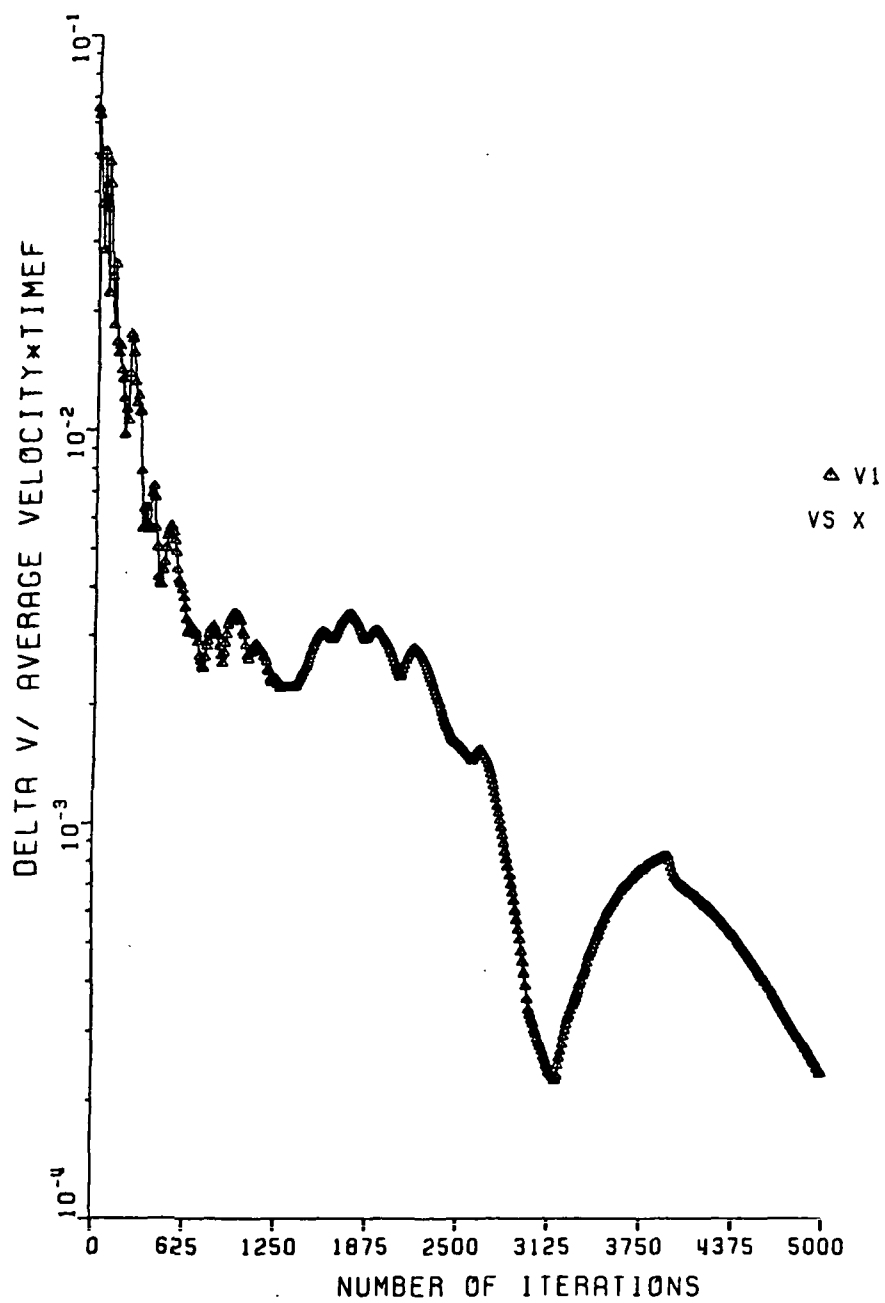


Fig. 3.7.15 Momentum Residual For Sajben's Diffuser

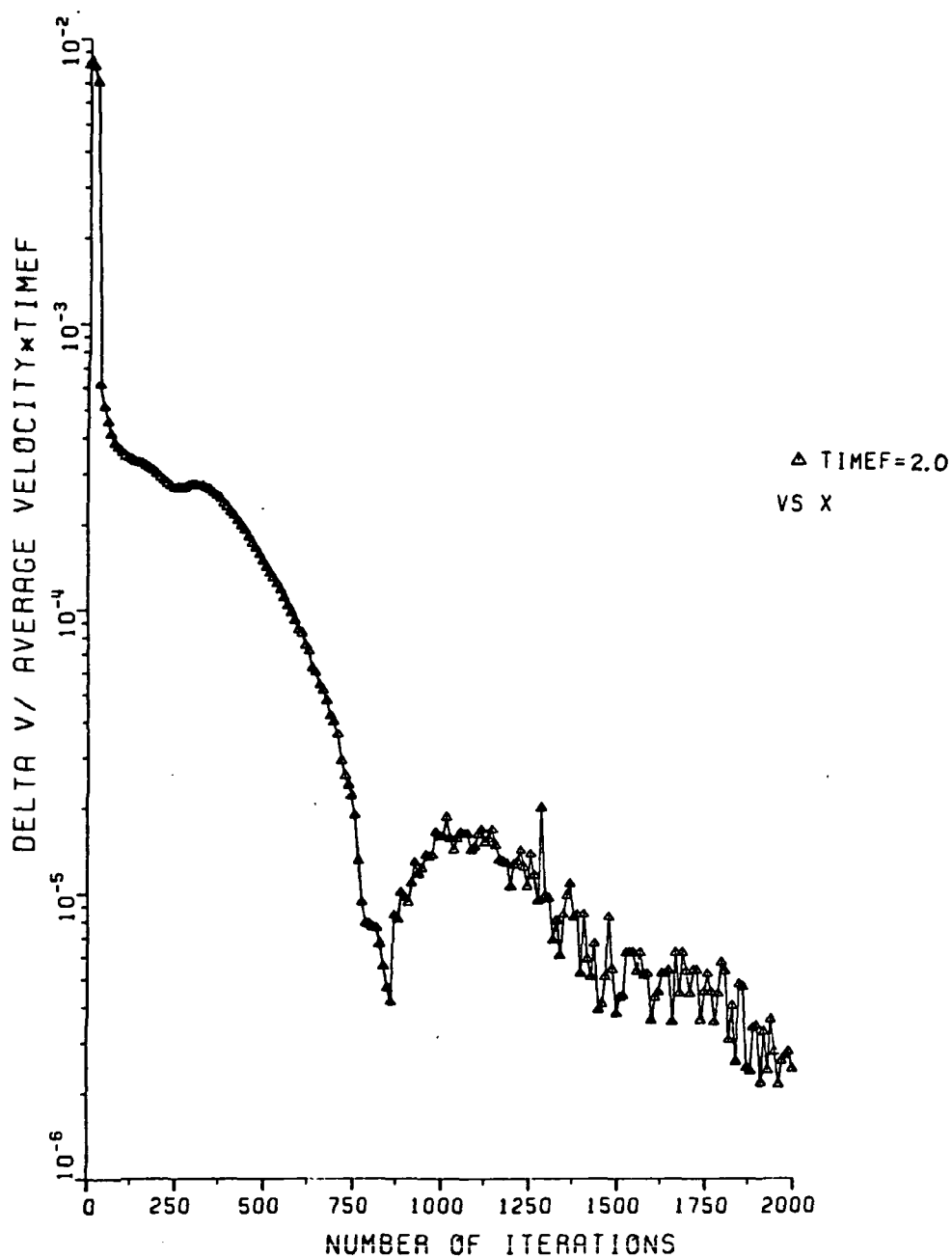


Fig. 3.7.16 Momentum Residual For Denton's Nozzle

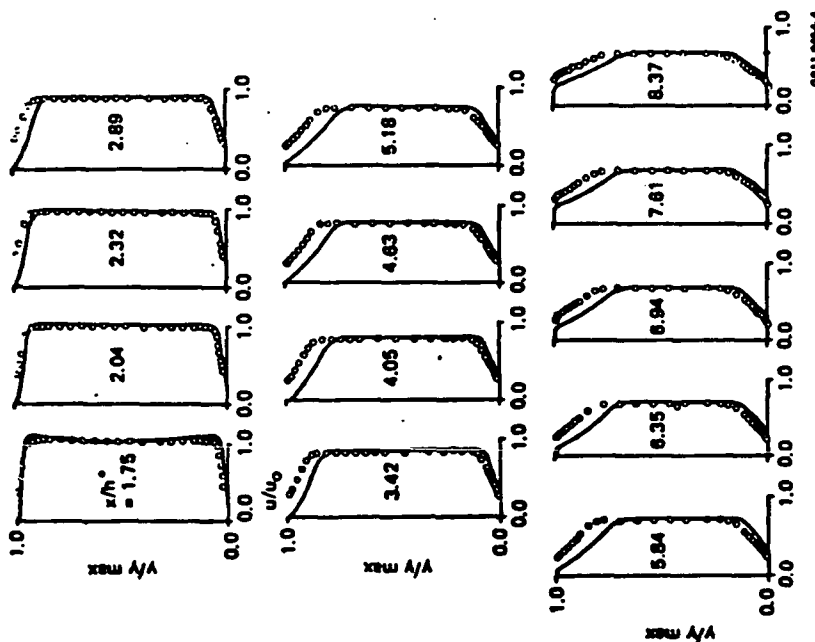


Fig. 7 Computed and measured velocity profiles. Model G.
 $R_p = 0.80$, $U_0 = 274$ m/s. ($\gamma_\infty = 10/9$,
 $Pr_t = Pr_b = 1.0$)

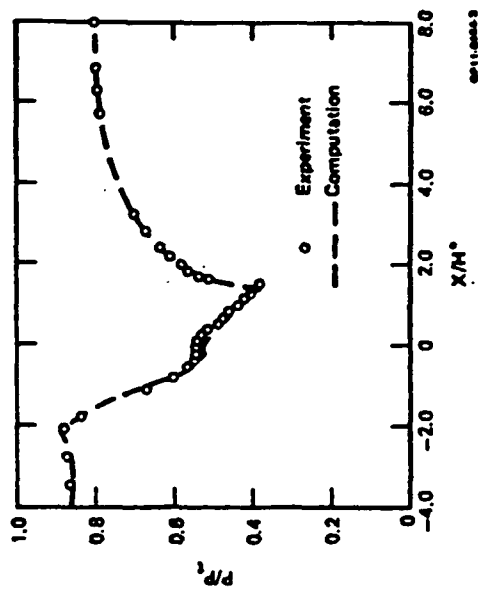


Fig. 6 Surface pressure distribution on upper wall. Model G.
 $R_p = 0.8$. ($\gamma_\infty = 10/9$, $Pr_t = Pr_b = 1.0$)

ORIGINAL PAGE IS
 OF POOR QUALITY

Fig. 3.7.17 Sample Results From Liou, Coakley, and Bergman

Liu, Shamroth, and McDonald (29) used this test case to verify their computational method which solves the governing equations using a consistently split linearized block implicit scheme. A mixing length model was used to model turbulent stresses. For the weak shock case, an exit static pressure of $0.807 \times P_{t,inlet}$ was used. They compared their computed wall static pressures with the experimental pressures and found good agreement (see Fig. 3.7.18). The variable σ , referred to in Fig. 3.7.18 is the value of the artificial dissipation parameter used in their calculations. They found that for values of σ less than 0.1 the solution was invariant. Also presented in Ref. 28 were static pressure and Mach number contour plots for this weak shock case. These contour plots are similar to those in Figs. 3.7.2 and 3.7.3. The shock definition in the present work is sharper than Liu et. al. but fewer axial grid points were used in their calculations. No comparison was made by Liu, Shamroth, and McDonald between the measured and computed velocity profiles.

Talcott and Kumar (30) also used the weak shock case for Sajben's diffuser as a test of their computer program's accuracy. They used an implicit MacCormack scheme to solve the governing equations and a Baldwin-Lomax mixing length turbulence model to predict the turbulent stresses. They also used an exit static pressure of $0.807 \times P_{t,inlet}$. Fig. 3.7.19 shows a sample of their results. They present a static pressure contour plot for this weak shock case. As with Liu et. al., the shock definition of Talcott and Kumar's method is not as sharp as that obtained using the present method but again they have used fewer axial grid points in their calculations. Also, the static pressure contours at the throat of the diffuser are erratic. A plot of wall static pressure is also presented. No comparison was made between the computed and measured velocity profiles.

In summary, the following observations can be made about the present calculations of the weak shock case in Sajben's diffuser.

1. There is better agreement between measured and calculated velocity profiles when the present method and static pressure specification are used.

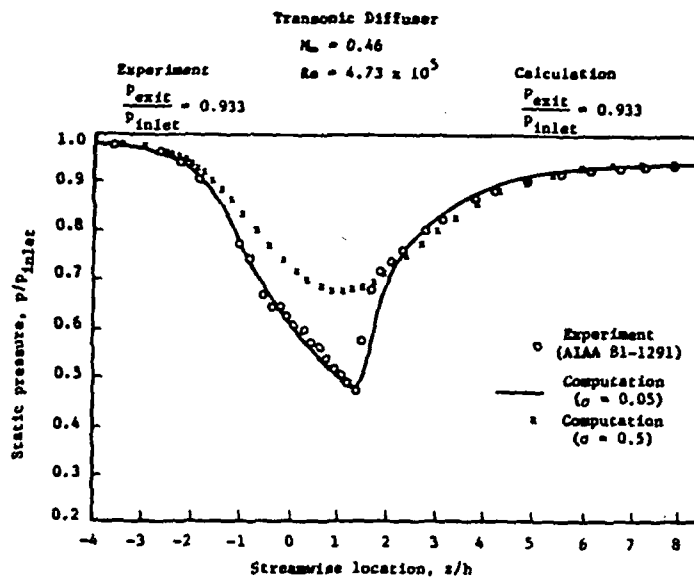
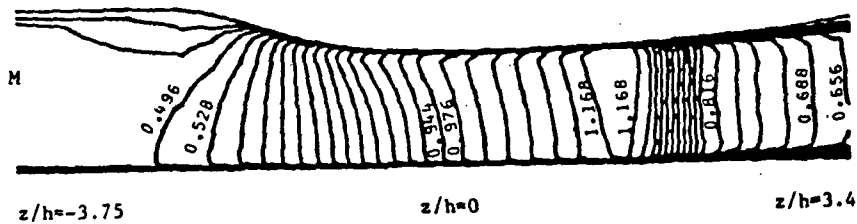
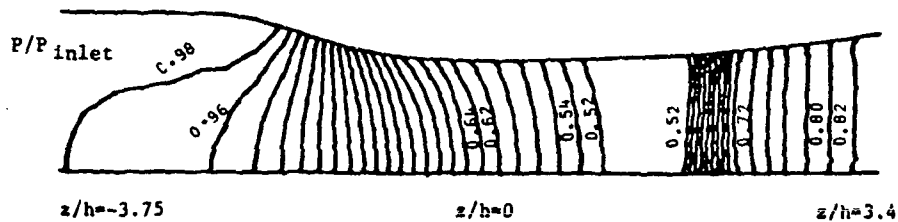


Fig. 3 - Bottom wall static pressure distribution.



(b) Transonic diffuser



(b) Transonic diffuser

Fig. 3.7.18 Sample Results From Liu, Shamroth, and McDonald

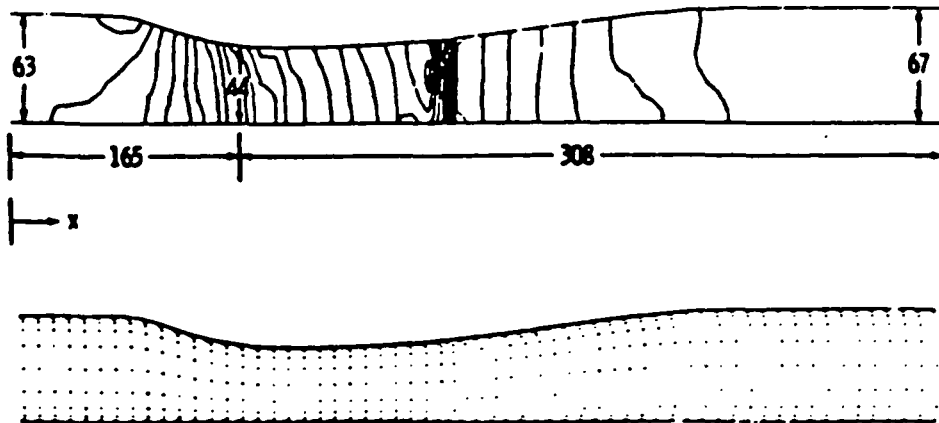


Fig. 2 Pressure contours and velocity vector field in inlet for turbulent flow ($P_b/P_i = 0.933$, $M_i \approx 0.46$).

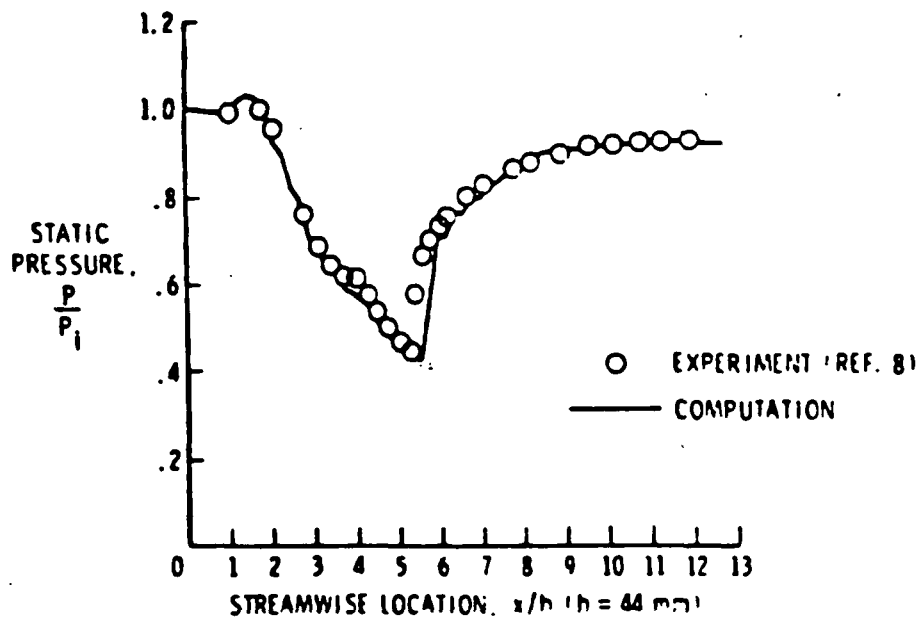


Fig. 3 Pressure distributions on the top surface of the inlet for turbulent flow ($M_i \approx 0.46$).

Fig. 3.7.19 Sample Results From Talcott and Kumar

2. The present method compares favorably with other methods in the areas of static pressure and Mach number contour predictions and wall static pressure prediction.
3. The agreement between calculated and measured mass averaged total pressure losses for the diffuser is excellent.

3.8 ENERGY EQUATION TEST CASES

A number of test cases will be used to explore various aspects of the more complete form of the energy equation discussed in section 2.10 (ENERGY EQUATION). In order of presentation, the test cases are

1. turbulent boundary layer flow in an adverse pressure gradient with an inlet freestream Mach number of 0.55.
2. flat plate turbulent boundary layer with a freestream Mach number of 0.95.
3. Sajben's diffuser calculations including the energy equation.
4. flat plate turbulent boundary layer with a freestream Mach number of 2.8.

Unless otherwise noted, the turbulent Prandtl number is a constant of 0.90 and the laminar Prandtl number is 0.73. The walls are adiabatic in all the calculations.

TURBULENT BOUNDARY LAYER IN AN ADVERSE PRESSURE GRADIENT

The geometry and grid used in this test case are identical to that used in Section 3.6 (Samuel and Joubert). The exit static pressure was reduced to $0.91P_{t,inlet}$ so that the inlet freestream Mach

number was increased to 0.55. The same inlet velocity profile was specified as in section 3.6. The purpose of this test case was to illustrate the advantage of the new formulation of the energy equation that was discussed in Section 2.10.

The work done due to pressure forces in the energy equation is

$$\text{work done due to pressure forces} = - \iint P \underline{u} \cdot d\underline{A} .$$

In the new formulation of the energy equation, the term

$$+ \frac{\bar{P}}{\rho} \iint \rho \underline{u} \cdot d\underline{A} \quad (3.8.1)$$

was added to the calculation of the energy error for the transient solution. The purpose of including this additional term, Eq. 3.8.1, was to remove the continuity error contribution to the energy error caused by the work done due to pressure forces. If the base form of the energy equation

$$\begin{aligned} \rho \frac{\delta e_t}{\delta t} \times \delta Vol = & - \iint \rho \underline{u} e_t \cdot d\underline{A} + \bar{e}_t \iint \rho \underline{u} \cdot d\underline{A} - \iint -k \nabla T \cdot d\underline{A} \\ & + \iint [\underline{u} \cdot (\mu \nabla \underline{u} + \mu \overline{\nabla \underline{u}^T})] \cdot d\underline{A} - \iint P \underline{u} \cdot d\underline{A} . \end{aligned} \quad (3.8.2)$$

is used in the current method, the transient solution results in a static temperature profile like that shown in Fig. 3.8.1 (represented as + 's). If the new form of the energy equation

$$\begin{aligned} \rho \frac{\delta h_t}{\delta t} \times \delta Vol = & \gamma - \iint \rho \underline{u} h_t \cdot d\underline{A} + \bar{h}_t \iint \rho \underline{u} \cdot d\underline{A} - \iint -k \nabla T \cdot d\underline{A} \\ & + \iint [\underline{u} \cdot (\mu \nabla \underline{u} + \mu \overline{\nabla \underline{u}^T})] \cdot d\underline{A} \end{aligned} \quad (3.8.3)$$

is used, the transient solution results in a static temperature profile like that shown in Fig. 3.8.1 (represented as triangles). The results presented in Fig. 3.8.1 are from calculations after 500 iterations. It can clearly be seen that the new formulation gives a better transient solution to the energy equation and it should therefore result in a reduction in the computer time required to reach a

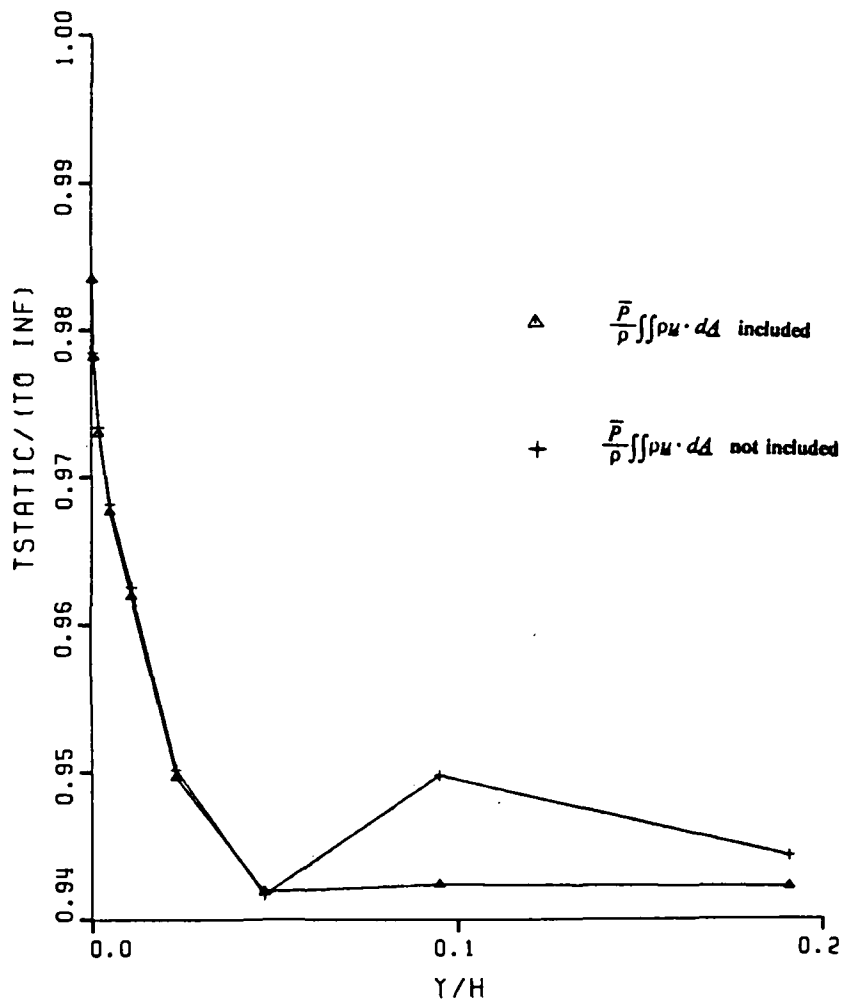


Fig. 3.8.1 Static Temperature Distribution Through The Boundary Layer For Samuel and Joubert Geometry at $M=0.55$, $x=200$ mm

steady state solution. Fig. 3.8.2 shows the corresponding total temperature profiles for the two formulations of the energy equation.

FLAT PLATE BOUNDARY LAYER AT $M = 0.95$

A turbulent boundary layer was calculated on the bottom wall of the geometry shown in Fig. 3.8.3. The height of the duct was 50 mm and the length of the duct was 200 mm. The computational grid shown in Fig. 3.8.3 consists of 21 axial grid points and 13 transverse grid points. The transverse distribution of grid points is shown in Table 3.8.1. The inlet boundary layer thickness was specified to be 10 % of the duct height. This grid placed 8 node points within the boundary layer. An absolute viscosity of 0.000018 kg/m s was used. The inlet total pressure was 105 kPa and the inlet total temperature was 300 K. The exit static pressure was $0.559 \times P_{t,inlet}$ which results in freestream Mach number of approximately 0.95.

The total temperature distribution through the boundary layer at the exit of the duct is shown in Fig. 3.8.4. The total temperature at the near wall point ($y/h = 0.0001665$) is 296.63 K which results in a recovery factor

$$r = \frac{(T_{aw} - T_{\infty})}{(T_{0\infty} - T_{\infty})} \quad (3.8.4)$$

of 0.927, where T_{aw} is the adiabatic wall temperature, T_{∞} is the freestream static temperature, and $T_{0\infty}$ is the freestream total temperature. The recovery factor for turbulent flow can be estimated by

$$r = Pr^{1/3} \quad (3.8.5)$$

For a Prandtl number of 0.73, the recovery factor is calculated from Eq. 3.8.5 to be 0.90. If an additional node point was located at $y/h = 0.000055$, the total temperature distribution remained essentially unchanged, however, the recovery factor changed to 0.910 because of the improved resolution of the flow near the wall. To calculate the recovery factor with reasonable accuracy, it

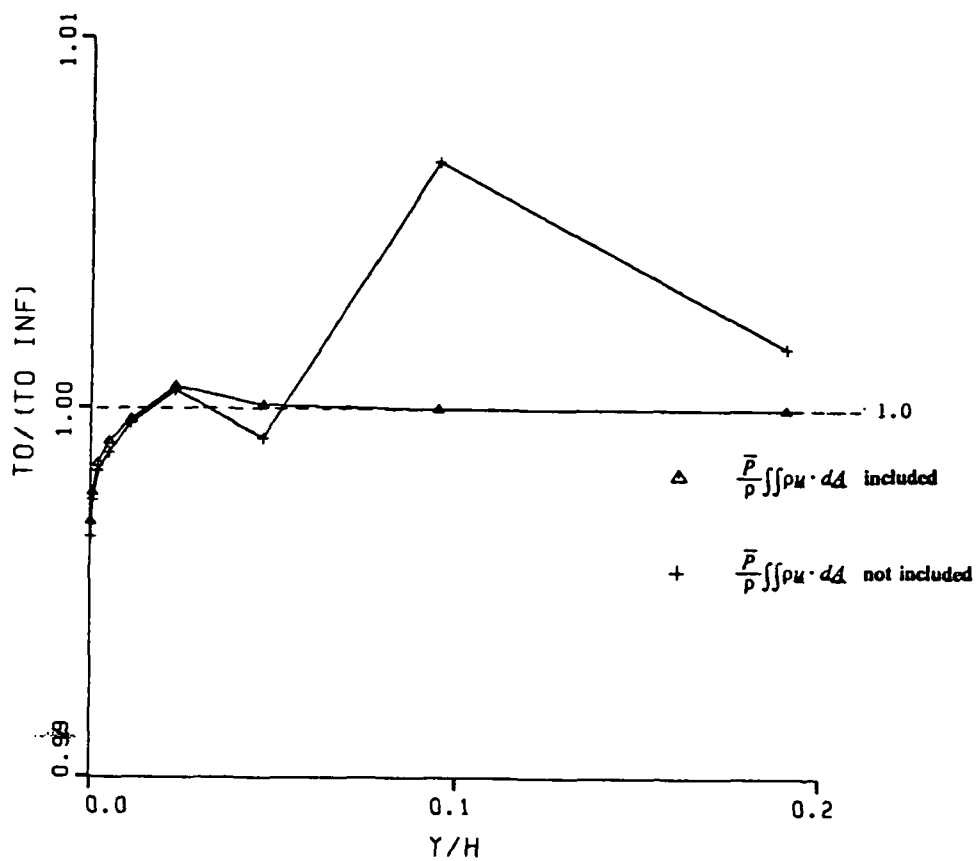


Fig. 3.8.2 Total Temperature Distribution Through The Boundary Layer For Samuel and Joubert Geometry at $M=0.55$, $x=200$ mm

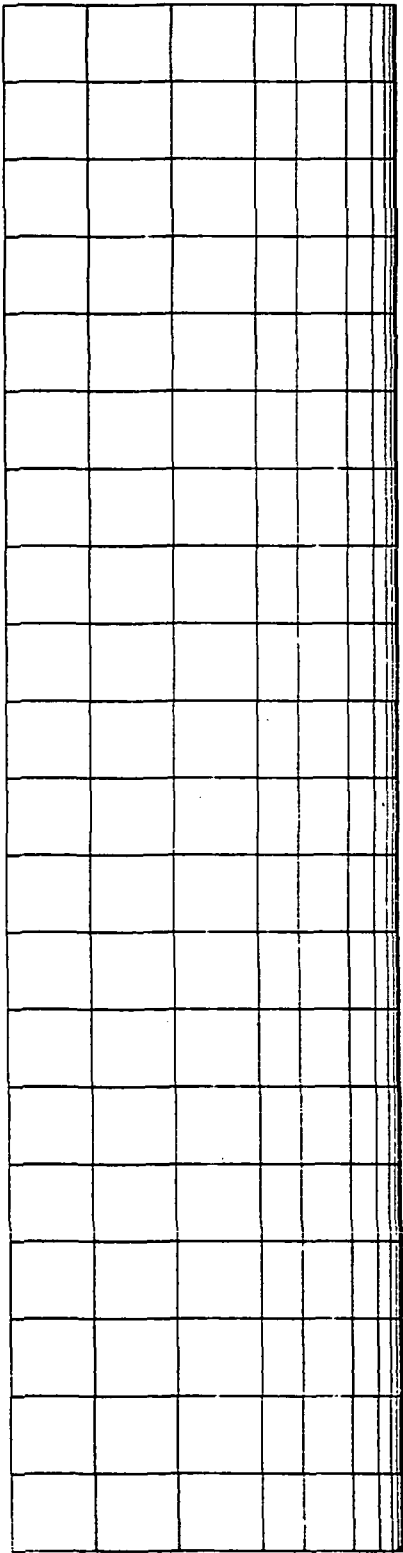


Fig. 3.8.3 Geometry and Grid For Boundary Layer Calculations at $M = 0.95$

Table 3.8.1 Transverse Distribution of Grid Points
For M = 0.95 Test Case

1	0.0001665
2	0.000665
3	0.0020
4	0.005
5	0.011
6	0.023
7	0.047
8	0.095
9	0.191
10	0.308
11	0.4675
12	0.6805
13	0.8935

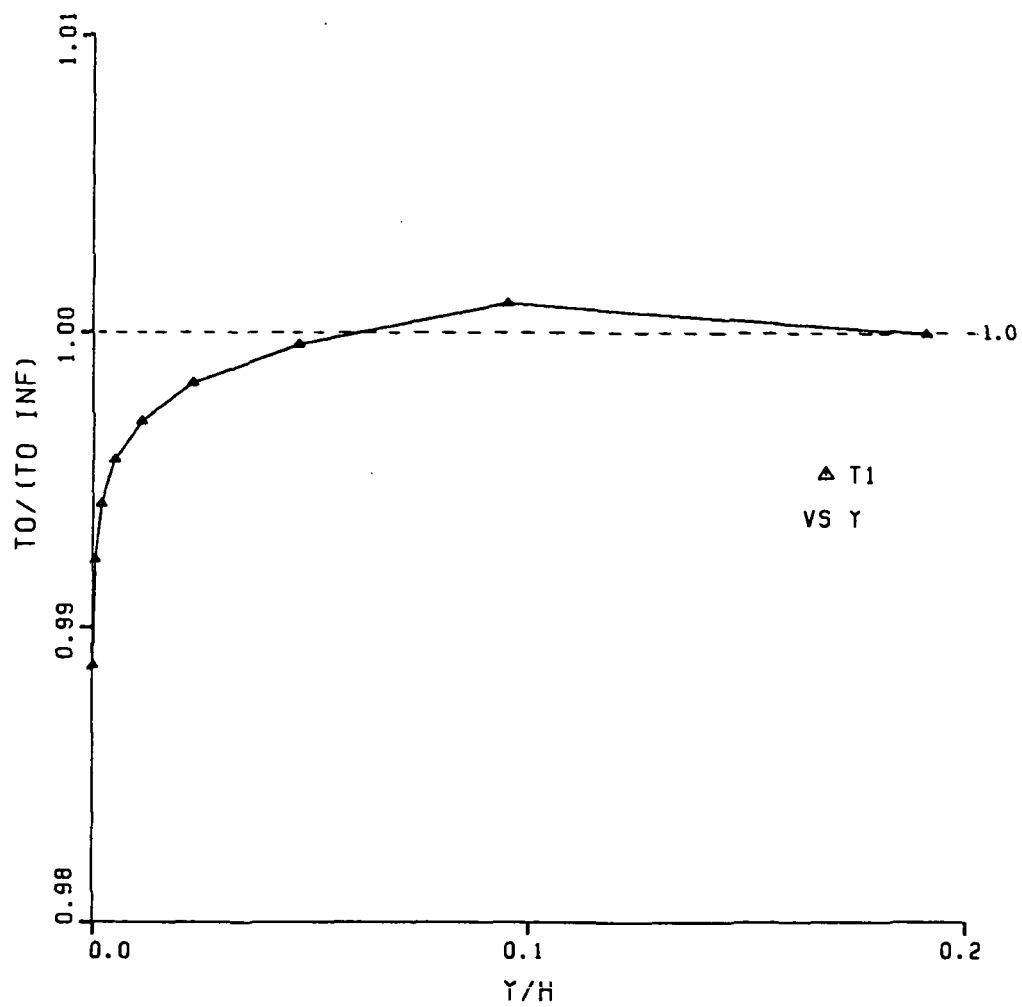


Fig. 3.8.4 Total Temperature Distribution For Flat Plate Boundary Layer at $M = 0.95$

was found that the near wall control volume boundary in the calculations needed to be at a distance of $y_+ < 10$.

Beginning at the wall, the total temperature shown in Fig. 3.8.4 is first less than freestream total temperature and then in the outer part of the boundary layer the total temperature becomes greater than the freestream total temperature. Since energy should be conserved for this adiabatic wall case, the mass averaged difference between the freestream and local total temperature should be conserved in this boundary layer. The quantity,

$$H = \sum \frac{\rho u (T_0 - T_{0\infty})}{\rho_{\infty} u_{\infty} T_{0\infty}} \frac{\Delta y}{\delta} \quad (3.8.6)$$

is plotted in Fig. 3.8.5. The residual does not go to zero at the freestream, however, the mass averaged total temperature for the boundary layer was $.999987 T_{0\infty}$.

When a laminar and turbulent Prandtl number of 1 was used in the calculations, the total temperature was essentially uniform throughout the boundary layer ($T_{sw} = 0.99997 T_{0\infty}$).

SAJBEN'S DIFFUSER CALCULATIONS INCLUDING THE ENERGY EQUATION

Calculations were made in Section 3.7 of transonic flow in Sajben's diffuser with the assumption of constant total temperature. The calculations were restarted here at 5000 iterations with the energy equation included. An additional 1500 iterations were required for these calculations to converge sufficiently. The boundary conditions and grid are identical to those discussed in Section 3.7.

A plot of static pressure contours is shown in Fig. 3.8.6. Fig. 3.8.7 shows a Mach number contour plot for the calculations. The results are essentially the same as those seen in Section 3.7 (see Figs. 3.7.2 and 3.7.3). The velocity profiles at an $x/h = 7.9$ are compared in Fig. 3.8.8. The profiles are very similar and the assumption of constant total temperature results in a solution which is only slightly different than the calculations that were made using the full form of the energy equation. Total temperature profiles are presented in Fig. 3.8.9 at two axial locations ($x/h = 0.9$ and $x/h = 2.3$)

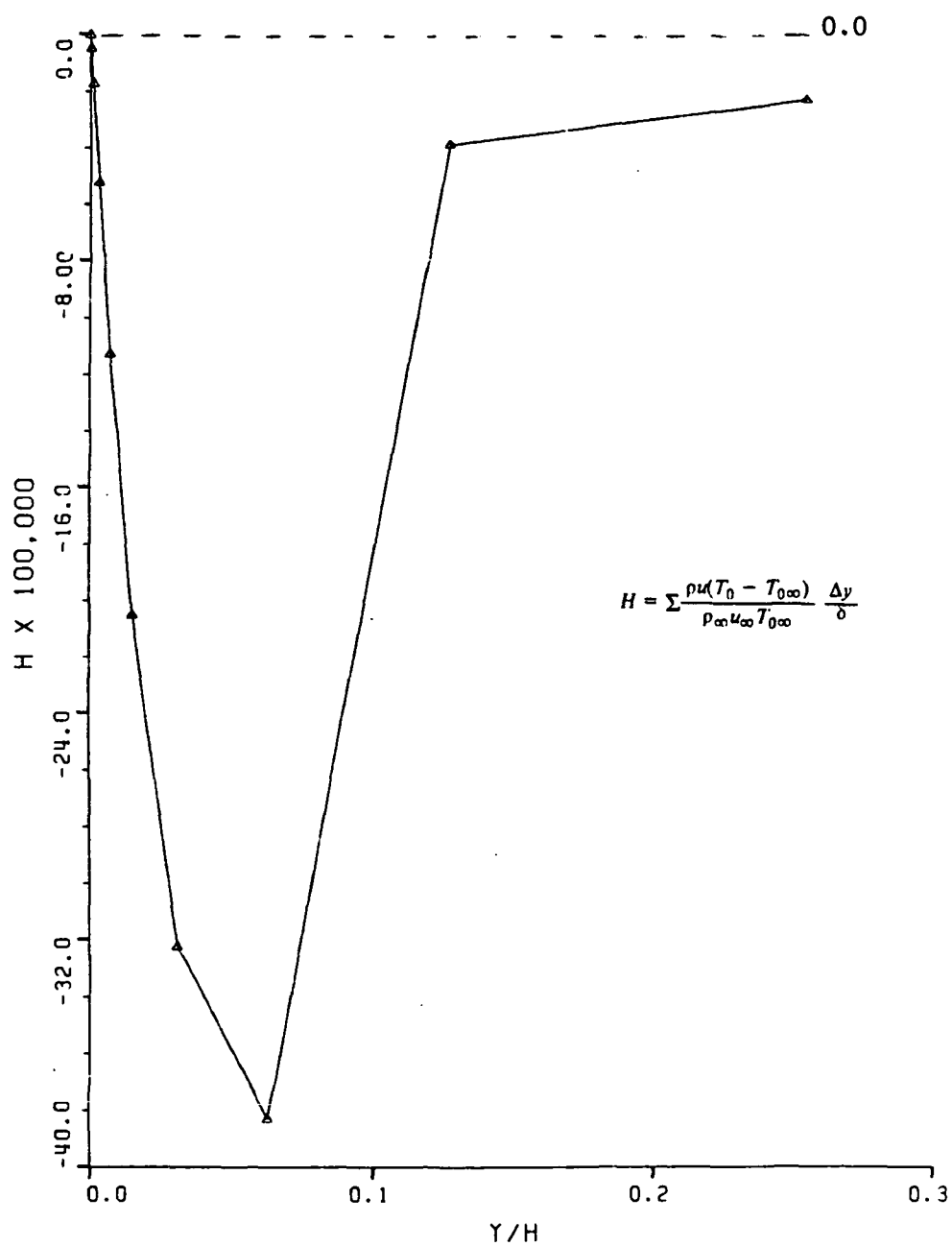


Fig. 3.8.5 Energy Residual For Flat Plate Boundary Layer
at $M = 0.95$

6500 ITERATIONS ENERGY EQUATION INCLUDED
P/P1 AT C = 1.00

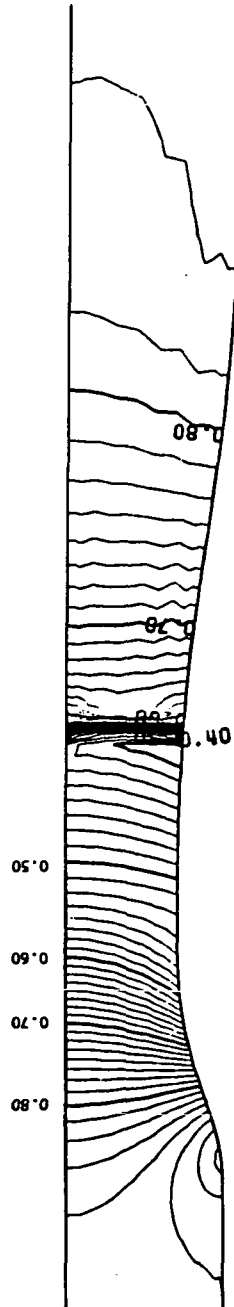


Fig. 3.8.6 Static Pressure Contours For Sajben's Diffuser
With Energy Equation

6500 ITERATIONS
ENERGY EQUATION
MACH AT C = 1.00

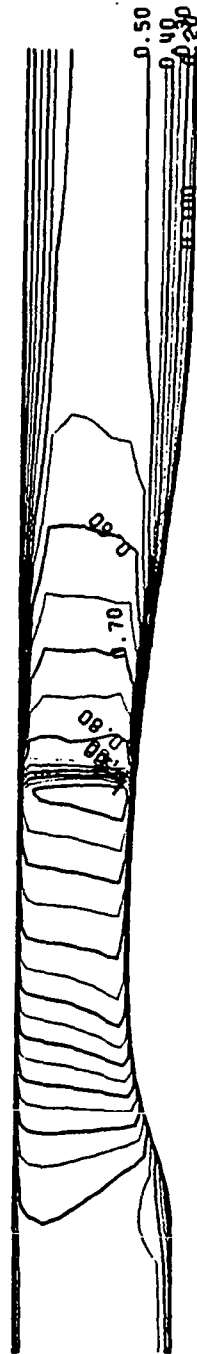


Fig. 3.8.7 Mach Number Contours For Sajben's Diffuser
With Energy Equation

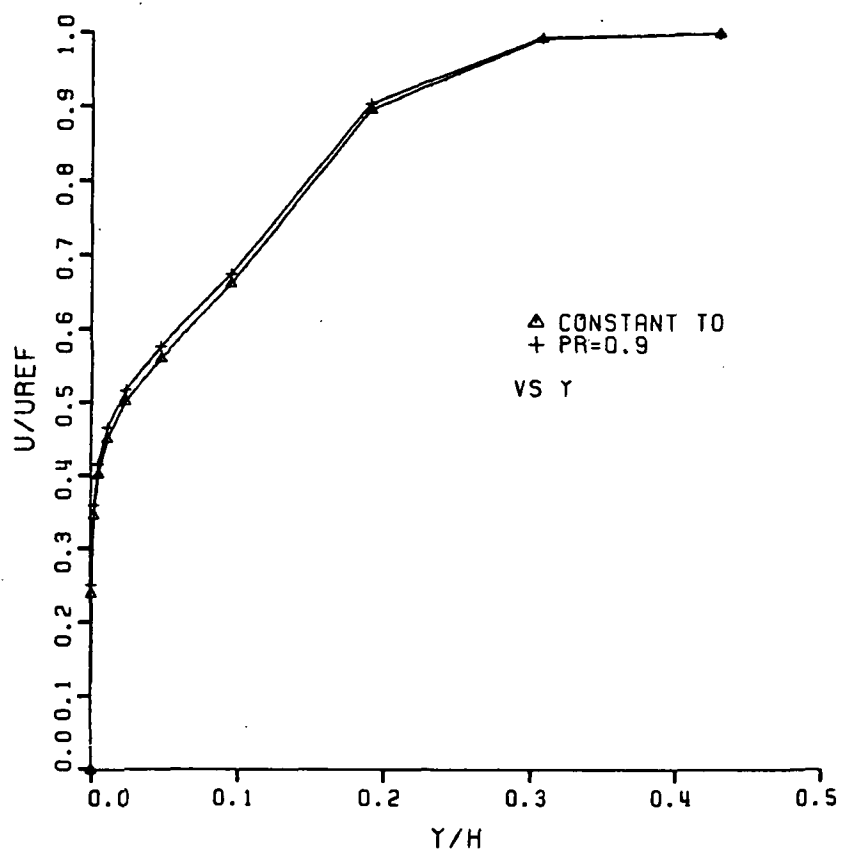


Fig. 3.8.8 Sajben's Diffuser Velocity Profiles at $x/h=7.9$

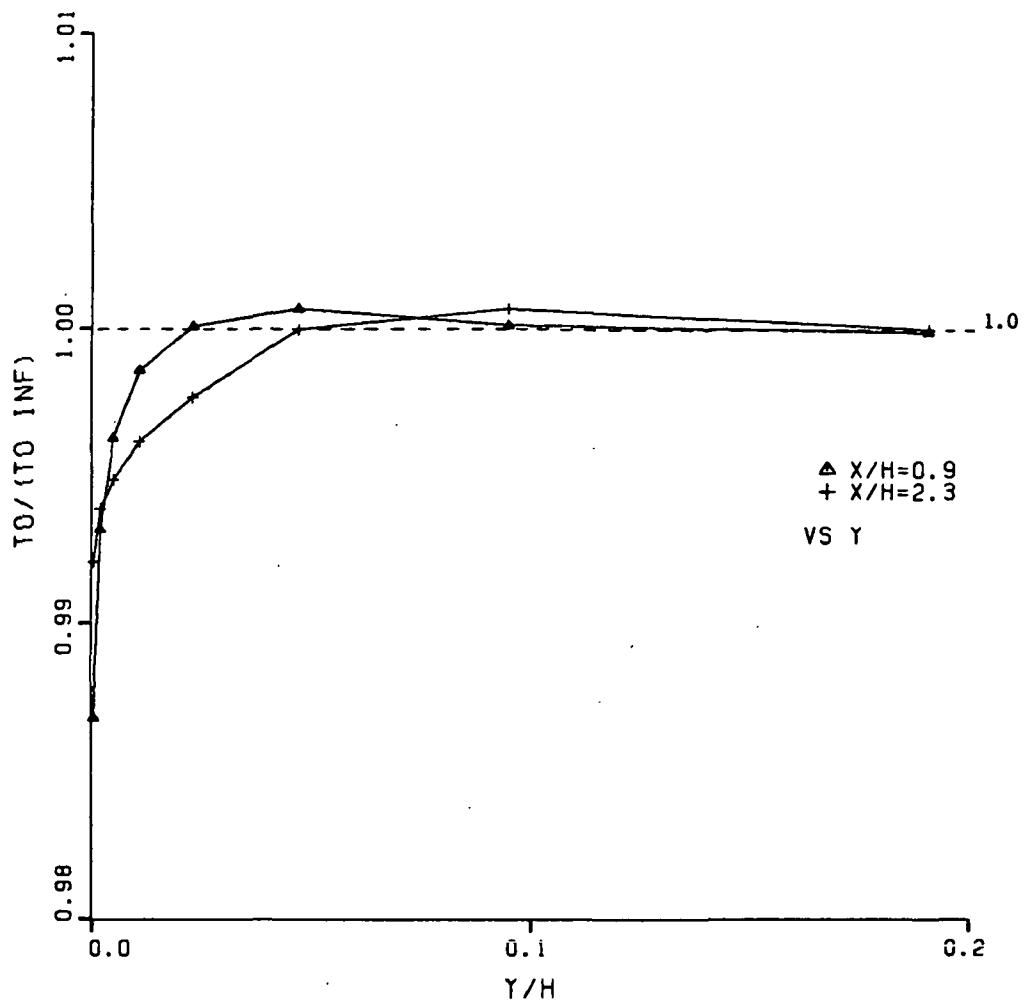


Fig. 3.8.9 Total Temperature Distribution For Sajben's Diffuser

) in the diffuser. The freestream velocity is supersonic at $x/h = 1.9$ (before the shock) and subsonic at $x/h = 3.5$ (after the shock). The calculated recovery factors of .95 and .98 are higher than the values of .93 and .97 expected from Eq. 3.8.5. The near wall control volume boundaries in these calculations were at $y^+ = 32$ and $y^+ = 23$ for the locations $x/h = 1.9$ and $x/h = 3.2$, respectively. These are greater than the minimum y^+ of 10 discussed earlier.

FLAT PLATE TURBULENT BOUNDARY LAYER AT $M = 2.8$

Van Driest (30) presents the total temperature distribution within a flat plate turbulent boundary layer with a freestream Mach number of 2.8. The experimental total temperature distribution is shown in Fig. 3.8.10. The geometry and grid for these calculations are shown in Fig. 3.8.11. The height of the duct was 63.5 mm and the length of the duct was 254 mm. The computational grid shown in Fig. 3.8.11 consists of 21 axial grid points and 14 transverse grid points. The transverse distribution of grid points is shown in Table 3.8.2. The inlet boundary layer thickness of 1/4 inch (6.35 mm) was 10 % of the duct height. The Reynolds number based upon axial distance is approximately 10^7 . To stabilize these supersonic calculations, the upwind effective density method (see section 2.4) was used and the upstream boundary conditions were modified. The inlet velocity, total temperature, and total pressure were specified at the upstream boundary. Three calculations were performed with different assumptions about the turbulent Prandtl number. These assumptions were

1. $Pr_t = 0.90$ $Pr_t = 0.73$
2. $Pr_t = 0.73$ $Pr_t = 0.73$
3. Pr_t varies linearly through the boundary layer from 0.9 at the wall to 0.66 in the freestream.

The turbulent Prandtl number is typically set equal to a constant of 0.9 in calculations (21). The calculated total temperature distribution through this boundary layer using a constant turbulent Prandtl number of 0.9 is shown in Fig. 3.8.12 (represented as triangles). The recovery factor is

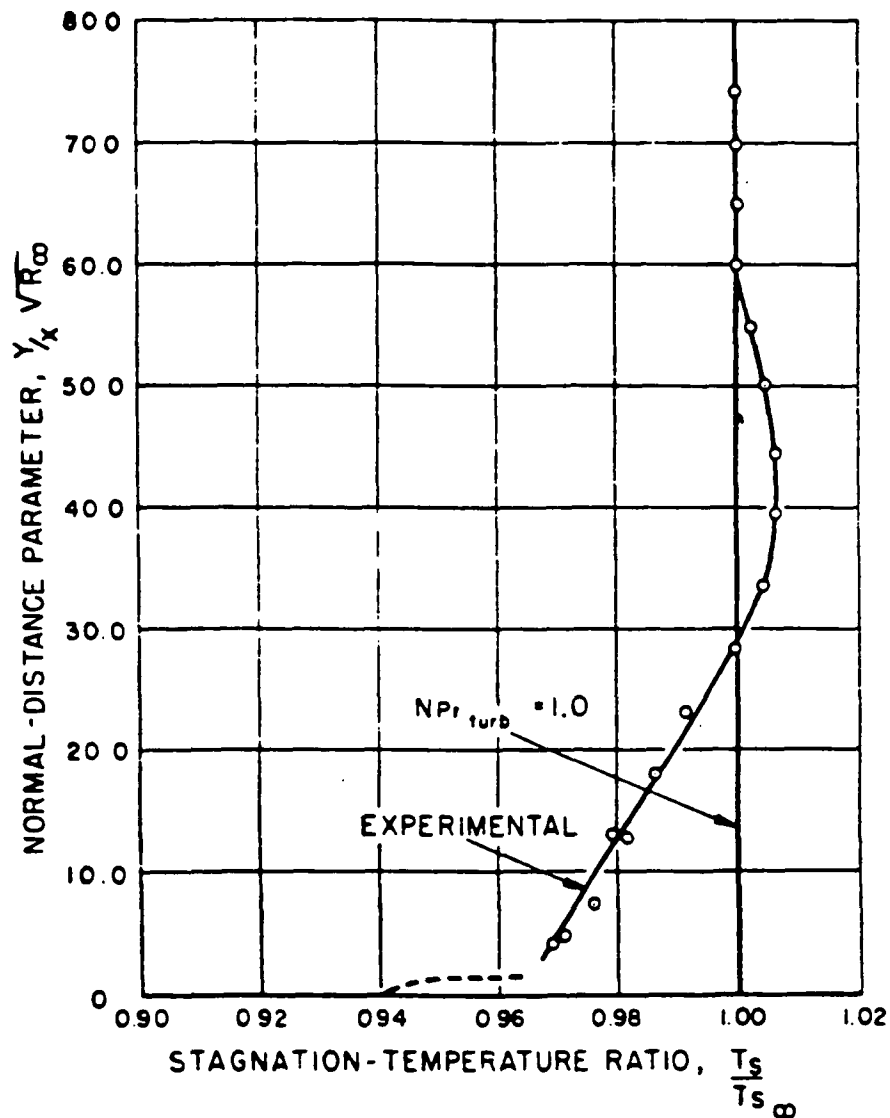


FIG. 24. Stagnation-temperature ratio variation across the turbulent boundary layer at $M_x = 2.8$.

Fig. 3.8.10 Experimental Total Temperature Distribution for Van Driest

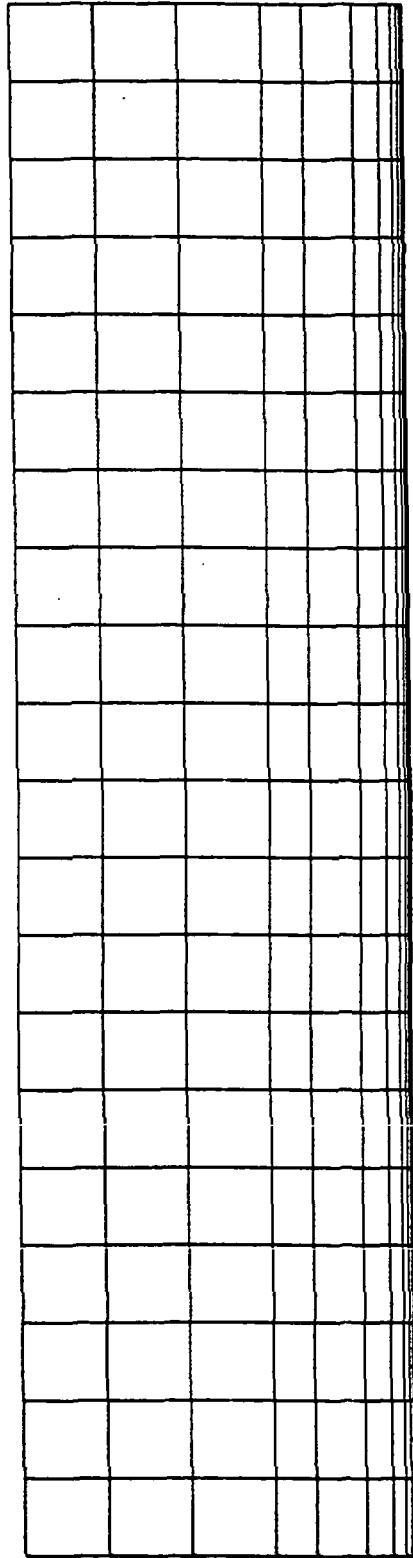


Fig. 3.8.11 Geometry and Grid For Boundary Layer Calculations at $M = 2.8$

Table 3.8.2 Transverse Distribution of Grid Points
For M = 2.8 Test Case

1	0.000055
2	0.00022
3	0.000665
4	0.0020
5	0.0050
6	0.0110
7	0.0230
8	0.0470
9	0.0950
10	0.1910
11	0.3080
12	0.4675
13	0.6805
14	0.8935

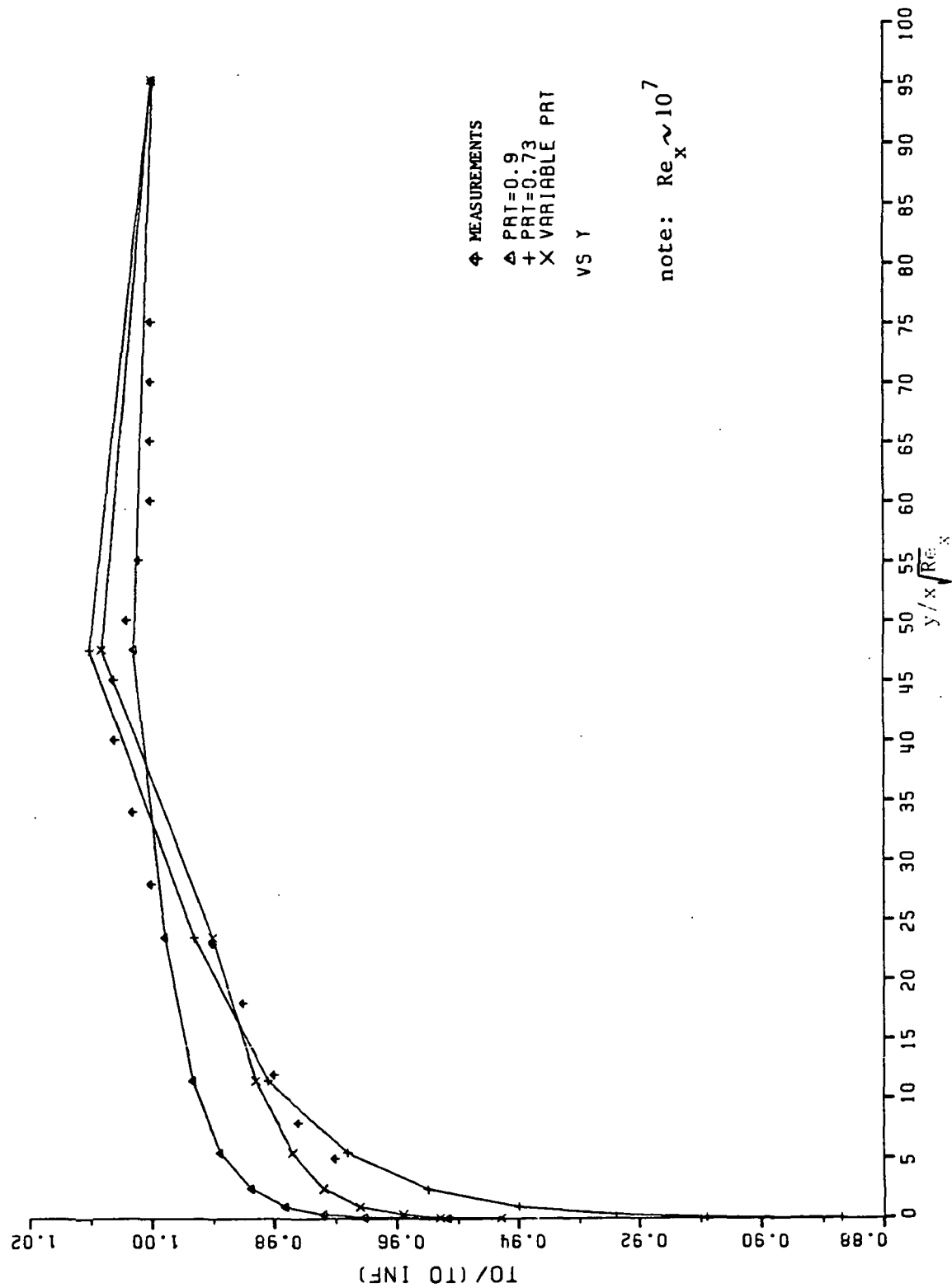


Fig. 3.8.12 Total Temperature Distribution For Flat Plate Boundary Layer at $M = 2.8$

calculated to be 0.920 which compares with the empirically determined value of 0.90. However, the distribution of total temperature through the boundary layer does not compare well with the experiment. If the turbulent Prandtl number is set equal to the laminar Prandtl number of 0.73, the total temperature distribution changes as seen in Fig. 3.8.12 (represented as + 's). The distribution through the outer part of the boundary layer has improved but the recovery factor of 0.813 does not compare well with the experimental value of 0.90. Schlichting (31) notes that the turbulent Prandtl number is not constant through the boundary layer. The experiments of H. Ludwig (32) for turbulent flow through a pipe shows that the Prandtl number varies from approximately 0.9 at the pipe wall to 0.66 at the center of the pipe. This distribution is shown in Fig. 3.8.13. The variation is almost linear. For the third set of calculations, the Prandtl number was assumed to vary linearly through the boundary layer from 0.9 at the wall to 0.66 at the edge of the boundary layer. The total temperature distribution for this case is shown in Fig. 3.8.12 (represented as X's). The total temperature distribution calculated using a variable Prandtl number is compared with the experimental results in Fig. 3.8.14. Both the distribution of total temperature through the boundary layer and the recovery factor of 0.90 are in good agreement with the experimentally measured values.

The calculation of turbulent flow over a flat plate with a freestream Mach number of 0.95 was rerun using this variable turbulent Prandtl number and these results are compared in Fig. 3.8.15 with the total temperatures which were obtained with a constant Prandtl number of 0.9. The recovery factor was calculated to be 0.89 when a variable Prandtl number was used; this is in reasonable agreement with the value of 0.90 expected using Eq. 3.8.5.

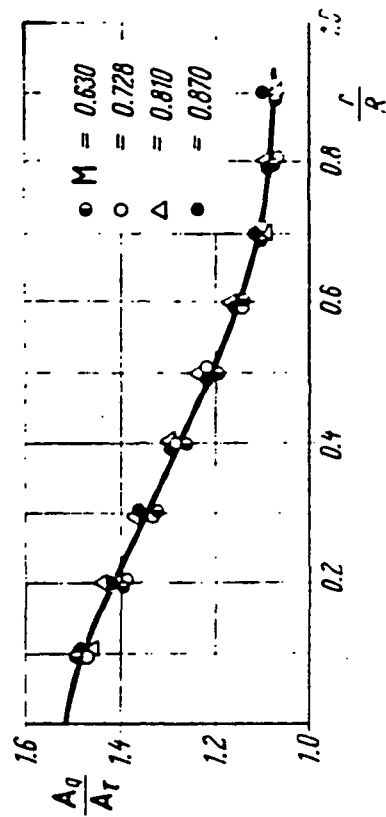


Fig. 23.2. Ratio of the turbulent transfer coefficients A_q/A_r over the length of a radius in turbulent pipe flow, after H. Ludwieg [44]

Reynolds number $R = 3.2 \times 10^4$ to 3.7×10^4 .

Fig. 3.8.13 Ratio of the Turbulent Transfer Coefficient Over the Length of a Radius in Turbulent Pipe Flow. Note $P_t = \frac{A_r}{A_q}$

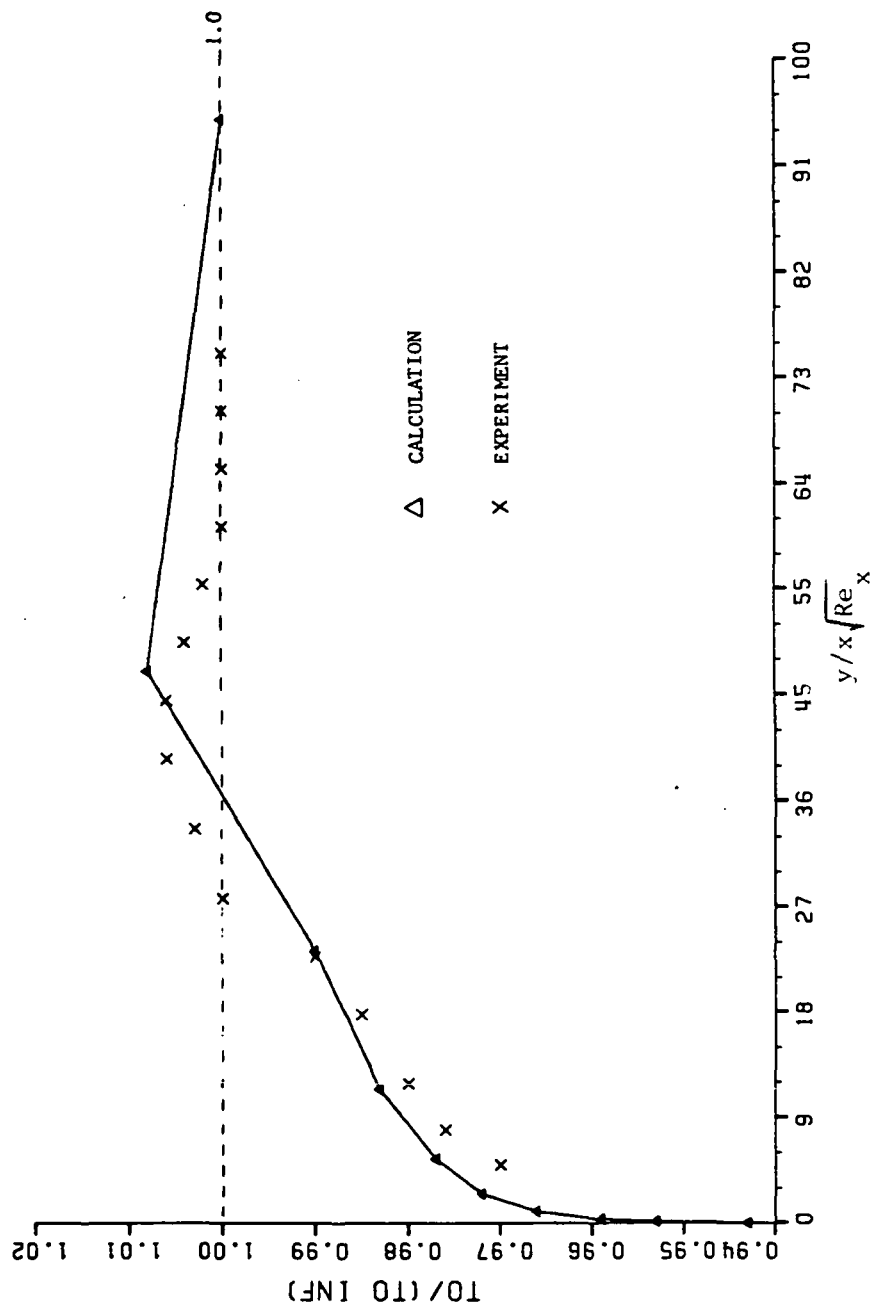


Fig. 3.8.14 Total Temperature Distribution For Flat Plate at $M=2.8$
Computation Vs Experiment

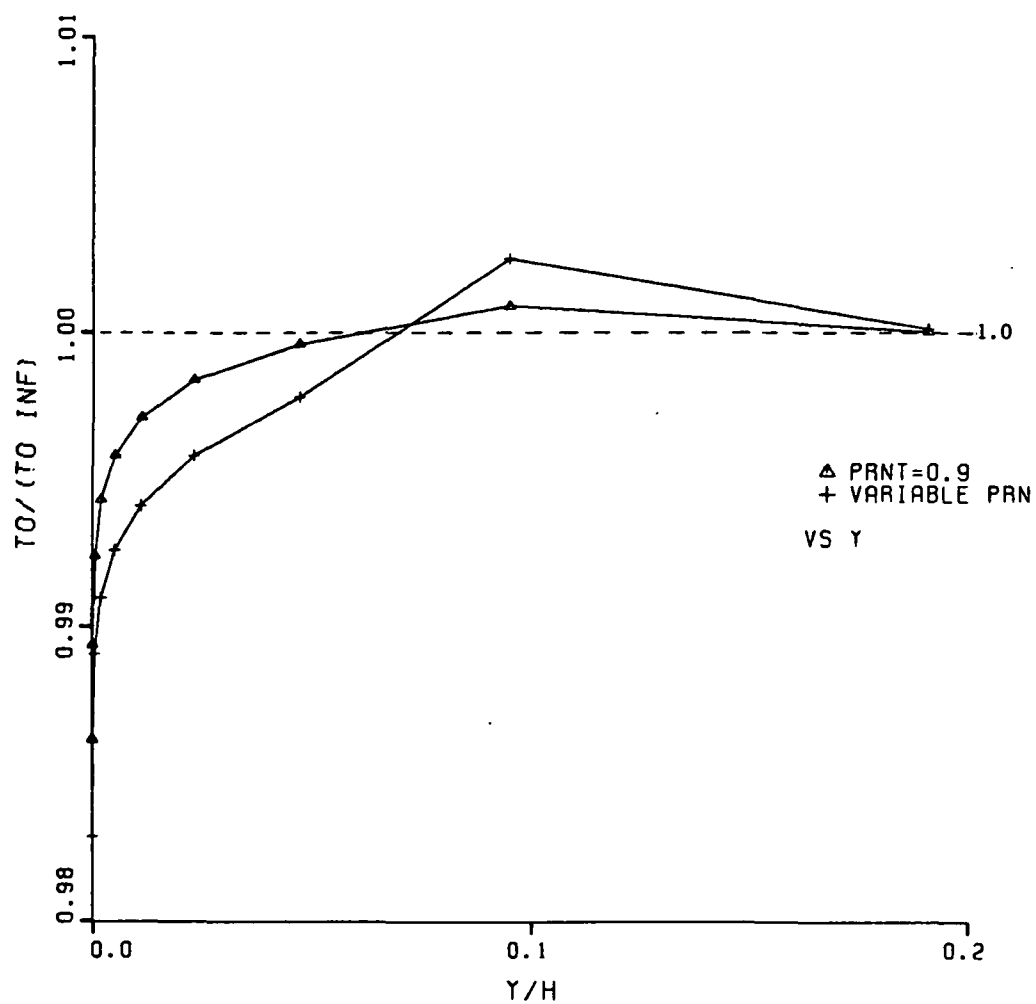


Fig. 3.8.15 Total Temperature Distribution For Flat Plate Boundary Layer at $M=0.95$ With Variable Prandtl Number

4.0 SUMMARY AND CONCLUSIONS

A finite volume time marching method has been extended to allow the calculation of laminar and turbulent flow in ducts. Both subsonic and supersonic flow can be calculated with the method. The starting point for the current method was the finite volume method of Denton (12). Denton's method is currently limited to inviscid flow. Viscous effects have been simulated by Denton and others using inviscid-viscous interaction approaches. The method that is presented in this dissertation solves the Reynolds-averaged form of the Navier-Stokes equations directly.

A number of features have been developed in the current work which allow the calculation of viscous flow with the finite volume time marching method. Some insight has also been shed upon the finite volume method in general in this work.

FEATURES OF THE FINITE VOLUME TIME MARCHING METHOD

The features which make the finite volume time marching method attractive can be summarized as

1. The calculations are performed entirely in the physical domain. No coordinate transformations are needed.

2. Because of the finite volume formulation, mass and momentum are conserved for any grid.
3. The explicit approach is attractive because of its simplicity.
4. When the Euler or Navier Stokes equations are solved using the time marching approach, shocks develop naturally as part of the solution.

ADVANCES MADE IN THE PRESENT WORK

Many changes were needed to create a finite volume time marching method capable of calculating two dimensional laminar and turbulent flow. A much higher level of understanding of the method was needed to extend the finite volume time marching method into the viscous flow regime. Features which are new to this finite volume time marching method can be summarized as

1. Control volumes were introduced which allow calculations to be made without smoothing of flow properties in the transverse direction. In particular, unlike Denton's method, there are the same number of control volumes as node points (same number of equations as unknowns).
2. Convective forms of the momentum and energy equations were used to update the velocity and the total enthalpy. However, at the steady state, the governing equations returned to the conservative form.
3. Time steps for use with the convective forms of the equations were derived. This resulted in time steps for the momentum and energy equations which are different from the time steps for the continuity equation. The time steps also vary spatially.
4. The pressure is updated directly from the continuity equation rather than through the equation of state to aid in the calculation of pressure gradients in boundary layers.

5. A new pressure interpolation scheme was introduced which has improved shock capturing properties when compared with the standard 2 and 3 point interpolation schemes. Pressure interpolation is necessary for stability but here a stability criterion has been employed in deriving a Mach number dependent interpolation scheme.
6. Viscous forces that act on the control volume faces were calculated in the non-orthogonal physical grid arrangement.
7. A multi-volume method for pressure changes in the boundary layer was introduced which allowed calculations to be made with very elongated control volumes. The multi-volume preserves the boundary layer approximation (static pressure changes through the boundary layer are small compared with the free stream velocity head).
8. A method of discretization called transverse upwind differencing was developed to strengthen the centerpoint coefficient of the equations. This differencing enhances the stability of the method when the mass fluxes through the transverse faces become large compared with the mass fluxes through the streamwise faces.
9. A new formulation for the energy equation was introduced which has improved transient behavior when compared with the standard formulation. The new formulation removes the influences of continuity and momentum errors from the energy equation during transients in the solution.

TEST CASES

A number of test cases were used to illustrate the accuracy and the features of the new method. A large range of flow conditions were studied in these test cases . The freestream Mach numbers varied from 0.075 in the Samuel and Joubert test case (section 3.6) to 2.8 in the Van Driest test case (section 3.8). The results obtained in this dissertation can be summarized as follows.

1. **FLAT PLATE LAMINAR BOUNDARY LAYER:** The velocity profiles in a laminar flat plate boundary layer agreed well with the theoretical results.
2. **INVISCID CALCULATIONS OF SAJBEN'S DIFFUSER:** The density and pressure update methods were compared here. When the density update method was used, the total pressure calculated using the effective pressure agreed with the theoretical distribution better than when the thermodynamic pressure was used. The total pressure distribution calculated using the effective density method agreed the best with the theoretical results.
3. **THE INFLUENCE OF TRANSVERSE SMOOTHING ON A STEP PROFILE IN A STRAIGHT DUCT:** A step profile in inlet Mach number was drastically altered by the transverse smoothing that is needed to stabilize the calculations using the old control volumes. When the new control volumes were used instead, the inlet Mach number profile changed very little through the duct.
4. **1-D COMPUTATIONAL TESTS OF SHOCK CAPTURING USING PRESSURE INTERPOLATION FORMULAE TO CALCULATE EFFECTIVE DENSITY:** Results from calculations using the 2 point, 3 point, and M&M interpolation formulas were compared with the theoretical 1-D solution through a converging-diverging nozzle. The new pressure interpolation scheme gave improved shock capturing properties when compared with the usual two and three point interpolation schemes. Overshoots and undershoots in properties were essentially eliminated when the Mach number dependent interpolation formula was used. All the interpolation formulae accurately predicted the overall total pressure loss through the shock.
5. **LAMINAR BOUNDARY LAYER IN TWO CONVERGING DUCTS:** A laminar boundary layer was calculated on the curved wall of two converging ducts. One of ducts had a non-smooth geometry which resulted in solutions which were not smooth. In Fig 3.5.5, the skin friction coefficients from the finite volume calculations were compared with the skin fric-

tion coefficients calculated using the integral method of Thwaites and the agreement was good. A number of multivolume methods and grid arrangements were investigated and a non-uniform grid was found to have better convergence properties than a uniform grid.

6. **SAMUEL AND JOUBERT INCOMPRESSIBLE TURBULENT BOUNDARY LAYER:** Incompressible turbulent boundary layer flow in an adverse pressure gradient was calculated using the current method. The agreement between the calculated and measured skin friction coefficient, turbulent shear stress distributions, and the mean velocity profiles was good.
7. **SAJBEN'S DIFFUSER CALCULATIONS:** Transonic viscous flow through a converging diverging nozzle was calculated. The computed and measured velocity profiles were in good agreement especially near the exit of the nozzle. The computed and measured shock location were compared in Fig. 3.7.6 and were found to be in good agreement. The ratio of $P_t/P_{t,inlet}$ was calculated to be .9615. This was in good agreement with the measured value of 0.965.
8. **ENERGY EQUATION TEST CASES:** Four test cases were used to investigate introduction of the new formulation of the energy equation into the method. The new formulation was seen to give improved transient behavior when compared with the standard formulation. For turbulent flow over a flat plate with a freestream Mach number of 0.95, the calculated recovery factor of .91 compared well with the empirically determined value (see Eq. 3.8.5) of 0.90. For flat plate boundary layer flow with a freestream Mach number of 2.8, the calculated total temperature profile was improved by using a variable Prandtl number through the boundary layer. The calculated recovery factor of 0.90 agreed very well with the empirically determined value of 0.9.

CONCLUSIONS

The following important observations were made from these test cases and other experience with the current method:

1. The geometry of the duct used in the calculations must be smooth to obtain smooth solutions (see section 3.5).
2. In the boundary layer region, a non-uniform grid in the transverse direction, with a factor of 2 ratio in grid spacing, is preferred for stability reasons. A factor of 2 spacing is preferred because the multi-volume procedure requires that pressure changes for each successively smaller multi-volume region decrease rapidly.
3. If a factor of approximately 2 in grid spacing is used in the multi-volume region, the multi-volume procedure may be simplified by using the control volume furthest from the wall as the basis for the time step to be used for the entire multivolume region (see section 3.5).
4. The new pressure interpolation scheme gives improved shock definition when its results are compared with the results from the 2 and 3 point interpolation schemes (see section 3.4).
5. The total pressure loss through a 1-D shock is predicted well by all of the interpolation schemes considered here(see section 3.4).
6. The Prandtl mixing length model for the eddy viscosity gave good results for all of the viscous test cases investigated.
7. The skin friction coefficients, velocity profiles, and turbulent shear stress distributions were calculated with good accuracy through the boundary layer with as few as 5 to 7 grid points in the boundary layer as was seen from the Samuel and Joubert results (section 3.6).
8. Smoothing of flow properties, either linear or non-linear, as used by Denton, can greatly degrade the accuracy of the results when large gradients in properties exist (see section 3.3).
9. Transverse upwind differencing was needed to stabilize the transient solution of some of the test cases, however, there was no upwinding retained at the steady state.

10. The height of the control volume just outside of the multi-volume region should be approximately equal to the sum of heights of the control volumes within the multivolume region. This arrangement is not necessary but is preferred so that pressure changes in the multi-volume and freestream regions match properly.
11. A time factor of 4.0 is typically required during the initial part of a solution, but the time factor can typically be changed to 2.0 later in the solution.
12. When the full energy equation was used, the adiabatic wall temperature was predicted well if a constant turbulent Prandtl number of 0.9 was used, however, the distribution of total temperature through the boundary layer was not predicted well (see section 3.8).
13. The total temperature distribution in the outer part of the boundary layer was improved if a simple linear variation in Prandtl number was assumed through the boundary layer (see section 3.8).
14. The new formulation of the energy equation gives improved transient solution behavior (see section 3.8).
15. The assumption of constant total temperature used in test cases 3.1-3.7 should not adversely affect the accuracy of those results (see section 3.8).

SUGGESTIONS FOR FURTHER WORK

The current work is limited to attached flow. An important contribution would be to extend the method to be able to calculate regions of backflow. This would be especially important in the area of transonic flow since when the Mach number upstream of a normal shock exceeds approximately 1.3 the flow will separate behind the shock. By the choice of control volumes, the flow direction in the present method must essentially be in the I grid direction. Therefore to permit the calculation of backflow, a different control volume arrangement may be needed.

The method could also be extended to calculate the flow through turbomachinery blade rows or blade rows as has been done by Dawes. The method may encounter problems at the leading and trailing edges of such geometries because of the long and thin control volume seen at the surfaces of the blades. By necessity, these long and thin control volumes must extend upstream and downstream of the leading and trailing edges, respectively. The current method has shown that it can calculate both laminar and turbulent flows, however, a model for transition would be needed if the method were to be applied to turbomachinery blade rows and cascades. The control volumes used in the present work have been extended to three dimensional inviscid flow (19), however, further work would be required to allow viscous calculations in three dimensions. Three dimensional effects could be partially modelled by using a quasi-3-D approach; for example, the end wall boundary layer effects could be modelled by including an axial velocity density ratio in the calculations.

As can be seen, there is much more to investigate in this area but the present contribution has provided significant and unique contributions to the understanding of the time marching finite volume method in general and what is required to extend the method to viscous flow in particular. Hopefully, this work will provide insight to future workers in the finite volume area and will also inspire workers to try approaches which are different than the current computational philosophy.

Appendix A. TRUNCATION ERROR OF PRESSURE INTERPOLATION EQUATION

The truncation error of the interpolated pressure used to calculate the density in Eq. 2.4.57 may be determined using a Taylor series analysis. The interpolated pressure P^* is given by

$$P_{I+1}^e = P_I + a_0(P_{I+1} - P_I) + a_1(P_{I+1} - P_{I-1})/2 + a_2(P_{I+1} - P_{I-2})/3 \quad (A.1.1)$$

and to determine the accuracy of P^* we will look at the magnitude of $P_{I+1}^e - P_{I+1}$. With grid spacing h , and expanding about $I+1$, we have

$$P_{I-2} = P - 3hP' + 9(h^2/2)p'' - O(h^3) \quad (A.1.2a)$$

$$P_{I-1} = P - 2hP' + 4(h^2/2)p'' - O(h^3) \quad (A.1.2b)$$

$$P_I = P - hP' + (h^2/2)p'' - O(h^3) \quad (A.1.2c)$$

$$P_{I+1} = P \quad (A.1.2d)$$

Therefore,

$$P_{I+1}^e - P_{I+1} = h(a_0 + a_1 + a_2 - 1)P' - (h^2/2)(a_0 + 2a_1 + 3a_2 - 1)P'' + O(h^3). \quad (A.1.3)$$

And if

$$a_0 + a_1 + a_2 = 1 \quad (A.1.4)$$

then the difference between P^* and P is of the order of h^2 , so that P^* is a second order accurate approximation for P .

Appendix B. VELOCITY GRADIENT IN A NON-ORTHOGONAL GRID

To calculate the velocity gradient, ∇u_L , for a nonorthogonal grid system, we must be able to transform gradients in the grid directions (I,J, and K) into gradients in the coordinate directions (x,y, and z). From the transformation law of a vector, the gradient of a scalar in one coordinate system can be related to the gradient in another coordinate system using the direction cosines between the two coordinate systems. We will use the cartesian system as our base coordinate system here. Let D_I, D_J , and D_K be directional vectors which have a direction parallel with the non-orthogonal coordinate system and span a unit change in I,J, or K respectively. These vectors are shown in Fig. A 2.1. They can be described in terms of their cartesian components. In other words, we can represent them as

$$D_I = a_1 i + b_1 j + c_1 k \quad (A.2.1)$$

$$D_J = a_2 i + b_2 j + c_2 k \quad (A.2.2)$$

$$D_K = a_3 i + b_3 j + c_3 k \quad (A.2.3)$$

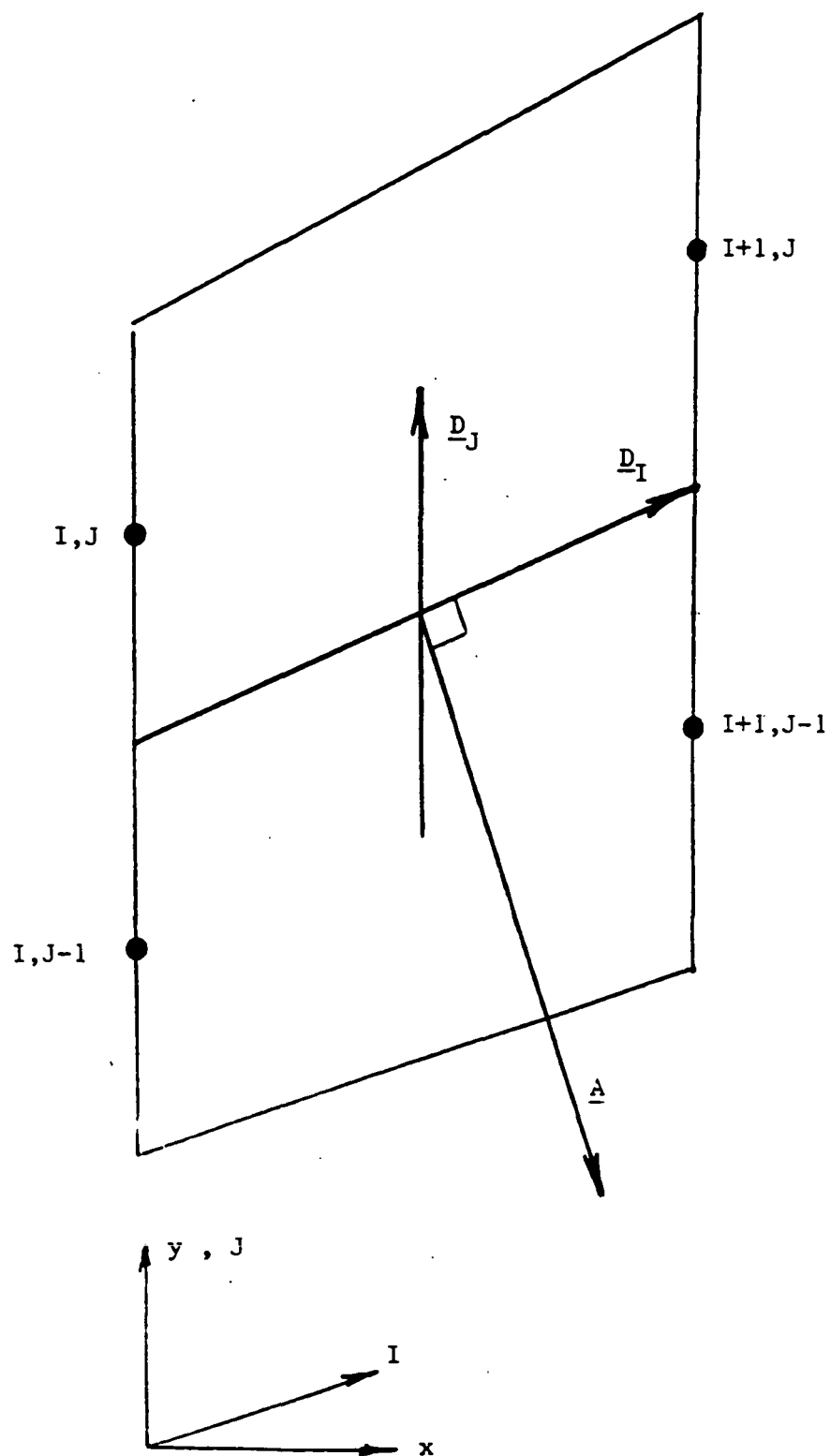


Fig. A2.1 Identification of Directional Vectors

where i, j , and k are unit vectors in the cartesian coordinate directions, and a, b , and c are the magnitudes of the components of the directional vectors.

The change of a variable u , from one point to another within a grid system can be represented as

$$\frac{\partial u}{\partial I} = u_{I+1} - u_I = \int_I^{I+1} d\mathbf{r} \cdot \nabla u \quad (A.2.4)$$

where \mathbf{r} is a position vector between the two nodes. Rather than dealing with a local derivative in a continuum, we are dealing with approximations of derivatives using finite changes. If the directional vector, \mathbf{D}_I , is chosen such that its termini correspond to the nodes at which the properties are evaluated in Eq. A.2.4, and taking ∇u as uniform between grid points,

$$\frac{\partial u}{\partial I} = (\mathbf{r}_{I+1} - \mathbf{r}_I) \cdot \nabla u. \quad (A.2.5)$$

But $\mathbf{D}_I = \mathbf{r}_{I+1} - \mathbf{r}_I$ therefore,

$$\frac{\partial u}{\partial I} = \mathbf{D}_I \cdot \nabla u \quad (A.2.6)$$

$$\frac{\partial u}{\partial J} = \mathbf{D}_J \cdot \nabla u \quad (A.2.7)$$

$$\frac{\partial u}{\partial K} = \mathbf{D}_K \cdot \nabla u \quad (A.2.8)$$

where I, J, and K are the coordinate indices for the non-orthogonal coordinate system. Expanding equations A 2.6, A 2.7, and A 2.8, we get

$$\frac{\partial u}{\partial I} = a_1 \frac{\partial u}{\partial x} + b_1 \frac{\partial u}{\partial y} + c_1 \frac{\partial u}{\partial z} \quad (A.2.9)$$

$$\frac{\partial u}{\partial J} = a_2 \frac{\partial u}{\partial x} + b_2 \frac{\partial u}{\partial y} + c_2 \frac{\partial u}{\partial z} \quad (A.2.10)$$

$$\frac{\partial u}{\partial K} = a_3 \frac{\partial u}{\partial x} + b_3 \frac{\partial u}{\partial y} + c_3 \frac{\partial u}{\partial z} \quad (A.2.11)$$

where $a_1 = D_{I,x}$, the x component of D_I ; $b_1 = D_{I,y}$ etc... Equations A.2.7, A.2.10, and A.2.11 can be combined into a single matrix equation,

$$\begin{Bmatrix} \frac{\partial u}{\partial I} \\ \frac{\partial u}{\partial J} \\ \frac{\partial u}{\partial K} \end{Bmatrix} = \begin{bmatrix} a_1 & b_1 & c_1 \\ a_2 & b_2 & c_2 \\ a_3 & b_3 & c_3 \end{bmatrix} \begin{Bmatrix} \frac{\partial u}{\partial x} \\ \frac{\partial u}{\partial y} \\ \frac{\partial u}{\partial z} \end{Bmatrix} \quad (A.2.12)$$

For the calculation of viscous stresses, Eq. 2.7.5, we need the gradients of velocity, ∇u_L , in cartesian coordinates. To obtain this gradient, we need to take the inverse of the above matrix $[A]$, in other words,

$$\begin{Bmatrix} \frac{\partial u}{\partial x} \\ \frac{\partial u}{\partial y} \\ \frac{\partial u}{\partial z} \end{Bmatrix} = \begin{bmatrix} a_1 & b_1 & c_1 \\ a_2 & b_2 & c_2 \\ a_3 & b_3 & c_3 \end{bmatrix}^{-1} \begin{Bmatrix} \frac{\partial u}{\partial I} \\ \frac{\partial u}{\partial J} \\ \frac{\partial u}{\partial K} \end{Bmatrix} \quad (A.2.13)$$

The inverse of matrix A, $[A]^{-1}$, will now be determined. From linear algebra,

$$[A]^{-1} = \frac{1}{|A|} (\text{adj}[A]) \quad (A.2.14)$$

where $|A|$ is the determinant of $[A]$ and $\text{adj}[A]$ is the adjoint of $[A]$. The determinant of $[A]$ is

$$\det[A] = \begin{vmatrix} a_1 & b_1 & c_1 \\ a_2 & b_2 & c_2 \\ a_3 & b_3 & c_3 \end{vmatrix} =$$

$$a_1 \begin{vmatrix} b_2 & c_2 \\ b_3 & c_3 \end{vmatrix} - b_1 \begin{vmatrix} a_2 & c_2 \\ a_3 & c_3 \end{vmatrix} + c_1 \begin{vmatrix} a_2 & b_2 \\ a_3 & b_3 \end{vmatrix} =$$

$$a_1(b_2c_3 - b_3c_2) - b_1(a_2c_3 - a_3c_2) + c_1(a_2b_3 - a_3b_2) . \quad (A.2.15)$$

This can be identified as

$$\det[A] = D_I \cdot (D_J \times D_K) \quad (A.2.16)$$

Now let us represent the adjoint of A , $\text{adj}[A]$, in the form

$$\text{adj}[A] = \begin{bmatrix} A_{11} & A_{12} & A_{13} \\ A_{21} & A_{22} & A_{23} \\ A_{31} & A_{32} & A_{33} \end{bmatrix} \quad (A.2.17)$$

where the components of the adjoint matrix are

$$A_{11} = \begin{vmatrix} b_2 & c_2 \\ b_3 & c_3 \end{vmatrix} = b_2c_3 - b_3c_2 \quad (A.2.18)$$

However, A_{11} , can be identified as the x-component of $\underline{D}_J \times \underline{D}_K$, in other words,

$$b_2c_3 - b_3c_2 = \text{x component of } \underline{D}_J \times \underline{D}_K \quad (A.2.19)$$

The components of the adjoint matrix, A_{12} and A_{13} , are the y and z components of $\underline{D}_J \times \underline{D}_K$. Both the results from the numerator and denominator of Eq. A.2.12, lead to the result that

$$\nabla u_L = \frac{\underline{D}_J \times \underline{D}_K}{D_I \cdot (\underline{D}_J \times \underline{D}_K)} \frac{\partial u_L}{\partial I} + \frac{\underline{D}_K \times \underline{D}_I}{D_I \cdot (\underline{D}_J \times \underline{D}_K)} \frac{\partial u_L}{\partial J} + \frac{\underline{D}_I \times \underline{D}_J}{D_I \cdot (\underline{D}_J \times \underline{D}_K)} \frac{\partial u_L}{\partial K} \quad (A.2.20)$$

This result can be generalized to the other two components of velocity, v and w. This is the result that is used to calculate velocity gradients in the current program.

REFERENCES

1. Jameson, A. "Steady-State Solution of the Euler Equations for Transonic Flow," Transonic, Shock, and Multidimensional Flows: Advances in Scientific Computing, Academic Press, Inc., 1982.
2. McDonald, P. W. , "The Computation of Transonic Flow Through Two Dimensional Gas Turbine Cascades," ASME Paper 71-GT-89.
3. Denton, J. D. , "Extension of the Finite Area Time Marching Method to Three-Dimensions," VKI Lecture Series 84, Transonic Flow in Axial Turbomachines, February 1976.
4. Singh, U. K. , "A Computation and Comparison with Measurement of Transonic Flow in an Axial Compressor Stage with Shock and Boundary Layer Interaction," ASME Paper 81-Gr/GT-5.
5. Singh, U. K. , "Computation of Transonic Flows in Cascade with Shock and Boundary Layer Interaction," Von Karmen Institute, Brussels, Lecture Series "Shock-Boundary Layer Interaction in Turbomachines," June 1980.
6. Green, J.E. "Application of Head's Entrainment Method to the Prediction of Turbulent Boundary Layers and Wakes in Compressible Flow," RAE Technical Report 72079, 1972.
7. Calvert, W. J. and Herbert, M. V., "An Inviscid-Viscous Interaction Method to Predict the Blade-to-Blade Performance of Axial Compressors," Aeronautical Quarterly, Vol XXXI, Part 3 (August 1980)
8. Calvert, W. J. , "An Inviscid-Viscous Interaction Treatment to Predict the Blade-to-Blade Performance of Axial Compressors With Leading Edge Normal Shock Waves," ASME Paper 82-GT-135.
9. Calvert, W. J. , "Application of an Inviscid-Viscous Interaction Method to Transonic Compressor Cascades," AGARD Conference Proceedings 135 "Viscous Flow in Turbomachines", Copenhagen, Denmark, 1983.
10. Green, J. E., Weeks, D. J. and Brooman, J. W. F. , "Prediction of Turbulent Boundary Layers and Wakes in Compressible Flow by a Lag-Entrainment Method," A.R.C. R&M 3771, 1972.

11. East, L. F., Smith, P. D. and Merryman, P. J. , "Prediction of the Development of Separated Turbulent Boundary Layers by the Lag-Entrainment Method," RAE Report TR 77046, ARC Paper No. 37435, 1977.
12. Denton, J.D., "An Improved Time Marching Method for Turbomachinery Calculations," ASME Paper 82-GT-239.
13. Denton, J. D., "A Method of Calculating Fully Three Dimensional Inviscid Flow through Any Type of Turbomachine Blade Row," Lecture Notes for ASME Short Course on 3-D Flows in Turbomachinery Blade Rows, Phoenix, AZ, March 1983.
14. Denton, J. D., "The Calculation of Fully Three Dimensional Flow through Any Type of Turbomachine Blade Row," Lecture Notes for ASME Short Course on 3-D Flows in Turbomachinery Blade Rows, Houston, TX, March 1985, and AGARD Lecture Series No. 140 on 3-D Computation Techniques Applied to Internal Flows in Propulsion Systems, Rome, Italy, Cologne, West Germany, and Paris, France, June 1985.
15. Van Hove, W., "Calculation of Three-Dimensional, Inviscid, Rotational Flow in Axial Turbine Blade Rows," ASME Paper No. 83-GT-119.
16. Holmes, D. G., and Tong, S. S. , "A Three-Dimensional Euler Solver for Turbomachinery Blade Rows," ASME Paper No. 84-GT-79.
17. Dawes, W. N. , "Computation of Off-Design Flows in a Transonic Compressor Rotor," ASME Paper No. 85-GT-1.
18. Subramanian, S. V., and Bozzola, R. , "Application of Runge Kutta Time Marching Scheme for the Computation of Transonic Flows in Turbomachines," NASA Technical Memorandum 86997, 1985.
19. Moore, J., Nicholson, S., and Moore, J.G. "Development of the Finite-Volume Time Marching Method For Improved Shock Capturing and Reduced Numerical Losses," V.P.I. & S.U. Turbomachinery Research Group Report No. JM/85-11, December 1985.
20. Nicholson, S., "Development of a Finite Volume Time Marching Method," V.P.I. & S.U. Turbomachinery Research Group Report No. JM/85-3, February 1985.
21. Anderson, D. A., Tannehill, J. C., and Pletcher, R. H. Computational Fluid Mechanics and Heat Transfer, Hemisphere Publishing Company, 1984.
22. Moore, J. G., Personal Communication
23. Bogar, T.J., Sajben, M. and Kroutil, J.C., "Characteristic Frequency and Length Scales in Transonic Diffuser Flow Oscillations," AIAA Paper 81-1291.
24. Salmon, J.T., Bogar, T.J., and Sajben, M. "Laser Velocimeter Measurements in Unsteady, Separated, Transonic Diffuser Flows," AIAA Paper 81-1197.
25. Cebeci, T. and Bradshaw, P. Momentum Transfer in Boundary Layers, Hemisphere Publishing Corporation 1977.
26. Kline, S.J. ,Cantwell, B.J., and Lilley, G.M., "Complex Turbulent Flows Computation-Experiment," 1980-81 AFOSR-HTTM-Stanford Conference on Complex Turbulent Flows, 1982.

27. Moore, J. and Moore, J.G., "Calculation of Five Turbulent Flows Using the Moore Cascade Flow Program," 1980-81 AFOSR-HTTM-Stanford Conference on Complex Turbulent Flows, Volume III, 1982.
28. Liou, M.S., Coakley, T.J., and Bergmann, M.Y., "Numerical Simulation of Transonic Flow in Diffusers," AIAA Paper No. 81-1240.
29. Liu, N.-S., Shamroth, S.J., and McDonald, H., "Numerical Solutions of Navier-Stokes Equations for Compressible Turbulent Two/Three Dimensional Flows in the Terminal Shock Region of an Inlet /Diffuser," NASA Contractor Report 3723, August 1983.
30. Talcott, N.A., and Kumar, A., "Two-Dimensional Viscous Simulation of Inlet/Diffuser Flows with Terminal Shocks," Journal of Propulsion, Vol. 1, No. 2, March-April 1985.
31. Van Driest, E. R., "Turbulent Boundary Layer in Compressible Fluids," Journal of the Aeronautical Sciences, Vol. 18, No. 3, March 1951.
32. Schlichting, H., Boundary Layer Theory, Sixth Edition, McGraw Hill, 1968.
33. Ludweig, H., Bestimmung des Verhältnisses der Austauschkoefizienten für Wärme und Impuls bei turbulenten Grenzschichten. ZFW 4, 73-81 (1956).

C-4